School of Engineering and Material Science,
Queen Mary University of London

The Finite Block Method: A Meshless Study of Interface Cracks in Bi-Materials

Perry Hinneh

A Thesis Submitted to Queen Mary University of London for the Degree of Doctor of Philosophy

Queen Mary and Westfield College

University of London

Mile End Road

London E1 4NS, UK

April 2018

Declarations

I, Perry Hinneh, confirm that the research included within this thesis is my own work or that where it has been carried out in collaboration with, or supported by others, that this is duly acknowledged below and my contribution indicated. Previously published material is also acknowledged below.

I attest that I have exercised reasonable care to ensure that the work is original, and does not to the best of my knowledge break any UK law, infringe any third party's copyright or other Intellectual Property Right, or contain any confidential material.

I accept that the College has the right to use plagiarism detection software to check the electronic version of the thesis.

I confirm that this thesis has not been previously submitted for the award of a degree by this or any other university.

Signature: Perry Hinneh

Date: 16/April/2018

Details of collaboration and publications:

See section 8.5 of this thesis.

Acknowledgements

With God and a little patience of Job all things are possible …

I would like to express my greatest appreciation and sincere respect for my supervisor Dr Pihua Wen. He has served as my fountain of knowledge during my seven years of research. He has always been supportive and positive when it comes to pushing me to work harder. Without his drive and patience for explaining some of the difficult mathematics, completing this research would have been very difficult. I have learned a lot from Dr Wen and I leave this research with a different mind-set and a different man.

The phrase no man is an island has never been so true until I decided to take on a PhD. My studies have been sustained by the efforts and hard work of my wife Rebecca Adu Hinneh, my mum Joyce Gaspard, my siblings Nathan Ofori, Gloria Gaspard, Gideon Gaspard and Glenda Gaspard. They are truly my source of inspiration and motivation for the last seven years of research. I want to thank my mum for all the cooking. Holding a full-time job and a part-time PhD can be difficult to make time for cooking so thank you very much. Nobody ever achieved anything on an empty stomach.

Finally, I would like to thank all my friends and family members around the world for all their support and encouragement. I really appreciate it.

Special thank you to;
Nathan Ofori
Ralph Caesar-Majias
Folayosoreoluwa Akinmayowa Oladele Osekita

Abstract

The ability to extract accurately the stress intensity factor and the T-Stress for fractured engineering materials is very significant in the decision-making process for in-service engineering components, mainly for their functionality and operating limit. The subject of computational fracture mechanics in engineering make this possible without resulting to expensive experimental processes.

In this thesis, the Finite Block Method (FBM) has been developed for the meshless study of interface stationary crack under both static and dynamic loading in bi-materials. The finite block method based on the Lagrangian interpolation is introduced and the various mathematical constructs are examined. This includes the use of the mapping technique. In a one-dimensional and a two-dimensional case, numerical studies were performed in order to determine the interpolation error.

The finite block method in both the Cartesian coordinate and the polar coordinate systems is developed to evaluate the stress intensity factors and the T-stress for interface cracks between bi-materials. Using the William's series for bi-material, an expression for approximating the stress and displacement at the interface crack tip is established. In order to capture accurately the stress intensity factors and the T-stress at the crack tip, the asymptotic expansions of the stress and displacement around the crack tip are introduced with a singular core technique.

The accuracy and capability of the finite block method in evaluating interface cracks is demonstrated by several numerical assessments. In all cases, comparisons have been made with numerical solutions by using the boundary collocation method, the finite element method and the boundary element method, etc.

Table of Contents

List of Tables

List of Figures

Abbreviations

BEM	Boundary Element Method
CCP	Centre Cracked Plate
CFD	Computational Fluid Dynamics
CFRP	Carbon Fibre Reinforces Plastics
DECP	Double Edge Cracked Plate Specimen
DEM	Diffuse Element Method
DEN	Double Edge Notched
DSIF	Dynamic Stress Intensity Factor
EFEM	Extended Finite Element Method
EFG	Element-free Galerkin Method
FBM	Finite Block Method
FDM	Finite Difference Method
FEM	Finite Element Method
FGM	Functionally Graded Materials
FSW	Friction Stir Welding
FVM	Finite Volume Method
LEFM	Linear Elastic Fracture Mechanics
LPC	Local Point Collocation Method
LSWF	Local Symmetric Weak Form
MLPG	Meshless Local Petrov-Galerkin Method
MLS	Moving Least Square
NDT	Non-Destructive Testing

NMM	Numerical Manifold Method
PDE	Partial Differential Equation
PIM	Point Interpolation Method
QPE	Quarter Point Element
RBF	Radial Basis Function
SBFEM	Scaled Boundary Finite Element Method
SECP	Single Edge Cracked Plate Specimen
SEN	Single Edge Notched
SIF	Stress Intensity Factors
SPH	Smooth Particle Hydrodynamic

Nomenclature

Latin Symbols

a	Crack length
$A^{(\alpha)}, B^{(\alpha)}, \ C^{(\alpha)}$	Coefficients for different media
$\mathbf{D}_{,x}, \mathbf{D}_{,y}$	Partial differential matrices
b_x and b_y	Body forces
c_0	Characteristic speed
E, G	Young's and shear modules
$F(\xi), G(\eta)$	Shape functions in mapped domain
$H(t)$	Heaviside function
K	Number of sample in Laplace domain
$K_I + iK_{II}$	Complex stress intensity factors
M, N	Number nodes
N_i	Shape function in physical domain
$n(n_x, n_y)$	Normal to the boundary
(r, θ)	Polar coordinate system
r_0	Size of singular core
R	Radius of disk
s_k	Laplace parameter

t_0	Characteristic time
T_0, σ	Free parameters of Laplace transformation
$T^{(\alpha)}$	T-stress
u_x^0, u_y^0, t_x^0 and t_y^0	Boundary Displacement and traction conditions
W	Width of plate
(x, y)	Coordinate in complex form
z	Complex variable

Greek Symbols

$\varepsilon, \hat{\kappa}$	Material parameters
Φ and Ψ	Stress functions of complex
Γ_u and Γ_σ	Displacement and traction boundaries
$\kappa^{(\alpha)}$	Parameter of material
λ_n	Eigen values
$\mu^{(\alpha)}$	Shear modulus
ρ	Mass density
$(\sigma_x, \sigma_y, \tau_{xy})$	Stress tensor
(ξ, η)	Coordinate in mapping domain

CHAPTER 1

Introduction

1.1. Background and Motivation of Research

In modern engineering, the ability to solve complex problems with the emphasis on reducing cost, material wastage and time-saving is vital for engineering firms to stay competitive. Firms also require efficient operational capabilities and processes to survive in a globalised competitive business environment. However, to achieve the above, engineers have to work at the pinnacle of efficient engineering analysis and manufacturing techniques. Engineers have to develop a better diagnosis of a given problem, collect high level reliable data, better formulation of the problem and eventually computational analysis of the problem without the cost of repeated experimentation.

Experimental data and the development of theoretical techniques for solving complex problems have expanded our understanding of various scientific phenomena. This includes the behaviour of elastic materials under tensile and shear loading, fluid flow around solid bodies and the behaviour of cracks in monolithic materials. Since the conception of computers, it has served as the best approach to resolving complex scientific and engineering problems by expediting numerical analysis. Hence, the taught subject of computational engineering.

Computational engineering has formed the basis for various engineering studies, mainly the three classical states of matter. In a much more practical explanation, computational engineering has a great influence on the design of aerospace products, automotive vehicles and motor sports to list a few. Airbus, a European aerospace giant design their aircraft in its entirety using computer aided engineering software. The wing profiles were optimised by running several computational analyses. The strength and stiffness of the structure were also analysed using a finite element program.

Formula One is also a competitive motor sport which thrives on continuous innovation. The design teams develop the racing cars with the aid of computational fluid dynamics (CFD) in order to determine the aerodynamic forces around the car. In turn, the extracted loads are utilised in Finite Element Analysis (FEA). The winglets and spoilers are also designed with the combination of wind tunnel experiments and CFD programs. Adjustments of the winglet and spoiler designs are critical to the competitive nature of motor sport. A minute change in drag, downforce and overloading of the car composite structure can influence the outcome of a race. Maclaren, the sports car manufacturer also designed the contour for the "McLAREN 12C" using CFD and wind tunnel testing for aerodynamic optimisation.

The real-life use of computational engineering analysis and the ability to predict material behaviour is a testament to the safe levels of mass transportation and the construction of high rise buildings. The need for computational engineering is more vital than ever before. The drive to cut cost by reducing repeated experiments has placed computational analysis at the centre of modern engineering design.

The advent of Finite Difference Method by "Sir Thomas Harriet" paved the way to simulate simple engineering problems. Over the years' scientist and engineers in pursuit of accurate simulations, predictions of system behaviour and responses have led the drive to develop several numerical methods. This includes the Finite Element Method (FEM), the Finite Volume Method (FVM), the Boundary Element Method (BEM), the Mesh Free or Meshless Method. The FEM method is very popular and widely used in industry. The FEM method has formed the basis for many forms of engineering and academic research. These numerical methods allow the analysis of many million degrees of freedom.

In solid mechanics, the behaviour of an elastic material under mechanical loading is described by a Partial Differential Equation (PDE). The governing PDE for material deformation is well established, and this is termed the equilibrium equation. An approach to solving PDE equations can be categorised into two numerical methods, the strong form and the weak form. In a strong form solution, the PDE is discretised and solved directly. A typical example is the Finite Difference Method (FDM). Conversely, a weak form method further establishes a series of equations which describe the same physical phenomena. In essence, the weak form gives an approximate solution to the problem. The finite element method is an established example of the weak form method.

Solving PDE by the strong method can give an accurate solution. However, such a method can be very difficult to solve when complex problems are encountered. In cases where the PDE is too difficult to solve, the weak form is employed. The weak numerical method permits a computing approximation which is an equivalent form of the equation we are trying to solve. Before achieving an approximating solution, the weak form requires the establishment of a series of algebraic equations. In the case of solid mechanics, large stiffness matrices for high degrees of freedom are generated. Nonetheless, the availability of powerful computer processors can expedite and handle this process.

Research into developing numerical methods by the weak form process has followed the same basic steps. These are the steps followed;

- Establish a strong form formulation representing the physical phenomena.
- Determine the weak form formulation.
- “Choose approximations for the unknown function”. This can be the displacement function.
- Apply the weight function.
- Solve the system of equations

1.2. Failure Analysis of Structures

Structural analysis formulations are used to determine the material capabilities under prescribed loads. Consider a building under buffeting winds. We can examine the structure under such conditions using numerical analysis. The structure can fail under high bending stresses or vibrations. A similar scenario can be observed under earthquakes and massive explosions. In the case of an aircraft or a bridge, the structure can experience high oscillations and cyclic loading during high wind conditions. This, in turn, can lead to a catastrophic failure of the structure by rupturing or fractural failure. Well-established numerical methods have been developed to study such structural failures.

The failure of engineering structures and sometimes engineering systems as a whole can lead to a catastrophic loss of lives. Most engineering structures are likely to fail by either the yield dominant or the fracture dominant.

Material failure by fracture is a significant part of this thesis. This is due to the difficulty in assessing the impact of cracks on a material strength. Research over the years has focused on characterizing the parameters necessary for crack initiation and propagation. These include the Griffith Energy Balance Approach, the Stress Intensity Approach, the Crack Opening Displacement Approach and the Rice's *J*-Integral Parameter.

The study of fracture mechanics is best conducted by experimental means. However, this presents new challenges in terms of test coupon design and manufacturing. Other challenges include the cost of material, the need for an experimental setup and the capability to extract accurate and reliable data from the experiment. Overcoming the challenges listed above does not necessarily mean the test coupon can replicate the exact behaviour of a structure during failure by means of material fracture.

Material failure by fracture has become vital due to the extensive use of composite materials and aerospace grade adhesives on modern spacecraft and aircraft designs. This is due to the drive to reduce mass and subsequently reduce the greenhouse gases from rocket launches of spacecraft and aircraft engines.

In order to qualify composite materials on a spacecraft or an aircraft for flight, all aspects of the structure needs to be checked and examined for defects. But firstly, engineers have to be sure the minimum acceptable defects can be detected and repaired. The use of Non-Destructive Testing (NDT) methods such as x-ray can reveal the existence of voids in adhesive joints. This defect can affect the shear stress distribution of the adhesive joint. The use of computational methods will give a good assessment of the stress distribution around the joint. In addition to this, the existence of small cracks in other aircraft components and the factors that contributes to crack growth can be explored using various computational techniques. The opportunity to use computational methods to evaluate the behaviour of cracks is therefore paramount to the future of not only spacecraft and aircraft but other sectors of engineering.

In addition, advances in computer power and numerical analysis techniques makes it possible to analyse a structure with critical levels of cracks. Using computational techniques, engineering components can be analysed if it comes under damage whilst in service. A detailed analysis of such a component can be carried out for different load cases, and a reasonable decision is made without resulting in the discarding of materials and generating waste. An experimental analysis will be at a disadvantage for such a case. The example stated above is one of many reasons why computational analysis plays an important role in modern engineering analysis and also in research.

Furthermore, the case has been made for the continuous development of new computational techniques, and this is attributable to the changing nature of engineering designs. Engineering designs have become complex as a result of complex living standards and the contributing factors of global warming. Building designs are no longer simple, weather patterns are not easily predictable, and the need for efficient transportation has led to complex vehicle designs and materials. All these improvements require new numerical techniques in order to perform a reasonable analysis. Moreover, the numerical skill and knowledge developed for one stream of science can be transferable and this was shown by Lucy [54]. The numerical technique developed for the study of astrophysics has now formed the building blocks for the meshless method.

1.3. Computational Challenges and the Need for Meshless Method

In recent years the demand to solve difficult computational analysis has become more significant. In the field of computational solid and fluid mechanics, simulations of large deformations using mesh-based methods such as the finite element method and the finite volume method can become difficult to achieve. In addition, mesh-based methods are not well suited to handle a discontinuity which does not align with the original mesh lines. In regards to an evolving discontinuity, mesh lines have to remain coincidental throughout the discontinuous analysis by re-meshing after every step in the analysis. This repeated adjustment can introduce computational errors in the analysis result. This also introduces a different level of computational difficulty mainly programming and debugging of errors in the code.

The above explanation is part of a broad view on the need to develop alternative numerical methods in order to eliminate or reduce some of the challenges listed. The argument for the continuous development of meshless method is therefore made strong.

Meshless methods have been under development for the past forty years with the initial work by Lucy [54] on the Smooth Particle Hydrodynamic (SPH) method. Since 1977, moderate levels of meshless method have been published. This was soon changed as researchers from the nineties began to pursue a more rigorous numerical alternative to mesh-based methods.

Recently, meshless methods became more prominent with the pioneering work of Nayroles [59] and later work by Belytschko [53]. Nayroles proposed the diffuse approximation method and the diffuse element method. The newly developed method found use in generating smooth approximating functions at known set points. This method also gave accurate derivatives of the function at these points [59]. The Element-free Galerkin Method (EFG) also proposed by Belytschko [53] followed a similar trend and mindset to improve the accuracy of meshless method.

The Element-Free Galerkin method uses the moving least square method and nodal data for interpolation. Belytschko's work showed some key advantages of meshless methods over the finite element method. The EFG method did not show signs of volumetric locking and the rate of convergence exceeded the equivalent FEM model. The Element-Free Galerkin method was used to successfully evaluate elasticity and heat

conduction problems. The EFG method has also been applied to the study of linear elastic fracture. Evidence shows that accurate level of stress intensity factor for a crack can be easily achieved by simply adding more nodes in the region near the crack tip [53].

The above paragraph has highlighted some of the positive traits of meshless method, and this is not an exhaustive list of the advantages of performing meshless analysis. More on this topic is covered in Chapter 2 of this thesis.

As it will be shown later, this research will continue with the current trend in numerical analysis by reducing the number of elements for the study of fracture mechanics.

1.4. Research Objectives

The study of fracture mechanics using the finite element method, the finite difference method and the boundary element method are well documented. However, these numerical methods are mesh based. This trait of the afore mentioned numerical methods present engineers and scientist with a challenge to model complex geometry. In the case of crack propagation, the analyst must refine the mesh repeatedly. The use of Extended Finite Element Method (XFEM) proposed by Belytschko [41] now automates such processes. Nonetheless, such a model still requires human intervention in setting up the model and partitioning the model to generate an acceptable mesh.

In fracture mechanics the aptitude of a cracked medium to fail under some remote loading is characterised by the fracture parameter called the stress intensity factor. Another important fracture parameter is the T-stress which affects the behaviour of crack propagation. The stress intensity factor and the T-stress as determined by the mesh-based numerical methods have proven to be dependent on the quality of the mesh at the crack tip. The mesh refinement around the crack tip can be tedious and the process in mesh refinement can become demanding.

The drive to solve boundary value problems and the failure of elastic solids with fewer emphases on meshing shows the need for more advance numerical methods. This is the purpose for the continuous research as presented in this thesis. This research has set out to successfully achieve the following contribution:

- The research will develop the meshless method called the finite block method (FBM) for the evaluation of static and dynamic interface cracks. The stress intensity factor and the T-stress are to be determined using the formulations developed for the finite block method.
- The finite block method will be compared against other numerical techniques. The techniques considered for comparison are the Displacement Correlation Technique (DCT) and the Proportionality Method (PM), both utilising the nodal displacements and the stresses from an FEA to evaluate an interface crack. The DCT and the PM methods are dependent on the choice of numerical method. Therefore, the outcome of any comparisons between the DCT method, the PM method and any other technique will reflect on the choice of numerical method used in approximating the nodal stress and displacement near the crack tip. As a consequence of this comparison, the research will take the opportunity to make some major improvements to the DCT and the PM methods. The improved results are to be compared against the results by the FBM method.

In this research, numerical analysis and results are extensively checked against established and published papers. This is deemed an acceptable method to check the validity of the proposed numerical method and the stress intensity factors. The development of the finite block method for interface crack and the analyses presented in this thesis are comprehensive.

1.5. Thesis Structure

This thesis is organised into several chapters. The three main chapters, namely chapters 4, 5 and 6 are around the author's journal papers. The thesis is summarised as follows:

Chapter 2 gives the literature review on the classical theory of fracture mechanics and this covers both static and dynamic fracture mechanics. The review extends to cover interface crack between bi-materials. An extensive review of cracks using the finite element method and the meshless methods is presented. The finite block method for elasticity, which forms the basis for this research is also covered.

Chapter 3 establishes the fundamentals of the finite block method. A one-dimensional derivative is developed using the Lagrangian series interpolation. The first

order differential matrix is also determined for one-dimensional uniformly arrange nodes. Using the first order differential matrix it is shown that higher order differential terms can be determined. Several numerical analyses for a one-dimensional case is presented. For a two-dimensional study, the mapping technique is developed for the finite block method. In all assessment of the finite block method, analytical solutions are provided for direct comparison.

Chapter 4 covers the setting-up of the finite block method for crack analysis. The well-developed numerical method utilises the Williams series to formulate the equations required to evaluate an interface crack. Due to the binary phenomena of the stress intensity factor at the interface crack tip, a singular core is used. This chapter explores the use of the singular core for analysing static bi-material cracks. Numerical calibration of the finite block method is also carried out in order to observe the varying effect of the various parameters. Numerical results for different types of cracks are reported.

Chapter 5 details the study of the T-stress. Firstly, an extensive review of the T-stress is given. This is followed by the finite block method derivation for extracting the T-stress. This chapter also explores the use of the singular core for analysing static bi-material cracks. Numerical calibration of the finite block method are also carried out in order to observe the varying effect of the various parameters. Numerical assessments for different crack lengths and bi-materials are reported.

In Chapter 6, an elastodynamic assessment of a cracked medium is presented. The dynamic stress intensity factor and the dynamic T-stress for interface crack between bi-materials is determined using the finite block method. The elastodynamic formulations developed for the finite block method is covered in this chapter.

The evaluation of static stress intensity factor and static T-stress for interface crack between bi-materials is well documented. However, the same cannot be said for the dynamic stress intensity factor and the dynamic T-stress for interface crack between bi-materials. The need for more published papers is therefore a necessity. The work reported in Chapter 6 will contribute to the computational study of interface crack between bi-materials.

Chapter 7 compares the finite block method against other numerical techniques used in determining the interface crack between bi-materials. In this chapter, the stress intensity factor for interface cracks is determined using the proportionality method and

the displacement correlation technique. In this chapter, both techniques employ the FEM method in calculating the stress intensity factor.

In practice, the accuracy of a DCT method and the PM method depends on the accurate calculations of the numerical method used in determining the displacement and the stress at the crack tip. Therefore, some major improvements to the DCT and the PM method is suggested. The proposed improvement is to reduce the transfer of error from the FEM method to the numerical techniques for crack evaluation.

Chapter 8 summarises the key findings and contributions. Suggestions for future research are also presented in this chapter.

1.6. Summary of Original Contributions

The research had an aim to develop an effective meshless alternative for computing the stress intensity factor and the T-stress for interface crack between bi-materials. The aims and objectives were successfully achieved and the technical details of the research are documented in Chapters 3 to 7 respectively. Owing to the success of this research, a detailed summary of the technical contributions to knowledge as presented in this thesis and published papers is documented in Chapter 8. An overview of the technical contribution is outlined as follows:

- For a two-dimensional analysis, the Lagrange series interpolation has been developed in conjunction with a square normalised domain and the mapping technique to approximate higher order partial differential equations. The interpolations are all in the strong form.
- The finite block method as presented in this research incorporates all the major advantages of meshless method. When comparing the finite block method against other meshless methods, parameters such as the size or number of nodes in a support domain is not required. A square normalised domain introduced at the start of every analysis is used instead.
- Using the Williams eigenfunction expansion approach, the finite block method accurately determines the stress intensity factor and the T-stress for interface crack between bi-materials.

- The finite block method as demonstrated in this research utilised only 8 blocks and a singular core to accurately determine the SIF and the T-stress. This means the computational effort is minimized.
- The finite block method accurately determines the dynamic stress intensity factor and the dynamic T-stress using only six blocks and a singular core. When compared against the finite element method, the finite block achieved the same level of accuracy and a reduction in the total computational time by using a small number of blocks. The finite block method also required less computational effort and less time in setting up the numerical model. In essence, the finite block method is an efficient numerical method when it comes to evaluating interface cracks between bi-materials.

CHAPTER 2

Literature Review

2.1. An Overview of Fracture Mechanics

In the study of fracture mechanics, the material is assumed to contain an existing crack. The existence of a crack creates a discontinuity in the material. Using various engineering techniques mainly Non-Destructive Testing (NDT), we can determine the presence of small cracks and defects in a material. Due to the availability of many NDT techniques, the right method or technique must be chosen in order to assess the material properly. Some typical NDT analysis techniques include the radiography (x-ray or gamma ray), the magnetic particle test and the ultrasonic test.

The existence of cracks in engineering materials in many cases is as a result of poor manufacturing techniques amongst others. The existence of trapped air or bubbles during the manufacturing process creates ring shaped voids within the material (Fig. 2.1). This leads to discontinuities and a reduction in overall material strength. Over time, the existing voids will develop, to fracture the material at a lower operating limit than it was originally designed. Under the right conditions for rupture, cracks stemming from voids in a material can propagate leading to a catastrophic failure. Small voids with the characteristics of a penny shaped crack is a common occurrence in adhesively bonded structure and composite materials where the cooling of temperatures is difficult

to control. The same can be said about other manufacturing processes that require air or water cooling.

The origin of cracks does not always stem from poor manufacturing processes. In some circumstances, the subcritical cracks will develop through corrosive stress and cyclic loading. Nonetheless, this can have a detrimental effect on the performance of a material if it exceeds the operating limits.

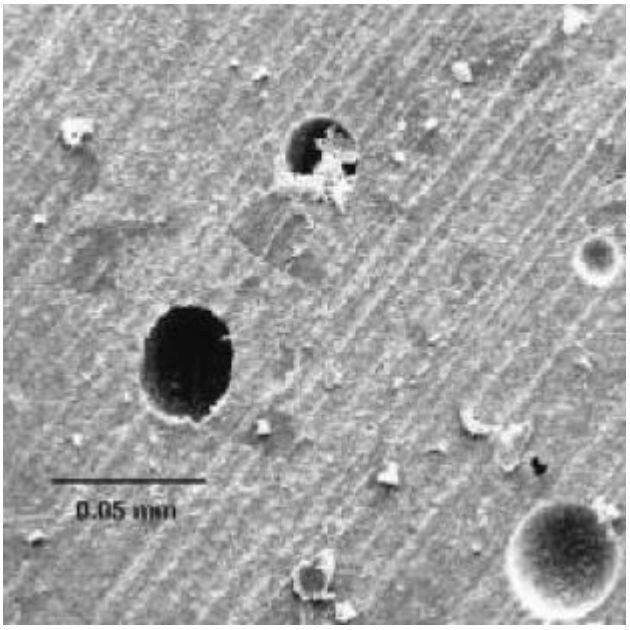

Figure 2.1 The existence of voids in an adhesive lap joint [8].

In fracture mechanics, as in many other engineering streams, the failure of a material in linear terms has to be quantified by a value. Consider Fig 2.2, an infinite plate with a centre crack is remotely loaded at a distance from the crack plane. It is observed that the stress becomes infinite as it approaches the crack tip and eventually stress singularity is achieved at the crack tip. Thus, the stress is inversely proportional to the square root of the radius.

In the study of fractures, the aptitude of a material with cracks to fail is determined by the stress intensity factor K. The stress intensity factor is a function of the material geometry, the forces applied and the boundary conditions. Another parameter for quantifying material failure by fracture is the energy release rate G [1].

Together, the two parameters form part of a material's fracture property and are defined as the critical values K_C and G_C. The subsequent sections of this chapter will expand on the field of fracture mechanics.

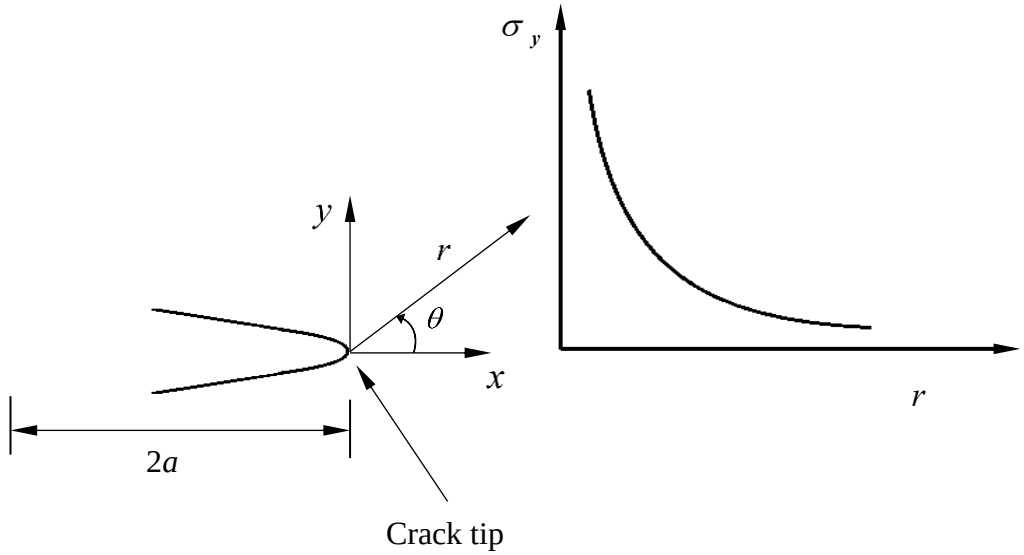

Figure 2.2 A plot of the stress profile ahead of the crack tip. σ_y is the stress component in the *y* direction and $\theta = 0$.

2.1.1 The Theory of Classical Fracture Mechanics

2.1.1.1 The Energy Balance Approach

Works by Griffith and Irwin has formed the basis for the study of Linear Elastic Fracture Mechanics (LEFM). Griffith has been credited with some of the early works on fracture analysis. Griffith's work studied the behaviour of brittle cracks in glass and consequently developed the concept of energy-based analysis for a cracked medium [4, 14]. In this concept, it was postulated that there is an energy balance in the cracked medium and that the process to create or form a new crack will result in a decrease in the total energy. Also, a process to extend an existing crack will render the total energy to remain constant.

The Griffith energy balance approach is best explained with the aid of a schematic diagram. As illustrated in Fig 2.3, an infinite plate is subjected to a uniform tensile load, which is applied remotely away from the crack plane. This set-up of the cracked plate under tensile loading is said to be under equilibrium conditions and the total energy is unchanged. Therefore, in order to extend the crack, the potential energy content of the plate is utilised to overcome the surface energy of the material. Also, according to the principle of minimum potential energy, the cracked plate under tensile load must remain in a state of equilibrium. Thus, in order to attain an equilibrium state for the cracked plate and the total energy due to the crack extension, the potential energy must decrease. Now, considering the 2D infinite plate in Fig 2.3 with a gradual increase in the crack area *dA*, the Griffith energy balance is given by [14]

$$\frac{dU}{dA} = \frac{d\Pi}{dA} + \frac{dW_s}{dA} = 0 \ , \tag{2.1}$$

also, Eq. (2.1) can be rearranged to give

$$-\frac{d\Pi}{dA} = \frac{dW_s}{dA} \ , \tag{2.2}$$

where U is the total energy, Π is the potential energy and W_s is the work required in order to create new surfaces. The subscript *s* stands for surface in this context. Griffith also established a relationship between the potential energy of the cracked plate and the applied stress using the Inglis stress analysis around an elliptical hole [165]

$$\Pi = \Pi_0 - \frac{\pi\sigma^2 a^2 B}{E} \ , \tag{2.3}$$

where *B* represents the thickness of the plate and Π_0 is the potential energy of a plate without a crack.

An introduction of a crack surface into the plate will require some level of energy. Therefore, the change in surface energy for a crack length $2a$ is expressed in the following manner

$$W_s = 4aB\gamma_s \ , \tag{2.4}$$

where γ_s is the surface energy per unit area (surface tension). Therefore, the availability of energy for crack extension is expressed as

$$-\frac{d\Pi}{dA}=\frac{\pi\sigma_0^2 a}{E} \quad \text{and} \tag{2.5}$$

$$\frac{dW_s}{dA}=2\gamma_s \ . \tag{2.6}$$

According to the definition in Eq. (2.2), the fracture stress is obtained by equating Eq. (2.5) and Eq. (2.6), which gives

$$\sigma_f=\left(\frac{2E\gamma_s}{\pi a}\right)^{1/2} . \tag{2.7}$$

It must be noted that the Griffith energy balance approach can be applied to different shapes of crack. This includes a penny shaped crack.

2.1.1.2 The Energy Release Rate

The energy release rate as developed by Irwin is based on the energy approach similar to the Griffith energy method for fracture. The energy release rate determines the availability of energy for crack extension. The energy release rate is also called the crack extension force. Irwin [164] defined the energy release rate as

$$G=-\frac{d\Pi}{dA} \ . \tag{2.8}$$

Therefore, considering Eq. (2.5), the energy release rate for a cracked plate of length *2a* in a plane stress state gives

$$G=\frac{\pi\sigma_0^2 a}{E} \ . \tag{2.9}$$

In order for fracture to occur, the energy release rate G must exceed the critical energy release rate G_C, i.e., $G \geq G_C$. The critical energy release rate which is also called the fracture toughness of the material is defined as

$$G_C=\frac{dW_s}{dA}=2w_f \ , \tag{2.10}$$

where w_f is the fracture energy and depending on the type of material, the fracture energy can be affected at the crack tip by the effects of plasticity and viscoplasticity. For a brittle material $w_f = \gamma_s$. Also, the fracture toughness is a parameter of the material which means it is independent of the applied loads and the geometry of the cracked body.

2.1.1.3 The Stress Intensity Approach

Work by Westergaard [3] focussed on the stress distribution around the crack tip. This was later examined by Irwin [2] to show that in the vicinity of the crack tip the stress is a function of the radius (considering the crack tip as the centre or the reference point for the radius) and the angle of elevation from the crack tip. The crack tip coordinate definition is shown in Fig. 2.2. Irwin then proceeded to develop the stress intensity approach as an alternative means to the energy approach for evaluating the stresses in the vicinity of the crack tip [14].

According to Irwin, the stress intensity factor is a measure of the stress singularity at the crack tip [2, 166]. The asymptotic stress field around the crack tip is expressed as

$$\sigma_{ij} = \frac{K}{\sqrt{2\pi r}} f_{ij}(\theta) + C, \tag{2.11}$$

where the subscripts i and j defines the rectangular coordinates x and y or the polar coordinates r and θ at the crack tip as illustrated in Fig. 2.3. *K* is the stress intensity factor and together $K/\sqrt{2\pi r}$ is the singularity term as $r \to 0$ and C represents higher-order terms in the equation. f_{ij} is the angular functions expressed in terms of θ only.

Furthermore, since there are different modes of crack, Eq. (2.11) can also be expressed in terms of mode I, mode II and mode III as follows

$$\sigma_{ij}^{\ I} = \frac{K_I}{\sqrt{2\pi r}} f_{ij}^{\ I}(\theta) + C, \tag{2.12}$$

$$\sigma_{ij}^{\ II} = \frac{K_{II}}{\sqrt{2\pi r}} f_{ij}^{\ II}(\theta) + C, \tag{2.13}$$

$$\sigma_{ij}^{\ III} = \frac{K_{III}}{\sqrt{2\pi r}} f_{ij}^{\ III}(\theta) + C, \tag{2.14}$$

Detailed explanation of the different modes of crack is covered in section 2.1.1.4 of this thesis. For the moment, the importance of the stress intensity factor as expressed in Eq. (2.11) is explained using an infinitely wide plate with a centre crack and subjected to mode I crack loading as shown in Fig. 2.3. However, a similar cracked model under a different loading such as mode II or mode III could have also been chosen to emphasize the importance of the stress intensity factor. Hence, there is no criteria for choosing mode I for this explanation apart from the prevalent use of mode I in explaining the stress intensity factor in many literatures. Considering the infinite plate with a crack as illustrated in Fig 2.3, a pure mode I crack loading is created if remotely applied stress σ_0 is perpendicular to the crack plane. Therefore, the stress at the crack tip can be treated to be proportional to the far field stress, leading to the agreement $K_I \propto \sigma_0$. The relationship between K_I and σ_0, was further developed after a review of the works by Westergaard and Irwin. This finally led to establishing an expression relating the mode I stress intensity factor K_I, the crack length a and the remotely applied stress σ_0, given as

$$K_I = \sigma_0 \sqrt{\pi a} \ . \tag{2.15a}$$

Similarly, the mode II stress intensity factor K_{II} of Eq. (2.15a) is achieved by remotely applying shear stress loads along the boundaries. As it is explained here, the concept of a wide infinite plate with a crack was used in formulating Eq. (2.15a). Conversely, a semi-infinite plate with an edge crack and subjected to a mode I loading will produce a different expression for a mode I stress intensity factor K_I. This is due to the difference in the boundary conditions for an infinite plate with a centre crack and a semi-infinite plate with an edge crack.

In section 2.1.1.2, the first fracture parameter, the energy release rate was discussed and now the second fracture parameter, the stress intensity factor has been introduced. As stated, the former is a measure of the energy required for crack extension and this method considers the global behaviour of the cracked body. Meanwhile, the stress intensity factor is a local parameter which characterises the displacements, the stresses and the strains at the crack tip. For a homogeneous isotropic material, a unique relationship exist between the energy release rate and the stress intensity factor.

By squaring all the terms in Eq. (2.15a) and substituting into Eq. (2.9) gives an expression for the energy release rate and the stress intensity factor K_I as

$$G = \frac{K_I^2}{E} \ . \tag{2.15b}$$

This expression is for a plane stress state analysis.

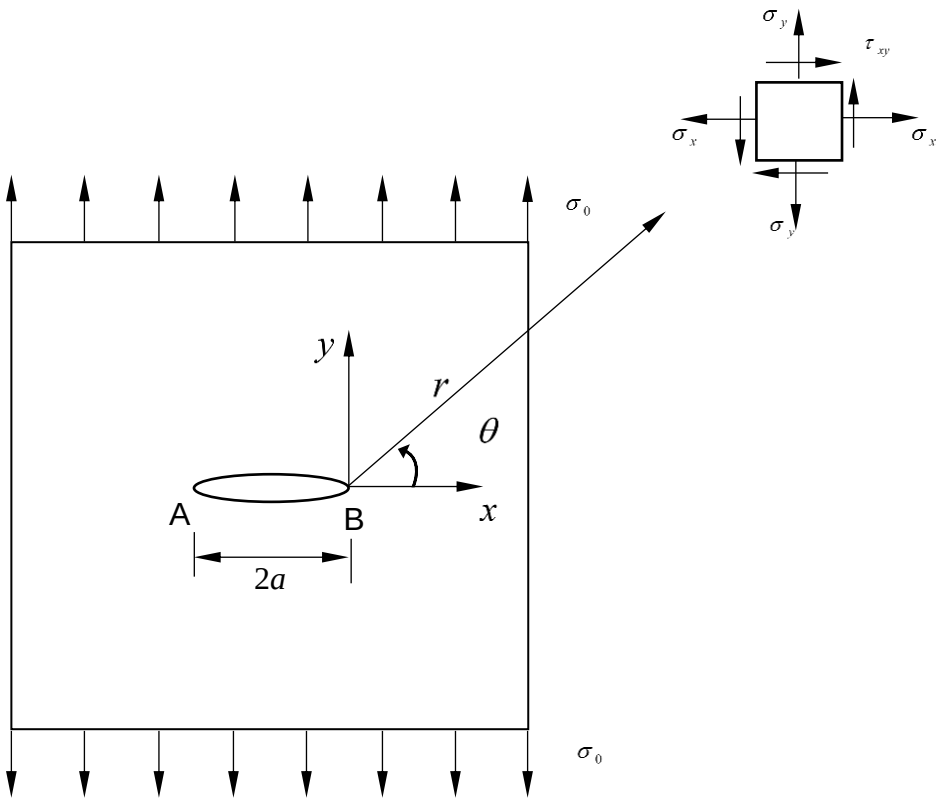

Figure 2.3 A through thickness crack in an infinite plate. The plate is subjected to a far field stress at the top and bottom.

2.1.1.4 Stress Intensity Factor and the Basic Modes of Fracture

The three basic modes of crack displacement deformations are the opening mode (Mode I), the sliding mode (Mode II) and the shear mode (Mode III). The different modes of crack displacement is illustrated in Fig. 2.4. Other displacement deformation includes the bending and the torsion mode. Therefore, by no means can we say all types of cracks are representative of these modes. Cracks in reality are sometimes irregular in shape and size, and this can present a different level of difficulty in trying to evaluate the stress and displacement fields. Nonetheless, it is ideal to model the cracks in terms of the modes shown in Fig. 2.4 for theoretical analysis.

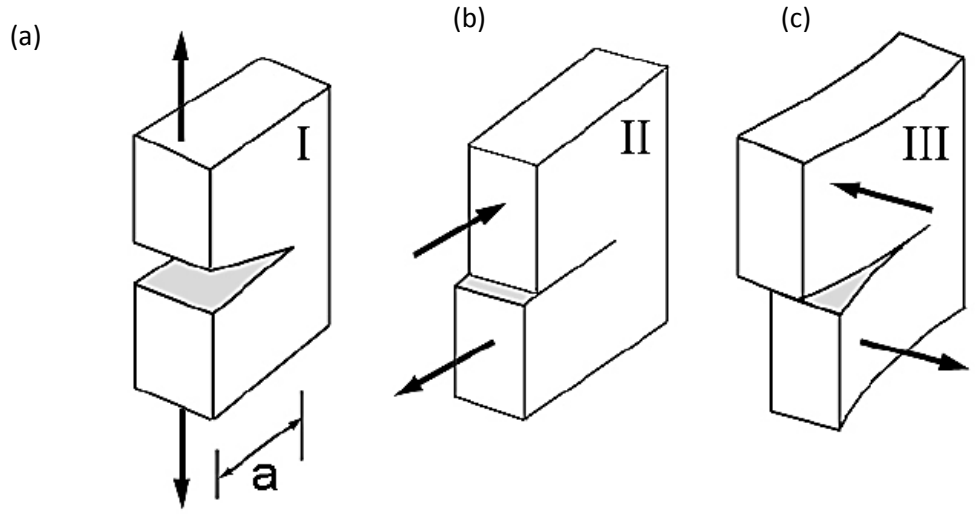

Figure 2.4 The three basic modes of crack displacement (a) Mode I (opening mode), (b) Mode II (sliding mode) and (c) Mode III (shear mode) [7].

For the different crack displacement modes in Fig. 2.4, the stress field near the crack tip is evaluated by considering a centre crack in an infinite plate. The plate is under biaxial loading as shown in Fig. 2.5.

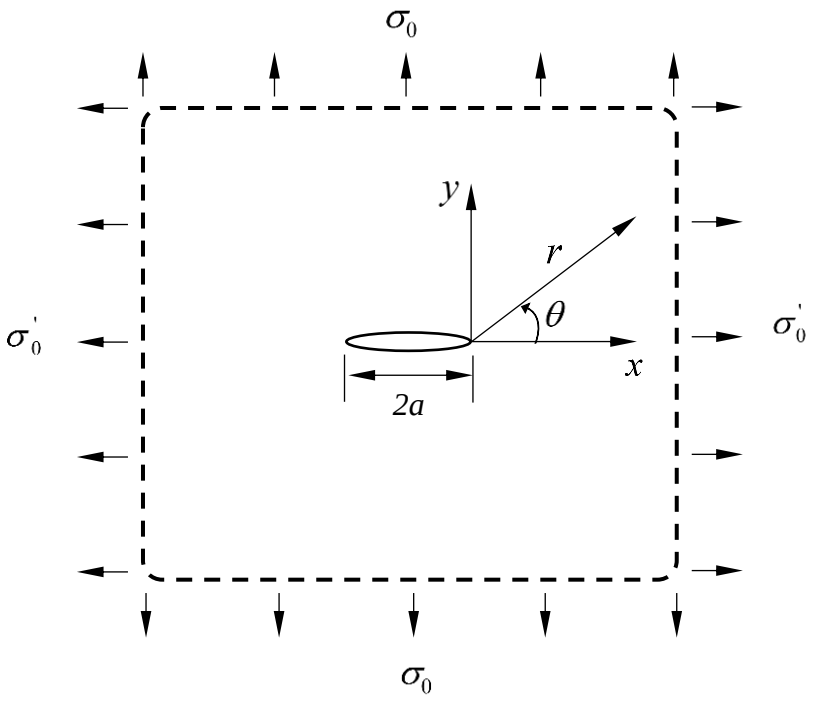

Figure 2.5 The biaxial loading of an isotropic infinite plate with a centre crack.

The stress field around a mode I crack is reviewed as part of this study. Taking the crack tip to be the origin of a polar coordinate system, the stress components near the crack tip of a biaxially loaded isotropic plate is given by [7]

$$\sigma_x = \frac{K_I}{\sqrt{2\pi r}} \cdot \cos\frac{\theta}{2}\left(1 - \sin\frac{\theta}{2}\sin\frac{3\theta}{2}\right), \tag{2.16a}$$

$$\sigma_y = \frac{K_I}{\sqrt{2\pi r}} \cdot \cos\frac{\theta}{2}\left(1 + \sin\frac{\theta}{2}\sin\frac{3\theta}{2}\right), \tag{2.16b}$$

$$\tau_{xy} = \frac{K_I}{\sqrt{2\pi r}} \cdot \sin\frac{\theta}{2}\cos\frac{\theta}{2}\cos\frac{3\theta}{2}\ . \tag{2.16c}$$

A similar solution exists for a mode II and mode III crack problem. The stress field for a mode II problem with an in-plane shear at infinity is given by

$$\sigma_x = -\frac{K_{II}}{\sqrt{2\pi r}} \cdot \sin\frac{\theta}{2}\left(2 + \cos\frac{\theta}{2}\cos\frac{3\theta}{2}\right), \tag{2.17a}$$

$$\sigma_y = \frac{K_{II}}{\sqrt{2\pi r}} \cdot \sin\frac{\theta}{2}\cos\frac{\theta}{2}\cos\frac{3\theta}{2} \ , \tag{2.17b}$$

$$\tau_{xy} = \frac{K_{II}}{\sqrt{2\pi r}} \cdot \cos\frac{\theta}{2}\left(1-\sin\frac{\theta}{2}\sin\frac{3\theta}{2}\right) \ . \tag{2.17c}$$

Equally, the stress field for Mode III

$$\tau_{xz} = \frac{K_{III}}{\sqrt{2\pi r}} \cdot \sin\frac{\theta}{2} \ , \tag{2.18a}$$

$$\tau_{yz} = \frac{K_{III}}{\sqrt{2\pi r}} \cdot \cos\frac{\theta}{2} \ . \tag{2.18b}$$

The displacement fields for mode I and mode II crack in the Cartesian coordinate system gives, for plane stress state [39]

$$u_x = \frac{K_I\sqrt{r}}{2\mu\sqrt{2\pi}}\left[\frac{2(1-\nu)}{1+\nu}\cos\frac{\theta}{2}+\sin(\theta)\sin\frac{\theta}{2}\right] + \frac{K_{II}\sqrt{r}}{2\mu\sqrt{2\pi}}\sin\frac{\theta}{2}\left[\frac{4}{1+\nu}+2\cos^2\frac{\theta}{2}\right] + (1-\nu^2)\frac{Tr}{E}\cos\theta \ , \tag{2.18c}$$

$$u_y = \frac{K_I\sqrt{r}}{2\mu\sqrt{2\pi}}\left[\frac{4}{1+\nu}\sin\frac{\theta}{2}-\sin(\theta)\cos\frac{\theta}{2}\right] + \frac{K_{II}\sqrt{r}}{2\mu\sqrt{2\pi}}\cos\frac{\theta}{2}\left[\frac{2(1-\nu)}{1+\nu}+2\sin^2\frac{\theta}{2}\right] - \nu(1+\nu)\frac{Tr}{E}\sin\theta \ . \tag{2.18d}$$

2.1.2 Dynamic Fracture Mechanics

Dynamic fracture is the study of cracked bodies subjected to dynamic loads in order to establish the growth, the arrest and branching of propagating cracks [9]. However, research in fracture mechanics tends to focus on stationary static crack. The study of dynamic fracture plays an important role in the failure of cracked bodies. Hence, dynamic fracture mechanics should be treated with equal relevance as stationary static cracks.

A cracked structure subjected to dynamic or time dependant loads has the stress intensity factor at the crack tip amplified. This is due to the dynamic effect. Thus, a similar cracked structure which might not fail under stationary static loading might fail under dynamic conditions.

Fracture dynamics can exist due to an abrupt loading or rapid crack growth. This in turn can cause stress waves to propagate through the cracked body, and these waves can reflect of free boundaries like the cracked plane [14]. However, this description gives the impression that fracture dynamics revolves around the impact loading of a cracked body. This review has categorised the various forms of fracture dynamic loadings in an attempt to simplify the complicated topic of fracture dynamics in the interest of the reader. Fracture dynamics can exist in a stationary form and in a case where the crack tip is propagating. The former is concerned with a cracked body under dynamic loading but with a crack tip spatial velocity equal to zero. The latter is due to a rapidly moving crack tip across a loaded structure. This occurrence is down to the structure becoming unstable as the crack extension overcomes the resistive force [9, 10].

In the study of dynamic fracture mechanics, we might be presented with a situation where the influence of "inertia forces, rate-dependant material behaviour and reflected waves" might be too great to ignore [14]. Typical example includes the rapid loading of a cracked body. However, this is not the case for applications of LEFM and elastic-plastic fracture mechanics analysis, where mainly static loading is considered. Furthermore, there is no criterion or standard for defining the rapidity of structural loading. Instead, decisions of loading can be based on "qualitative reasoning" and well-known solutions to certain problems [9].

The study of dynamic fracture is made complex if the above effects are included in the analysis. In a case where the inertia, the material rate-dependent and the reflected waves are ignored, the analysis reduces to a quasi-static state and the problem is easily solved. Depending on the problem, we can ignore some of the above effects influencing the analysis. The concept of reducing a complex dynamic problem to a reasonably solvable one is a branch of dynamic fracture mechanics called "Elastodynamic Fracture Mechanics" [14]. In this research, materials with linear behaviour are studied using the established theories of elastodynamics.

Elastodynamic study of a cracked body is imperative in understanding how cracks interact with elastic waves. This is relevant when performing NDT test of cracked materials with the aid of an ultrasonic wave [15, 16]. The results from the NDT test will show how the ultrasonic waves are scattered by the crack and the pattern of the scatter can reveal the location of the crack, the orientation of the crack and the crack profile.

Elastodynamics is relevant in evaluating cases of rapid impact or loadings such as a bird strike on an aircraft, a submarine colliding with an unwarranted structure, a missile or projectile impact on a target, etc. These examples including the sudden impact of a bird strike on an aircraft can induce a transient response. Thus, an existing crack in such a structure might become agitated and the SIF can exceed the critical limits for crack propagation.

2.1.2.1 Stress and Displacement Field for a Stationary Crack Under Dynamic Loading

It is observed that the stress field at the crack tip of a stationary crack under static loading takes the same form as that under dynamic loading. Therefore, the Laplace transform of the stress intensity factor in the vicinity of the crack tip is inverted to give the dynamic asymptotic stress and displacement distributions [10]. The dynamic stress and displacement field as expressed by the Williams expansion is given by [11, 12]

$$\sigma_x(r,\varphi,t)=\frac{K_I(t)}{\sqrt{2\pi r}}\cos\frac{\varphi}{2}\left[1-\sin\frac{\varphi}{2}\sin\frac{3\varphi}{2}\right]- \frac{K_{II}(t)}{\sqrt{2\pi r}}\sin\frac{\varphi}{2}\left[2+\cos\frac{\varphi}{2}\cos\frac{3\varphi}{2}\right]+T(t)\ , \tag{2.19}$$

$$\sigma_y(r,\varphi,t)=\frac{K_I(t)}{\sqrt{2\pi r}}\cos\frac{\varphi}{2}\left[1+\sin\frac{\varphi}{2}\sin\frac{3\varphi}{2}\right]+\frac{K_{II}(t)}{\sqrt{2\pi r}}\sin\frac{\varphi}{2}\cos\frac{\varphi}{2}\cos\frac{3\varphi}{2}\ , \tag{2.20}$$

$$\sigma_{xy}(r,\varphi,t)=\frac{K_I(t)}{\sqrt{2\pi r}}\cos\frac{\varphi}{2}\sin\frac{\varphi}{2}\cos\frac{3\varphi}{2}+\frac{K_{II}(t)}{\sqrt{2\pi r}}\cos\frac{\varphi}{2}\left[1-\sin\frac{\varphi}{2}\sin\frac{3\varphi}{2}\right]\ , \tag{2.21}$$

$$u_x(r,\varphi,t)=\frac{K_I(t)}{4\mu}\sqrt{\frac{r}{2\pi}}\left[(2\kappa-1)\cos\frac{\varphi}{2}-\cos\frac{3\varphi}{2}\right]+$$

$$\frac{K_{II}(t)}{4\mu}\sqrt{\frac{r}{2\pi}}\left[(2\kappa+3)\sin\frac{\varphi}{2}-\sin\frac{3\varphi}{2}\right]+(1-\nu^2)\frac{T(t)r}{E}\cos\varphi\ , \tag{2.22}$$

$$u_y(r,\varphi,t)=\frac{K_I(t)}{4\mu}\sqrt{\frac{r}{2\pi}}\left[(2\kappa+1)\sin\frac{\varphi}{2}-\sin\frac{3\varphi}{2}\right]-$$

$$\frac{K_{II}(t)}{4\mu}\sqrt{\frac{r}{2\pi}}\left[(2\kappa-3)\cos\frac{\varphi}{2}+\cos\frac{3\varphi}{2}\right]-\nu(1+\nu)\frac{T(t)r}{E}\sin\varphi\ , \tag{2.23}$$

where r and φ are the planar polar coordinate system centred at the crack tip, μ is the shear modulus and $\kappa=\frac{3-\nu}{1+\nu}$ for plane stress and $\kappa=3-4\nu$ for plane strain. $T(t)$ is the dynamic T-stress. $K_I(t)$ and $K_{II}(t)$ are the dynamic stress intensity factors for mode I and mode II respectively.

2.1.3 Interface Crack of Bi-material

2.1.3.1 Overview of Bi-material

The use of bi-material in engineering construction has always existed. Ancient structures like the pyramids in Egypt, the Aztecs structure in South America, Hadrian's wall in Great Britain and many more were constructed by joining different materials together. The combination of bricks and mortar is a simple case of a bi-material. In modern times, advances in material technology has led to the development of complex bi-materials. This includes soldering of electronic components and welding of high tensile steel for high rise buildings, bridges, ships, to name a few. Other forms of bi-materials include composites with Fibre Reinforced Plolymer (FRP) and aluminium honeycomb sandwich panels.

The designing and manufacturing of spacecraft is another sector of engineering where bi-materials are used extensively. For spacecraft design, the requirement to minimise the weight of the structure has led to new material designs and different ways of holding the structure together. On some spacecraft joints the number of titanium bolts have been reduced in favour of adhesive bonded joints. Other areas of the spacecraft

structure where aluminium metal plates are used has now been replaced by aluminium-honeycomb sandwich panels.

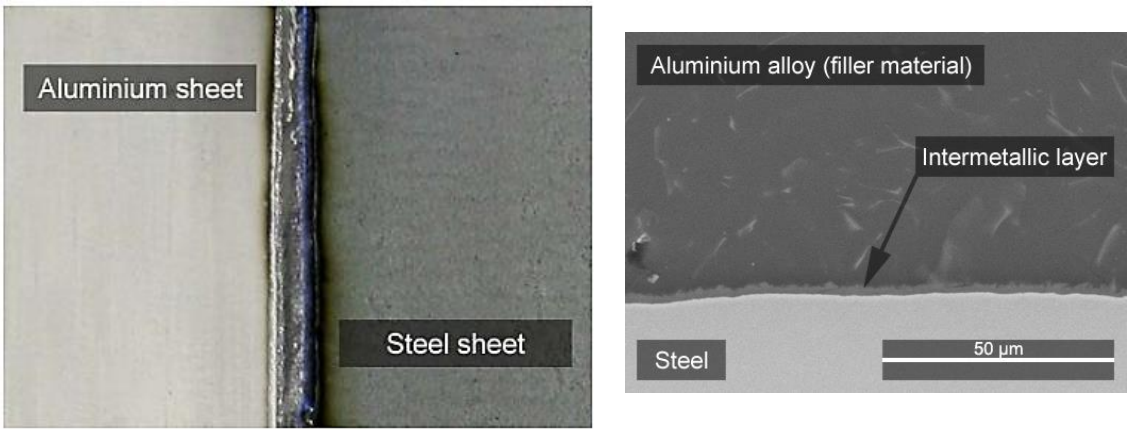

(a) (b)

Figure 2.6 (a) The weld bead of an aluminium and steel joint. (b) An inspection shows the formation of a thin intermetallic layer. This bi-material interface shows an irregular surface close to the aluminium and a smooth surface near the steel [29].

The use of Carbon Fibre Reinforced Plastic (CFRP) composite has also been well received across the automotive and aerospace industry. Spacecraft central structures are often built with CFRP. At the same time, the use of metal panels on super-cars has been replaced by the availability of CFRP. The construction of yachts has been made easier by applying layers of CFRP to a precast or a mould.

The advantages of using bi-materials as outlined above does also present engineers with some challenges, and this research will focus on the development of cracks and voids along the interface boundary of the different materials. These defects are mainly caused by flaws in the manufacturing of the interface bonds, thermal effects and operational use of the bi-material. Fig. 2.6 shows an intermetallic layer after the joining of two metal sheets by welding. A closer inspection of the welded joint reveals some level of imperfection.

Forcing two metals together by conventional welding involves fusion at high temperatures [25]. The HY-80 high yield strength and low-alloy steel is a strong

material and often used in military applications and ship building. The welding of HY-80 has been investigated by Savage [24]. The work shows that the use of hydrogen electrodes in the welding process develops small grades of cracks within the weld fusion boundary [24]. Friction Stir Welding (FSW) was developed by TWI as an alternative to the conventional solid weld. The FSW can also join together dissimilar materials showing some level of incompatibility [27]. However, the FSW method also presents engineers with a unique form of defects. The following defects are formed during an FSW welding; the lack of heat and irregular stirring during the welding can produce cavities and groves defects [26]. A picture showing the different outcomes of the FSW welding is shown in Fig. 2.7.

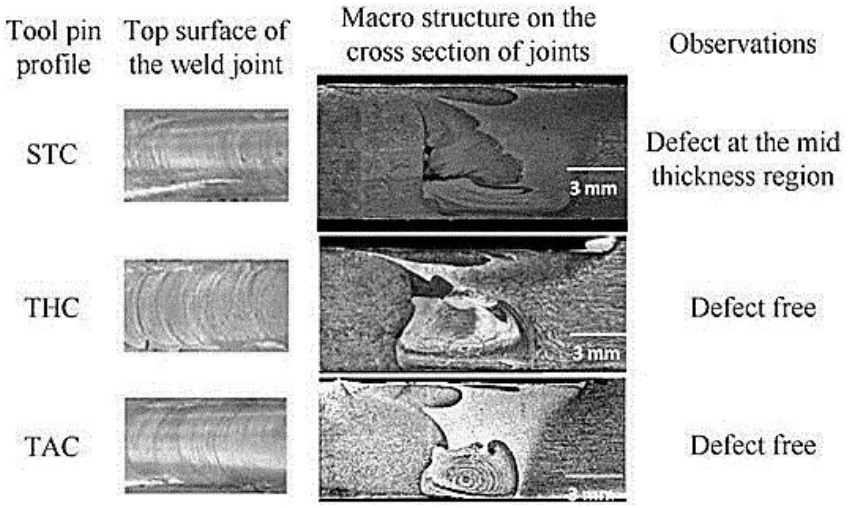

Figure 2.7 Macrograph view of an FSW weld using three different weld pins [28]. The top picture shows a defect along the weld interface. The subsequent pictures show no defect after the weld.

In the case of soldering, electrical components are joined together using a solder wire or filler metal. The constant use of electrical devices and mechanical impact by a sudden drop of handheld devices can generate micro cracks at the soldered joints. Furthermore, the cooling and warming of the on-board components will induce thermo-cyclic effect which can also lead to fracture at the solder bond interface [47].

Some metals can be difficult to weld and this is a common attribute of aluminium alloys. During the welding process, aluminium oxide (Al_2O_3) forms a layer or coating

which is unfavourable to a welded bond. Employing friction welding techniques at high pressure will abrasively remove the layer of oxidation [30]. In the case of a welded joint we can have a build-up of voids in the weld. Another case where voids can form is the manufacturing process of adhesive bonds. The voids in adhesive joints are mainly caused by bubbles of trapped air. It can now be accepted that bi-materials does have an imperfect joint along the bonded interface [18]. Therefore, the design failure along the interface of bi-materials demands a good understanding of the failure mechanisms. In this research, the fracture characteristic of defects along the interface of bi-materials is investigated.

2.1.3.2 Interface Crack Stress and Displacement Field

Theoretical research of interface crack has become prominent in the last five decades. Some of the early pioneering work on interface crack research includes Williams [18] attempt to resolve developing fault lines in geology. The developing fault lines between layers of rock strata produce interfaces which need to be characterised and understood. Zak and Williams [23] also employed the eigenfunction method to investigate the stress singularity ahead of a perpendicular crack tip which terminates at the bi-material bond line. Fig. 2.8 shows a typical set-up of an interface crack. The asymptotic analysis around an interface crack tip by Williams [18] has shown that the stress and displacement field are oscillatory in nature. This behaviour is strikingly different to that of a cracked homogeneous body. Further work by Erdogan has established the magnitude of the oscillatory region at the interface crack tip to be "10^{-6} of the crack length" and this is small indeed.

Mathematically, the oscillatory phenomena at the crack tip predict the interpenetration or the overlapping of opposite faces behind the crack tip [21]. However, this can be corrected if the opposite faces are considered to be "mutually convex" [17]. Attributable to the oscillatory behaviour at the crack tip, a simple mode I loading of a crack body will result in a mixed mode effect at the crack tip. Therefore, the stress intensity factor as recognised in a homogeneous cracked body is not well defined when analysing an interface crack. The mode I and mode II stress intensity factors are coupled together at the interface crack tip.

The stress and displacement fields of an interface crack tip as determined by Williams [18] is expressed as follows [17]

$$\sigma \sim r^{-1/2}\begin{pmatrix}\sin\\ \cos\end{pmatrix}(\varepsilon \log r) \quad \text{and} \quad u \sim r^{1/2}\begin{pmatrix}\sin\\ \cos\end{pmatrix}(\varepsilon \log r) \tag{2.24}$$

$$\text{where} \quad \varepsilon = \frac{1}{2\pi}\log\left(\frac{1-\beta}{1+\beta}\right), \quad \beta = \frac{\mu_1(\kappa_2 - 1) - \mu_2(\kappa_1 - 1)}{\mu_1(\kappa_2 + 1) + \mu_2(\kappa_1 + 1)} \quad \text{and} \tag{2.25}$$

$$\kappa_i = \begin{cases} 3 - 4\nu_i & \text{Plane stress} \\ \dfrac{3-\nu_i}{1+\nu_i} & \text{Plane strain} \end{cases}. \tag{2.26}$$

The Dundur parameter β ranges between $-1/2$ and $1/2$, and reduces to zero for identical materials.

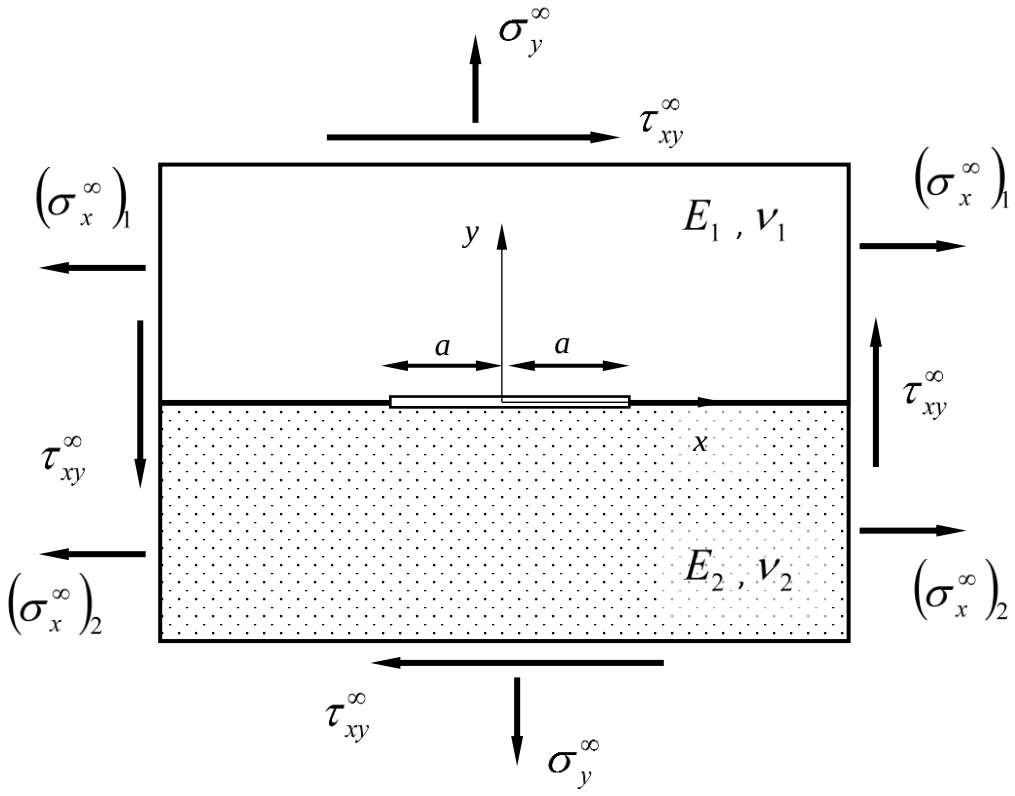

Figure 2.8 A bi-material plate with a centre interface crack subjected to tensile and shear loadings at infinite.

Considering Fig. 2.8, this is a plate under uniform tensile and shear loading as defined by Rice and Sih [19]. For a crack length of *2a*, the stress intensity factors K_I and K_{II} are given by

$$K_I = \frac{K_{0I}}{\cosh(\pi\varepsilon)}\sqrt{\pi a} \ , \tag{2.27}$$

where

$$K_{0I} = \sigma_y^{\infty}\left[\cos(\varepsilon\log(2a)) + 2\varepsilon\sin(\varepsilon\log(2a))\right] + \tau_{xy}^{\infty}\left[\sin(\varepsilon\log(2a)) - 2\varepsilon\cos(\varepsilon\log(2a))\right] \ ,$$

$$K_{II} = \frac{K_{0II}}{\cosh(\pi\varepsilon)}\sqrt{\pi a} \ , \tag{2.28}$$

where

$$K_{0II} = \tau_{xy}^{\infty}\left[\cos(\varepsilon\log(2a)) + 2\varepsilon\sin(\varepsilon\log(2a))\right] - \sigma_y^{\infty}\left[\sin(\varepsilon\log(2a)) - 2\varepsilon\cos(\varepsilon\log(2a))\right] \ .$$

From Eq. (2.27) and (2.28), the expression for the stress intensity factors is a mixture of the tensile and shear stress fields. Also, in a similar loading format as shown in Fig. 2.8 and without the shear stress loading the stress intensity factors are given by [17]

$$K^* = K_I + iK_{II} = \left(\frac{K_{0I} + iK_{0II}}{\cosh(\pi\varepsilon)}\right)\sqrt{\pi a} \ , \tag{2.29}$$

From Eq. (2.29) where $K_I^2 + K_{II}^2$ does not contain the logarithm factor, we can express the complex stress intensity factors in terms of

$$K_I^2 + K_{II}^2 = \frac{\left(\sigma_y^{\infty}\right)^2 \pi a\left(1 + 4\varepsilon^2\right)}{\cosh^2(\pi\varepsilon)} \ . \tag{2.30}$$

In Eq. (2.29) a mixed mode effect is still observed at the interface crack tip in the absence of the shear stress loading. Ahead of the crack tip, the normal and shear stresses intertwine across the interface. At the crack opening behind the crack tip, a shearing and opening displacement is an occurrence. The stress intensity factors as expressed above can be determined using the following simplified expressions in terms of stress [17, 20]

$$\sigma_y + i\tau_{xy} = \frac{K_I + iK_{II}}{\sqrt{2\pi r}} r^{i\varepsilon} \ . \tag{2.31}$$

Similarly, behind the crack tip, the stress intensity factor for an interface crack is expressed in terms of the crack opening displacement by [20, 21]

$$\delta_y + i\delta_x = \frac{4}{\sqrt{2\pi}} \frac{(r)^{i\varepsilon}}{(1+2i\varepsilon)\cosh(\pi\varepsilon)} \frac{K}{E^*} \sqrt{r} \ , \tag{2.32}$$

$$\frac{1}{E^*} = \frac{1}{E_1} + \frac{1}{E_2} \quad , \tag{2.33}$$

where the subscript 1 and 2 for the Young's modulus denotes material 1 and 2.

Also, $\delta_x = u_x^+ - u_x^-$ and $\delta_y = u_y^+ - u_y^-$, (2.34)

where $+$, $-$ indicates the upper and lower surface.

In addition, the normal and shear stress singularity field fluctuates slowly along the cracked interface according to

$$r^{i\varepsilon} = \cos(\varepsilon \ln(r)) + i \sin(\varepsilon \ln(r)) \ . \tag{2.35}$$

This section has reported broadly on the complications in trying to determine the stress intensity factors at the interface crack tip considering the presence of oscillatory singularities. Many researchers have proposed solutions in order to bypass the oscillatory singularity. Comninou [17] and other researchers have explored some ideas in order to solve the oscillatory issues. Work by Atkins [22] considers a three-layer approach where the third or middle material contains the crack. This way the crack exists in a homogeneous body. This approach will do away with any singularity effect. However, this method has its criticisms and challenges. The interface has now changed and no longer representative of a case where the crack actually exists along the interface which is the subject of interest.

2.2. Computational Fracture Mechanics

The study of fracture mechanics is best conducted by experimental means. However, the experimental approach presents researchers with some challenges in terms of test coupon design and manufacturing. In addition, the cost of material, the need for an experimental setup and the capability to extract accurate and reliable data from the experiment can prove to be difficult to achieve. Overcoming the challenges listed above

does not necessarily mean the test coupon can replicate the exact behaviour of a structure during failure by means of material fracture.

The challenges listed in the paragraph above can be resolved differently with modern computational analysis. Modern advances in computational power and numerical analysis techniques makes it possible to analyse a structure with critical levels of cracks. Computational techniques allow in-service components to be analysed if a fault develops whilst in service. A detailed analysis can be carried out for different load cases and a reliable result is achieved. An experimental analysis will be at a disadvantage for such a case. The example stated above is one of many reasons why computational analysis plays an important role in modern engineering analysis and also in research. Some of the popular numerical techniques include the Finite Difference Method (FDM), the Finite Element Method (FEM), the Finite Volume Method (FVM), the Boundary Element Method (BEM) and the Meshless Method amongst others.

The finite element technique has played an important role in studying fracture mechanics over the years. The Boundary Element Method is another popular numerical method used for the study of fracture mechanics. Both these methods utilise elements in their analysis. The use of elements in simulating fracture mechanic and elastostatic problems presents its own challenges. This includes singularity issues at the crack tip and the need for fundamental and particular solutions for integrating the domain and the boundary.

2.3. The Finite Element and Boundary Element Analysis of Cracks

FEM is a well-established method for the study of solid mechanics. FEM has also been employed in the study of fluids and thermal behaviours of engineering systems. The firm status of FEM pertains to the generality of the numerical formulation and the availability of commercially developed FEM programs like ABAQUS, ANSYS and NASTRAN.

FEM fracture mechanics determines the variation in crack surface displacements and the asymptotic expression for the stress in the vicinity of the crack tip. By plotting a variation of grid point stress leading to the crack tip versus the grid point radius from the crack tip, the stress intensity factor can be extrapolated [37]. Such simple approach

to determine the SIF is easily achieved for a homogeneous analysis. The determination of the SIF by the finite element method works in conjunction with numerous methods. This includes the *J*-Integral method as developed by Rice [31] and several displacement techniques based on the near crack tip displacement [32, 33].

In addition to FEM fracture mechanics, advance numerical techniques exist and these can adequately calculate the stress intensity factor for arbitrary fracture load configurations. Moreover, these numerical techniques sufficiently determine the stress intensity factors for complex cases like interface cracks and cracks in Functionally Graded Materials (FGM).

For the boundary element method, several papers have been published which covers the investigation of interface crack [35, 36]. Lee [36] investigated bi-material interface crack of an elastic and viscoelastic material using the boundary element method. The extended finite element method (XFEM) is a much more versatile version of the finite element method [40, 41, 42]. The XFEM incorporates the partition of unity method which allows the modelling of discontinuity in the case of cracks. For this, the XFEM has a range of applications including dynamic fracture mechanics and crack propagation [43, 44].

The standard FEM elements available for general boundary and domain analysis lack the ability to represent the stress singularity at the crack tip. Both FEM and BEM modelling of cracks has been enhanced with the advent of the Quarter Point Element (QPE) developed by Barsom [38]. The square root singularity term is incorporated in the quarter point element and this has improved the approximation of the stress intensity factor. Tan and Gao [45] investigated interface crack using a quadratic quarter point element developed for boundary element method. This near crack tip element resolves the difficulties of interface crack pertaining to oscillatory effects at the crack tip [45].

The T-stress as discovered by Williams [18] is a component of the non-singularity stress around the crack tip. The T-stress is regarded as a significant fracture parameter, and several numerical approaches to determine this parameter is continuously evolving. J. and V. Sladek employed the boundary element method to investigate the T-stress for an interface crack [34]. The quarter point element for the boundary element method was utilised by Tan and Wang [39] to determine the T-stress at the crack tip. Also, work by

Sladek [12] developed formulations which allowed the expedient analysis of the T-stress using the conventional crack tip quarter point element for FEM.

FEM and BEM are not only limited to stationary crack analysis but have equal importance in analysing dynamic cracks in order to determine the Dynamic Stress Intensity Factor (DSIF). In addition to FEM and BEM, there are a wide range of numerical methods available for dynamic analysis. Kim and Paulino [106] extended the interaction integral method originally developed to determine the SIF of a stationary crack to the evaluation of cracks subjected to dynamic loading. In the evaluation of dynamic stress intensity factor, the interaction integral method was formulated to work in conjunction with the FEM method. Fedelinski and Sladek also determined the DSIF using the *J*-Integral in conjunction with the boundary element method [49].

2.4. Meshless Method

2.4.1 An Overview of Meshless Method

The traditional mesh-based methods, mainly the FEM and BEM method have several drawbacks and constraints which can limit their ability to tackle difficult engineering and scientific problems. Some of the drawbacks include element locking, tedious meshing of complex geometries, difficulty in determining derivative solutions, etc.

In the context of FEM and BEM, an elastic body can be discretised by using a set of elements and grid points to represent the domain and the boundaries. On the other hand, the meshless method can represent the same elastic body and its boundaries by using a range of grid points scattered or organised around the body. In essence, the meshless method can be defined as the process of establishing a system of algebraic equations for a given problem without the need for meshes (combined use of elements and grid points). The displacement and stress fields can now be approximated locally at the grid points.

The meshless method has become a popular research topic and the development of meshless method has continued for the last 30 years. Some of the earlier developed meshless methods include the Smooth Particle Hydrodynamics (SPH), the Element Free

Galerkin method (EFG), Meshless Local Petrov-Galerkin method (MLPG), Point Interpolation Method (PIM), Local Point Collocation method (LPC) and many more.

The intentions of the meshless method is to solve the governing partial differential equations of a given problem by means of using only the grid points. However, this approach can be difficult to achieve. Hence, the development of several meshless methods to solve challenging problems. For this, the various meshless methods can be categorised in the order of mesh reduction up to what can be described as a truly meshless method. Some meshless methods require the use of background cells to compute the analysis. The EFG method and the MLPG method may use this method of meshless analysis. The use of background cells can be robust, reliable and in some cases easier to generate by automated means. The final category consists of a case where no mesh is utilised in the analysis. The local point collocation method may belong to this meshless method.

2.4.2 Smooth Particle Hydrodynamics (SPH)

The Smooth Particle Hydrodynamics method was initially developed to study the various phenomenon in astrophysics [50]. The SPH method has been classified as a true meshless method [51] and possibly the oldest meshless method. SPH is a meshless particle method and therefore does not need a grid mesh to interpolate material derivative. In SPH a physical body or system is reconstructed by particles which have physical properties. The particles are said to interact with each other within a limit controlled by a weight function.

Smooth Particle Hydrodynamics is based on the Lagrangian method developed by Lucy [54] and Gingold [55]. The fundamentals of the SPH method is the ability to express any function in terms of the spatial particles representing the problem domain. This is achieved by integral interpolation of the function [50]. The particle representation in computational solid mechanic problems is a positive feature of the SPH method. This allows the handling of large deformations in solid matter. Similar representation using mesh-based methods is difficult to achieve. Such large body deformations are seen during an explosion, high speed impact and crack propagation.

The SPH method and algorithms were developed for the study of astrophysics as stated above. Inherently, the methods and algorithms were based on probability theories and this worked well in studying the various astrophysical phenomenon. However, a direct application to analyse computational fluid mechanics and computational solid mechanics presents a different set of challenges. This includes challenges of stability and accuracy in reproducing the governing differential equations. Nonetheless, research continues to develop the SPH method to improve the reliability, efficiency and accuracy of the numerical solutions [56 – 58].

2.4.3 Element Free Galerkin Method (EFG)

The Element Free Galerkin method was briefly described in Chapter 1 of this thesis. This section will expand on the formulation and construction of the EFG method. Belytschko [53] developed the EFG method by modifying the Diffuse Element Method (DEM) and employing the Moving Least Square method (MLS) for the interpolation.

EFG method follows the meshless construct by representing the problem domain and the boundary with a set of grid points. A set of system algebraic equations is then established using the Galerkin method. In terms of solid mechanics, the Galerkin method is formulated in order to handle the essential boundary conditions using the Lagrange multipliers.

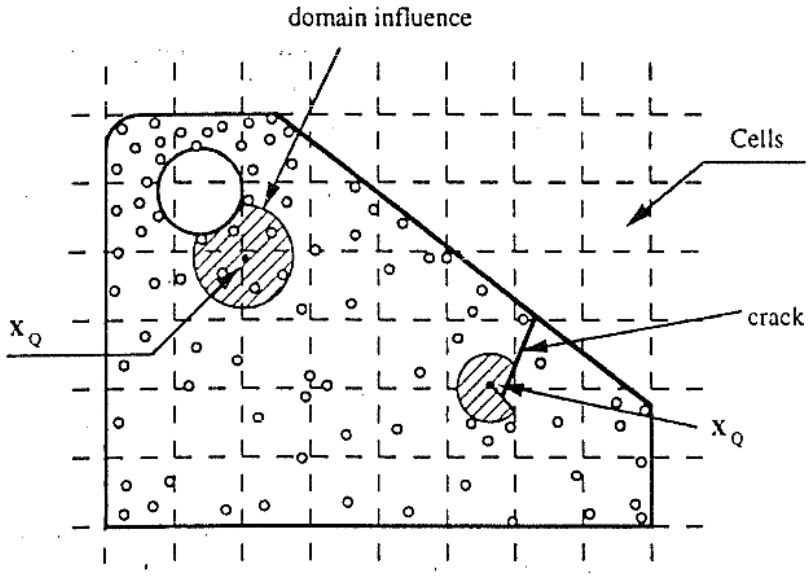

Figure 2.9 EFG method: Cell and quadrature points representation in the domain [53].

The system equations are computed using the Gauss integration scheme. In order to deal with the domain integration in EFG method, a background mesh of cells overlays the problem domain. Integration points are distributed across the background cells and the accuracy of the integration is controlled by the cell density of integration points as represented in Fig. 2.9. The field functions mainly displacement and stresses at a point in the problem domain can be determined using nodal parameters and a support domain.

The EFG method has been well received by researchers, and in addition to the patch test carried out by Belytchko [53], the EFG method has also been used in the analysis of arbitrary Kirchhoff shells [60]. Hegen [61] also combined EFG method and FEM in order to take advantage of their positive traits. The EFG method is applied in the critical regions such as near a crack tip and the FEM method is used for representing the remaining region deemed less significant in influencing the results at the crack tip. Restricting EFG to a small critical region can reduce the computational time which is seen as a disadvantage when performing an analysis with only the EFG method. The hybrid approach of combining EFG method and FEM method can give an accurate result for the stress intensity factor.

2.4.4 Meshless Local Petrov-Galerkin Method (MLPG)

The Meshless Local Petrov-Galerkin method (MLPG) as developed by Atluri and Zhu [52, 62] is termed to be truly meshless. In the EFG method the problem is solved by the global weak form over the entire problem domain and background cells are used for the domain integration. Alternatively, the MLPG method adopts the Local Symmetric Weak Form (LSWF) approach by defining a small localised sub-domain which is located within the global domain. This is illustrated in Fig. 2.10.

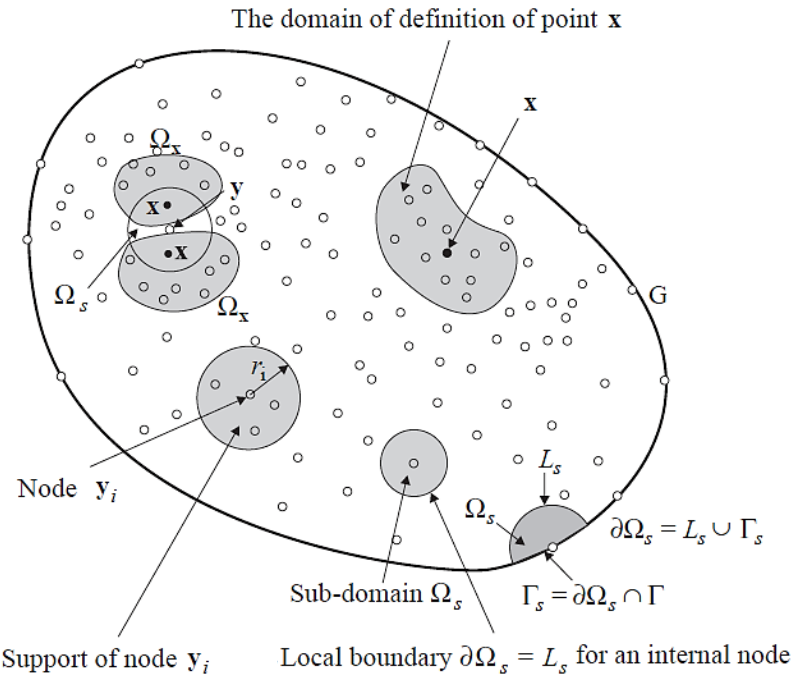

Figure 2.10 The problem domain, the sub-domains and prescribed boundary conditions as defined by Atluri [52, 62]

In the MLPG method, the local weak form integrations are based on the Petrov-Galerkin residual formulation. Which allow for flexibility to choose a trial function and a weight function independently. Akin to the EFG method, the moving least square approximation is implemented in the MLPG method for constructing the shape functions.

The MLPG method can be computationally expensive when compared with other numerical methods like FEM where element equations mainly shape functions and other systems equations are pre-determined. However, by combining the MLPG method with the FEM method and the Boundary Element Method (BEM) by Liu and Gu [66], we can improve the solution efficiency.

When we consider the application of the MLPG method, Aturi [64] was able to successfully solve elasto-statics problems. MLPG has been applied to the study of static and dynamic (stability, free vibration and forced vibration) of beams [63, 65].

2.4.5 Meshless Collocation Method

Meshless collocation method is an alternative form of meshless method based on the strong form. In the preceding sections, the focus has been to explain meshless methods based on the weak form. Other established strong forms of meshless methods include the Irregular Finite Difference Method (IFDM) and the Finite Point Method (FPM).

Adversely, the strong form meshless methods stated above can become unstable with the usage of irregular nodes. The approximated result can also be less accurate. Inadequate collocation points in the sub-domain may result in significant margins of error [68]. Review of several numerical methods based on the collocation method shows the variety of interpolation and approximation techniques. These include the moving least square method, the radial basis function, and the least-square collocation method [67 - 70].

Over the years much effort has been devoted to advancing the Finite Point Method (FPM) to achieve stability and accurate results. Oñate [70] worked on stabilizing the FPM for the analysis of convection-diffusion and fluid flow type problems. Oñate [69] also showed that the stabilized quadratic FPM developed for 2D and 3D elasticity problems can produce higher accuracy result than the standard FEM. Also, Galerkin based methods can produce accurate results when compared with a collocation-based method. However, the computational effort for the collocation method is much less than the Galerkin equivalent analysis.

2.4.6 Point Interpolation Method

Point Interpolation Method (PIM) is a meshless technique where the shape function is constructed using polynomial interpolation functions. The problem domain is discretised by field nodes and the field function at any point in the domain Ω is defined as $u(x)$. Employing nodes in a local support domain, the field function $u(x)$ at a point x_Q is interpolated using polynomials as follows [73, 74, 75]

$$u(x, x_Q) = \sum_{i=1}^{n} p_i(x) a_i(x_Q) = P^T(x) a(x_Q) \ , \tag{2.36}$$

where n is the number of nodes in the support domain of node x_Q, $p_i(x)$ is the monomials and $a_i(x_Q)$ is the unknown coefficient yet to be determined and this is expressed as

$$a(x_Q) = \begin{pmatrix} a_1 \\ a_2 \\ a_3 \\ \vdots \\ a_n \end{pmatrix} . \tag{2.37}$$

For a one-dimensional problem, the basis is given as $P^T = \left[1, x\ , x^2, \ldots x^n\right]$ and for a two-dimensional case $P^T = \left[1, x,\ y,\ xy,\ , \ldots\right]$.

The approximation of the field function $u(x)$ for node x_Q using nodes in the support domain will yield a set of algebraic equations which must be solved. By enforcing the field function $u(x)$ to be satisfied at the nodes within the support domain, the field function in Eq. (2.36) is now expressed in terms of the nodal values and this is express as

$$u_i = P^T(x_i)a \quad , \tag{2.38}$$

where u_i is the nodal value of u at $x = x_i$ and $i = 1 \ldots n$. Eq. (2.38) can also be written in a matrix form as

$$\mathbf{u} = \mathbf{P}_Q \boldsymbol{a} \quad . \tag{2.39}$$

Thus, the unknown coefficient $\boldsymbol{a}$ is determined by

$$\boldsymbol{a} = \mathbf{P}_Q^{-1}\mathbf{u} \quad . \tag{2.40}$$

Substituting Eq. (2.40) into Eq. (2.36) gives

$$u(x, x_Q) = \mathbf{P^T}(x)\mathbf{P}_Q^{-1}\mathbf{u} \quad , \tag{2.41}$$

where the shape function is defined by

$$\Phi(x) = \mathbf{P^T}(x)\mathbf{P}_Q^{-1} = \left[\phi_1(x),\ \phi_2(x),\ \ldots\ldots \phi_n(x)\right] \quad . \tag{2.42}$$

2.4.7 Meshless Method Vs Mesh-based Method

This literature review has highlighted some of the strengths of the ongoing developments and capabilities of meshless method. A comparison of meshless and mesh-based method, mainly Finite Element Method is outlined below.

- Elements and grid point: FEM uses structured mesh to represent the domain while meshless method might use background cells. Truly meshless uses only grid points in the domain and along the boundary.
- Mesh generation: Mesh for FEM are predetermined and the user has to choose the best suited elements for the analysis. Mesh generation can be difficult for complex geometries and models. In terms of meshless method, the grid point generation for a complex geometry can be relatively easy and less demanding.
- Construction of shape function: For FEM, the shape function is predetermined and it depends on the element. The shape function for meshless method depends on the grid points or the background cells if used in the analysis.
- Computational speed: In the case of the same number of nodes, the FEM method can be faster. The moderate speed of the meshless method is down to the setup of large system equations and shape functions during the analysis. However, this is compensated by the time saving in setting up the model.
- Accuracy of analysis: FEM is an accurate numerical method and this is demonstrated by its commercial success. FEM is very accurate when compared with the finite difference method. In the meantime, meshless method can be equally accurate when compared with FEM. For a linear analysis, meshless method can be more accurate than FEM.
- Commerciality and availability of software: FEM method is very popular and widely used across industry. Many software for FEM analysis are available in shops. FEM is widely trusted and has become the standard for checking and verifying newly developed numerical programs. Meshless method on the other has a few written programs but the pace and the necessity for science and engineering analysis is fast growing.

2.5. The Finite Block Method

2.5.1 Overview

The finite block method is a new meshless point collocation method proposed by Li and Wen [71]. The finite block method simply divides the physical domain into blocks and the boundaries of the blocks are connected by nodes. The governing partial differential equation for the system is derived in terms of the nodal values. This process is achieved by employing the mapping technique for each block until the entire domain is mapped. In this process, the stress and displacement continuities along the finite block boundary is maintained.

Li and Wen [71] demonstrated the capabilities of the finite block method by performing several numerical examples. This include the study of stationary heat conduction for an anisotropic nozzle, the transient heat conduction for an isotropic ring, a plate with a circular hole and the evaluation of a three-dimensional heat conduction problem in a Functionally Graded Material (FGM). Comparing the achieved results for the examples stated above with the analytical equivalent showed a high degree of accuracy for the finite block method.

Further development by Wen and Li [72] saw the implementation of finite block method for elasticity. Considering a 2D case in the Cartesian coordinate system, the practical domain is transformed by a square normalised domain using the mapping technique. A partial differential of a function in the practical domain is then determined with respect to the normalised domain axis. Thus, we can now deduce the first order partial differential matrices for the function in the practical domain. In the case of elasticity this is the displacement differential matrix in the Cartesian coordinate system. Exploring the relationship between stress and strain, and the displacement differential, a matrix is formed in terms of the equilibrium equation for a 2D plane stress. The matrix equation reduces to a series of algebraic equations which is then solved to determine the displacement for each node. The work by Wen and Li [72] on elasticity was used to evaluate a cantilever beam in a functionally graded media. This process is further expanded in Chapter 3 due to the relevance of elasticity in the study of material fracture.

CHAPTER 3

Finite Block Method: Interpolation of Field Variable

3.1. Introduction

In computational engineering, the unknown field function mainly displacement at a given point is determined by an approximation technique. Some of the established approximation techniques include the Moving Least Square method (MLS), the Radial Basis Function method (RBF), the Lagrange series interpolation and the Point Interpolation Method (PIM). The formulation of these approximation techniques eventually leads to the construction of the shape function which is central to the numerical process to determine the unknown field function.

In the case of finite element method, the shape function is based on the characteristics of the element. In most cases, the shape function for FEM analysis is predetermined prior to the analysis. Therefore, applying elements designated for a model exhibiting simple geometry might not be suitable for a model with large deformations, and this can lead to an inaccurate result. The inaccuracies of the result is due to the limitations of the element shape function and the inability to perform multiple complex analyses. Thus, several types of elements have been developed for modelling different types of problems in FEM.

By contrast to the finite element method, the meshless method shape functions are determined during the analysis and not before the analysis. This means the shape function varies at different points in the domain and no two shape functions are necessarily the same.

In the meshless method, the shape function construction employs a small number of nodes at the point of interest. The selected nodes used in constructing the meshless shape function are described as the local support domain. Shape functions are easily constructed with regular node arrangement. However, for irregular node arrangement, the shape function construction can be challenging.

In this research, the Lagrange approximation is employed in the interpolation of finite blocks for a given problem. Therefore, the construction of the Lagrange series interpolation is presented in this chapter. The consistency of the interpolation, the continuity, nodal arrangement and other influencing parameters are explored in this chapter. As expected, the interpolation error is discussed in order to understand the strength and limitations of the Lagrange series interpolation.

3.2. Evaluation of Differential Matrix by the Lagrange Series Interpolation: One-Dimensional Problem

3.2.1 Derivatives for One-Dimensional Regular Node Distribution

For a one-dimensional problem, a group of nodes are evenly arranged on a straight line as shown in Fig. 3.1. Arrangement of the nodes is defined by

$$\xi_i = -1 + \frac{2(i-1)}{N-1}, \quad i = 1,2,\ldots,N. \tag{3.1}$$

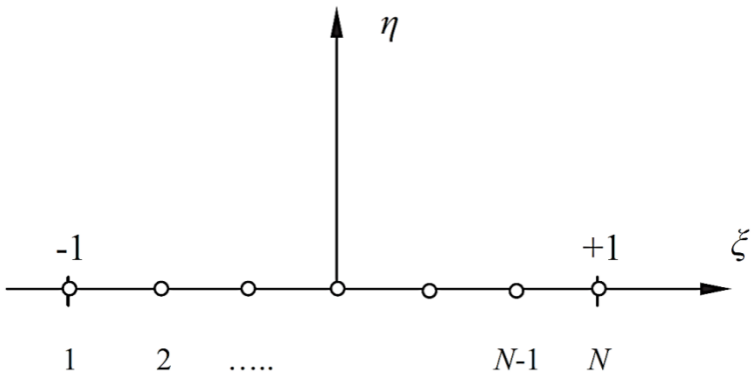

Figure 3.1 One-dimensional evenly distributed collocation points.

The first order differential of a function $u(\xi)$ can be evaluated using the Lagrange series interpolation method. The function $u(\xi)$ is approximated by the following expression

$$u(\xi)=\sum_{k=1}^{N} a_k \xi^{k-1} \quad , \quad -1 \le \xi \le 1 \; . \tag{3.2}$$

where $\{a_k\}_{k=1}^{N}$ is the coefficient defined by

$$\begin{bmatrix} 1 & \xi_1 & \xi_1^2 & \dots & \xi_1^{N-1} \\ 1 & \xi_2 & \xi_2^2 & \dots & \xi_2^{N-1} \\ \dots & \dots & \dots & \dots & \dots \\ 1 & \xi_N & \xi_N^2 & \dots & \xi_N^{N-1} \end{bmatrix} \begin{pmatrix} a_1 \\ a_2 \\ \dots \\ a_N \end{pmatrix} = \begin{pmatrix} u_1 \\ u_2 \\ \dots \\ u_N \end{pmatrix} \; . \tag{3.3}$$

The function $u(\xi)$ can also be expressed in terms of the Lagrange series interpolation and the nodal values in the form

$$u(\xi)=\sum_{j=1}^{N} \prod_{\substack{k=1 \\ k\neq j}}^{N} \frac{(\xi-\xi_k)}{(\xi_j-\xi_k)} u_j \; , \tag{3.4}$$

where the nodal value is expressed as $\{u_k\}_{k=1}^{N}$.

The determined first order derivative of the function is given by

$$\frac{du}{d\xi} = u'(\xi) = \sum_{k=2}^{N} (k-1) a_k \xi^{k-2} \ , \tag{3.5}$$

and the equivalent Lagrange series interpolation is given by

$$\frac{du}{d\xi} = \sum_{j=1}^{N} u_j \prod_{k=1, k\neq j}^{N} (\xi_j - \xi_k)^{-1} \sum_{i=1}^{N} \prod_{k=1, k\neq j, k\neq i}^{N} (\xi - \xi_k) \ , \tag{3.6}$$

The derivative of the function $u(\xi)$ can be expressed in a matrix form

$$\mathbf{U}_{\xi} = \mathbf{D}_0 \mathbf{u} \ \ , \tag{3.7}$$

where $\mathbf{U}_{\xi} = \left[u_1^{'}, u_2^{'}, \ldots u_N^{'}\right]^T$ is the vector of nodal value of the first order derivative which is derived with respect to the ξ coordinate, $\mathbf{D}_0$ is the first order differential matrix for a one-dimensional case and $\mathbf{u}_{\xi} = \left[u_1, u_2, \ldots u_N\right]^T$.

Considering Fig. 3.1 where a total of 7 nodes are used to define the one-dimensional problem. The first order differential matrix for nodal arrangement from 2 up to 7 is given by

$$\mathbf{D}_0 = \frac{1}{2}\begin{pmatrix} -1 & 1 \\ -1 & 1 \end{pmatrix}_{2\times 2} \ , \quad \mathbf{D}_0 = \frac{1}{2}\begin{pmatrix} -3 & 4 & -1 \\ -1 & 0 & 1 \\ 1 & -4 & 3 \end{pmatrix}_{3\times 3} \ , \quad \mathbf{D}_0 = \frac{1}{4}\begin{pmatrix} -11 & 18 & -9 & 2 \\ -2 & -3 & 6 & -1 \\ 1 & -6 & 3 & 2 \\ -2 & 9 & -18 & 11 \end{pmatrix}_{4\times 4} \ ,$$

$$\mathbf{D}_0 = \frac{1}{20}\begin{pmatrix} -147 & 360 & -450 & 400 & -225 & 72 & -10 \\ -10 & -77 & 150 & -100 & 50 & -15 & 2 \\ 2 & -24 & -35 & 80 & -30 & 8 & -1 \\ -1 & 9 & -45 & 0 & 45 & -9 & 1 \\ 1 & -8 & 30 & -80 & 35 & 24 & -2 \\ -2 & 15 & -50 & 100 & -150 & 77 & 10 \\ 10 & -72 & 225 & -400 & 450 & -360 & 147 \end{pmatrix}_{7\times 7} \ . \tag{3.8}$$

It is observed that the matrix $\mathbf{D}_0 = (d_{ij})$ follows the pattern $d_{ij} = -d_{N+1-i,N+1-j}$ $(i, j = 1,2,\ldots\ldots, N)$ and $\sum_{j=1}^{N} d_{ij} = 0$ $(i = 1,2,\ldots\ldots, N)$.

3.3. Numerical Assessment 1

3.3.1 One-Dimensional Regular Node Arrangement

The convergence and accuracy of the interpolation technique is demonstrated by estimating the second order derivative of a given function. By employing the following function

$$u(x, y) = \cos(2x) - x^2 e^{5y} + 3y^2 \ , \tag{3.9}$$

where the second order derivative is also given by

$$\frac{\partial^2 u}{\partial x^2} = -4\cos(2x) - 2e^{5y} \ , \qquad -1 \le x \le 1 \ , \ -1 \le y \le 1 \ . \tag{3.10}$$

In this study, a regular nodal distribution is considered and the number of nodes varies from 3 to 9 respectively. Table 3.1 shows the average errors for the different nodal configurations. In this case the average error is defined as

$$\varepsilon_{error} = \frac{\sum_{i=1}^{N} \left| w_i - w_i^* \right|}{N} \ , \tag{3.11}$$

where w_i is the numerical solution and w_i^* represent the analytical solution.

Number of Nodes N	ε_{error_1}	ε_{error_2}
3	1.69×10^{-1}	3.78×10^{0}
4	9.76×10^{-2}	2.46×10^{0}
5	8.04×10^{-3}	6.76×10^{-1}
7	2.58×10^{-4}	4.49×10^{-2}
8	5.06×10^{-4}	3.06×10^{-2}
9	1.75×10^{-5}	1.46×10^{-3}

Table 3.1 ε_{error_1} is the average relative error between the FBM interpolation and the exact solution of Eq. (3.9) and ε_{error_2} represent the average relative error between the FBM interpolation and the analytical solution of Eq. (3.10).

Fig. 3.2 to 3.5 shows the plotting of the second order derivatives using a total number of node N = 3, 5, 7 and 9. Regular nodal distribution was used to obtaining this result.

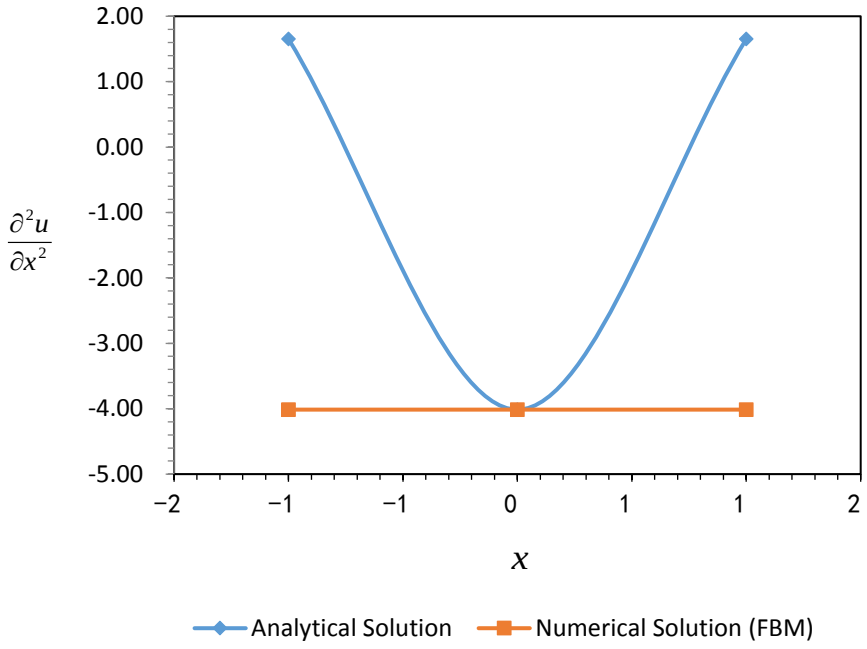

Figure 3.2 Comparing the analytical and numerical solution for the second order derivative of Eq. (3.9), for $y = -1$. Employing a total number of nodes N = 3.

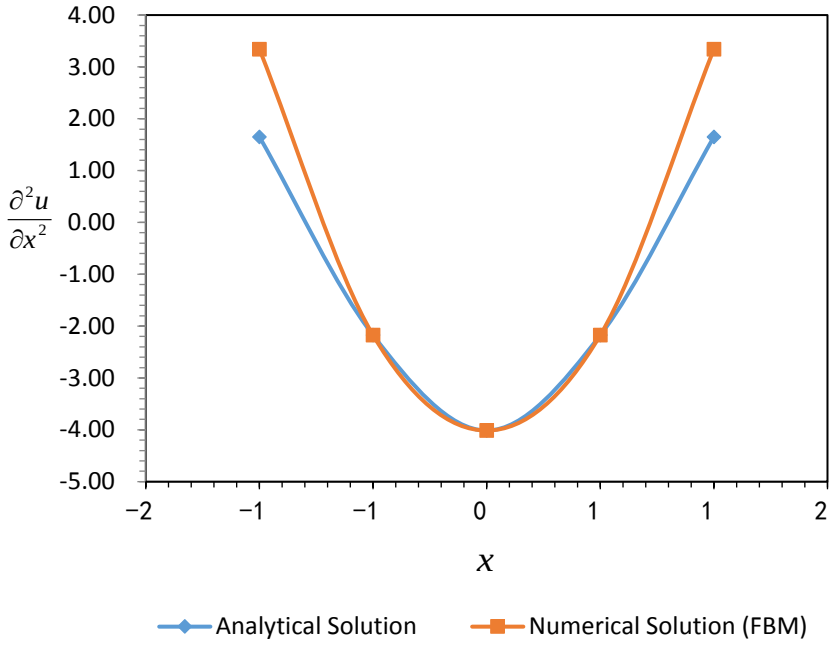

Figure 3.3 Comparing the analytical and numerical solution for the second order derivative of Eq. (3.9), for $y = -1$. Employing a total number of nodes $N = 5$.

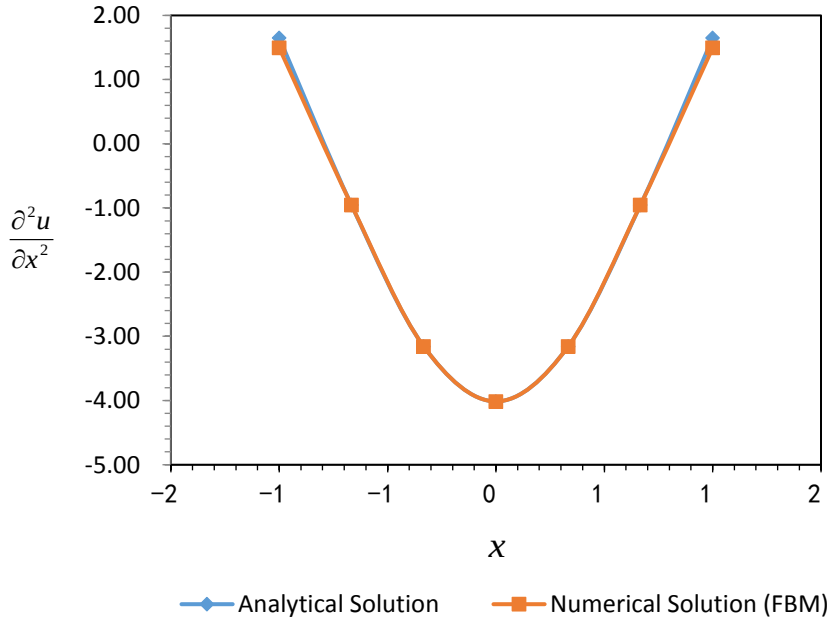

Figure 3.4 Comparing the analytical and numerical solution for the second order derivative of Eq. (3.9), for $y = -1$. Employing a total number of nodes $N = 7$.

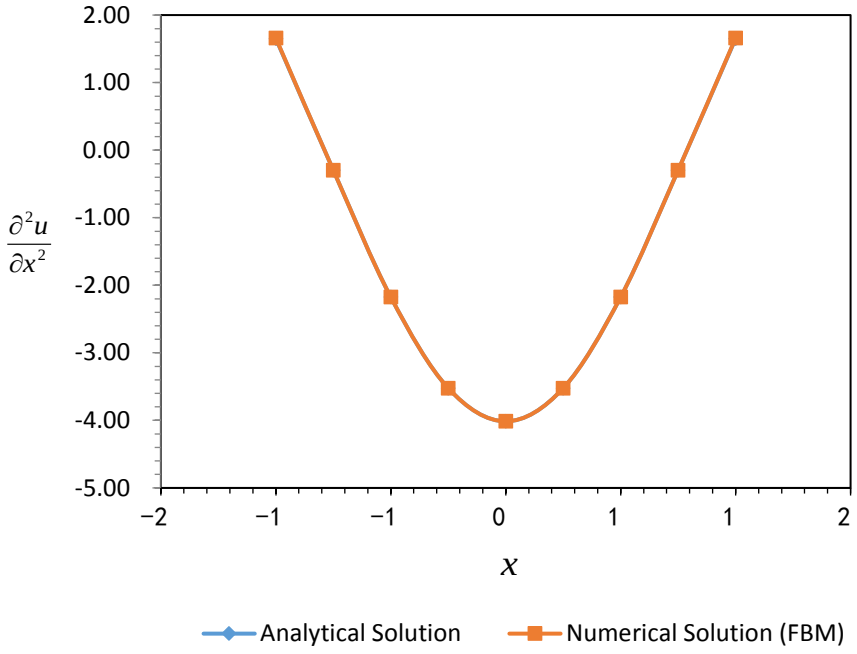

Figure 3.5 Comparing the analytical and numerical solution for the second order derivative of Eq. (3.9), for $y = -1$. Employing a total number of nodes $N = 9$.

The approximation of the second order derivative of the function in Eq. (3.9) using the Lagrange series interpolation is plotted in Fig 3.2 through 3.5. The exact solutions are compared with the Lagrange approximation by considering all values of x for $y = -1$. For $N = 3$, the second order differential is interpolated as a constant. This is depicted in Fig. 3.2. This is due to an inadequate number of nodes for the interpolation of a parabolic function.

Interpolation along the boundary by the Lagrange approximation can be shown to be challenging. From Fig. 3.2 we can see the effects of approximating with a small number of nodes. The relative error for approximating values of Eq. (3.10) using nodes $N = 3$ is too high and this is given in Table 3.1 to be over 3.78. However, this was resolved by increasing the number of nodes. At $N = 7$ the average relative error decreased significantly to less than 5% and the error further decreases to 0.11% when the number of nodes was increased to $N = 9$. Also, to achieve a reasonable or highly accurate result using a regular node distribution, the nodal density along the boundary and the domain are increased simultaneously. Hence, we cannot increase nodes in targeted areas or areas of interest. Nonetheless, it can be seen from Fig. 3.3 to 3.5, the Lagrange series interpolation can produce accurate results for the second order

differential as expressed in Eq. (3.10) by simply increasing the global nodal density for the analysis.

3.4. Numerical Assessment 2

3.4.1 One-Dimensional Irregular Node Arrangement

The first order differential matrix $\mathbf{D}_0$ as determined for a one-dimensional case is a function of the nodal arrangement. Therefore, the equivalent first order differential matrix for a one-dimensional case with an irregular node distribution is presented in this section. The numerical analysis described in section 3.3.1 is repeated in this section in order to ascertain the effect of the nodal arrangement on the accuracy of the numerical result.

For a one-dimensional problem, a group of irregular nodes arranged on a straight line is shown in Fig. 3.6 below. The arrangement of the nodes is selected to be Chebyshev's roots, as

$$\xi_i = -\cos\left(\frac{\pi(i-1)}{N-1}\right), \quad i = 1,2,\ldots,N \ . \tag{3.12}$$

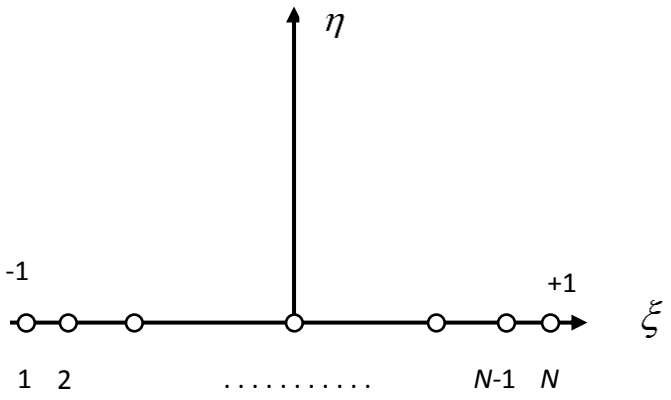

Figure 3.6 One-dimensional irregular distributed collocation points.

In this assessment of the Lagrange series interpolation, the function in Eq. (3.9) is examined with an irregular node distribution. The average relative error for the analysis

is presented in Table 3.2. Fig. 3.7 to 3.9 shows the plotting of the second order derivative of Eq. (3.9), using a total number of node N = 5, 7 and 9.

Number of Nodes N	ε_{error_1}	ε_{error_2}
3	1.95×10^{-1}	3.78×10^{0}
5	6.59×10^{-3}	4.35×10^{-1}
7	6.62×10^{-5}	1.65×10^{-2}
9	1.50×10^{-5}	7.11×10^{-4}

Table 3.2 ε_{error_1} is the average relative error between the FBM interpolation and the exact solution of Eq. (3.9) and ε_{error_2} represent the average relative error between the FBM interpolation and the analytical solution of Eq. (3.10).

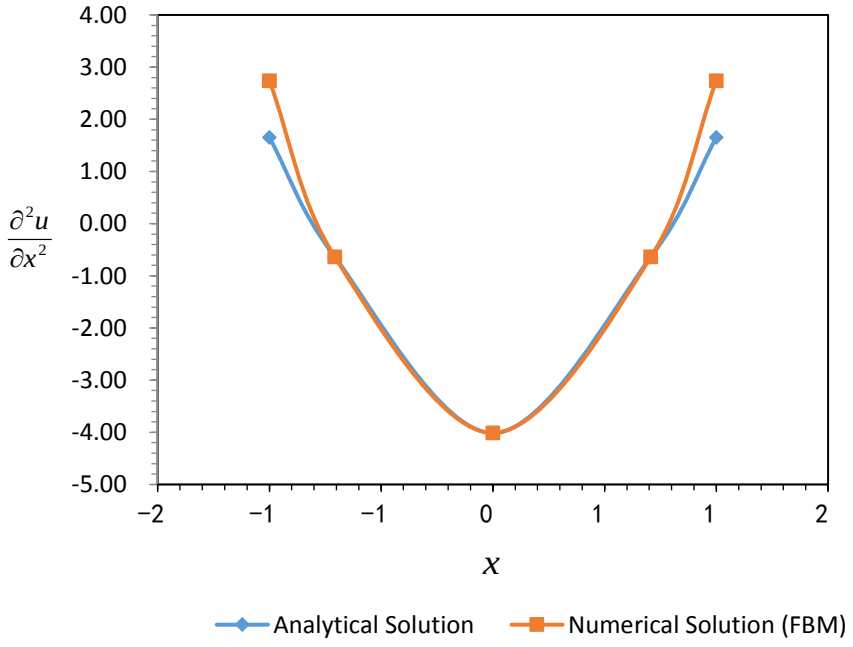

Figure 3.7 Comparing the analytical and numerical solution for the second order derivative of Eq. (3.9), for $y = -1$. Employing a total number of nodes N = 5.

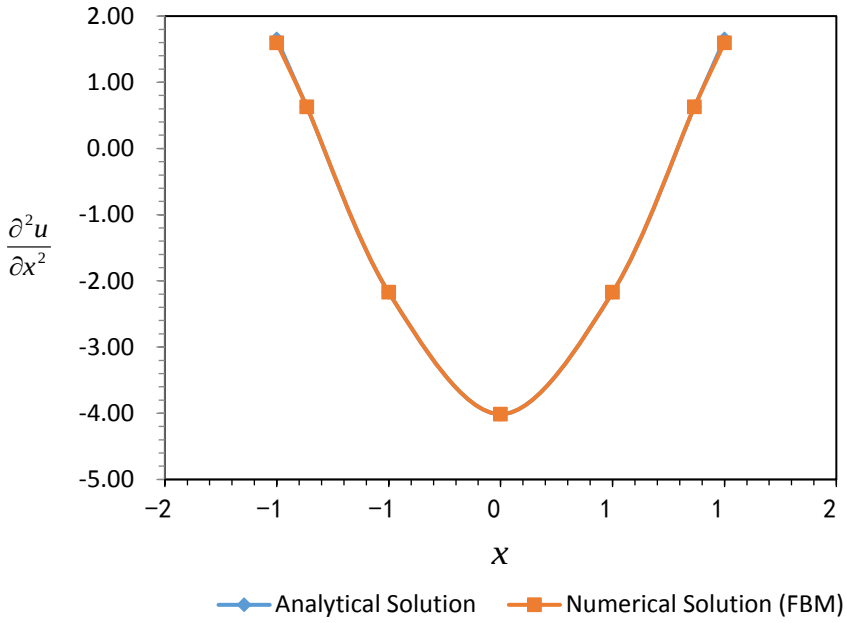

Figure 3.8 Comparing the analytical and numerical solution for the second order derivative of Eq. (3.9), for $y = -1$. Employing a total number of nodes $N = 7$.

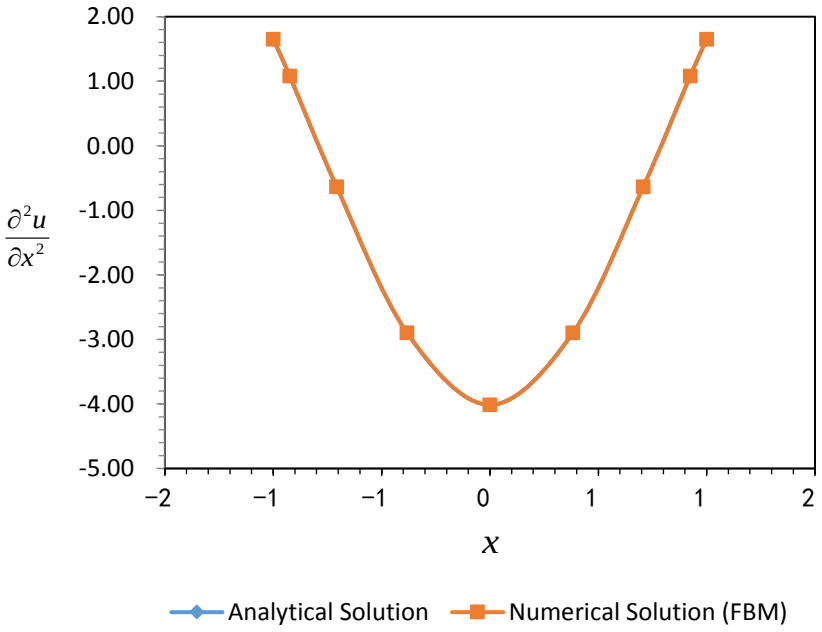

Figure 3.9 Comparing the analytical and numerical solution for the second order derivative of Eq. (3.9), for $y = -1$. Employing a total number of nodes $N = 9$.

The regular node distribution analysis as presented in Numerical Assessment 1 section 3.3 shows that the accuracy of the result was improved by increasing the total number of nodes. However, this approach will lead to a high computational cost when a large model is to be analysed. To avoid such an issue, the area of interest in a model should be targeted and the number of nodes in that region should be increased. A typical case where such a requirement will be of great benefit is the study of the fields near a crack tip. In this section 3.4.1, such a technique was examined by using an irregular node distribution arrangement and the number of nodes was increased near the boundary for better approximation of the defined functions. For the same number of nodes $N = 7$ as used in the regular distribution, the Lagrange approximation method with an irregular node distribution attains a lower average relative error. This is reported in Table 3.2 to be 1.65%. In addition, it can be deduced from Table 3.1 and 3.2 that both the regular and the irregular nodal arrangements can be equally effective for the Lagrange series interpolation when using higher number of nodes.

3.5. Evaluation of Differential Matrix by the Lagrange Series Interpolation; Two-Dimensional Problem

3.5.1 Derivatives for Two-Dimensional Regular Node Distribution

The study of finite block method in a two-dimensional sense is best described with the aid of a normalised square domain. In this study, the normalised square domain has been assigned the coordinate system $\xi o \eta$ and this is depicted in Fig. 3.10. In addition, local collocation points describing the domain and the boundary are also prescribed.

Following the same manner as described for the one-dimensional method above, we can define a two-dimensional smooth function $u(\xi,\eta)$ across the normalised domain. Also, we define in terms of each nodal value the partial derivative

$$u_{\xi}(\xi,\eta) = \frac{\partial u}{\partial \xi}(\xi,\eta) \quad , \tag{3.13a}$$

$$u_{\xi}(\xi_P,\eta_P) = \frac{\partial u}{\partial \xi}(\xi_P,\eta_P) \quad , \tag{3.13b}$$

where the number for the point P is determined by the expression $P = N \times (j-1) + i$. The values of i and j denote the number of horizontal lines (rows) and vertical lines (columns) respectively. The numbering system as expressed here is therefore utilised globally in the subsequent analysis in this report.

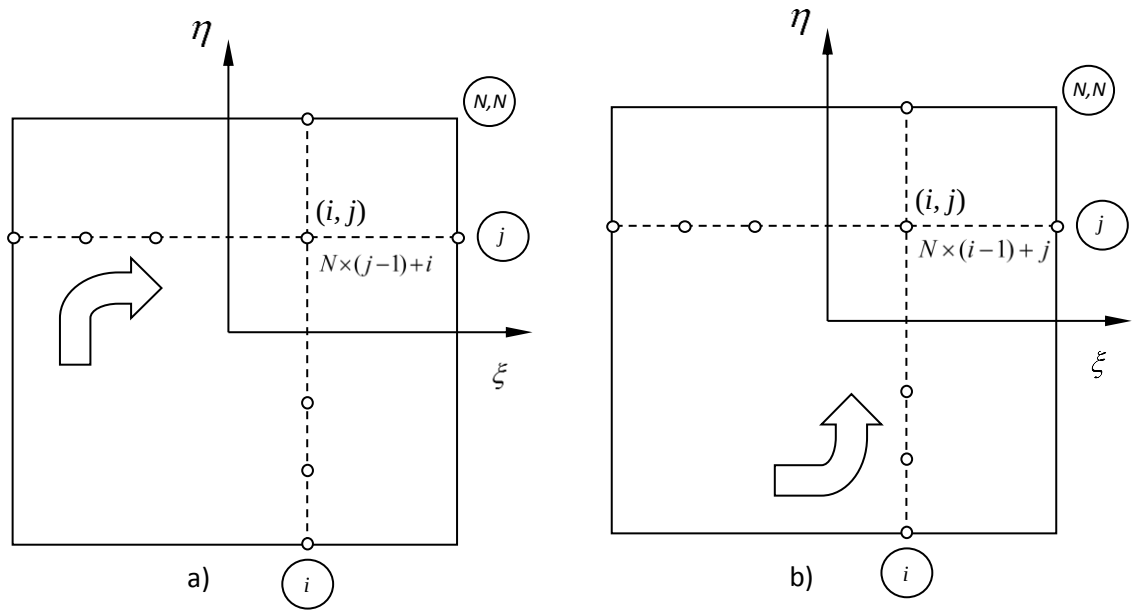

Figure 3.10 A square normalised domain with coordinate system $\xi o \eta$. a) global numbering system b) local numbering system.

Eq. (3.13) can also be reworked in a matrix form as

$$\mathbf{U}_{\xi} = \mathbf{D}_{\xi}\mathbf{u} \ , \tag{3.14}$$

The vector derivative of the nodal values U_{ξ} is defined by

$$U_{\xi} = \begin{pmatrix} U_{\xi_1} \\ U_{\xi_2} \\ \vdots \\ U_{\xi_M} \end{pmatrix} \ , \tag{3.15}$$

where *M* is the total number of nodes given by $M = N \times N$.

For a square domain with normalised coordinate system and numbering, the first order differential matrix in the global numbering system for all nodes is given by

$$\mathbf{D}_{\xi} = \underbrace{\begin{pmatrix} \mathbf{D}_0 & 0 & 0 & 0 \\ 0 & \mathbf{D}_0 & 0 & 0 \\ \cdots & \cdots & \cdots & \cdots \\ 0 & 0 & 0 & \mathbf{D}_0 \end{pmatrix}}_{N^2} . \tag{3.16}$$

In this case $\mathbf{D}_0$ is the differential matrix for a one-dimensional nodal distribution with dimensions $N \times N$ as expressed in Eq. (3.8). In a similar manner, the partial differential with respect to the η direction is given by

$$\mathrm{U}_{\eta}(\xi,\eta) = \frac{\partial \mathrm{u}}{\partial \eta}(\xi,\eta) \ , \tag{3.17a}$$

$$\mathrm{U}_{\eta}(\xi_P,\eta_P) = \frac{\partial \mathrm{u}}{\partial \eta}(\xi_P,\eta_P) \ . \tag{3.17b}$$

Using the local numbering system for the collocation points $P = N \times (i-1) + j$, Eq. (3.17) can be expressed in a matrix form as

$$\overline{\mathbf{U}}_{\eta} = \mathbf{D}_{\xi}\overline{\mathbf{u}} \ . \tag{3.18}$$

Furthermore, Eq. (3.18) can be written in terms of a transformed matrix using the global numbering system as

$$\mathbf{U}_{\eta} = \mathbf{T}\overline{\mathbf{U}}_{\eta} \ \text{ and } \ \mathbf{u} = \mathbf{T}\overline{\mathbf{u}} \ . \tag{3.19}$$

After establishing that the collocation points in the global numbering system $P = N \times (j-1) + i$ equates to the collocation point in the local numbering system $P = N \times (i-1) + j$, this leads to a situation where all elements in the transformation matrix $\mathbf{T}$ are zero except at

$$\mathbf{T}_{N\times(j-1)+i,\,N\times(i-1)+j} = 1 \ , \ \ i, j = 1,2,\ldots,N . \tag{3.20}$$

By re-organising the number of nodes, Eq. (3.19) can be reworked to give

$$\mathbf{U}_{\eta} = \mathbf{T}\mathbf{D}_{\xi}\mathbf{T}^{-1}\mathbf{u} = \mathbf{D}_{\eta}\mathbf{u}, \quad \mathbf{T}^{-1} = \mathbf{T}^{T} \ . \tag{3.21}$$

In essence, the formulation as determined in Eq. (3.21) can be utilised in resolving higher order derivatives. In the case of a two-dimensional domain, a general expression for the higher order derivatives with respect to ξ and η can be written in the form

$$U_{\xi\eta}^{(mn)}(\xi_p,\eta_p)=\frac{\partial^{(m+n)}\mathrm{u}}{\partial\xi^m\partial\eta^n}(\xi_p,\eta_p)\ . \tag{3.22}$$

Thus, nodal values of Eq. (3.22) is determined in a matrix form as

$$\mathbf{U}_{\xi\eta}^{(mn)}=\mathbf{D}_{\xi}^{m}\mathbf{D}_{\eta}^{n}\mathbf{u}\quad . \tag{3.23}$$

3.6. Finite Block Method: Derivatives of a Two-Dimensional Problem Using the Mapping Technique

The critical feature of the finite block method is the ability to divide the physical domain of a plate (2D case) into blocks. Using a similar technique as performed in the finite element method, a two-dimensional quadratic element or block expressed in the form of a normalised domain can be mapped onto a real or a physical domain, and vice versa using the appropriate transformation equations. The technique of mapping an irregular mesh in real space into a structured mesh in a normalised space is described as the 'Boundary-Fitted Coordinate Method" [89]. Some of the desirable features of the boundary-fitted coordinate method is the flexibility of modelling curved boundaries and at the same time keeping the features of a structured mesh [90].

For the finite block method, the governing equations are satisfied in the strong form at certain collocation points. Therefore, for a two-dimensional analysis this feature of the FBM method is maintained. The first order partial differential matrix can be obtained directly using the mapping technique based on the Lagrange series interpolation.

Since a 2D block analysis is under consideration, we begin by defining a two-dimensional block or element with 8 nodes as illustrated in Fig. 3.11. A square normalised domain with 8 nodes has been deliberately chosen for the mapping of the geometry.

A smooth function $u(\xi,\eta)$ can be approximated in the domain $|\xi|\le 1$ and $|\eta|\le 1$ as

$$u(\xi,\eta)=\sum_{i=1}^{M}\sum_{j=1}^{N}F(\xi,\xi_i)G(\eta,\eta_j)u_l \ , \tag{3.24}$$

where M and N are the number of collocation points along the two axes, u_l indicates the nodal value, $l=(j-1)M+i$, with uniformly distributed nodes at $\xi_i=-1+2(i-1)/(M-1)$, $i=1,2,...,M$, $\eta_j=-1+2(j-1)/(N-1)$, $j=1,2,...,N$, and two polynomial functions

$$F(\xi,\xi_i)=\prod_{\substack{m=1\\ m\neq i}}^{M}\frac{(\xi-\xi_m)}{(\xi_i-\xi_m)},\ G(\eta,\eta_j)=\prod_{\substack{n=1\\ n\neq j}}^{N}\frac{(\eta-\eta_n)}{(\eta_j-\eta_n)}. \tag{3.25}$$

The total number of nodes is given by $Q=M\times N$.

The first order partial differential is determined straight away with respect to ξ and η respectively

$$\frac{\partial u}{\partial \xi}=\sum_{i=1}^{M}\sum_{j=1}^{N}\frac{\partial F(\xi,\xi_i)}{\partial \xi}G(\eta,\eta_j)u_l \ , \quad \frac{\partial u}{\partial \eta}=\sum_{i=1}^{M}\sum_{j=1}^{N}F(\xi,\xi_i)\frac{\partial G(\eta,\eta_j)}{\partial \eta}u_l \ , \tag{3.26}$$

where

$$\frac{\partial F(\xi,\xi_i)}{\partial \xi}=\frac{\partial}{\partial \xi}\prod_{\substack{m=1,\\ m\neq i}}^{M}\frac{(\xi-\xi_m)}{(\xi_i-\xi_m)}=\sum_{l=1}^{M}\prod_{k=1,k\neq i,k\neq l}^{M}(\xi-\xi_k)\Bigg/\prod_{m=1,m\neq i}^{M}(\xi_i-\xi_m) \ , \tag{3.27}$$

$$\frac{\partial G(\eta,\eta_j)}{\partial \eta}=\frac{\partial}{\partial \eta}\prod_{\substack{n=1,\\ n\neq j}}^{N}\frac{(\eta-\eta_n)}{(\eta_j-\eta_n)}=\sum_{l=1}^{N}\prod_{k=1,k\neq i,k\neq l}^{N}(\eta-\eta_k)\Bigg/\prod_{n=1,n\neq j}^{N}(\eta_j-\eta_n) \ . \tag{3.28}$$

In the same manner as the finite element method, a quadratic element used in a two-dimensional problem in the Cartesian coordinate system (x,y) can be mapped using a square in a mapping domain (ξ,η), by using a set of quadratic shape functions with 8 nodes as shown in Fig. 3.11(b). The quadratic shape functions are defined below as

$$N_i(\xi,\eta)=\frac{1}{4}(1+\xi_i\xi)(1+\eta_i\eta)(\xi_i\xi+\eta_i\eta-1) \ , \quad i=1,2,3,4, \tag{3.29a}$$

$$N_i(\xi,\eta)=\frac{1}{2}(1-\xi^2)(1+\eta_i\eta) \ , \quad i=5,7, \tag{3.29b}$$

$$N_i(\xi,\eta) = \frac{1}{2}(1-\eta^2)(1+\xi_i\xi)\ , \qquad i = 6,8. \tag{3.29c}$$

The partial differentials of the above shape functions with respect to the normalised axis is given by

$$\frac{\partial N_i}{\partial \xi} = \frac{\xi_i}{4}(1+\eta_i\eta)(2\xi_i\xi+\eta_i\eta) \quad \text{and} \tag{3.30a}$$

$$\frac{\partial N_i}{\partial \eta} = \frac{\eta_i}{4}(1+\xi_i\xi)(\xi_i\xi+2\eta_i\eta) \quad \text{for} \quad i = 1,2,3,4, \tag{3.30b}$$

$$\frac{\partial N_i}{\partial \xi} = -\xi(1+\eta_i\eta) \quad \text{and} \tag{3.30c}$$

$$\frac{\partial N_i}{\partial \eta} = \frac{\eta_i}{2}(1-\xi^2) \quad \text{for} \quad i = 5,7, \tag{3.30d}$$

$$\frac{\partial N_i}{\partial \xi} = \frac{\xi_i}{2}(1-\eta^2) \quad \text{and} \tag{3.30e}$$

$$\frac{\partial N_i}{\partial \eta} = -\eta(1+\xi_i\xi) \quad \text{for} \quad i = 6,8\ . \tag{3.30f}$$

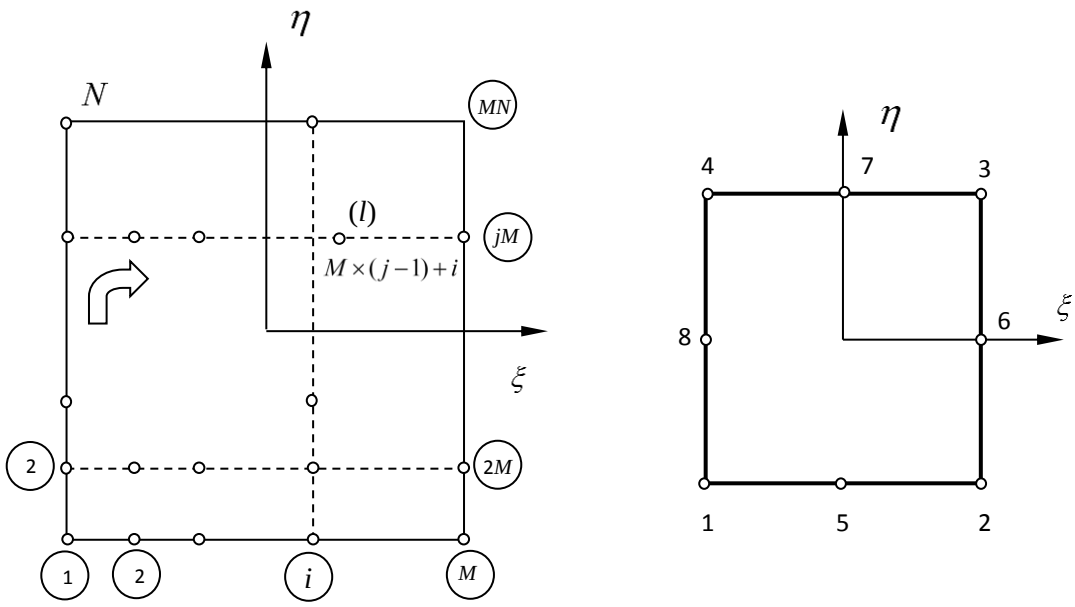

(a) (b)

Figure 3.11 Two-dimensional node distribution in the mapping domain: (a) the local numbering system of the nodes; (b) the square domain with 8 nodes for the mapping of the geometry.

Also, using the same approach as the finite element method, a quadratic block (element) in the FBM method can be mapped using a square normalised domain, shown in Fig. 3.11(b), as

$$x=\sum_{k=1}^{8}N_k(\xi,\eta)x_k,\ \ y=\sum_{k=1}^{8}N_k(\xi,\eta)y_k \quad , \tag{3.31}$$

where (x_k, y_k) denotes the coordinate of nodes k.

The first order partial differentials of the function $u(x, y)$ in the Cartesian coordinate system are therefore obtained by

$$\frac{\partial u}{\partial x}=\frac{1}{J}\left(\beta_{11}\frac{\partial u}{\partial \xi}+\beta_{12}\frac{\partial u}{\partial \eta}\right) \quad , \tag{3.32a}$$

$$\frac{\partial u}{\partial y}=\frac{1}{J}\left(\beta_{21}\frac{\partial u}{\partial \xi}+\beta_{22}\frac{\partial u}{\partial \eta}\right)\ , \tag{3.32b}$$

where

$$\beta_{11}=\frac{\partial y}{\partial \eta},\beta_{12}=-\frac{\partial y}{\partial \xi},\beta_{21}=-\frac{\partial x}{\partial \eta},\beta_{22}=\frac{\partial x}{\partial \xi}\ ,\quad J=\beta_{22}\beta_{11}-\beta_{21}\beta_{12}\ . \tag{3.33}$$

Then, substituting Eq. (3.26) into Eq. (3.32) gives

$$\frac{\partial u}{\partial x}=\frac{1}{J}\sum_{i=1}^{M}\sum_{j=1}^{N}\left[\begin{array}{l}\beta_{11}\dfrac{\partial F(\xi,\xi_i)}{\partial \xi}G(\eta,\eta_j)+\\ \beta_{12}F(\xi,\xi_i)\dfrac{\partial G(\eta,\eta_j)}{\partial \eta}\end{array}\right]u_l=D_{xl}(\xi,\eta)u_l\ , \tag{3.34a}$$

$$\frac{\partial u}{\partial y}=\frac{1}{J}\sum_{i=1}^{M}\sum_{j=1}^{N}\left[\begin{array}{l}\beta_{21}\dfrac{\partial F(\xi,\xi_i)}{\partial \xi}G(\eta,\eta_j)+\\ \beta_{22}F(\xi,\xi_i)\dfrac{\partial G(\eta,\eta_j)}{\partial \eta}\end{array}\right]u_l=D_{yl}(\xi,\eta)u_l\ , \tag{3.34b}$$

Finally, the nodal values of the first order partial differentials in Eq. (3.34) can be written, in a matrix form, as

$$\mathbf{u}_{,x}=\mathbf{D}_{,x}\mathbf{u}\ ,\ \mathbf{u}_{,y}=\mathbf{D}_{,y}\mathbf{u}\ , \tag{3.35}$$

where the vectors of the nodal value of the first order partial differentials

$$\mathbf{u}_{,x}=\left\{\frac{\partial u(x_1,y_1)}{\partial x},\frac{\partial u(x_2,y_2)}{\partial x},...,\frac{\partial u(x_Q,y_Q)}{\partial x}\right\}^{\mathrm{T}}, \tag{3.36a}$$

$$\mathbf{u}_{,y}=\left\{\frac{\partial u(x_1,y_1)}{\partial y},\frac{\partial u(x_2,y_2)}{\partial y},...,\frac{\partial u(x_Q,y_Q)}{\partial y}\right\}^{\mathrm{T}}, \tag{3.36b}$$

are the vectors of the nodal value of displacement $\mathbf{u}=\{u_k\}^{\mathrm{T}}$, and the partial differential matrices

$$\mathbf{D}_{,x}=\left\{D_{kl,x}(\xi_k,\eta_k)\right\}\ ,\ \mathbf{D}_{,y}=\left\{D_{kl,y}(\xi_k,\eta_k)\right\}\ ,\ \ (k,l=1,2,...,Q),$$

where the total number of nodes is given by $Q=M\times N$.

In addition, for the *L*-th order derivatives in two-dimensions with respect to both coordinates *x* and *y*,

$$u_{xy}^{(mn)}(x,y)=\frac{\partial^{m+n}u(x,y)}{\partial x^m\partial y^n},\quad m+n=L\ , \tag{3.37}$$

can be approximated in a matrix form, in terms of the first order partial differential matrices $\mathbf{D}_{,x}$ and $\mathbf{D}_{,y}$, as

$$\mathbf{u}_{,xy}^{(mn)}=\mathbf{D}_{,x}^{m}\mathbf{D}_{,y}^{n}\mathbf{u}\ , \tag{3.38}$$

3.7. Numerical Assessment 3

The finite block method is investigated for a two-dimensional case using one block. Fig. 3.12 shows the block with the nodes on the boundary and the domain. This is the block in the transformed domain after the mapping process has been applied. In this investigation, several regular node distributions with dimensions ranging from 3 x 3 to 11 x 11 are considered. The coordinates of the regular node arrangement are given by

$$\xi_i=-1+\frac{2(i-1)}{N-1},\quad i=1,2,\ldots,N\ , \tag{3.39}$$

$$\eta_j=-1+\frac{2(j-1)}{N-1},\quad j=1,2,\ldots,N\ . \tag{3.40}$$

The first and second order derivative of Eq. (3.9) is applied across the 2D block in order to observe the accuracy of the finite block method using the mapping technique. The first order differential of Eq. (3.9) is given by

$$\frac{\partial u}{\partial x}=-2\sin(2x)-2xe^{5y},\qquad 0\le x\le 1\ ,\ 0\le y\le 1. \tag{3.41}$$

The average relative error between the finite block method and the exact solutions are reported in Table 3.3. Furthermore, a plot of the second order differential of Eq. (3.9) across the 2D domain and the boundary is presented in Fig. 3.13. The plot between the exact solution and the numerical method (FBM) considers the values of all *x* at *y* = 0.5.

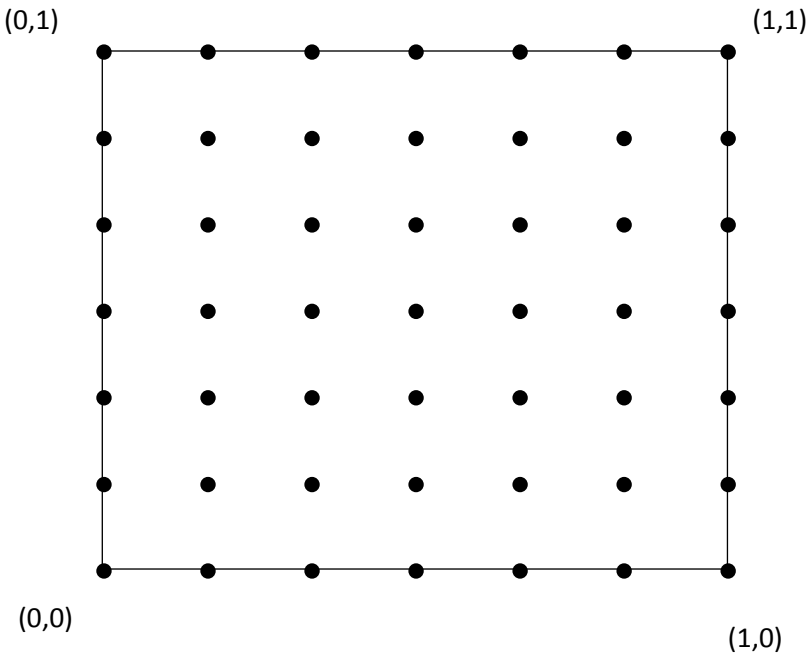

Figure 3.12 One block representing the transformed domain with regular node distribution. A 7 x 7 node distribution.

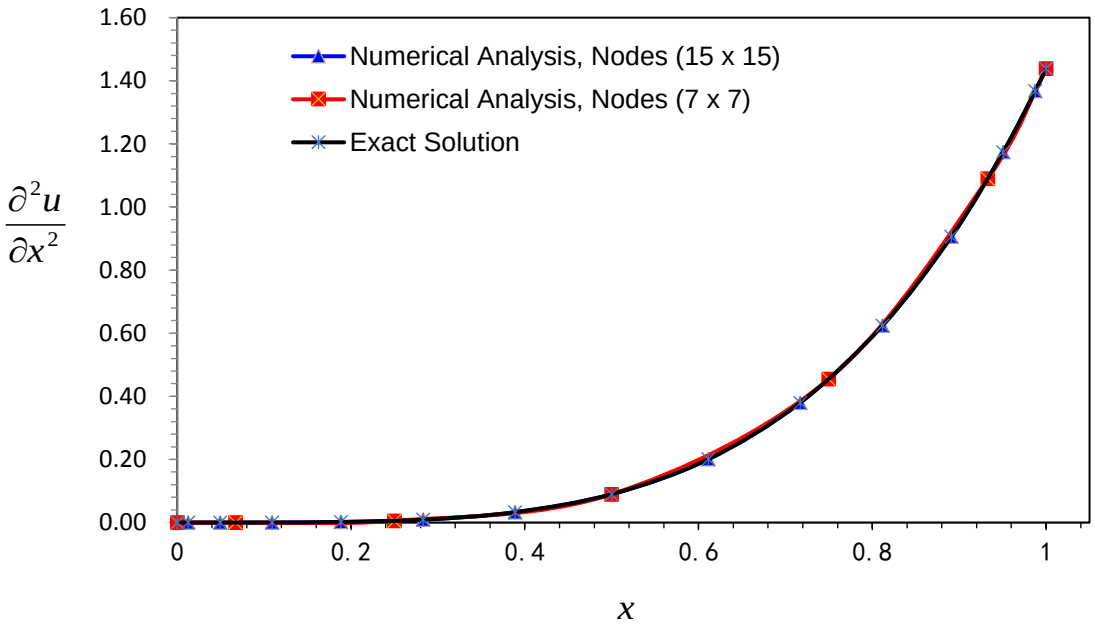

Figure 3.13 Comparing the exact solution of Eq. (3.10) and the FBM method approximation as determined by 7 x 7 and 15 x 15 nodal distribution. The solution plotted is for all values of x at $y = 0.5$.

Number of Nodes N	ε_{error_1}	ε_{error_2}	ε_{error_3}
3	2.40×10^{-3}	4.27×10^{-1}	1.93×10^{0}
5	2.83×10^{-4}	1.35×10^{-2}	1.53×10^{-1}
7	5.64×10^{-6}	1.97×10^{-4}	3.60×10^{-3}
9	5.37×10^{-8}	1.65×10^{-6}	4.11×10^{-5}
11	3.07×10^{-10}	8.82×10^{-9}	2.83×10^{-7}

Table 3.3 ε_{error_1} is the average relative error between the FBM interpolation of Eq. (3.9) across the domain and the exact solution of Eq. (3.9). ε_{error_2} represent the average relative error between the FBM interpolation and the analytical solution for the first order partial differential equation of Eq. (3.9). ε_{error_3} is the average relative error between the FBM interpolation and the analytical solution of Eq. (3.10).

In a 2D case study, a single block with a regular node distribution is considered. The result of using the mapping technique to transform the nodes from the normalised square domain onto the transformed or practical domain is shown in Fig 3.12. By varying the number of nodes, the relative average error is determined for Eq. (3.9), Eq. (3.10) and Eq. (3.41) respectively. The results are presented in Table 3.3.

According to Table 3.3, the interpolation error increases when the order of derivative goes up. But interpolation of the actual function in Eq. (3.9) shows an error less than 1% even for N = 3. However, the relative error is controlled by simply increasing the number of nodes.

In addition, the result extracted from across the domain for all values of x at y = 0.5 is shown in Fig. 3.13. The exact solution is compared against the finite block approximation for N = 7 and 15. From Fig. 3.13, it can be said that a highly accurate result was determined by the finite block method at both the boundary and the domain.

Therefore, for a 2D case, the Lagrange approximation technique in conjunction with the mapping technique is an adequate interpolation method for the finite block analysis.

3.8. Summary

In this chapter, the Lagrange series interpolation is introduced. The one-dimensional and two-dimensional differential matrices were constructed in terms of the nodal values. The accuracy of setting up the differential matrix was assessed by several numerical examples. In both the one-dimensional and the two-dimensional case, regular and irregular nodal distributions were considered. In addition, the effects of the nodal arrangements and the number of collocation points were observed. In all cases, the numerical results were compared with analytical solutions.

The mapping technique is discussed in this chapter for two-dimensional problems. The mapping technique is one of the essential components of the finite block method. Analysis of a two-dimensional case was carried out and the interpolation error was reported. The comparison of analytical results and numerical results of the FBM method shows acceptable accuracies.

CHAPTER 4

Finite Block Method: Stationary Interface Crack

4.1. Introduction

The finite block method has already been applied to the study of heat conduction in functionally graded materials [71] and anisotropic elasticity problems [72]. In this chapter, the formulation for the finite block method is presented for the analysis of interface crack.

Firstly, the Williams [18] series for describing interface crack stress and displacement is considered (Appendix B1). The problem domain is then divided into blocks and the partial differential operators are determined in terms of the nodal values. The Lagrange series interpolation is used for evaluating 1D and 2D differential matrix. For the 1D case, the first order derivative matrix is formed using a set of nodes collocated on a straight line. Beyond this, higher order derivatives can be easily achieved. For multi-dimensional problems, any order of partial differential matrices is achieved directly by transforming the local numbering system of the matrix to a global numbering system. At each node, the multi-dimension partial differential can be obtained from the "one-dimension derivative matrix" of the first order. This is seen as a computational advantage when compared with the MLS and the RBF method, where

interpolation is done via a support domain. Using the mapping technique for each block, a quadratic type element block is used in transforming the real domain into the transformed domain using the square normalised mapping domain. A set of linear equations based on the governing equilibrium equation and boundary conditions in terms of stress is obtained. This is then used to determine the nodal values of stress and displacement along the bi-material boundary and near the crack tip. Eventually, the interface stress intensity factor is calculated using the Williams expansion series.

The method as introduced in this chapter differs from the conventional FEM crack analysis where quarter-point elements are used for modelling the crack tip. In this study, a singular core is introduced around the crack tip in a way that allows the accurate capture of the interface stress intensity factor.

4.2. Interface Crack Formulation for Bi-Material

4.2.1 Williams Series for Bi-material Interfacial Crack

Investigating the interface crack in bi-materials, Williams first utilized the eigenfunction expansion approach to analyse the asymptotic nature of the dominant stress singularity at the crack tip. But first Williams [18] sought a solution which allowed the normal stress and the shear stress to vanish along the crack face, also the displacement and the stress must be continuous along the bond line of the two materials which forms the bi-material. Such a solution as explained in Appendix B1 can be found by expressing the stress and the displacement (in the polar form) in terms of the biharmonic stress function [18,104,169]. Nonetheless, the complex potential function method developed by Kolosov and Muskhelishvili [170] meets these requirements and it is a convenient method for evaluating a two-dimensional crack problem [170]. According to the complex potential method, the displacement and the stresses are formulated in terms of analytical functions by means of complex variables. Therefore, by solving the analytical function using a prescribed boundary condition the stresses and the displacement around the crack tip is also determined. Using the Muskhelishvili formalism, the displacements (u_x, u_y) and stresses $(\sigma_x, \sigma_y, \tau_{xy})$ surrounding the crack tip can be presented in terms of complex potentials Φ and Ψ as [170]

$$2\mu^{(\alpha)}\left[u_x^{(\alpha)}+iu_y^{(\alpha)}\right]=\kappa^{(\alpha)}\Phi^{(\alpha)}(z)-z\overline{\Phi}'^{(\alpha)}-\overline{\Psi}^{(\alpha)}(z)\ , \tag{4.1a}$$

$$\sigma_x^{(\alpha)}+\sigma_y^{(\alpha)}=2\left[\Phi'^{(\alpha)}(z)+\overline{\Phi}'^{(\alpha)}(z)\right], \tag{4.1b}$$

$$\sigma_y^{(\alpha)}-i\tau_{xy}^{(\alpha)}=\Phi'^{(\alpha)}(z)+\overline{\Phi}'^{(\alpha)}(z)+z\overline{\Phi}''^{(\alpha)}(z)+\overline{\Psi}'^{(\alpha)}(z)\ , \tag{4.1c}$$

where superscript $\alpha=1,2$ refer to the material above the crack plane (1) and material below the crack plane (2), coordinate $z=re^{i\theta}$ in the complex, the primes denote derivatives with respect to *z* and the over bars represent the complex conjugate, $\mu^{(\alpha)}$ is the shear modulus and

$$\kappa^{(\alpha)}=\begin{cases}3-4\nu^{(\alpha)} & \text{for plane strain}\\ \dfrac{3-\nu^{(\alpha)}}{1+\nu^{(\alpha)}} & \text{for plane stress}\end{cases}, \tag{4.2}$$

in which $\nu^{(\alpha)}$ indicates the Poisson's ratio. The Muskhelishvili formalism as stated in Eq. (4.1) is derived in Appendix B2 of this thesis.

The potentials Φ and Ψ are analytic everywhere except at the crack tip. Therefore, four analytic complex functions, two for each medium, are assumed as a power series of the complex variable of *z* as

$$\Phi^{(\alpha)}=A^{(\alpha)}z^{\lambda},\ \Psi^{(\alpha)}=B^{(\alpha)}z^{\lambda}+C^{(\alpha)}z^{\bar{\lambda}}\ , \tag{4.3}$$

where constants $A^{(\alpha)},B^{(\alpha)},\ C^{(\alpha)}$ and as yet unknown eigenvalue λ are assumed to be complex in general. Considering the boundary traction conditions gives

$$\left[\sigma_y^{(1)}-i\tau_{xy}^{(1)}\right]_{\theta=\pi}=0,\ \left[\sigma_y^{(2)}-i\tau_{xy}^{(2)}\right]_{\theta=-\pi}=0\ . \tag{4.4}$$

After substituting Eq. (4.3) into Eq. (4.1c), we can now proceed to enforce the boundary conditions at Eq. (4.4) which gives

$$\lambda z^{\lambda-1}\left(A^{(1)}+\overline{C}^{(1)}e^{-2\pi i\lambda}\right)+\bar{\lambda}\bar{z}^{\bar{\lambda}-1}\left(\overline{\lambda A}^{(1)}+\overline{B}^{(1)}\right)=0\ , \tag{4.5a}$$

$$\lambda z^{\lambda-1}\left(A^{(2)}+\overline{C}^{(2)}e^{2\pi i\lambda}\right)+\bar{\lambda}\bar{z}^{\bar{\lambda}-1}\left(\overline{\lambda A}^{(2)}+\overline{B}^{(2)}\right)=0\ . \tag{4.5b}$$

These two equations produce

$$B^{(1)} = -\lambda A^{(1)},\ \overline{C}^{(1)} = -A^{(1)} e^{2\pi i\lambda} \quad , \tag{4.6a}$$

$$B^{(2)} = -\lambda A^{(2)},\ \overline{C}^{(2)} = -A^{(2)} e^{-2\pi i\lambda} \quad . \tag{4.6b}$$

On the other hand, the stress and displacement continuities on the bonded line give

$$\left[u_x + iu_y\right]^{(1)}_{\theta=0} = \left[u_x + iu_y\right]^{(2)}_{\theta=0} \ , \tag{4.7a}$$

$$\left[\sigma_y - i\tau_{xy}\right]^{(1)}_{\theta=0} = \left[\sigma_y - i\tau_{xy}\right]^{(2)}_{\theta=0} \quad . \tag{4.7b}$$

Then it reduces to the solution of the characteristic equation

$$e^{4\pi i\lambda} - (1-\hat{\kappa}) e^{2\pi i\lambda} - \hat{\kappa} = 0 \ , \tag{4.8}$$

where

$$\hat{\kappa} = \frac{\kappa^{(1)}\mu^{(2)} + \mu^{(1)}}{\kappa^{(2)}\mu^{(1)} + \mu^{(2)}} \quad , \tag{4.9}$$

along with the relationship

$$\mu^{(2)}\left(\kappa^{(1)} A^{(1)} - \overline{C}^{(1)}\right) = \mu^{(1)}\left(\kappa^{(2)} A^{(2)} - \overline{C}^{(2)}\right) \ , \tag{4.10a}$$

$$\mu^{(2)}\left(\lambda A^{(1)} + B^{(1)}\right) = \mu^{(1)}\left(\lambda A^{(2)} + B^{(2)}\right) \ , \tag{4.10b}$$

$$A^{(1)} + C^{(1)} = A^{(2)} + C^{(2)} \ , \tag{4.10c}$$

The characteristic Eq. (4.8) gives two solutions

$$e^{2\pi i\lambda} = 1 \ \text{ and} \tag{4.11a}$$

$$e^{2\pi i\lambda} = -\hat{\kappa} \ , \tag{4.11b}$$

and the corresponding sets of eigenvalue are

$$\lambda_n = n \ \text{ for } n = 0,\ 1,\ 2, \ldots \text{, (Integer)} \tag{4.12}$$

$$\lambda_n = n + \tfrac{1}{2} - i\varepsilon \ \text{ for } n = 0,\ 1,\ 2, \ldots \text{, (Complex)} \tag{4.13}$$

where $\varepsilon = \ln(\hat{\kappa})/2\pi$.

There are two sets of solutions for λ_n given by Eq. (4.12) and (4.13) which are investigated further in sections 4.2.1.1 and 4.2.1.2. Where the corresponding solutions for the displacement and stress are defined.

4.2.1.1 Solution (A): Integer Eigenvalues

Substituting Eq. (4.12) into Eq. (4.11a) and Eq. (4.10a) gives

$$\overline{C}_I^{(1)} = -A_I^{(1)},\ \overline{C}_I^{(2)} = -A_I^{(2)} \quad \text{and} \quad \frac{A_I^{(2)}}{A_I^{(1)}} = \frac{\mu^{(2)}\left(1+\kappa^{(1)}\right)}{\mu^{(1)}\left(1+\kappa^{(2)}\right)} = \beta \ . \tag{4.14}$$

Therefore, in the upper and lower half plane, we have

$$2\mu^{(\alpha)}\left(u_x^{(I\alpha)} + iu_y^{(I\alpha)}\right) = \sum_{n=0}^{\infty} A_{In}^{(\alpha)} r^n \left(\kappa^{(\alpha)} e^{in\theta} + e^{-in\theta}\right) + \sum_{n=0}^{\infty} n\overline{A}_{In}^{(\alpha)} r^n \left(e^{-in\theta} - e^{-i(n-2)\theta}\right), \tag{4.15a}$$

$$\sigma_x^{(I\alpha)} + \sigma_y^{(I\alpha)} = 2\sum_{n=0}^{\infty} nA_{In}^{(\alpha)} r^{n-1} e^{i(n-1)\theta} + 2\sum_{n=0}^{\infty} n\overline{A}_{In}^{(\alpha)} r^{n-1} e^{-i(n-1)\theta} \ , \qquad \alpha = 1,2 \ , \tag{4.15b}$$

$$\begin{aligned} \sigma_y^{(I\alpha)} - i\tau_{xy}^{(I\alpha)} &= 2i\sum_{n=0}^{\infty} nA_{In}^{(\alpha)} r^{n-1} \sin(n-1)\theta + \\ &\sum_{n=0}^{\infty} n(n-1)\overline{A}_{In}^{(\alpha)} r^{n-1}\left(e^{-i(n-3)\theta} - e^{-i(n-1)\theta}\right). \end{aligned} \tag{4.15c}$$

4.2.1.2 Solution (B): Complex Eigenvalues

Same as in section 4.2.1.1, substituting Eq. (4.13) into Eq. (4.11b) and Eq. (4.10a) results

$$\overline{C}_C^{(1)} = \hat{\kappa}A_C^{(1)},\ \overline{C}_C^{(2)} = A_C^{(2)} / \hat{\kappa} \ \text{ and } \ \frac{A_C^{(2)}}{A_C^{(1)}} = \hat{\kappa} \ . \tag{4.16}$$

Therefore, the displacements and stresses in the upper and lower half plane are given as

$$\begin{aligned} 2\mu^{(\alpha)}\left(u_x^{(C\alpha)} + iu_y^{(C\alpha)}\right) &= \sum_{n=0}^{\infty} A_{Cn}^{(\alpha)} r^{\lambda_n}\left(\kappa^{(\alpha)} e^{i\lambda_n\theta} + e^{-2\pi i\lambda_n(-1)^{\alpha} - i\lambda_n\theta}\right) + \\ &\sum_{n=0}^{\infty} \overline{\lambda}_n \overline{A}_{Cn}^{(\alpha)} r^{\overline{\lambda}_n}\left(e^{-i\overline{\lambda}_n\theta} - e^{-i(\overline{\lambda}_n - 2)\theta}\right), \end{aligned} \tag{4.17a}$$

$$\sigma_x^{(C\alpha)}+\sigma_y^{(C\alpha)}=2\sum_{n=0}^{\infty}\lambda_n A_{Cn}^{(\alpha)} r^{\lambda_n-1}e^{i(\lambda_n-1)\theta}+ \quad \alpha=1,2 \quad , \tag{4.17b}$$
$$2\sum_{n=0}^{\infty}\overline{\lambda}_n \overline{A}_{Cn}^{(\alpha)} r^{\overline{\lambda}_n-1}e^{-i(\overline{\lambda}_n-1)\theta}$$

$$\sigma_y^{(C\alpha)}-i\tau_{xy}^{(C\alpha)}=\sum_{n=0}^{\infty}\lambda_n A_{Cn}^{(\alpha)} r^{\lambda_n-1}\left(e^{i(\lambda_n-1)\theta}+e^{-2\pi i\lambda_n(-1)^{\alpha}-i(\lambda_n-1)\theta}\right)+ \quad . \tag{4.17c}$$
$$\sum_{n=0}^{\infty}\overline{\lambda}_n(\overline{\lambda}_n-1)\overline{A}_{Cn}^{(\alpha)} r^{\overline{\lambda}_n-1}\left(e^{-i(\overline{\lambda}_n-3)\theta}-e^{-i(\overline{\lambda}_n-1)\theta}\right)$$

Solutions for the stress and displacement series in Eq. (4.15) and Eq. (4.17) are worked to construct the general solutions for two-dimensional plate with a straight interfacial crack as the following

$$u_x^{core,\alpha}=u_x^{(I\alpha)}+u_x^{(C\alpha)},$$

$$u_y^{core,\alpha}=u_y^{(I\alpha)}+u_y^{(C\alpha)} \quad ,$$

$$\sigma_x^{core,\alpha}=\sigma_x^{(I\alpha)}+\sigma_x^{(C\alpha)}, \tag{4.18}$$

$$\sigma_y^{core,\alpha}=\sigma_y^{(I\alpha)}+\sigma_y^{(C\alpha)},$$

$$\tau_{xy}^{core,\alpha}=\tau_{xy}^{(I\alpha)}+\tau_{xy}^{(C\alpha)}.$$

It can be observed from Eq. (4.15) that there are no singular stresses in the solution. From Eq. (4.17), the singular stresses can be found when $n=0$

$$\sigma_y^{(\alpha)}+i\tau_{xy}^{(\alpha)}=\overline{A}_{C0}^{(1)}\left(\frac{1}{2}+i\varepsilon\right)(1+\hat{\kappa})r^{-\frac{1}{2}+i\frac{\varepsilon}{2}}=\frac{K}{\sqrt{2\pi}}r^{-\frac{1}{2}+i\frac{\varepsilon}{2}} \quad , \tag{4.19}$$

where K is the stress intensity factors in the complex form defined by

$$\frac{K}{\sqrt{\pi a}}=\frac{K_I+iK_{II}}{\sqrt{\pi a}}=\overline{A}_{C0}^{(1)}\left(\frac{1}{2}+i\varepsilon\right)(1+\hat{\kappa})\sqrt{2/a} \quad . \tag{4.20}$$

For the finite block method, all the coefficients for the set of solutions for $A_{Cn}^{(1)}$ $(n=0,1,...N_b\text{-}1)$ should be determined by the specified boundary conditions of the traction and displacement, here N_b is the number of boundary collocation point.

4.3. Finite Block Method in Various Coordinate Systems

4.3.1 Finite Block Method in Cartesian Coordinate System

Consider a 2D elasticity with domain Ω enclosed by boundary Γ in isotropic media in a Cartesian coordinate system. The constitutive equations for two-dimensional plane-stress state in the Cartesian coordinate system are

$$\sigma_x = \frac{E}{(1-\nu^2)}\left(\varepsilon_x + \nu\varepsilon_y\right), \quad \sigma_y = \frac{E}{(1-\nu^2)}\left(\varepsilon_y + \nu\varepsilon_x\right),$$

$$\tau_{xy} = G\gamma_{xy} \ , \quad G = \frac{E}{2(1+\nu)} \ , \tag{4.21}$$

where, E, ν are the Young's modulus and the Poisson's ratio, G is the shear modulus. The strains can be expressed with displacements as

$$\varepsilon_x = \frac{\partial u_x}{\partial x} \ , \ \varepsilon_y = \frac{\partial u_y}{\partial y} \ , \ \gamma_{xy} = \frac{\partial u_y}{\partial x} + \frac{\partial u_x}{\partial y} \ . \tag{4.22}$$

For two-dimensional static problem in a Cartesian coordinate, the equilibrium equations are

$$\frac{\partial \sigma_x}{\partial x} + \frac{\partial \tau_{xy}}{\partial y} + b_x = 0, \quad \frac{\partial \tau_{xy}}{\partial x} + \frac{\partial \sigma_y}{\partial y} + b_y = 0 \ , \tag{4.23}$$

where b_x and b_y are the body forces. Introducing the first order differential matrices in Eq. (3.35) into the stresses in Eq. (4.21) yields for each node P in the physical domain

$$\begin{aligned}
\boldsymbol{\sigma}_x &= \frac{E}{1-\nu^2}\left(\mathbf{D}_{,x}\mathbf{u}_x + \nu\mathbf{D}_{,y}\mathbf{u}_y\right), \\
\boldsymbol{\sigma}_y &= \frac{E}{1-\nu^2}\left(\nu\mathbf{D}_{,x}\mathbf{u}_x + \mathbf{D}_{,y}\mathbf{u}_y\right), \\
\boldsymbol{\tau}_{xy} &= \frac{E}{2(1+\nu)}\left(\mathbf{D}_{,y}\mathbf{u}_x + \mathbf{D}_{,x}\mathbf{u}_y\right),
\end{aligned} \tag{4.24}$$

where the stress vectors of the nodal value $\boldsymbol{\sigma}_x = \{\sigma_{xk}\}^T$, $\boldsymbol{\sigma}_y = \{\sigma_{yk}\}^T$, $\boldsymbol{\tau}_{xy} = \{\tau_{xyk}\}^T$, $\mathbf{u}_x = \{u_{xk}\}^T$, $\mathbf{u}_y = \{u_{yk}\}^T$. Substituting the stresses from Eq. (4.24) into the equilibrium equations in (4.23) for each collocation point P gives

$$\left(\mathbf{D}_{,x}^2+\frac{1-\nu}{2}\mathbf{D}_{,y}^2\right)\mathbf{u}_x+\frac{1+\nu}{2}\mathbf{D}_{,x}\mathbf{D}_{,y}\mathbf{u}_y+\frac{1-\nu^2}{E}\mathbf{b}_x=\mathbf{0}\ ,$$

$$P\in\Omega \tag{4.25}$$

$$\frac{1+\nu}{2}\mathbf{D}_{,x}\mathbf{D}_{,y}\mathbf{u}_x+\left(\mathbf{D}_{,y}^2+\frac{1-\nu}{2}\mathbf{D}_{,x}^2\right)\mathbf{u}_y+\frac{1-\nu^2}{E}\mathbf{b}_y=\mathbf{0}\ ,$$

where $\mathbf{b}_x=\{b_{xk}\}^T$ and $\mathbf{b}_y=\{b_{yk}\}^T$ are the nodal value vectors of the body forces. The boundary conditions of the displacements and the tractions are described as

$$\begin{aligned}&u_x(P)=u_x^0(P)\ ,\\&u_y(P)=u_y^0(P)\ ,\end{aligned}\qquad P\in\Gamma_u \tag{4.26}$$

for the displacements and

$$\begin{aligned}&\sigma_x(P)n_x(P)+\tau_{xy}(P)n_y(P)=t_x^0(P)\ ,\\&\tau_{xy}(P)n_x(P)+\sigma_y(P)n_y(P)=t_y^0(P)\ ,\end{aligned}\qquad P\in\Gamma_\sigma \tag{4.27}$$

for the tractions, where u_x^0, u_y^0, t_x^0 and t_y^0 are the given boundary values of the displacement and the traction on the boundaries Γ_u and Γ_σ respectively, $n(n_x,n_y)$ is the outward normal to the boundary. It is observed that there are $2Q=2(M\times N)$ linear algebraic equations both from Eq. (4.25) and boundary conditions from Eq. (4.26) and (4.27) in the case of one block. By solving a set of linear algebraic equations, all nodal values of the displacements $(\mathbf{u}_x,\mathbf{u}_y)$ can be obtained.

In the case with more than one block, the connection conditions on the interface $\Gamma_{\text{int}}^{(\text{I},\text{II})}$ between two blocks (I, II) must be satisfied as follows

$$\begin{aligned}&u_x^{\text{I}}=u_x^{\text{II}},\ u_y^{\text{I}}=u_y^{\text{II}}\ ,\\&\qquad\qquad P\in\Gamma_{\text{int}}^{(\text{I},\text{II})}\\&t_x^{\text{I}}+t_x^{\text{II}}=0,\ t_y^{\text{I}}+t_y^{\text{II}}=0\ .\end{aligned} \tag{4.28}$$

4.3.2 Finite Block Method in Polar Coordinate System

For two-dimensional plane-stress state in the polar coordinate system, we have

$$\sigma_r = \frac{E}{(1-\nu^2)}\left(\varepsilon_r + \nu\varepsilon_\theta\right),$$

$$\sigma_\theta = \frac{E}{(1-\nu^2)}\left(\varepsilon_\theta + \nu\varepsilon_r\right), \tag{4.29}$$

$$\tau_{r\theta} = G\gamma_{r\theta}\ .$$

The strains can be expressed with displacements as

$$\varepsilon_r = \frac{\partial u_r}{\partial r},$$

$$\varepsilon_\theta = \frac{1}{r}\frac{\partial u_\theta}{\partial \theta} + \frac{u_r}{r}, \tag{4.30}$$

$$\gamma_{r\theta} = \frac{\partial u_\theta}{\partial r} + \frac{1}{r}\frac{\partial u_r}{\partial \theta} - \frac{u_\theta}{r}.$$

The equilibrium equations give

$$\frac{\partial \sigma_r}{\partial r} + \frac{1}{r}\frac{\partial \tau_{r\theta}}{\partial \theta} + \frac{\sigma_r - \sigma_\theta}{r} + b_r = 0\ ,$$

$$\frac{\partial \tau_{r\theta}}{\partial r} + \frac{1}{r}\frac{\partial \sigma_\theta}{\partial \theta} + \frac{2\tau_{r\theta}}{r} + b_\theta = 0\ , \tag{4.31}$$

where b_r and b_θ are the body forces. Same as differential matrices application in the Cartesian coordinate system, the nodal values of stresses in Eq. (4.29) are written, in matrix form, as

$$\boldsymbol{\sigma}_r = \frac{E}{1-\nu^2}\left[\mathbf{D}_{,r}\mathbf{u}_r + \nu\hat{\mathbf{R}}\left(\mathbf{D}_{,\theta}\mathbf{u}_\theta + \mathbf{u}_r\right)\right],$$

$$\boldsymbol{\sigma}_\theta = \frac{E}{1-\nu^2}\left[\nu\mathbf{D}_{,r}\mathbf{u}_r + \hat{\mathbf{R}}\left(\mathbf{D}_{,\theta}\mathbf{u}_\theta + \mathbf{u}_r\right)\right], \tag{4.32}$$

$$\boldsymbol{\tau}_{r\theta} = \frac{E}{2(1+\nu)}\left(\mathbf{D}_{,r}\mathbf{u}_\theta + \hat{\mathbf{R}}\mathbf{D}_{,\theta}\mathbf{u}_r - \hat{\mathbf{R}}\mathbf{u}_\theta\right),$$

where $\boldsymbol{\sigma}_r = \{\sigma_{rk}\}^T$, $\boldsymbol{\sigma}_\theta = \{\sigma_{\theta k}\}^T$, $\boldsymbol{\tau}_{r\theta} = \{\tau_{r\theta k}\}^T$, $\hat{\mathbf{R}} = \mathbf{diag}[1/r_k]$ the coordinate correspondence $r \to x$ and $\theta \to y$ and then: $\mathbf{D}_{,r} = \mathbf{D}_{,x}$, $\mathbf{D}_{,\theta} = \mathbf{D}_{,y}$. Applying differential matrices over the equilibrium equations in Eq. (4.31) for each collocation point P in the domain gives

$$\begin{aligned} &\mathbf{D}_{,r}\boldsymbol{\sigma}_r + \hat{\mathbf{R}}\mathbf{D}_{,\theta}\boldsymbol{\tau}_{r\theta} + \hat{\mathbf{R}}(\boldsymbol{\sigma}_r - \boldsymbol{\sigma}_\theta) + \mathbf{b}_r = \mathbf{0}\ , \\ &\qquad\qquad P \in \Omega \\ &\mathbf{D}_{,r}\boldsymbol{\tau}_{r\theta} + \hat{\mathbf{R}}\mathbf{D}_{,\theta}\boldsymbol{\sigma}_\theta + 2\hat{\mathbf{R}}\boldsymbol{\tau}_{r\theta} + \mathbf{b}_\theta = \mathbf{0}\ . \end{aligned} \tag{4.33}$$

Substituting Eq. (4.32) into Eq. (4.33) gives a set of linear algebraic equations in terms of the nodal values of displacements as the following

$$\begin{aligned} &\left[(\mathbf{D}_{,r} + \hat{\mathbf{R}})(\mathbf{D}_{,r} + \nu\hat{\mathbf{R}}) + \frac{1-\nu}{2}\hat{\mathbf{R}}\mathbf{D}_{,\theta}\hat{\mathbf{R}}\mathbf{D}_{,\theta} - \hat{\mathbf{R}}(\nu\mathbf{D}_{,r} + \hat{\mathbf{R}})\right]\mathbf{u}_r \\ &+\left[\nu(\mathbf{D}_{,r} + \hat{\mathbf{R}})\hat{\mathbf{R}} + \frac{1-\nu}{2}\hat{\mathbf{R}}\mathbf{D}_{,\theta}(\mathbf{D}_{,r} - \hat{\mathbf{R}}) - \hat{\mathbf{R}}^2\mathbf{D}_{,\theta}\right]\mathbf{u}_\theta + \frac{1-\nu^2}{E}\mathbf{b}_r = \mathbf{0}\ , \end{aligned} \tag{4.34a}$$

$$\begin{aligned} &\left[\frac{1-\nu}{2}(\mathbf{D}_{,r} + 2\hat{\mathbf{R}})\hat{\mathbf{R}}\mathbf{D}_{,\theta} + \hat{\mathbf{R}}\mathbf{D}_{,\theta}(\nu\mathbf{D}_{,r} + \hat{\mathbf{R}})\right]\mathbf{u}_r \\ &+\left[\frac{1-\nu}{2}(\mathbf{D}_{,r} + 2\hat{\mathbf{R}})(\mathbf{D}_{,r} - \hat{\mathbf{R}}) + \hat{\mathbf{R}}\mathbf{D}_{,\theta}\hat{\mathbf{R}}\mathbf{D}_{,\theta}\right]\mathbf{u}_\theta + \frac{1-\nu^2}{E}\mathbf{b}_\theta = \mathbf{0}\ . \end{aligned} \tag{4.34b}$$

It is clear, for the Cartesian coordinate and the polar coordinate systems, only the first order partial differential matrices are involved.

4.4. The Finite Block Configuration at the Crack Tip

To capture the singular stresses accurately, special treatments should be introduced. In order to determine all coefficients in the Williams' series, i.e. $A_{In}^{(1)}$ and $A_{Cn}^{(1)}$ $(n = 0,1,..,N_b\text{-}1)$, a singular polygonal core is introduced centred at the crack tip, as shown in Fig. 4.1, where r_0 is the radius of the circle with dash lines, which indicates the size of the singular core and $P(r_k, \theta_k)$ $(k = 1,...N_b)$ is the coordinate of the collocation point on the interface between the block and the core.

4.4.1 The Relationship Between the Singular Core and the Williams Series in Cartesian Coordinate

Each side of the polygon corresponds to an interface with six blocks. Patently, there are six blocks surrounding the hexagonal core, as shown in Fig. 4.1. In the Williams' series of stress and displacement in Eq. (4.18), we consider the finite terms with truncation number N_b. On the interface between the block and the singular core (r_k, θ_k), we have the following connection conditions:

$$\begin{aligned} &u_x^{core,\alpha} = u_x^{(I)}, \\ &u_y^{core,\alpha} = u_y^{(I)}, \\ &t_x^{core,\alpha} + t_x^{(I)} = 0, \\ &t_y^{core,\alpha} + t_y^{(I)} = 0. \end{aligned} \qquad P(r_k, \theta_k) \quad (k = 1,2,..., N_b). \tag{4.35}$$

In the numerical procedure, the unknowns include the nodal displacements $[\mathbf{u}_x, \mathbf{u}_y]$ for each block $(L_\Lambda = M_\Lambda \times N_\Lambda)$ and coefficients $A_{In}^{(1)}$ and $A_{Cn}^{(1)}$ $(n = 0,1,.., N_b - 1)$ in the Williams' series. With the same number of algebraic equations from the governing equations in the domain of each block, connection condition along the interfaces between blocks and along the interfaces between the singular core and the blocks, all unknowns can be obtained. The stress intensity factors are evaluated from Eq. (4.20) successively.

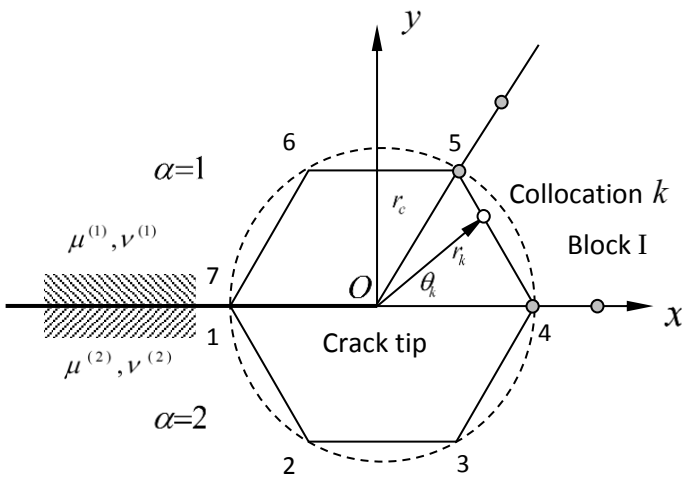

Figure 4.1 A polygonal singular core and collocation points on the interfaces.

4.4.2 The Relationship Between the Singular Core and the Williams' Series in Polar Coordinate

For a simple case, two blocks are sufficient in the numerical procedure as shown in Fig. 4.2(a). Two blocks in the coordinate (r,θ) shown in Fig. 4.2(b) can be mapped using the square normalised domain. In the Williams' series of stress and displacement in Eq. (4.18), we consider the finite terms with truncation number N_b. We suppose that there are N_b collocation points along the interfaces between the blocks and the circular core $(r_k = r_c, -\pi \le \theta_k \le \pi)$ with four connection equations in polar coordinate system as

$$u_r^{core,\alpha}(r_k,\theta_k) = u_r^{(I,II)}(r_k,\theta_k)\ , \tag{4.36a}$$

$$u_\theta^{core,\alpha}(r_k,\theta_k) = u_\theta^{(I,II)}(r_k,\theta_k)\ , \tag{4.36b}$$

$$\sigma_r^{core,\alpha}(r_k,\theta_k) = \sigma_r^{(I,II)}(r_k,\theta_k)\ , \tag{4.36c}$$

$$\tau_{r\theta}^{core,\alpha}(r_k,\theta_k) = \tau_{r\theta}^{(I,II)}(r_k,\theta_k)\ . \tag{4.36d}$$

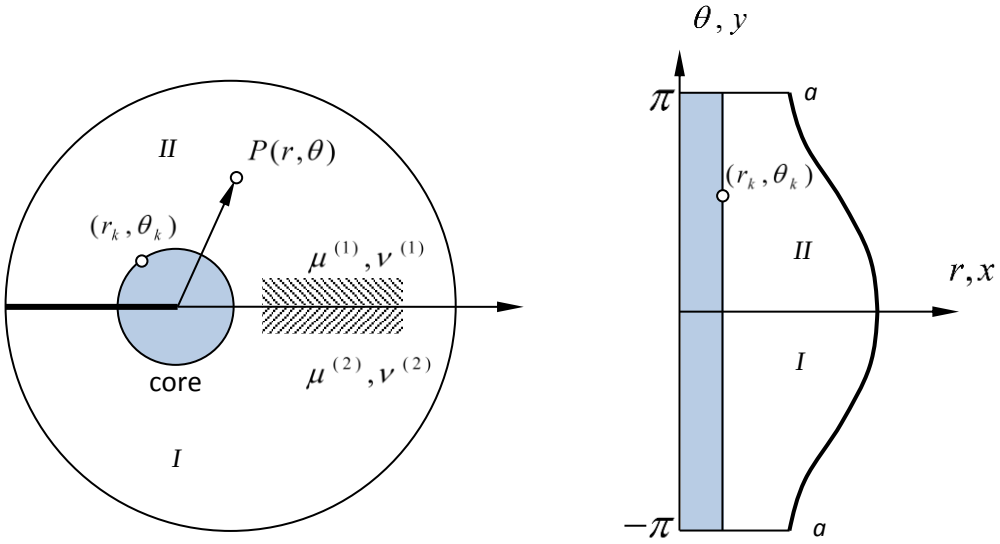

(a) (b)

Figure 4.2 Finite blocks and circular core centred at the crack tip of radius r_0 in the polar coordinate with interfaces: (a) two blocks and (r,θ) system; (b) two blocks and (r,θ) system.

The Williams' solutions in polar coordinate can be represented by

$$u_r^{core,\alpha} + iu_\theta^{core,\alpha} = e^{-i\theta}\left(u_x^{core,\alpha} + iu_y^{core,\alpha}\right), \tag{4.37}$$

for the displacements and

$$\begin{aligned} &\sigma_r^{core,\alpha} + \sigma_\theta^{core,\alpha} = \sigma_x^{core,\alpha} + \sigma_y^{core,\alpha}, \\ &\sigma_\theta^{core,\alpha} - \sigma_r^{core,\alpha} + 2i\tau_{r\theta}^{core,\alpha} = e^{2i\theta}\left(\sigma_y^{core,\alpha} - \sigma_x^{core,\alpha} + 2i\tau_{xy}^{core,\alpha}\right), \end{aligned} \tag{4.38}$$

for the stresses [171].

4.5. Numerical Assessment 1

4.5.1 Parameter Study

Firstly, consider a circular disk with an edge crack loaded by constant normal tractions σ_0 along the circumference as shown in Fig. 4.3. Suppose that the crack tip is located at the centre of the disk and the crack length $a = R$. A plane stress assumption is considered. The number of collocation point along each side are equal $M_I = N_I = M_{II} = N_{II} = M$. So, the number of collocation points on the interface between blocks and core is $2\times(M-2)$ and the truncation terms $N_c = M-2$. The disk is centred at the crack tip. Two semi-rings, upper and lower are mapped into normalised domain with precisely two blocks. The numerical results of the stress intensity factor are shown in Table 4.1 for the different number of nodes M where $\mu^{(2)} = 2\mu^{(1)}$, $\nu^{(1)} = \nu^{(2)} = 0.3$ and $r_c / R = 0.2$. Numerical solutions with the boundary collocation method are listed in Table 4.1 for comparison. It is apparent that the agreement is excellent. Table 4.2 shows the results of the stress intensity factors for the different ratios $\mu^{(2)}/\mu^{(1)}$ when the number of node $M = 16$ and $r_0 / R = 0.2$.

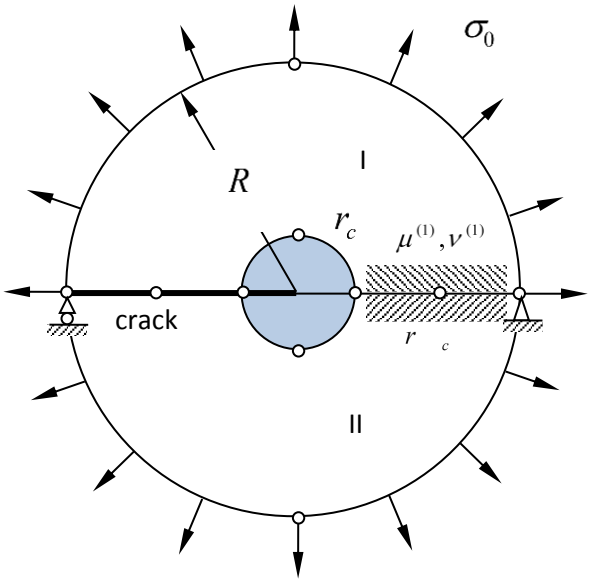

Figure 4.3 A circular disk with an edge crack. The disk is loaded radially along the circumference.

Table 4.3 shows the numerical results with variation of the Poisson ratio $\nu^{(2)}$ where the number of node $M = 16$, $\mu^{(2)} / \mu^{(1)} = 2$ and $r_c / R = 0.2$. In addition, the accuracy and convergence are also observed and the results are listed in Table 4.4. In this case, $\nu^{(1)} = \nu^{(2)} = 0.3$ for the different core sizes.

M	$K_I / \sigma_0 \sqrt{\pi a}$	$K_{II} / \sigma_0 \sqrt{\pi a}$
9	3.1668	0.0572
11	3.1753	0.0584
13	3.1760	0.0591
15	3.1755	0.0598
BCM	3.1668	0.0616

Table 4.1 Normalised stress intensity factor versus the number of node. The FBM results are compared against the BCM results.

$\mu^{(2)} / \mu^{(1)}$	$K_I / \sigma_0 \sqrt{\pi a}$		$K_{II} / \sigma_0 \sqrt{\pi a}$	
	FBM	BCM	FBM	BCM
1	3.1772	3.1721	0.0000	0.0000
2	3.1720	3.1710	0.0614	0.0616
3	3.1636	3.1693	0.0870	0.0859
4	3.1621	3.1674	0.0976	0.0963
5	3.1597	3.1656	0.1025	0.1009
6	3.1568	3.1640	0.1044	0.1028
7	3.1555	3.1626	0.1050	0.1032
8	3.1529	3.1614	0.1049	0.1030
9	3.1530	3.1603	0.1045	0.1024
10	3.1514	3.1593	0.1036	0.1016

Table 4.2 Normalised stress intensity factor versus the ratio of $\mu^{(2)} / \mu^{(1)}$. The FBM results are compared against the BCM results.

$\nu^{(2)}$	$K_I / \sigma_0 \sqrt{\pi a}$		$K_{II} / \sigma_0 \sqrt{\pi a}$	
	FBM	BCM	FBM	BCM
0.0	3.1720	3.1626	-0.0383	-0.0376
0.1	3.1825	3.1651	-0.0088	-0.0047
0.2	3.1716	3.1679	0.0272	0.0284
0.3	3.1720	3.1710	0.0614	0.0616
0.4	3.2077	3.1745	0.0970	0.0949

Table 4.3 Normalised stress intensity factor versus the ratio of $\nu^{(2)}$. The FBM results are compared against the BCM results.

r_c / R	$K_I / \sigma_0 \sqrt{\pi a}$	$K_{II} / \sigma_0 \sqrt{\pi a}$
0.20	3.1720	0.0614
0.25	3.1675	0.0647
0.30	3.1626	0.0641
0.35	3.1493	0.0669
0.40	3.1368	0.0686
BCM	3.1710	0.0616

Table 4.4 Normalised stress intensity factor versus the core size r_c / R. The FBM results are compared against the BCM results.

The stress intensity factor as reported in Tables 4.1 to 4.4 are determined using the Williams series expansion and the finite block method. In order to improve the accuracy of the approximation of the coefficients of the singular terms of the Williams series and eventually the stress intensity factor correctly, a singular core as shown in Fig. 4.1 is centred around the crack tip.

The assessment of stress intensity factor using the finite block method began with a parameter study. A circular disk with an edge crack in the polar coordinate system shown in Fig. 4.3 was used in the parameter study. The disk is centred at the crack-tip. Two semi-rings, upper and lower are mapped into normalised domain with precisely two blocks. In this case, the two blocks used represent materials 1 and 2, and the singular core is centred at the crack tip. The first parameter under consideration is the number of nodes and the stress intensity factor values were compared against the boundary collocation method. The results are reported in Table 4.1. For M = 9 the K_I value achieved by the finite block method is effectively the same as that produced by the boundary collocation method. However, due to the magnitude of the K_{II} value, further increase in the number of nodes was required. Around M = 15, the relative error for the K_{II} value between the finite block method and the boundary collocation method is determined to be 0.0292%. This value is significantly small even for an interface crack.

In Table 4.3, a variation in the Poisson's ratio between the two materials was varied by increasing $\nu^{(2)}$ of the lower block II. The stress intensity factor values determined shows stable results when compared to the boundary collocation method. At a larger $\nu^{(2)}$ value of 0.4, the relative error for the K_I value gives 0.0105% and the K_{II} value gives 0.0221%.

Table 4.4 reports on the effect of the core size on the stress intensity factor results. At a core size of r_c / R = 0.40 the relative error for the K_I value between the finite block method and the boundary collocation method is calculated to be 0.0108% and the K_{II} value gives 0.114%. For the minimum value considered in this study r_c / R = 0.20, the relative error for the K_I value gives 0.0003% and the K_{II} value gives 0.003%. Based on the above assessment, it can be said that some of the parameters deemed essential can be easily handled by the finite block method. As can be seen from the significantly low error margins, the influence on the stress intensity factor results can be controlled and reduced to a bare minimum.

4.6. Numerical Assessment 2

4.6.1 Cartesian Coordinate System

In order to demonstrate the effectiveness of the finite block method in determining the stress intensity factor for an interface crack, a bi-material plate with a centre crack (CCP) and a bi-material plate with an edge crack (SEN) were analysed. In both cases the CCP and the SEN specimens were analysed for various elastic moduli ratios, mainly $E^{(1)} / E^{(2)}$, and crack length *a*.

4.6.1.1 Analysis of Bi-material Plate with a Centre Crack

The bi-material plate with a centre crack has a uniform tensile load σ_0 applied at the top and bottom of the plate as shown in Fig. 4.4. Owing to the symmetry with respect to the *y* axis, it is equivalent to solve the boundary value problem for a half plate with four blocks for each material (upper and lower media) with plane strain state and Poisson ratios $\nu^{(1)} = \nu^{(2)} = 0.3$. The size of the polygonal core $r_0 / W = 0.2$ and the crack

length $a/W =$ 0.4, 0.5 and 0.6. For each block, the control number of collocation point density is given by $M_\Lambda = N_\Lambda = M$ $(\Lambda = I, II, ..., VIII)$.

The results of stress intensity factors (SIF) versus the ratio of Young's modulus $E^{(1)}/E^{(2)}$ are shown in Fig. 4.5 to 4.10 for the different cases. The equivalent centre crack analysis was carried out using ABAQUS, a finite element analysis program to check the finite block method. Also, the solutions given by Song using the scaled boundary finite element method (SBFEM) [76] are provided for comparison. The stress intensity factors K_I and K_{II} are normalised by $\sigma_0\sqrt{\pi a}$.

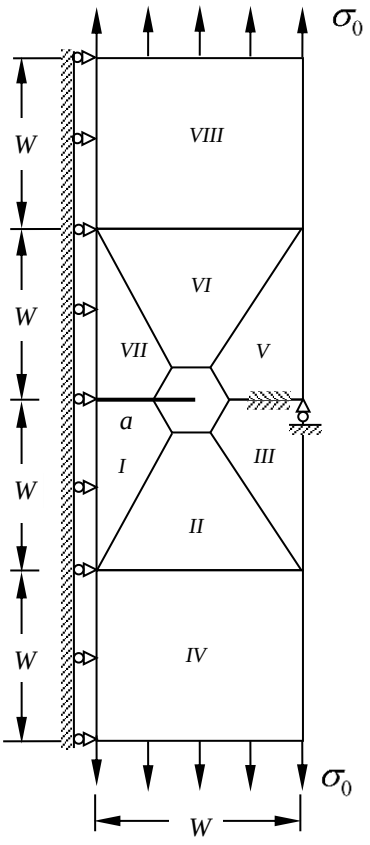

Figure 4.4 A finite block setup of a bi-material plate with a centre crack and uniformly loaded at the top and bottom.

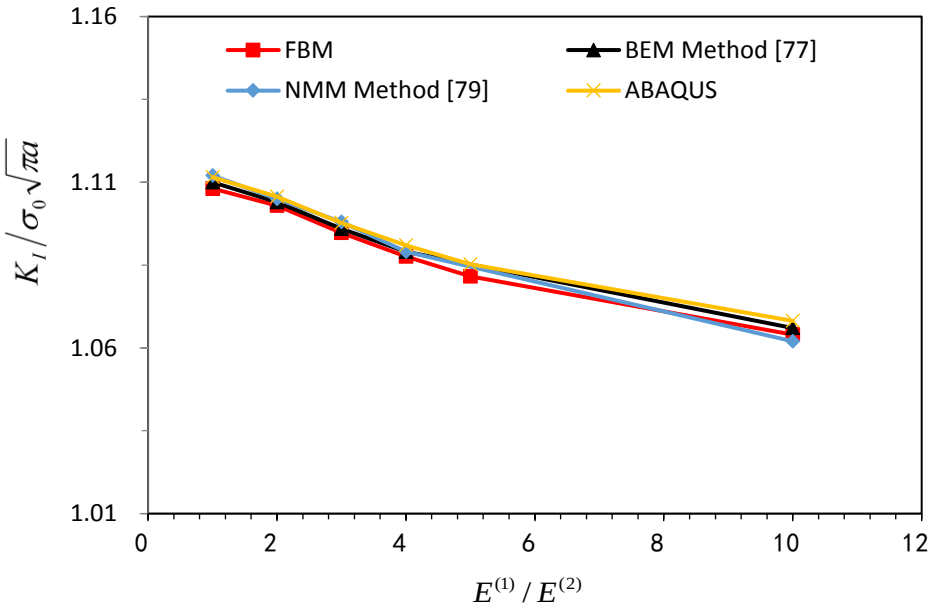

Figure 4.5 Normalised K_I stress intensity factor for various elastic modulus combinations. Centre crack length $a/W = 0.4$.

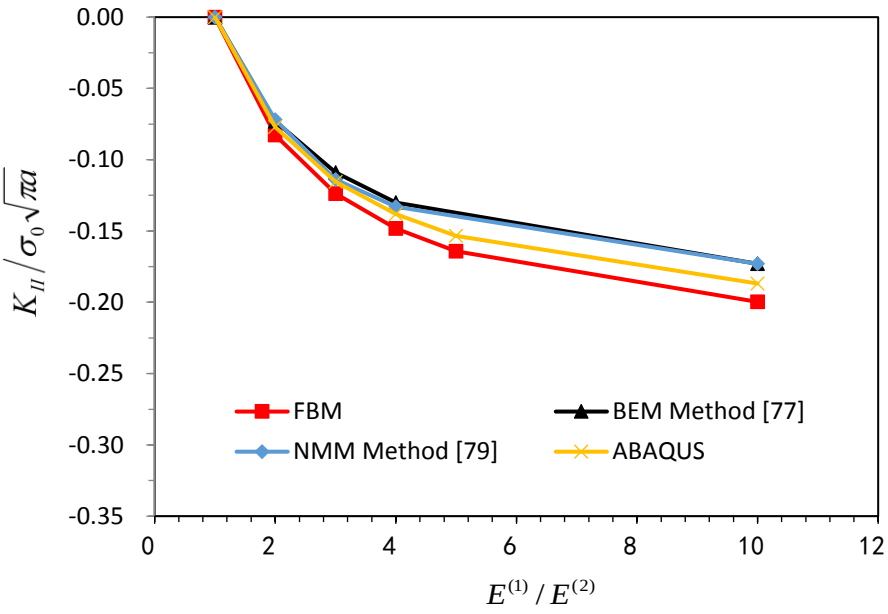

Figure 4.6 Normalised K_{II} stress intensity factor for various elastic modulus combinations. Centre crack length $a/W = 0.4$.

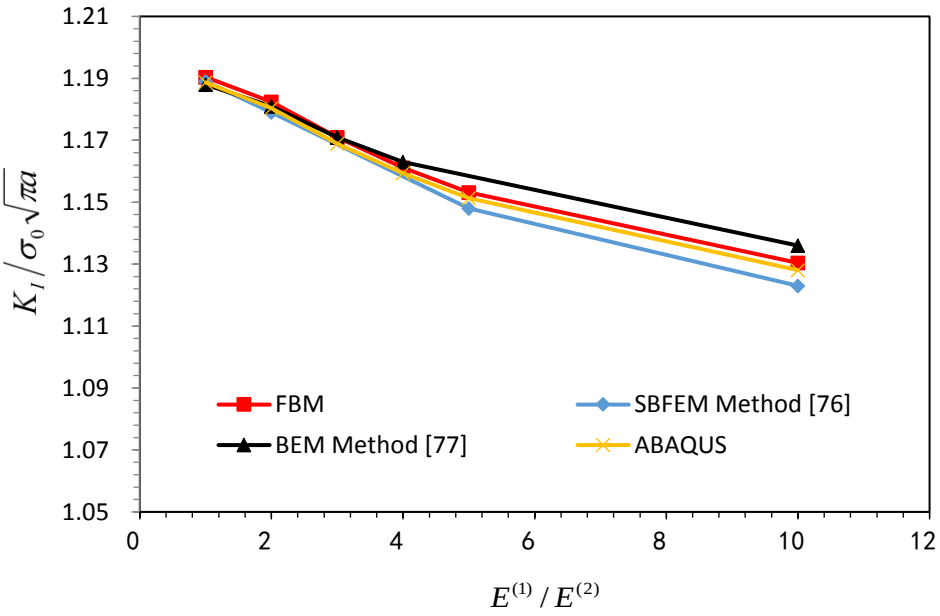

Figure 4.7 Normalised K_I stress intensity factor for various elastic modulus combinations. Centre crack length $a/W = 0.5$.

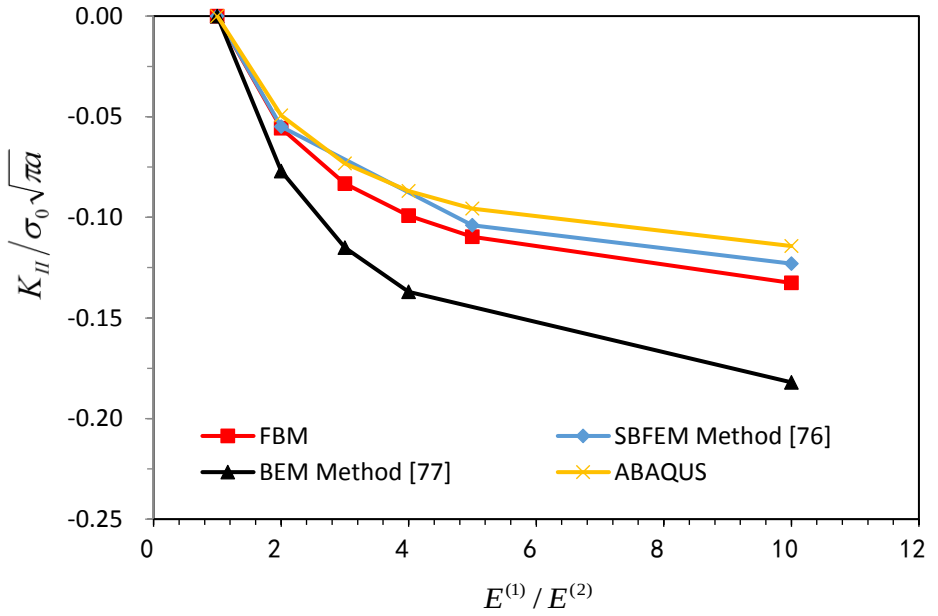

Figure 4.8 Normalised K_{II} stress intensity factor for various elastic modulus combinations. Centre crack length $a/W = 0.5$.

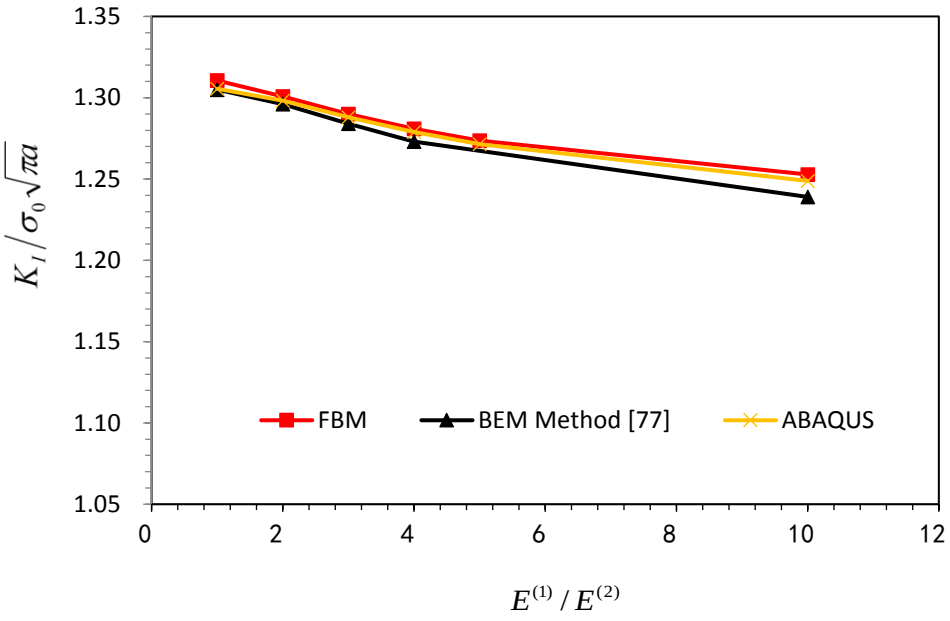

Figure 4.9 Normalised K_I stress intensity factor for various elastic modulus combinations. Centre crack length $a/W = 0.6$.

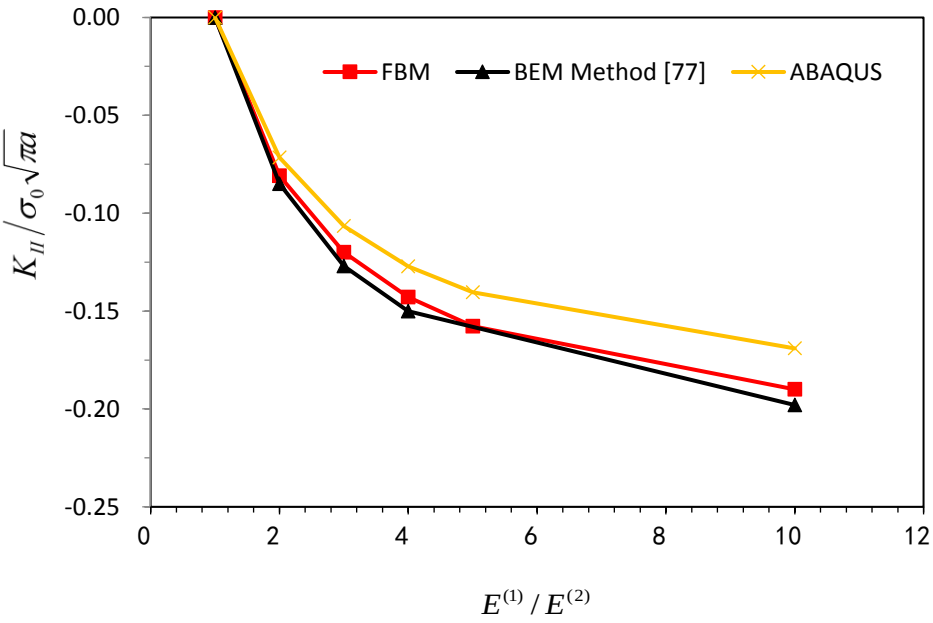

Figure 4.10 Normalised K_{II} stress intensity factor for various elastic modulus combinations. Centre crack length $a/W = 0.6$.

4.6.1.2 Analysis of Bi-Material Plate with An Edge Crack

In order to demonstrate the effectiveness of the finite block method and its application, the analysis has been extended to the evaluation of a single edge notched (SEN) bi-material specimen. The SEN bi-material plate has a uniform tensile load σ_0 applied at the top and bottom of the plate as shown in Fig. 4.11. Owing to the symmetry with respect to the *y* axis, it is equivalent to solve the boundary value problem for a half plate with four blocks for each material (upper and lower media). All other analysis parameters remain unchanged as prescribed for the centre crack analysis.

The results of stress intensity factors (SIF) versus the ratio of Young's modulus $E^{(1)}/E^{(2)}$ are shown in Fig. 4.12 and 4.13 for the different cases. The equivalent edge crack analysis was carried out using FEM (ABAQUS). Also, the solutions given by [35] are provided for comparison.

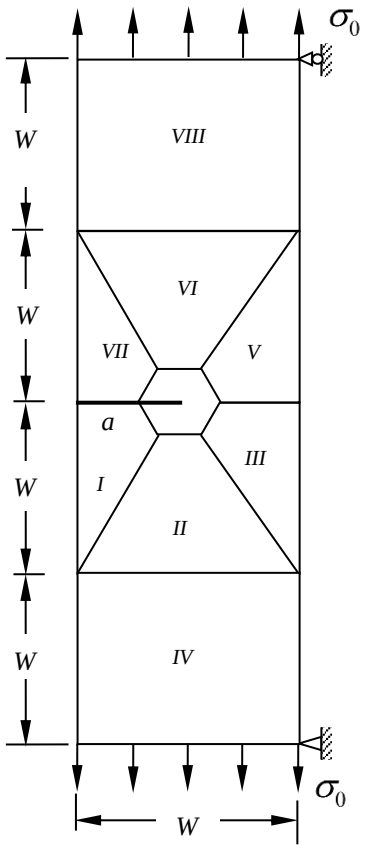

Figure 4.11 A finite block set-up of a bi-material plate with an edge crack and uniformly loaded at the top and bottom.

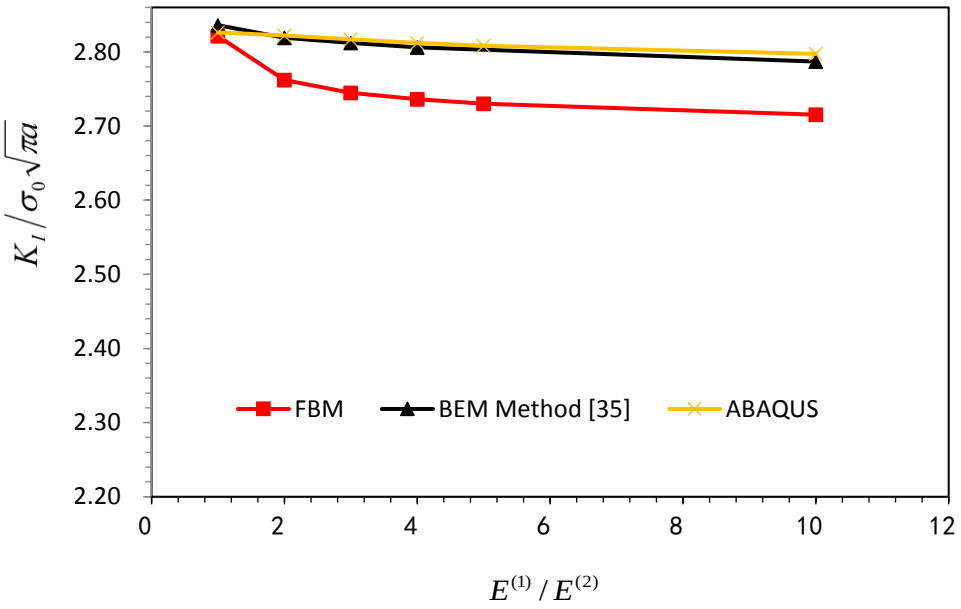

Figure 4.12 Normalised K_I for various elastic modulus combinations, $E^{(1)}/E^{(2)}$. Edge crack with length $a/W = 0.5$.

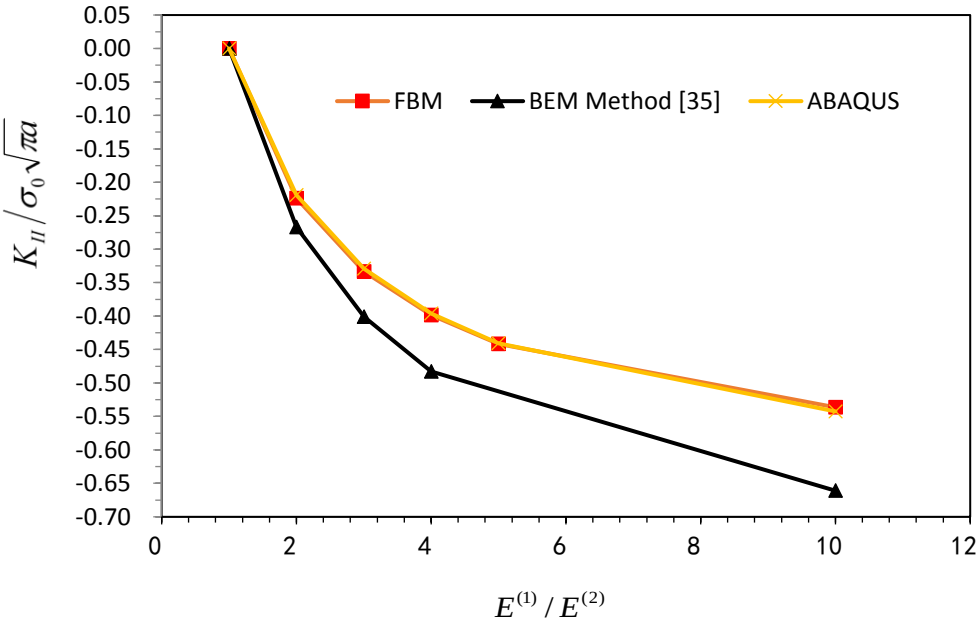

Figure 4.13 Normalised K_{II} for various elastic modulus combinations, $E^{(1)}/E^{(2)}$. Edge crack with length $a/W = 0.5$.

(a)

$E^{(1)}/E^{(2)}$	FBM	BEM [35], Error (%)	[ABAQUS], Error (%)
	$K_I/\sigma_0\sqrt{\pi a}$	$K_I/\sigma_0\sqrt{\pi a}$	$K_I/\sigma_0\sqrt{\pi a}$
1	2.8213	0.52	0.18
2	2.7623	2.05	2.17
3	2.7449	2.44	2.62
4	2.736	2.56	2.79
5	2.73	-	2.87
10	2.7153	2.64	3.02

(b)

$E^{(1)}/E^{(2)}$	FBM	BEM [35], Error (%)	[ABAQUS], Error (%)
	$K_{II}/\sigma_0\sqrt{\pi a}$	$K_{II}/\sigma_0\sqrt{\pi a}$	$K_{II}/\sigma_0\sqrt{\pi a}$
1	0.0001	0.00	0.00
2	-0.2237	16.22	2.14
3	-0.3337	16.78	1.31
4	-0.3988	17.43	0.69
5	-0.4416	-	0.21
10	-0.5363	18.87	1.15

Table 4.5 The tables show the error margins between the FBM and the relevant references. The column headed FBM contain the actual values of the SIF while the remaining columns shows the percentage errors. (a) stress intensity factors K_I and (b) stress intensity factors K_{II} for an edge crack, length $a/W = 0.5$.

In numerical assessment 2, further analysis by the finite block method was performed on a bi-material 2D plate with an interface centre crack and an edge crack. For the centre crack, the K_I and K_{II} values at *a/W* = 0.4, 0.5 and 0.6 all shows a good agreement when compared against the reference values. The results of the stress intensity factors depicted in Fig 4.5 to 4.10 shows the accuracy of the finite block method.

For the edge crack at *a/W* = 0.5, Fig. 4.12 is seen to show a wider gap between the calculated K_I values and the reference values. This is due to the close proximity of the calculated K_I value for every $E^{(1)}/E^{(2)}$ at the crack tip. But a calculation of the relative error reported in Table 4.5 (a) shows a very good approximation of the K_I value by the finite block method. At $E^{(1)}/E^{(2)}$ = 10 where the error is greatest, the relative error between the finite block method and FEM (ABAQUS) is calculated to be 3.02%. This is within an acceptable margin of error of less than 5%.

From Table 4.5 (a), the calculated highest relative error for the K_I value equals 2.64% when compared against the BEM method [35] and 3.02% when compared against FEM (ABAQUS). This is influenced by the high elastic modulus ratio $E^{(1)}/E^{(2)}$ = 10. In comparing the K_{II} values from the BEM method [35] and the FEM (ABAQUS), Table 4.5 (b) shows that the finite block method is far more accurate than the BEM method [35]. At the same time, the highest relative error between the FBM calculated result and the FEM (ABAQUS) equal 2.14%.

4.7. Numerical Assessment 3

4.7.1 A Disk with An Edge Crack

In this assessment, we consider a circular disk with an edge crack, loaded by a constant normal traction σ_0 along the circumference as shown in Fig. 4.3. Suppose that the crack tip is located at the centre of the disk and the crack length $a = R$. A plane stress assumption is considered. The number of collocation points along each side are equal $M_I = N_I = M_{II} = N_{II} = M$. So, the number of collocation points on the interface between blocks and core is $2\times(M-2)$ and the truncation terms $N_c = M-2$.

Two semi-rings, upper and lower are mapped into normalised domain with precisely two blocks. The numerical results of the stress intensity factor are shown in Fig. 4.15 and 4.16 for the different ratios $\mu^{(2)} / \mu^{(1)}$ where the number of node M = 8 and 16, and $r_0 / R = 0.2$. In this study, the crack length $a = R = 0.5$ and d is the diameter of the circle. The equivalent circular crack analysis was carried out using FEM (ABAQUS), to check the finite block method results. Details of the FEM (ABAQUS) model for the edge crack disk is shown in Fig. 4.14 below.

Details of ABAQUS Analysis for Circular Edge Crack

- Analysis performed using ABAQUS version 6.9-2.
- ABAQUS quadratic element type: CPS8R
- The FEM model converged after 4851 nodes and 1600 elements.
- Quarter point elements with ABAQUS singularity control was employed in this analysis.

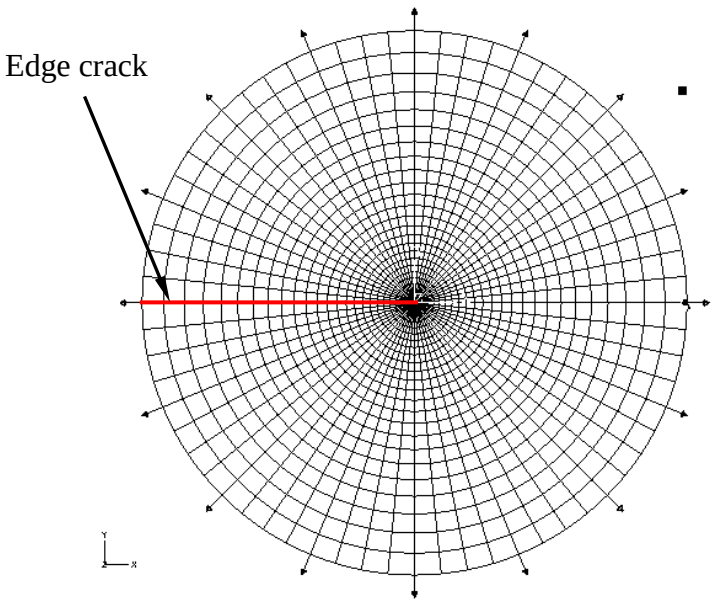

Figure 4.14 FEM model of a circular crack disk with a normal traction around the circumference and crack tip at the centre. The FEM (ABAQUS) model has a sweeping mesh in the direction of the crack tip.

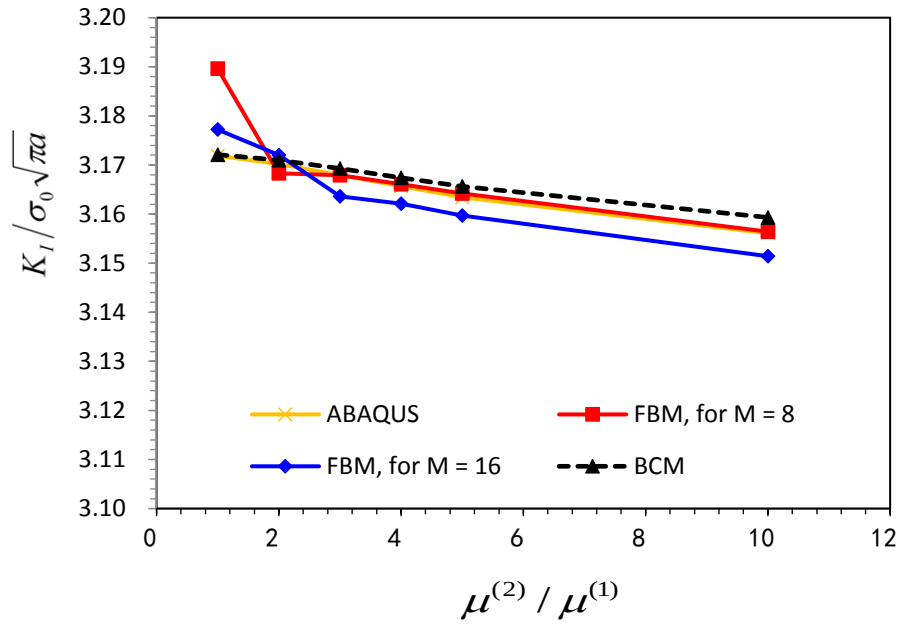

Figure 4.15 Normalised stress intensity factor K_I versus the ratio of $\mu^{(2)}/\mu^{(1)}$ for crack length $a = R = 0.5$.

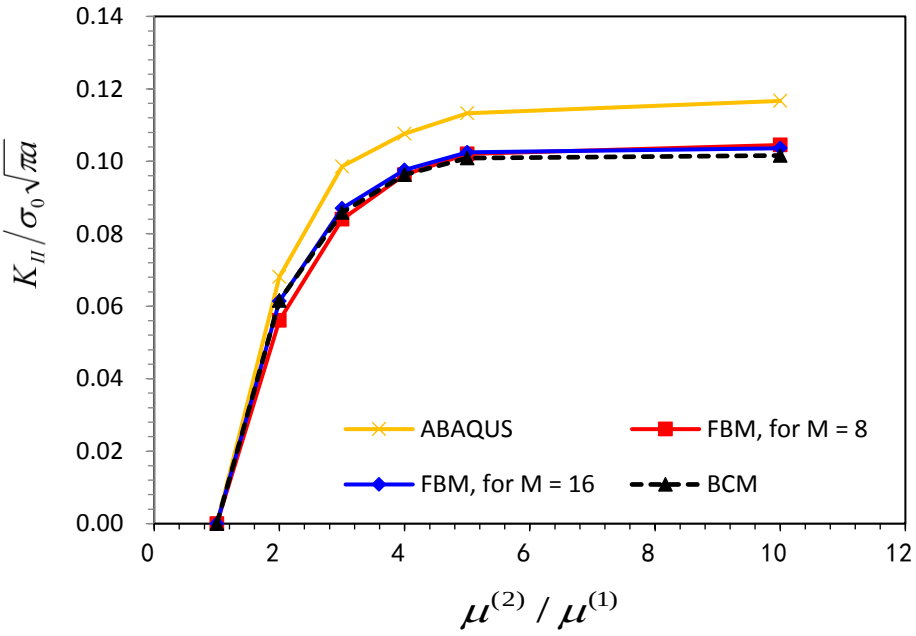

Figure 4.16 Normalised stress intensity factor K_{II} versus the ratio of $\mu^{(2)}/\mu^{(1)}$ for crack length $a = R = 0.5$.

Numerical Assessment 3 examines the stress intensity factors for a circular disk with an edge crack. The K_I and K_{II} values as calculated by the finite block method is compared against the FEM (ABAQUS) and the boundary collocation method on Fig. 4.15 and 4.16. The K_I value plot shows a marginal difference between the FEM (ABAQUS) method and the boundary collocation method. Also, by increasing the number of nodes from M = 8 to M = 16 had little influence on the result between the FEM (ABAQUS) method and the finite block method.

For the K_{II} value reported in Fig. 4.16, the K_{II} value is slightly higher for the FEM (ABAQUS) method when compared against the finite block method. It should be noted that the K_{II} value can be difficult to determine due to the miniature size of the values at the crack tip. The K_{II} values at the crack tip shows no significant change by increasing the number of nodes from M = 8 to M = 16. However, it can be said that the results by the finite block method is very close to the boundary collocation results.

4.8. Summary

In this chapter, the interface crack formulation for the finite block method is developed. By combining the finite block method with the Williams' series of stress functions, the stress intensity factor and other coefficients of the regular terms in the Williams' series can be obtained directly for a stationary static case. An expression of the William's series in terms of both the Cartesian and the polar coordinate system are also given.

A singular core centred at the crack tip was introduced as part of a special treatment to determine the stress intensity factor. A polygon and a circular core were applied in this study. In order to demonstrate the capabilities of the finite block method in calculating the stress intensity factor, several numerical assessments of interface crack were carried out. This includes analyses of a 2D plate with a centre crack and a 2D plate with an edge crack. Also, a parameter study was performed using a circular disk with an edge crack. This was to gain an understanding of the parameters influencing the accuracy of the stress intensity factor values as determined by the finite block method. FEM (ABAQUS) solutions are also reported and used for comparison. The FBM result also shows good agreement with the boundary collocation method. In

all cases, the obtained results were compared with reference papers, the boundary collocation method and FEM (ABAQUS).

CHAPTER 5

Finite Block Method: Evaluation of T-stress for a Bi-Material Interface Crack

5.1. Introduction

In fracture mechanics, the conventional theory is to characterise the state of material failure only by the stress intensity factor. In the case of a homogeneous plate under tensile loading, it is widely accepted that only the perpendicular component of stress at the crack tip affects the material mode-I loading. This method of characterising material failure was established from the work by Irwin's development of crack tip stress intensity factor theory. Over the years several works by researchers including Sladek [114, 147] have shown that other factors are at play at the crack tip. The investigations have shown that fracture failure is influenced by a stress component called the T-stress, which acts parallel to the crack plane. Therefore, the influence of this parallel loading at the crack tip must be considered during fracture assessment.

An extensive review of the T-stress from the last six decades has been conducted by Gupta [91]. In the review, several analytical and experimental techniques are presented. Experimental techniques for evaluating the T-stress include the "photoelastic

method" [91]. Using a photoelastic material and a dedicated wavelength of light, we can observe a dark fringe and a light fringe effect. Fig. 5.1 below shows the photoelastic fringes without the effects of the T-stress. The second image in Fig. 5.2 shows the forward leaning of the fringes due to the influence of the T-stress.

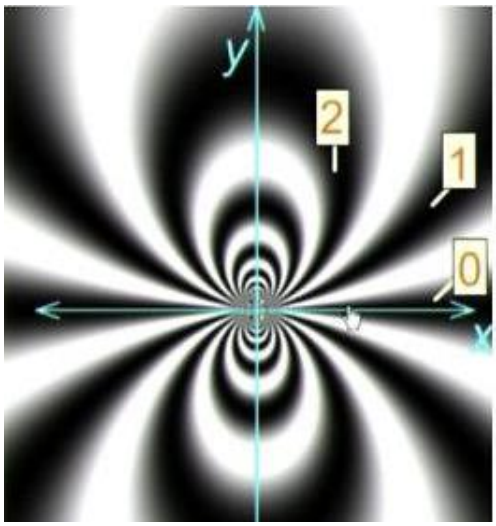

Figure 5.1 Photoelastic fringes without the presents of the T-stress. [91]

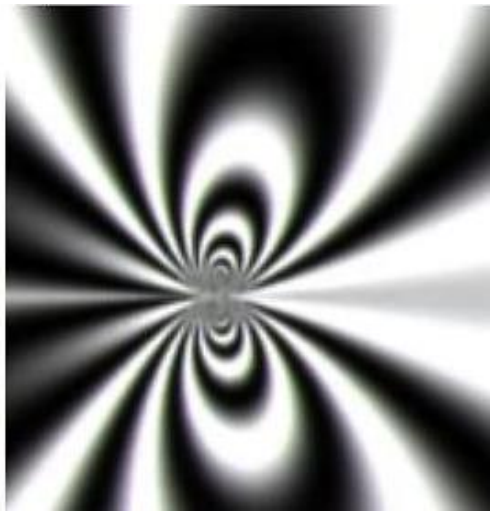

Figure 5.2 Photoelastic fringes showing the forward leaning effect of the T-stress. [91]

Further experiments have considered the influence of the T-stress in predicting crack behaviour. This includes evaluating the crack path [148, 149, 150, 151] and the fracture

angles [152]. In all, the use of the T-stress theory in predicting crack path and fracture angles gives reliable predictions when compared with experimental data.

In addition, many analytical methods for evaluating the T-stress also exist. This includes the stress distribution method, the weight function technique, the Eshelby *J*-Integral method and the Eigen series expansion method. The weight function technique and the Green function method have been developed by Fett [81, 92, 93, 96] to determine the T-stress for a single and a double edge circular disk under several boundary conditions. At the same time, Fett [92, 93] and Li [94] used the weight function technique to determine the stress intensity factor and the T-stress for a rectangular plate with an edge crack. In order to verify the accuracy of the weight function solutions, a finite element analysis of the problem was conducted and the result shows good agreement. Li [94] concluded that the weight function method as developed is adequate to obtain a solution for the T-stress and the stress intensity factors. Also, Kfouri [97] proposed the use of the Eshelby theorem to calculate the T-stress by expressing the T-stress in terms of the *J*-Integral method. This approach is deemed to be accurate when compared with the Eigen function expansion of stress [34, 97]. The accuracy of this method is derived from the distance taken by the *J*-Integral path away from the crack tip. Therefore, avoiding the crack tip singularity terms during the analysis.

The numerical study of T-stress has predominantly been conducted by the FEM method. Ayatollahi [84] used the finite element method to determine the T-stress which became part of a study into brittle and ductile fracture under mixed mode loading. Additionally, the T-stress for several test specimens were determined by Wang [153] using the finite element analysis. The test specimens include the SECP, DECP and CCP. Other numerical techniques including the boundary element method have also been employed in the evaluation of the T-stress. Tan [39] used the "quarter point crack tip elements" in conjunction with the boundary element method to determine the T-stress.

In recent years, more research on the T-stress regarding interfacial cracks, anisotropic and functionally graded materials (FGM) as well as adhesive materials has become the focus of many researchers [111, 154, 155, 156, 157]. In terms of anisotropic materials and FGM, Kim and Paulino [86] discovered that the difference in elastic

modulus has a direct effect on the calculated T-stress. Employing the path independent *M*-Integral technique and the "Subregion boundary element method", Sladek [34] computed the T-stress for interfacial cracks. The solution considered a point force applied directly at the crack tip and in the direction parallel to the interface crack plane. The interface crack problem is solved by choosing a properly suited auxiliary solution which reflects a relationship between the T-stress and the mutual *M*-Integral method. Several test specimens were analysed by this technique and the T-stress for a homogeneous and a bi-material case was presented. The study by Sladek [34] covers a finite plate with a centre crack, a finite plate with a single edge notch and a finite plate with double edge notch.

The T-stress is an important fracture parameter in respect of fracture behaviour and crack stability. This is because the T-stress has certain effects on the crack growth direction, the shape and size of the plastic zone, the crack tip constraint and the fracture toughness [98, 99, 101, 102]. Chen [103] also attested to the practical use of the T-stress method by predicting "crack-growth trajectory in narrow-body fuselages"

Therefore, this chapter is organised as follows; an overview of the stress distribution which indicates the T-stress is introduced for a homogeneous cracked body. The finite block method approach to modelling interface crack and the extraction of the T-stress using the eigenfunction approach is presented. The capability of the finite block method is illustrated by analysing several test cases. Test specimens covered in this study include a plate with a centre crack, a plate with a single edge notch and a double edge notch plate.

5.2. The T-stress in a Homogeneous Cracked Body

For a homogeneous elastic body under pure mode I fracture loading, the components of the stress field at the front of the crack tip is described by the William stress field solution. This is expressed mathematically for a two-dimensional case as [82, 87, 100, 101, 104]

$$\sigma_x = \frac{K_I}{\sqrt{2\pi r}}\cos\frac{\theta}{2}\left(1-\sin\frac{\theta}{2}\sin\frac{3\theta}{2}\right)+T+A\sqrt{r}\cos\frac{\theta}{2}\left(1+\sin^2\frac{\theta}{2}\right)+O(r)\ , \tag{5.1a}$$

$$\sigma_y = \frac{K_I}{\sqrt{2\pi r}}\cos\frac{\theta}{2}\left(1+\sin\frac{\theta}{2}\sin\frac{3\theta}{2}\right)+A\sqrt{r}\cos\frac{\theta}{2}\left(1-\sin^2\frac{\theta}{2}\right)+O\left(r^{3/2}\right), \tag{5.1b}$$

$$\tau_{xy} = \frac{K_I}{\sqrt{2\pi r}}\cos\frac{\theta}{2}\sin\frac{\theta}{2}\cos\frac{3\theta}{2}-A\sqrt{r}\sin\frac{\theta}{2}\cos^2\frac{\theta}{2}+O\left(r\right) \ . \tag{5.1c}$$

where the stress components σ_x , σ_y and τ_{xy} define the stress state at arbitrary points around the crack tip, r and θ are the polar coordinates as defined in Fig. 2.3. The T in Eq. (5.1a) is termed the T-stress. *A*, *B* and *O* in Eq. (5.1) and Eq. (5.2) are constants.

From Eq. (5.1), the T-stress is defined as the second non-singular term in the Williams solution. For the purposes of a two-dimensional study, it is convenient to consider only the *T* term for now. As it happens, the stress field for mode II loading is also given by the following expression

$$\sigma_x = \frac{-K_{II}}{\sqrt{2\pi r}}\sin\frac{\theta}{2}\left(2-\cos\frac{\theta}{2}\cos\frac{3\theta}{2}\right)+B\sqrt{r}\sin\frac{\theta}{2}\left(2+\cos^2\frac{\theta}{2}\right)+O\left(r\right), \tag{5.2a}$$

$$\sigma_y = \frac{K_{II}}{\sqrt{2\pi r}}\sin\frac{\theta}{2}\cos\frac{\theta}{2}\cos\frac{3\theta}{2}-B\sqrt{r}\sin\frac{\theta}{2}\cos^2\frac{\theta}{2}+O\left(r^{3/2}\right), \tag{5.2b}$$

$$\tau_{xy} = \frac{K_{II}}{\sqrt{2\pi r}}\cos\frac{\theta}{2}\left(1-\sin\frac{\theta}{2}\sin\frac{3\theta}{2}\right)+B\sqrt{r}\cos\frac{\theta}{2}\left(1+\sin\frac{\theta}{2}\sin\frac{3\theta}{2}\right)+O\left(r^{3/2}\right). \tag{5.2c}$$

However, it can be observed from Eq. (5.2) that the T-stress term is not replicated in the mode II fracture loading.

The T-stress of a homogeneous cracked medium can be evaluated using the well-established method of interaction integral. Implementation of the interaction integral method and the boundary integral method in finite element analysis [84, 88] and the boundary element method [107] has been well reported for evaluating the T-stress in homogeneous crack bodies. The popular commercial FEM program ABAQUS also utilise the interaction integral method for extracting the stress intensity factor and the T-stress. Further explanation on the interaction integral approach and it application on homogeneous and interface crack is given in [77, 108, 110].

5.3. Determination of the T-stress By the Finite Block Method

5.3.1 The Eigenfunction Approach

Following on from Chapter 4, the eigenfunction expansion approach to analyse the asymptotic nature of the stress field at the crack tip is extended to the extraction of the T-stress in interface crack media. The T-stress formulation for interface crack is developed from Eq. (4.15). The equation is repeated here for clarity.

The integer eigenvalue expression for the stress and displacement is given by

$$2\mu^{(\alpha)}\left(u_x^{(I\alpha)}+iu_y^{(I\alpha)}\right)=\sum_{n=0}^{\infty}A_{In}^{(\alpha)}r^n\left(\kappa^{(\alpha)}e^{in\theta}+e^{-in\theta}\right)+\sum_{n=0}^{\infty}n\overline{A}_{In}^{(\alpha)}r^n\left(e^{-in\theta}-e^{-i(n-2)\theta}\right), \tag{5.3a}$$

$$\sigma_x^{(I\alpha)}+\sigma_y^{(I\alpha)}=2\sum_{n=0}^{\infty}nA_{In}^{(\alpha)}r^{n-1}e^{i(n-1)\theta}+2\sum_{n=0}^{\infty}n\overline{A}_{In}^{(\alpha)}r^{n-1}e^{-i(n-1)\theta}\ , \qquad \alpha=1,2 \tag{5.3b}$$

$$\sigma_y^{(I\alpha)}-i\tau_{xy}^{(I\alpha)}=2i\sum_{n=0}^{\infty}nA_{In}^{(\alpha)}r^{n-1}\sin(n-1)\theta+\sum_{n=0}^{\infty}n(n-1)\overline{A}_{In}^{(\alpha)}r^{n-1}\left(e^{-i(n-3)\theta}-e^{-i(n-1)\theta}\right). \tag{5.3c}$$

The corresponding complex eigenvalues expression for the stress and displacement is given by

$$2\mu^{(\alpha)}\left(u_x^{(C\alpha)}+iu_y^{(C\alpha)}\right)=\sum_{n=0}^{\infty}A_{Cn}^{(\alpha)}r^{\lambda_n}\left(\kappa^{(\alpha)}e^{i\lambda_n\theta}+e^{-2\pi i\lambda_n(-1)^{\alpha}-i\lambda_n\theta}\right)+\sum_{n=0}^{\infty}\overline{\lambda}_n\overline{A}_{Cn}^{(\alpha)}r^{\overline{\lambda}_n}\left(e^{-i\overline{\lambda}_n\theta}-e^{-i(\overline{\lambda}_n-2)\theta}\right), \tag{5.4a}$$

$$\sigma_x^{(C\alpha)}+\sigma_y^{(C\alpha)}=2\sum_{n=0}^{\infty}\lambda_nA_{Cn}^{(\alpha)}r^{\lambda_n-1}e^{i(\lambda_n-1)\theta}+2\sum_{n=0}^{\infty}\overline{\lambda}_n\overline{A}_{Cn}^{(\alpha)}r^{\overline{\lambda}_n-1}e^{-i(\overline{\lambda}_n-1)\theta}\ , \qquad \alpha=1,2\ , \tag{5.4b}$$

$$\sigma_y^{(C\alpha)} - i\tau_{xy}^{(C\alpha)} = \sum_{n=0}^{\infty} \lambda_n A_{Cn}^{(\alpha)} r^{\lambda_n - 1}\left(e^{i(\lambda_n - 1)\theta} + e^{-2\pi i\lambda_n(-1)^{\alpha} - i(\lambda_n - 1)\theta}\right) + \sum_{n=0}^{\infty} \overline{\lambda}_n(\overline{\lambda}_n - 1)\overline{A}_{Cn}^{(\alpha)} r^{\overline{\lambda}_n - 1}\left(e^{-i(\overline{\lambda}_n - 3)\theta} - e^{-i(\overline{\lambda}_n - 1)\theta}\right). \quad (5.4c)$$

From Eq. (5.3), the T-stress can be found when $n=1$ and the T-stresses in two different media is given as

$$T^{(\alpha)} = 4A_{11}^{(\alpha)}, \ \alpha = 1,2 \text{ and } T^{(2)} = \beta T^{(1)} . \quad (5.5)$$

It means that the T-stress has a jump over the interface and the gap depends on the ratio β as defined in Eq. (4.14). For the finite block method, all the coefficients for the integer solutions including $A_{In}^{(1)}$ $(n = 0,1,...N_b - 1)$ should be determined by the specified boundary conditions of the traction and displacement, here N_b is the number of boundary collocation point.

5.4. Numerical Assessment 1

5.4.1 Parameter Study

The parameters influencing the accurate calculation of the T-stress of a circular disk with an edge crack similar to Fig. 4.3 is considered. The circular disk is loaded by a constant normal traction σ_0 along the circumference. A plane stress assumption is considered and the number of collocation points along each side are equal $M_I = N_I = M_{II} = N_{II} = M$. Hence, the number of collocation points on the interface between the blocks and the core is $2\times(M-2)$ and the truncation terms $N_c = M - 2$. The disk is centred at the crack tip. Two semi-rings, upper and lower are mapped into a normalised domain with precisely two blocks. The numerical results of the T-stress are shown in Table 5.1 for the different number of nodes M where $\mu^{(2)} = 2\mu^{(1)}$, $\nu^{(1)} = \nu^{(2)} = 0.3$ and $r_c / R = 0.2$. Numerical solutions with the Boundary Collocation Method (BCM) are also reported in Table 5.1 for comparison. It is apparent that the agreement is excellent.

Table 5.2 also shows the results of the T-stress for different ratios $\mu^{(2)}/\mu^{(1)}$ when the number of nodes $M=16$ and $r_0/R=0.2$. The results for the T-stress given by Fett [118] for a semi-crack disk with homogeneous media, i.e. $\mu^{(2)}/\mu^{(1)}=1$, $T=1.896\sigma_0$. This value is compared against the T-stress value achieved by the FBM method and it shows a good result. Table 5.3 shows the numerical results for a variation of the Poisson's ratio $\nu^{(2)}$ where the number of nodes $M=16$, $\mu^{(2)}/\mu^{(1)}=2$ and $r_c/R=0.2$.

In addition, the accuracy and the convergence of the study is observed and the results are reported in Table 5.4 in the case of $\nu^{(1)}=\nu^{(2)}=0.3$ with different core size. It is apparent, the best results can be obtained when $r_c/R=0.2$.

M	$T^{(2)}/\sigma_0$
9	2.5659
11	2.5492
13	2.5446
15	2.5432
BCM	2.5424

Table 5.1 Normalised T-stress versus the number of nodes.

$\mu^{(2)}/\mu^{(1)}$	$T^{(2)}/\sigma_0$	
	FBM	BCM
1	1.8966	1.8961
2	2.5391	2.5425
3	2.8771	2.8816
4	3.0875	3.0928
5	3.2330	3.2378
6	3.3385	3.3437
7	3.4192	3.4247
8	3.4849	3.4886
9	3.5367	3.5404
10	3.5784	3.5832

Table 5.2 Normalised T-stress versus the ratio of $\mu^{(2)}/\mu^{(1)}$.

$\nu^{(2)}$	$T^{(2)}/\sigma_0$	
	FBM	BCM
0.0	2.5451	2.5393
0.1	2.5443	2.5403
0.2	2.5374	2.5414
0.3	2.5391	2.5425
0.4	2.5479	2.5436

Table 5.3 Normalised T-stress versus the variation of Poisson's ratio $\nu^{(2)}$.

r_c / R	$T^{(2)} / \sigma_0$
0.20	2.5391
0.25	2.5133
0.30	2.5234
0.35	2.4913
0.40	2.4632
BCM	2.5425

Table 5.4 Normalised T-stress versus the core size r_c / R compared with the BCM.

Using the disk with an edge crack from Fig. 4.3, parameters with the potential to influence the calculated T-stress values were examined. From Table 5.1, the calculated T-stress values were compared against the boundary collocation method. By increasing the number of nodes from M = 9 to M = 15, the lowest achieved relative error between the finite block method and the boundary collocation method equals 3.14 x 10^{-4}%. This is significantly small and almost negligible. Clearly, the number of nodes at the crack tip is a contributing factor in terms of accuracy of the T-stress result.

In Table 5.2, the T-stress results are reported after varying the shear modulus between block I and block II. The T-stress values from Table 5.2 shows a stable result for all values determined by the finite block method when compared against the boundary collocation method. The relative error margin is calculated to be 1.7 x 10^{-3}%. Certainly, this error value is very small.

5.5. Numerical Assessment 2

In order to demonstrate the effectiveness of the finite block method in determining the T-stress value for an interface crack, a bi-material plate with a centre crack (CCP), a single edge notched (SEN) and a double edge notched (DEN) were analysed. In all three cases the CCP, SEN and the DEN specimens were analysed for various elastic modulus ratios, mainly $E^{(1)}/E^{(2)}$, and crack length a.

5.5.1 Analysis of a Bi-material Plate with a Centre Crack

A bi-material plate with a centre crack has a uniform tensile load σ_0 applied at the top and bottom of the plate, similar to Fig. 4.4. Owing to the symmetry with respect to the *y* axis, it is equivalent to solve the boundary value problem for a half plate with four blocks for each material (upper and lower media) with plane strain state and Poisson's ratios $\nu^{(1)} = \nu^{(2)} = 0.3$. The size of the polygonal core $r_0/W = 0.2$ and several crack lengths are considered $a/W = 0.4,\ 0.5,$ and 0.6. For each block, the control number of collocation point density is given by $M_\Lambda = N_\Lambda = M$ ($\Lambda = I, II, ..., VIII$).

Results of the T-stress versus the ratio of Young's modulus $E^{(1)}/E^{(2)}$ are shown in Fig. 5.3, 5.4 and 5.5 for the different crack lengths. The solutions given by Song using the Scaled Boundary Finite Element Method (SBFEM) [76] and by Sladek using the Boundary Element Method (BEM) [34] are provided for comparison. The T-stress as presented here is normalised to the stress $K_0/\sqrt{\pi a}$, $K_0 = \sqrt{K_I^2 + K_{II}^2}$. Also, the reported T-stress results considers the effect of material 2.

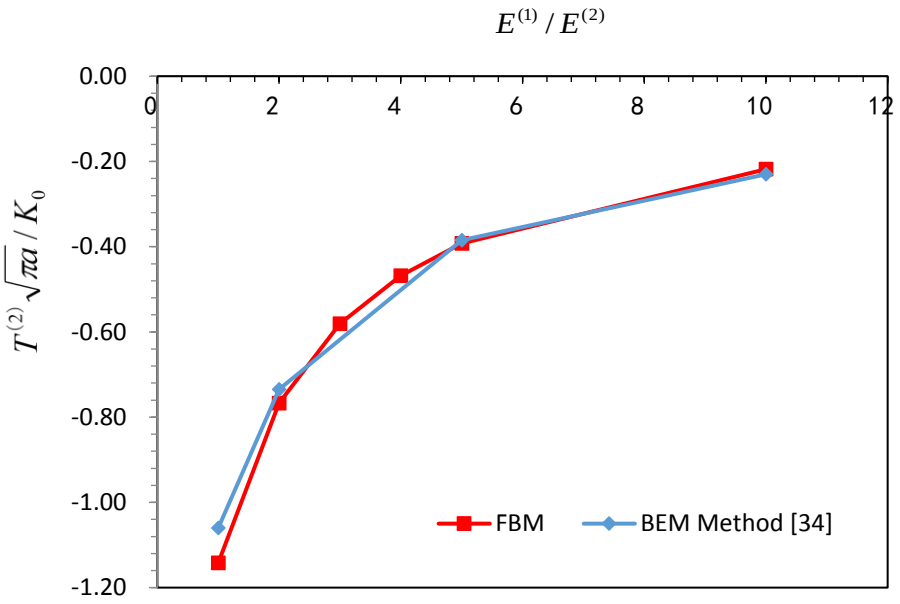

Figure 5.3 Normalised T-stress of a centre cracked plate (CCP) with various elastic modulus combinations. Centre crack length $a/W = 0.4$.

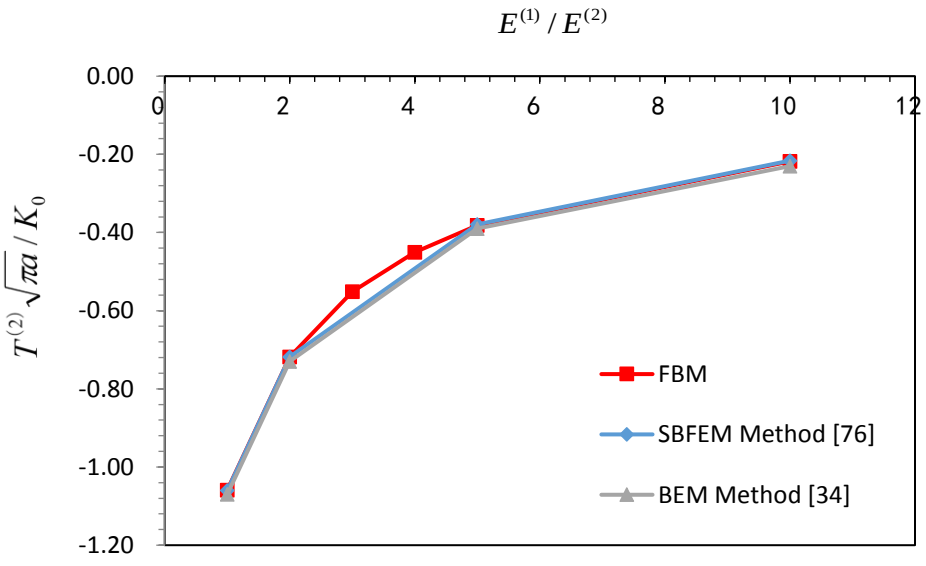

Figure 5.4 Normalised T-stress of a centre cracked plate (CCP) with various elastic modulus combinations. Centre crack length $a/W = 0.5$.

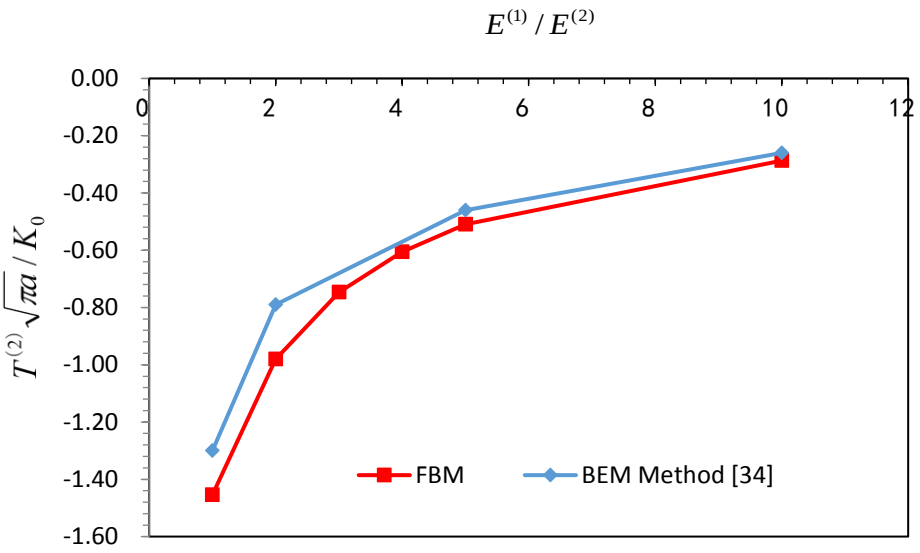

Figure 5.5 Normalised T-stress of a centre cracked plate (CCP) with various elastic modulus combinations. Centre crack length $a/W = 0.6$.

In view of the T-stress results shown in Fig. 5.3 to 5.5, the finite block method has demonstrated it can produce very good results for different bi-material combinations.

By directly comparing the finite block result for the T-stress against the boundary element method [34] and the SBFEM method [76], for $a/W = 0.5$, we can see that the T-stress values are almost a perfect match. However, as the crack length is increased to $a/W = 0.6$, the error converges as the bi-material stiffness increases. This indifference in the calculated T-stress value is due to the block arrangement. Nonetheless, the impact of the block arrangement on the T-stress as shown in Fig. 5.5 is minimal.

5.5.2 Analysis of a Bi-material Plate with an Edge Crack

The bi-material plate with a single edge notched (SEN) shown in Fig. 4.11 is considered for the next T-stress assessment. The SEN bi-material plate has a uniform tensile load σ_0 applied at the top and bottom of the plate. Due to the symmetry of the plate with respect to the y axis, it is equivalent to solve the boundary value problem for a half plate with four blocks for each material (upper and lower media). All other

analysis parameters remain unchanged as per the description of the single edge notched (SEN) analysis in section 4.6.1.2. The size of the polygonal core $r_0/W = 0.2$ and crack lengths considered a/W = 0.4 and 0.5.

Results of the T-stress versus the ratio of Young's modulus $E^{(1)}/E^{(2)}$ are shown in Fig. 5.6 and 5.7 for the different crack lengths. The solutions given by Sladek using the Boundary Element Method (BEM) [34] are provided for comparison. The T-stress as presented here is normalised to the stress $K_0/\sqrt{\pi a}$, $K_0 = \sqrt{K_I^2 + K_{II}^2}$. Also, the reported T-stress results considers the effect of material 2.

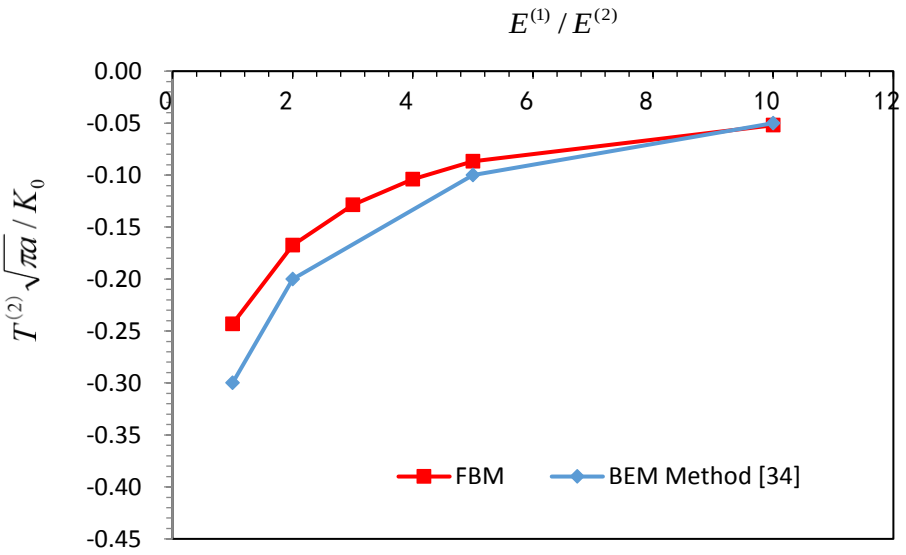

Figure 5.6 Normalised T-stress of a single edge notched (SEN) with various elastic modulus combinations. Edge crack length a/W = 0.4.

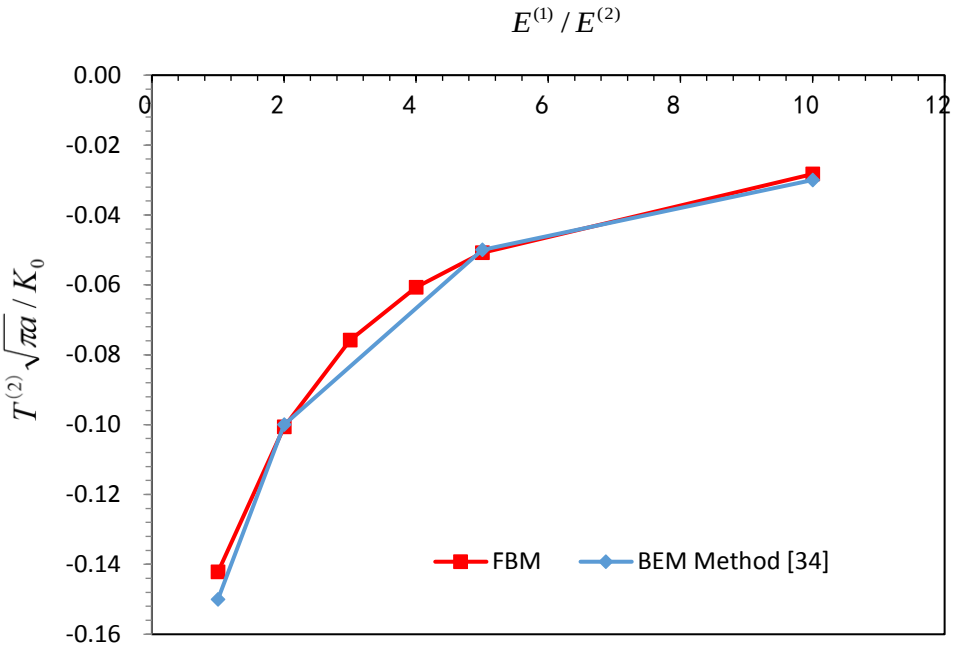

Figure 5.7 Normalised T-stress of a single edge notched (SEN) with various elastic modulus combinations. Edge crack length $a/W = 0.5$.

For a crack length $a/W = 0.4$, the plotted T-stress result (Fig. 5.6) shows a slight difference between the FBM method and the BEM method by Sladek [34]. At the same time when the crack length a$/W = 0.5$, Fig. 5.7, the gap closes significantly. This is due to the slight distortion in the block arrangement at the crack tip. Therefore, to achieve good results, it is recommended that the blocks should be organised or arranged in a way that produces a geometric symmetry of blocks around the crack tip. Hence, an even geometric representation on either flank of the crack tip. This explanation must be taken seriously if one is to produce accurate results by the finite block method.

5.5.3 Analysis of a Bi-material Plate with a Double Edge Crack

The finite block method is employed to evaluate a double edge notched (DEN) bi-material specimen. A uniform tensile load is applied at the top and bottom of the plate as shown in Fig. 5.8. Owing to the symmetry with respect to the y axis, it is equivalent to solve the boundary value problem for a half plate with four blocks for each material

(upper and lower media) with plane strain state and Poisson ratios $\nu^{(1)} = \nu^{(2)} = 0.3$. The size of the polygonal core $r_0 / W = 0.2$ and crack length a/*W* = 0.5.

For each block, the control number of collocation point density is given by $M_\Lambda = N_\Lambda = M\,(\Lambda = I, II, ..., VIII)$.

Results of the T-stress versus the ratio of elastic modulus is shown in Fig. 5.9. The solutions given by Sladek using the boundary element method (BEM) [34] are provided for comparison. The T-stress as presented here is normalised to the stress $K_0 / \sqrt{\pi a}$, $K_0 = \sqrt{K_I^2 + K_{II}^2}$. Also, the reported T-stress results considers the effect of material 2.

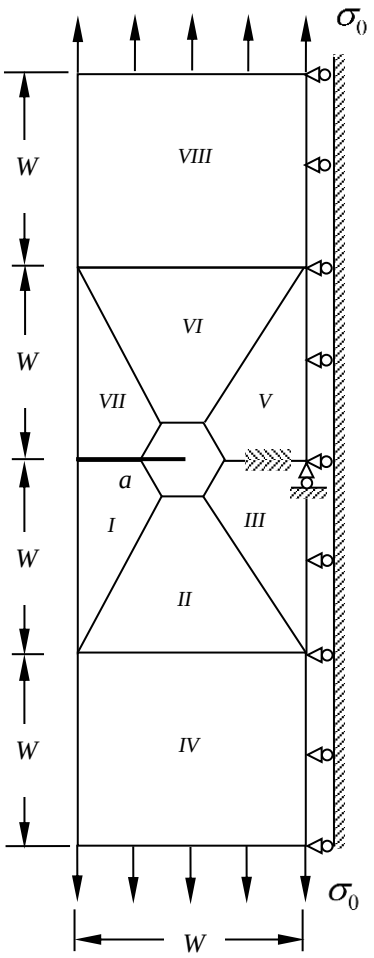

Figure 5.8 A finite block setup of a bi-material plate with a double edge crack. The tensile loads are uniformly applied at the top and bottom of the plate. Crack length *a/W* = 0.5.

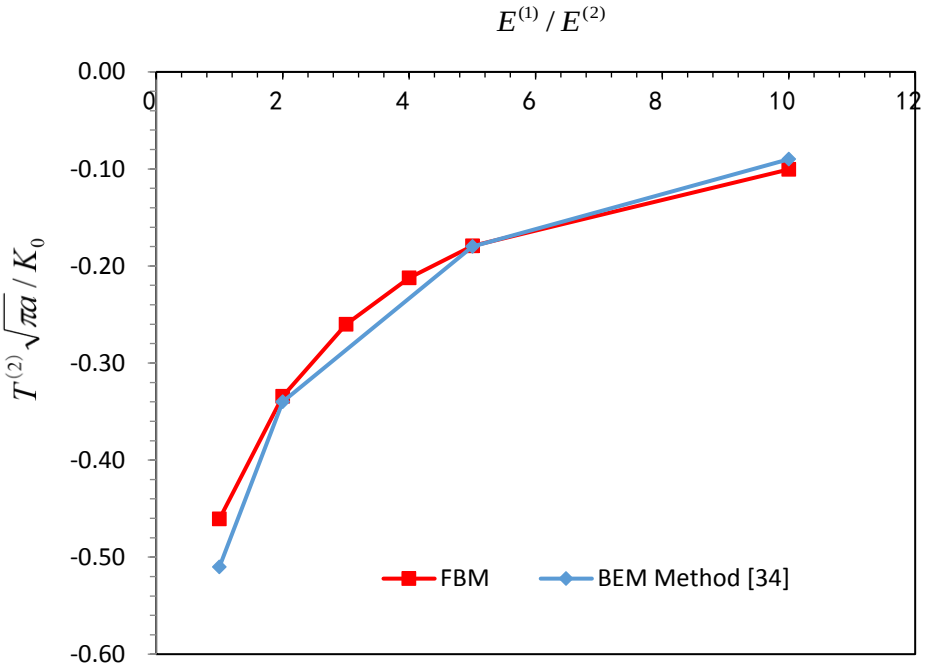

Figure 5.9 Normalised T-stress of a double edge notched (DEN) with various elastic modulus combinations. Double edge crack of length $a/W = 0.5$.

By applying an organised block arrangement with symmetry (equal block lengths behind and ahead of the crack tip) around the crack tip for a double edge crack, the finite block method produced very good result as presented in Fig. 5.9. Again, the finite block method with the Lagrange series interpolation has demonstrated it can determine the T-stress of an interface crack with only 8 blocks.

In all cases of the finite block method evaluation of the T-stress for an interface crack, several material combinations were considered. The analysis plotted in Fig. 5.9 is shown to be stable for bi-materials in the range $E^{(1)}/E^{(2)} = 1$ to $E^{(1)}/E^{(2)} = 10$.

5.6. Summary

In this chapter, the T-stress which is an important fracture parameter is extensively discussed. An expression for the T-stress at the crack tip was developed for the finite block method in conjunction with the William's series expansion and the eigenfunction approach.

Several numerical assessments were considered as part of this study. A 2D plate with a centre crack (CCP), a single edge notched (SEN) and a double edge notched (DEN) were successfully analysed. The accuracy attainable by the finite block method and the crack tip singular core is clearly visible when compared with the boundary element method [34] and the SBFEM method [76].

CHAPTER 6

Determination of Dynamic Stress Intensity Factor and the Dynamic T-stress for Bi-Materials Using the Finite Block Method

6.1. Introduction

A brief introduction on dynamic stress intensity factor was fore-mentioned in Chapter 2 of the literature review. As noted, the dynamic stress intensity factor is a significant characteristic of a cracked body. A good understanding and determination of the dynamic stress intensity factor and the dynamic T-stress will assist in deciding the operating limits of a cracked engineering component. The study of dynamic fracture mechanics can be categorised into an experimental study and a computational study.

Experimental investigation of dynamic stress intensity factor (DSIF) has been a subject of interest by many researchers. The aim is to gain a good understanding of the effects and influence of DSIF on material failure. In dynamic fracture mechanics, the emphasis is on the fracture toughness of the material. The effect of the dynamic loading can lead to the fracture of the material. Additionally, research shows that the dynamic

fracture toughness is a function of the rate of change in the stress intensity factor. Works by many researchers including Dally and Baker [126], and Kalthoff [46] have shown that the dynamic fracture toughness is much higher than the static fracture toughness. Dynamic loading of a single edge notch (SEN) by Owen [127, 128] at low loading rate obtained a dynamic fracture toughness of < 10^4 MPa $\sqrt{m}s^{-1}$. A follow-up experiment by Owen [127], used a split Hopkinson bar test which gave a dynamic fracture toughness of > 10^5 MPa $\sqrt{m}s^{-1}$. Further work by Owen [128] produced similar results. Therefore, it can be deduced that at low loading rates (K < 10^4 MPa $\sqrt{m}s^{-1}$), the dynamic fracture toughness is approximately the same as quasi-static value. However, at higher loading rates, a steep rise of the dynamic fracture toughness is seen when compared with quasi static results.

In addition to experimental studies, a great deal of work on numerical investigations of a cracked body under dynamic loading continues to be published. Using the finite element method, Basu and Narasimhan [129] investigated the influence of "inertia and strain rate sensitivity" on fracture initiation due to mode I dynamic loading.

By contrast, limited research has been devoted to the study of T-stress of a cracked media under dynamic loading. Earlier work on this feature by Koppenhoefer [112] considered the impact loading of a pre-cracked Charpy specimen where the *Q*-Stress is determined. The T-stress is considered to be equivalent to the *Q*-Stress for a ductile solid under dynamic loading [112]. In this case, *Q* is the stress triaxiality. The study by Koppenhoefer shows a negative *Q*-Stress for the loading history. Basu also investigated the triaxiality parameter *Q* for a single edge notch (SEN) specimen under dynamic loading [130]. One of the main conclusions drawn from their investigation is said to be the inexistence of constraint loss under static loading. In effect, the SEN specimen under high loading rate shows a strong negative *Q*-Stress value.

To evaluate the stress intensity factors accurately for both static and dynamic cases, many new techniques have been developed recently. The extended finite element method was applied to dynamic cracks in a piezoelectric solid by Bui [120], Liu [121], Bui [122] and Yu [119]. The singular edge-based smoothed finite element method for stationary dynamic crack problems in 2D elastic solids was demonstrated by Liu [116].

It is also understandable that each of these numerical methods has its own advantages and disadvantages.

In this chapter, the dynamic stress intensity factor and the dynamic T-stress is evaluated for a bi-material media with an interface crack. The William's solutions for a static case is used to replace the transformed solution in the process of resolving the complexity of the William's solution in the transformed domain. This is then incorporated in the finite block method to determine the complex dynamic stress intensity factors and the dynamic T-stress for an interface crack. Due to the lack of exact analytical solution for the dynamic loading of a bi-material plate with a centre or an edge crack, the numerical result obtained by the finite element analysis (ABAQUS) are presented on the same figures for comparison.

6.2. The Concept of Elastodynamic Fracture Mechanics

6.2.1 Elastodynamic Analysis

In solving elastodynamic problems, one can approach it by the time-domain or the frequency-domain method. The time dependent approach requires time integration of the domain at every time step increment [131]. The frequency-domain approach requires the use of the Laplace transform in solving the initial problem in the Laplace transform domain before proceeding to a solution in the real domain by the inversion Laplace transform method such as the one proposed by Durbin [115]. Another dynamic technique called the Newmark time integration method was proposed by Newmark [141] and this can be incorporated in FEM methods for the evaluation of structure dynamics [116].

6.2.2 Equation of Motion for a Cracked Elastic Medium

In general, the study of dynamic fracture mechanics considers the inertial effects during the dynamic loading. Therefore, to describe the dynamic behaviour of a cracked medium under body forces, the governing equation of the medium is expressed. For a 2D homogeneous, isotropic and elastic body $\Omega \in \Re^2$ bounded by boundary $\Gamma = \Gamma_u \cup \Gamma_t$

and $\Gamma_u \cap \Gamma_t = 0$ with an initial traction-free crack boundary represented by Γ_C as shown in Fig. 6.1.

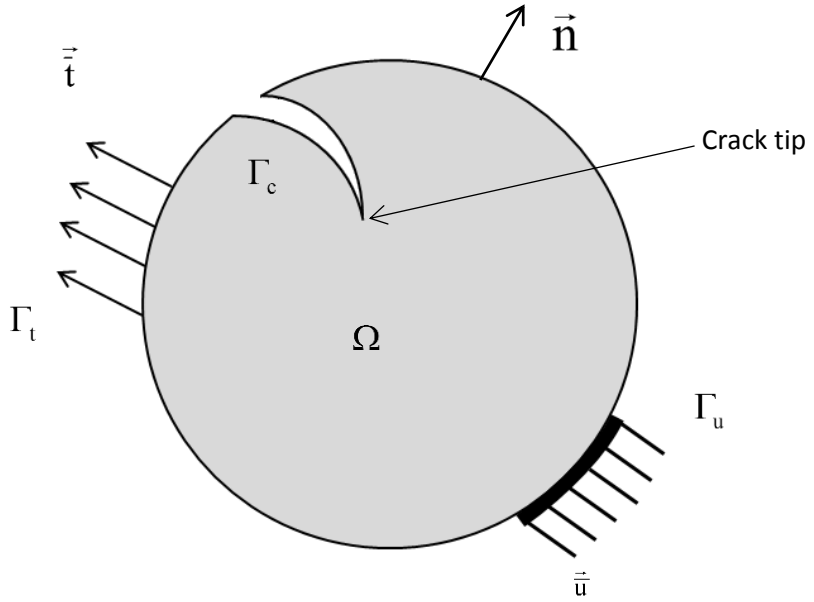

Figure 6.1 A 2D domain with notations for the governing equation.

6.3. Finite Block Method in Elastodynamic

For a two-dimensional dynamic problem in a Cartesian coordinate system, the equilibrium equations are given by

$$\frac{\partial \sigma_x}{\partial x} + \frac{\partial \tau_{xy}}{\partial y} + b_x - \rho \frac{\partial^2 u_x}{\partial t^2} = 0 \ ,$$

$$(x, y) \in \Omega \ , \tag{6.1}$$

$$\frac{\partial \tau_{xy}}{\partial x} + \frac{\partial \sigma_y}{\partial y} + b_y - \rho \frac{\partial^2 u_y}{\partial t^2} = 0 \ .$$

where b_x and b_y are the body forces. Substituting Eq. (4.21) and (4.22) into Eq. (6.1) gives, for plane stress state

$$\frac{E}{\left(1-\nu^2\right)}\left(\frac{\partial^2 u_x}{\partial x^2}+\frac{1-\nu}{2}\frac{\partial^2 u_x}{\partial y^2}+\frac{1+\nu}{2}\frac{\partial^2 u_y}{\partial x\partial y}\right)+b_x=\rho\frac{\partial^2 u_x}{\partial t^2}\ ,$$

$$\frac{E}{\left(1-\nu^2\right)}\left(\frac{\partial^2 u_y}{\partial y^2}+\frac{1-\nu}{2}\frac{\partial^2 u_y}{\partial x^2}+\frac{1+\nu}{2}\frac{\partial^2 u_x}{\partial y\partial x}\right)+b_y=\rho\frac{\partial^2 u_y}{\partial t^2}\ . \tag{6.2}$$

The expression relating the stress and strain as expressed in the finite block method is given by Eq. (4.25). For the dynamic case, substitute the stresses from Eq. (4.25) into the equilibrium Eq. (6.1) and (6.2) for each collocation point P which gives

$$\left(\mathbf{D}_{,x}^2+\frac{1-\nu}{2}\mathbf{D}_{,y}^2\right)\mathbf{u}_x+\frac{1+\nu}{2}\mathbf{D}_{,x}\mathbf{D}_{,y}\mathbf{u}_y+\frac{1-\nu^2}{E}\mathbf{b}_x=\frac{1-\nu^2}{E}\rho\frac{\partial^2\mathbf{u}_x}{\partial t^2}\ ,$$

$$P\in\Omega \tag{6.3}$$

$$\frac{1+\nu}{2}\mathbf{D}_{,x}\mathbf{D}_{,y}\mathbf{u}_x+\left(\mathbf{D}_{,y}^2+\frac{1-\nu}{2}\mathbf{D}_{,x}^2\right)\mathbf{u}_y+\frac{1-\nu^2}{E}\mathbf{b}_y=\frac{1-\nu^2}{E}\rho\frac{\partial^2\mathbf{u}_y}{\partial t^2}\ .$$

where $\mathbf{b}_x=\{b_{xk}\}^T$ and $\mathbf{b}_y=\{b_{yk}\}^T$ are the nodal value vectors of the body forces. The boundary conditions of the displacements and the tractions are described as

$$u_x(P)=\bar{u}_x^0(P)\ ,\qquad u_y(P)=\bar{u}_x^0(P)\ ,\qquad P\in\Gamma_u\ , \tag{6.4}$$

for the displacements and

$$\sigma_x(P)n_x(P)+\tau_{xy}(P)n_y(P)=\bar{t}_x^0(P),$$

$$P\in\Gamma_t \tag{6.5a}$$

$$\tau_{xy}(P)n_x(P)+\sigma_y(P)n_y(P)=\bar{t}_y^0(P),$$

for the traction. The initial conditions are set to zero when $t=0$, given $u_x=u_y=\partial u_x/\partial x=\partial u_y/\partial y=0$.

Alternative expression for Eq. (6.5a) gives

$$\frac{E}{(1-\nu^2)}\left[\left(\frac{\partial u_x}{\partial x}+\nu\frac{\partial u_y}{\partial y}\right)n_x(P)+\frac{1-\nu}{2}\left(\frac{\partial u_x}{\partial y}+\nu\frac{\partial u_y}{\partial x}\right)n_y(P)\right]=\bar{t}_x^0(P)\ ,$$

$$P\in\Gamma_t \tag{6.5b}$$

$$\frac{E}{(1-\nu^2)}\left[\frac{1-\nu}{2}\left(\frac{\partial u_x}{\partial y}+\nu\frac{\partial u_y}{\partial x}\right)n_x(P)+\left(\frac{\partial u_y}{\partial y}+\nu\frac{\partial u_x}{\partial x}\right)n_y(P)\right]=\bar{t}_y^0(P)\ ,$$

for the tractions, where $\bar{u}_x^0, \bar{u}_y^0, \bar{t}_x^0$ and $\bar{t}_y^0$ are the given boundary values of the displacement and the traction on the boundaries Γ_u and Γ_t respectively and $n(n_x, n_y)$ is the outward normal to the boundary.

The Laplace transformation of a function $f(t)$ in real time domain into the Laplace domain is defined as

$$\tilde{f}(s) = \int_0^\infty f(t) e^{-st} dt \ , \tag{6.6}$$

in which s is the Laplace transform parameter.

By applying the Laplace transformation over both sides of the equilibrium Eq. (6.3) [143] for zero initial condition give

$$\begin{aligned} &\left(\mathbf{D}_{,x}^2 + \frac{1-\nu}{2} \mathbf{D}_{,y}^2 \right) \tilde{\mathbf{u}}_x + \frac{1+\nu}{2} \mathbf{D}_{,x} \mathbf{D}_{,y} \tilde{\mathbf{u}}_y + \frac{1-\nu^2}{E} \tilde{\mathbf{b}}_x = \frac{1-\nu^2}{E} \rho s^2 \tilde{\mathbf{u}}_x \ , \\ &\frac{1+\nu}{2} \mathbf{D}_{,x} \mathbf{D}_{,y} \tilde{\mathbf{u}}_x + \left(\mathbf{D}_{,y}^2 + \frac{1-\nu}{2} \mathbf{D}_{,x}^2 \right) \tilde{\mathbf{u}}_y + \frac{1-\nu^2}{E} \tilde{\mathbf{b}}_y = \frac{1-\nu^2}{E} \rho s^2 \tilde{\mathbf{u}}_y \ . \end{aligned} \tag{6.7}$$

$\tilde{\mathbf{b}}_x$ and $\tilde{\mathbf{b}}_y$ are the body forces, $\tilde{\mathbf{u}}_x$ and $\tilde{\mathbf{u}}_y$ are the displacement matrix expressed in the Laplace domain.

With zero body forces and zero initial condition, Eq. (6.7) reduces to

$$\begin{aligned} &\left(\mathbf{D}_{,x}^2 + \frac{1-\nu}{2} \mathbf{D}_{,y}^2 \right) \tilde{\mathbf{u}}_x + \frac{1+\nu}{2} \mathbf{D}_{,x} \mathbf{D}_{,y} \tilde{\mathbf{u}}_y - \frac{1-\nu^2}{E} \rho s^2 \tilde{\mathbf{u}}_x = \mathbf{0} \ , \\ &\frac{1+\nu}{2} \mathbf{D}_{,x} \mathbf{D}_{,y} \tilde{\mathbf{u}}_x + \left(\mathbf{D}_{,y}^2 + \frac{1-\nu}{2} \mathbf{D}_{,x}^2 \right) \tilde{\mathbf{u}}_y - \frac{1-\nu^2}{E} \rho s^2 \tilde{\mathbf{u}}_y = \mathbf{0} \ . \end{aligned} \qquad P \in \Omega \tag{6.8}$$

Similar to the stationary crack analysis, and in the case of one block there are $2Q = 2(M \times N)$ linear algebraic equations both from Eq. (6.8) and boundary conditions from Eq. (6.4) and (6.5). By solving the set of linear algebraic equations, all nodal values of the displacements can be obtained.

For two blocks and above, the connection conditions on the interface $\Gamma_{\text{int}}^{(I,II)}$ mainly the displacement and the traction between two blocks (I, II) must be satisfied as follows

$$\begin{aligned}&\tilde{\mathbf{u}}_x^I(\mathbf{x},s)=\tilde{\mathbf{u}}_x^{II}(\mathbf{x},s),\ \tilde{\mathbf{u}}_y^I(\mathbf{y},s)=\tilde{\mathbf{u}}_y^{II}(\mathbf{y},s)\ ,\\ &\qquad\qquad\qquad\qquad P\in\Gamma_{\text{int}}^{(I,II)}\\ &\tilde{\mathbf{t}}_x^I(\mathbf{x},s)+\tilde{\mathbf{t}}_x^{II}(\mathbf{x},s)=0,\ \tilde{\mathbf{t}}_y^I(\mathbf{y},s)+\tilde{\mathbf{t}}_y^{II}(\mathbf{y},s)=0\ .\end{aligned}\tag{6.9}$$

In solving the Laplace Transform, the inverse strategy proposed by Durbin [115] was adopted. This is a simple and an accurate technique. Selecting $(\mathrm{K}+1)$ samples in the transformation space $s_k, k=0,1,...,\mathrm{K}$, the transformed variables $\tilde{f}(P,s_k)$ are obtained by the FBM. Then, the time dependent function $f(P,t)$ can be approximated by

$$f(P,t)=\frac{2e^{\sigma t/T_0}}{T_0}\left[-\frac{1}{2}\tilde{f}(P,\frac{\sigma}{T_0})+\sum_{k=0}^{K}\mathrm{Re}\left\{\tilde{f}\left(P,(\sigma+2k\pi i)/T_0\right)e^{2k\pi ti/T_0}\right\}\right],\tag{6.10}$$

where $\tilde{f}(P,s_k)$ denotes the transformed variable in the Laplace domain and the parameter of the Laplace transform $s_k=(\sigma+2k\pi i)/T_0\quad(i=\sqrt{-1})$, in which σ and T_0 are two free normalised parameters. The parameter T_0 depends on the observing period in the time domain. In the follow-up examples, all variables are normalised for the sake of convenience for the analysis. The other optional method is the time-domain method and for this, the finite difference technique should be used [118].

As the Williams solution in the transformed domain is too complicated even for the homogeneous case $(E^{(2)}=E^{(1)}=E)$ to be obtained, the Williams solution for a static case is utilised instead. The conclusion made by Li [167] states that the Williams solution can replace the transformed solutions in the transformed domain with Deng's series [117] for isotropic media if the radius of the core is small enough.

6.4. Numerical Assessment 1

6.4.1 Dynamic Loading of a Finite Block Plate with a Central Crack

Consider a square plate with a central crack of length *2a* loaded by uniformly distributed normal tractions $\sigma_0 H(t)$ on the top as shown in Fig. 6.2, where $H(t)$ is a Heaviside function. Due to the symmetry with respect to *y* axis, only half of the plate is modelled with plane stress assumption, Poisson's ratio $\nu^{(1)} = \nu^{(2)} = 0.3$ and the mass density $\rho^{(1)} = \rho^{(2)} = \rho$.

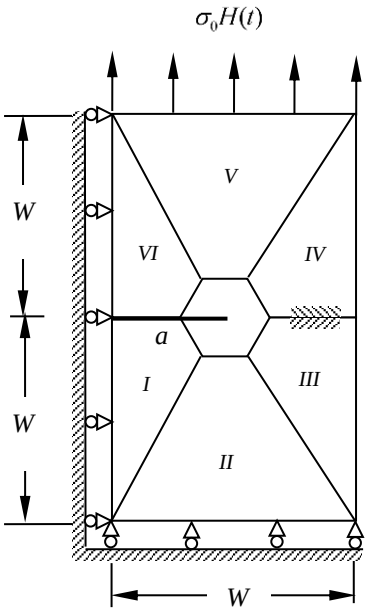

Figure 6.2 Rectangular plate containing central crack under dynamic load.

Firstly, a homogeneous material plate simply supported on the bottom is considered for the first assessment. In the Laplace transform and the inverse procedure, the free parameter K is a variable. Therefore, an optimum value for K must be determined in the early stages of this study. The free parameter K is tested using the following values, K = 10, 15, 20 and 25. Other parameters in Eq. (6.10) are defined as;

$\sigma = 5$ and $T_0 / t_0 = 20$, where $t_0 = W / c_0$ and velocity $c_0 = \sqrt{E / \rho}$. The plate is divided into six blocks with a singular core size $r_0 / W = 0.2$ and the number of collocation point density $M = 8$.

Fig. 6.3 to 6.8 shows the variations of the normalised mode I and II stress intensity factor and the normalised T-stress plotted against the normalised time $c_0 t / W$. The impact of the various values of K on the calculated K_I, K_{II} and T-stress as determined by the FBM method are compared. The FBM dynamic results and the numerical results by the FEM method (ABAQUS) are presented in the same figures for comparison.

Due to the unavailability of an exact analytical solution of a cracked plate under dynamic loads, it is within reason to use an established numerical method to validate the FBM dynamic analysis. There are many commercial packages available for numerical analysis. The most popular of these is the commercial software ABAQUS which has an already verifiable FEM numerical codes. Therefore, it is rational to repeat the dynamic analysis with ABAQUS in order to validate the FBM dynamic analysis. For this purpose, a homogeneous plate is first analysed to establish the accuracy of the FBM and also, several parameters were varied in order to optimise the FBM method for dynamic analysis. Further down in this chapter, the true capabilities of the FBM method is tested by performing several analyses on interface cracks between bi-materials.

Additionally, successive numerical assessments reported in this chapter will show that the FBM method can achieve the same level of accuracy as ABAQUS but using minimum computational effort. As explained in the FBM dynamic model, it can be observed that less work is required in setting-up the dynamic model for analysis.

Contrary to the FBM modelling process, the FEM model for the dynamic analysis proved to be difficult and challenging as it was observed. The FBM analysis requires several blocks, 6 in total. Meanwhile, ABAQUS requires a high mesh density in order to achieve a mesh convergence. The mesh convergence study is reported in Appendix C. An attempt to localised the mesh density at the crack tip was very difficult to achieve. A mesh partitioning was applied to the whole model and a transitional mesh was applied as we move from the fine mesh region to the coarse mesh region. This

process proved to be time consuming when trying to achieve a structured mesh. Therefore, the only outcome was to increase the global mesh density in a structured form. This then resulted in a converged mesh suitable for the dynamic analysis.

Details of the FEM model (ABAQUS) as used in this study is explained below:

Details of the ABAQUS Dynamic Analysis

In this chapter, the finite block dynamic analysis was verified by performing the same dynamic analysis using ABAQUS. In ABAQUS the user is presented with two types of dynamic analysis. These are the implicit and the explicit method. The explicit method in ABAQUS determines the values of dynamic quantities at $t+\Delta t$, and these values are based entirely on the availability of the dynamic quantities at time *t*. However, the implicit dynamic analysis is performed by direct time integration using the central difference operator.

As reported in ABAQUS, the explicit method is conditionally stable and the limits of the stability is based on the duration for an elastic wave to cross the smallest element dimension in the model [133]. This might lead to an early termination of the analysis by ABAQUS if the analysis does not converge for a given time interval. The implicit method overcomes this stability issues by solving for the dynamic quantities at $t+\Delta t$.

The implicit scheme in ABAQUS uses an operator defined by Hilber and Huges [168], and the backwards Euler operator for the time integration. Effectively the Huges operator is a generalised form of the Newmark operator with a capability to control the numerical damping [133].

Some level of numerical damping is required since a change in the time step induces some level of noise into the solution. By introducing some numerical damping into the analysis removes the high-frequency noise from the solution.

In the ABAQUS implicit dynamic analysis, no material damping was necessarily required or specified. By using the ABAQUS default settings where the Hilber-Hughes Operator Parameter $\alpha = -0.05$ is recommended, the remaining damping parameters are adjusted accordingly during the analysis.

Based on the explanation outlining the differences between the explicit and the implicit dynamic methods, the implicit dynamic method was employed in this study. Using the parameters defined below, several analyses for an interface crack between a bi-material as described per FBM dynamic analysis was conducted. The dynamic stress intensity factors and the T-stress as determined by the implicit dynamic method is plotted on the same graph alongside the results attained by the FBM.

ABAQUS Implicit Dynamic Analysis Parameters

- Analysis performed using ABAQUS version 6.9-2.
- Type of analysis: Fixed Time Increments
- Time Increment = 0.01
- Time Period = 16.0
- Material density, elastic modulus and the Poisson's ratio is the same as defined for the model used in the FBM dynamic analysis.
- Hilber-Hughes Operator Parameter $\alpha = -0.05$

To ensure that the results produced by ABAQUS is accurate, a mesh convergence study was conducted on the FEM model dedicated for the dynamic analysis. Detailed explanation of the mesh convergence study is reported in Appendix C of this thesis. From the convergence study, the analysis began to converge when a total of 800 elements was applied to the FEM model. Furthermore, since it is recommended by ABAQUS to use a high mesh density when performing a dynamic analysis via the implicit method, it is within reason to opt for a mesh with 8978 elements. This will ensure the FEM model converges during the analysis. As it was the case, all the ABAQUS implicit dynamic analysis was run successfully without any premature terminations.

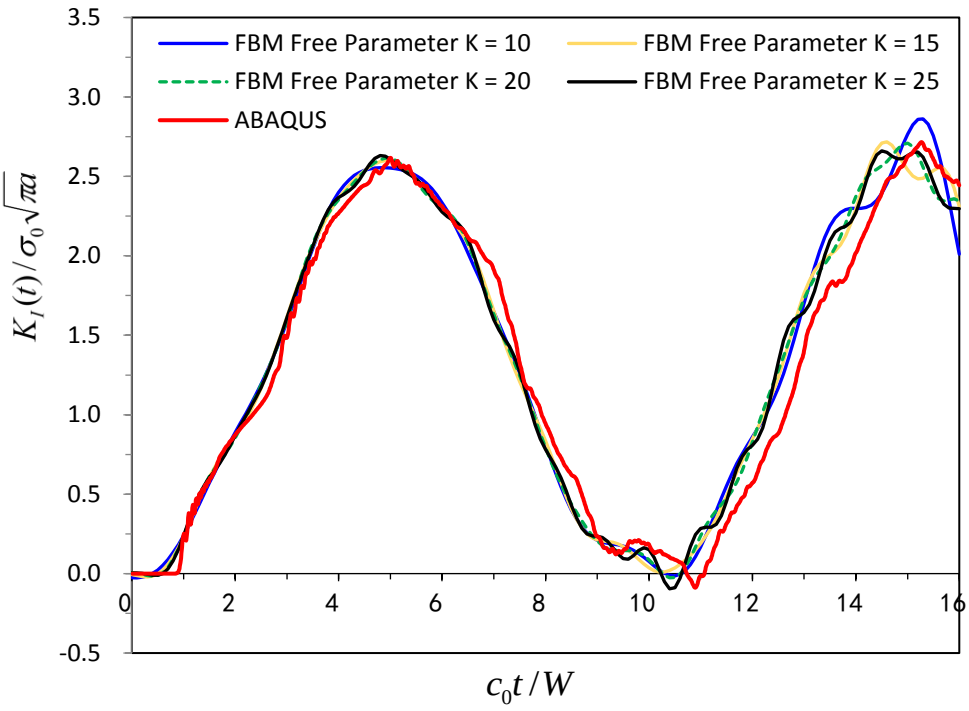

Figure 6.3 Normalised stress intensity factor $K_I(t)/\sigma_0\sqrt{\pi a}$ versus the normalised time $c_0 t/W$. The graph shown here compares the effects of the free parameter K on the results.

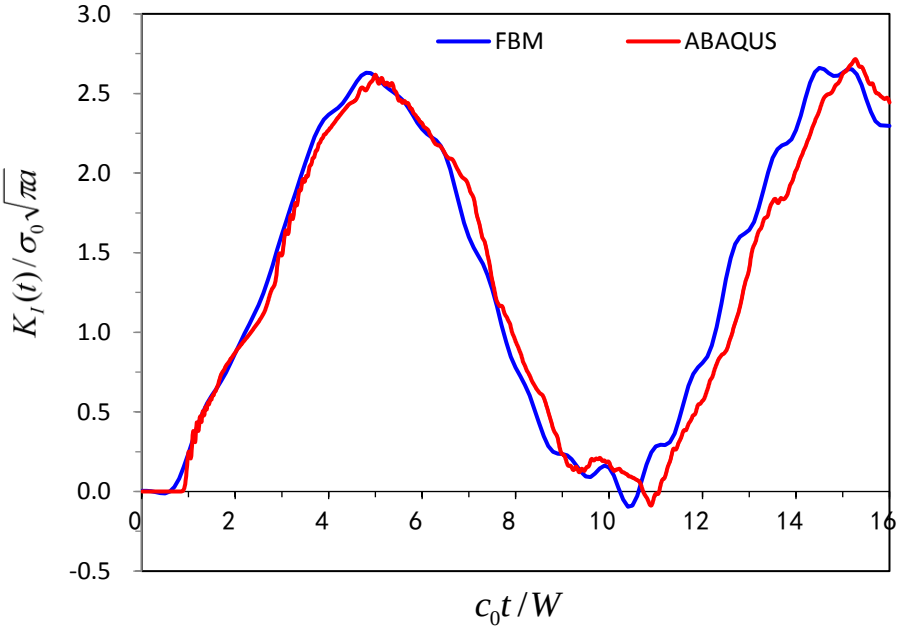

Figure 6.4 Normalised stress intensity factor $K_I(t)/\sigma_0\sqrt{\pi a}$ versus the normalised time $c_0 t/W$. The graph shown here has the results for free parameter K = 10, 15 and 20 omitted.

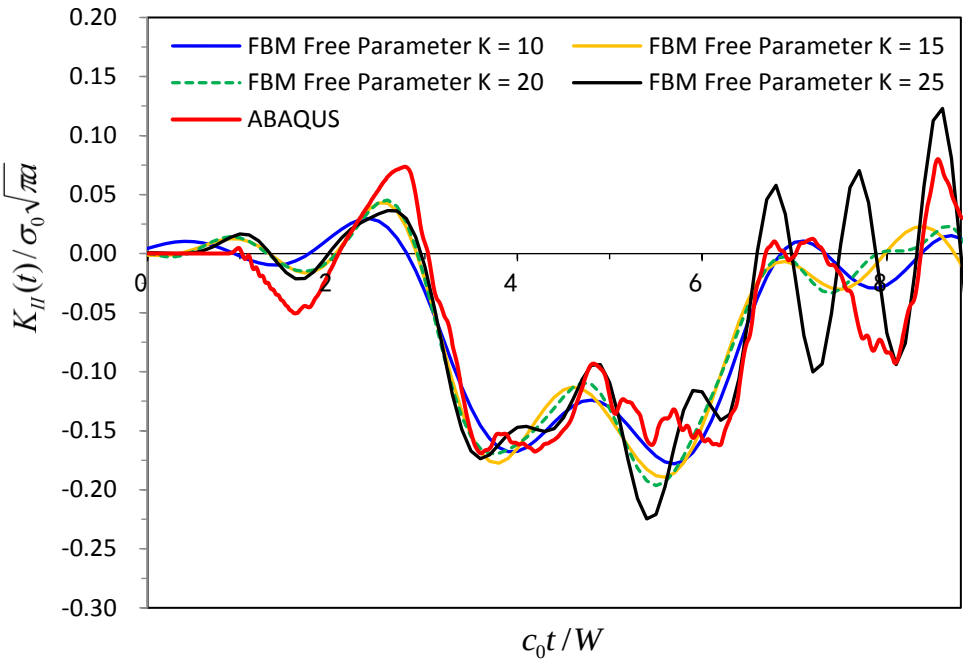

Figure 6.5 Normalised stress intensity factor $K_{II}(t)/\sigma_0\sqrt{\pi a}$ versus the normalised time $c_0 t/W$. The graph shown here compares the effects of the free parameter K on the results.

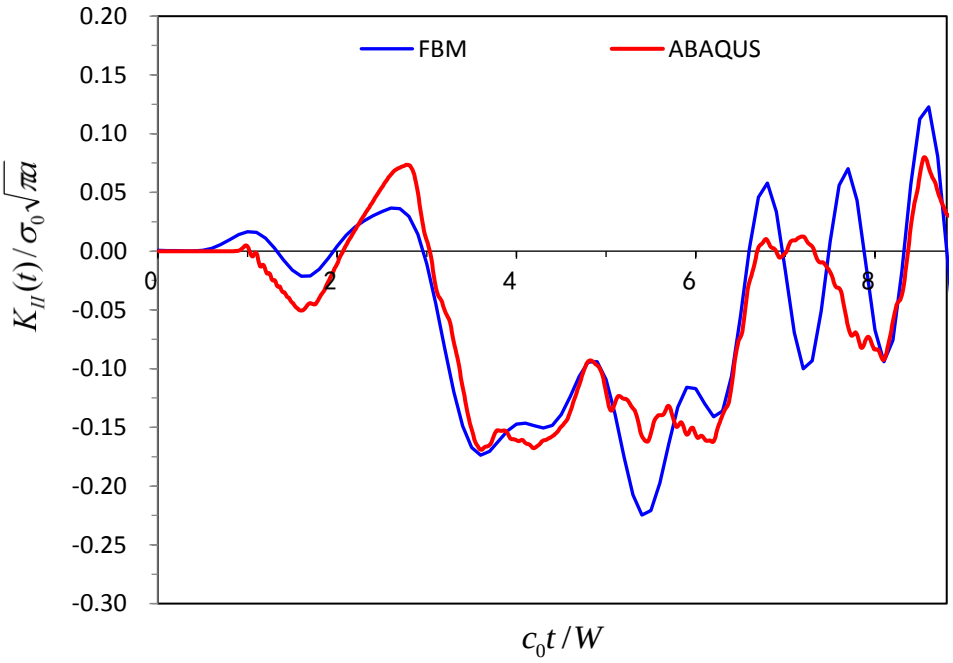

Figure 6.6 Normalised stress intensity factor $K_{II}(t)/\sigma_0\sqrt{\pi a}$ versus the normalised time $c_0 t/W$. The graph shown here has the results for free parameter K = 10, 15 and 20 omitted.

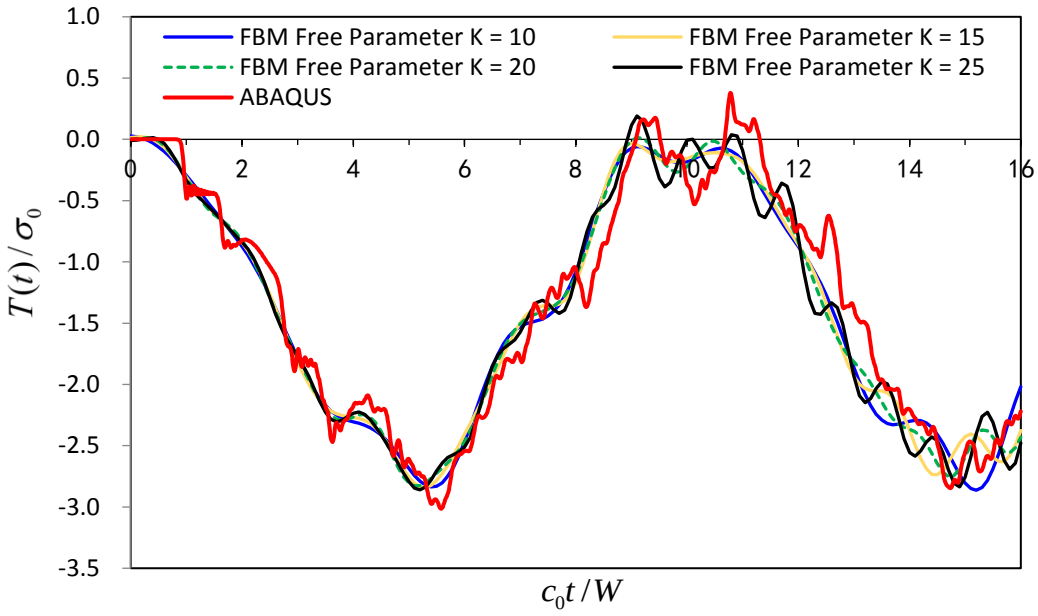

Figure 6.7 Normalised T-stress $T(t)/\sigma_0$ versus the normalised time $c_0 t/W$. The graph shown here compares the effects of the free parameter K on the results.

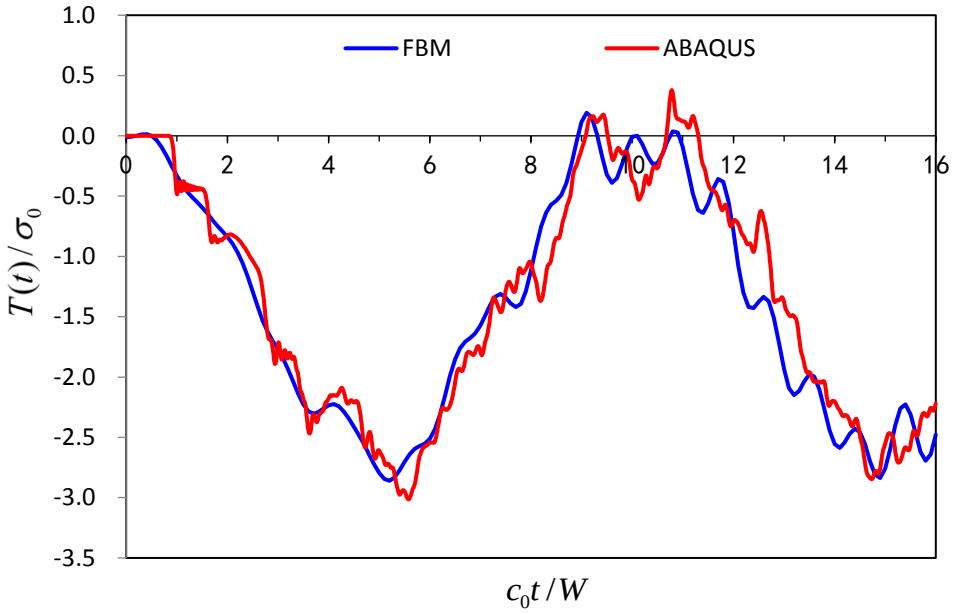

Figure 6.8 Normalised T-stress $T(t)/\sigma_0$ versus the normalised time $c_0 t/W$.The graph shown here has the results for free parameter K = 10, 15 and 20 omitted.

Initial analysis of a homogeneous plate as calculated by the finite block method is shown in Fig. 6.3 through 6.8. The FBM plotted results of the dynamic stress intensity factors $K_I(t)$ and $K_{II}(t)$ against the FEM (ABAQUS) equivalent in Fig. 6.3 to 6.6 shows that the achieved results are in phase with the ABAQUS analysis. For a moderate level of collocation point density M = 8, the result shows the finite block method can produce very good results when compared with ABAQUS where a large number of elements is utilised in the analysis.

For an isotropic analysis, the finite block method is capable of calculating the dynamic stress intensity factor for mode II crack easily. Owing to the small values of the $K_{II}(t)$ stresses, a singular core size of $r_0/W = 0.2$ and a collocation point density of $M = 8$ was adequate enough to produce very good result. When it comes to the dynamic T-stress, Fig. 6.7 and 6.8 exhibits no signs of instability and the wave profile is almost a perfect match against the FEM (ABAQUS) results.

In this study, the optimum value for the free parameter K is determined to be 25. After varying the free parameter K from 10 to 25, it is clear from Fig 6.3, 6.5 and 6.7, the impact of the free parameter on the SIF and the T-stress is minimum. Therefore, it is acceptable to use K = 25 for successive analysis.

6.5. Numerical Assessment 2

6.5.1 Convergence Study: number of nodes *M*

In order to observe the convergence of the finite block method under dynamic loading, different densities of collocation points are considered. A similar two-dimensional plate with a centre crack, six blocks and a singular core (Fig. 6.2) as described in Numerical Assessment 1 is utilised in this study.

For simplicity, a homogeneous plate and a singular core size $r_0/W = 0.2$ is maintained for the different number of collocation points. The corresponding dynamic stress intensity factors for the different node numbers M = 7, 8 and 9 are shown in Fig. 6.9 through 6.13.

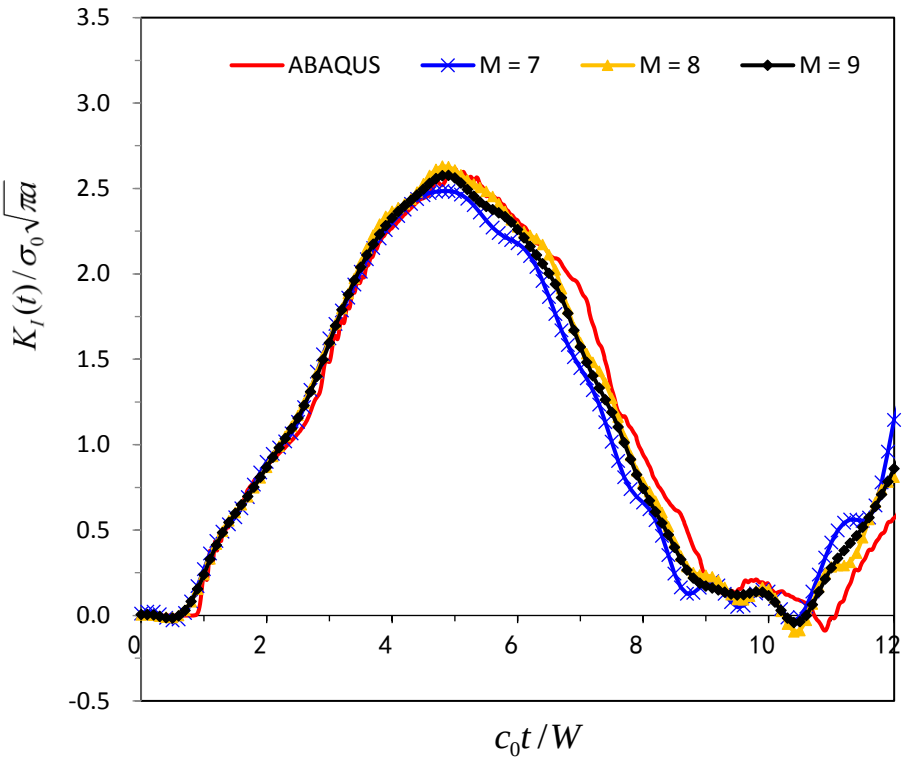

Figure 6.9 Normalised stress intensity factor $K_I(t)/\sigma_0\sqrt{\pi a}$ for the different collocation point densities versus the normalised time $c_0 t/W$.

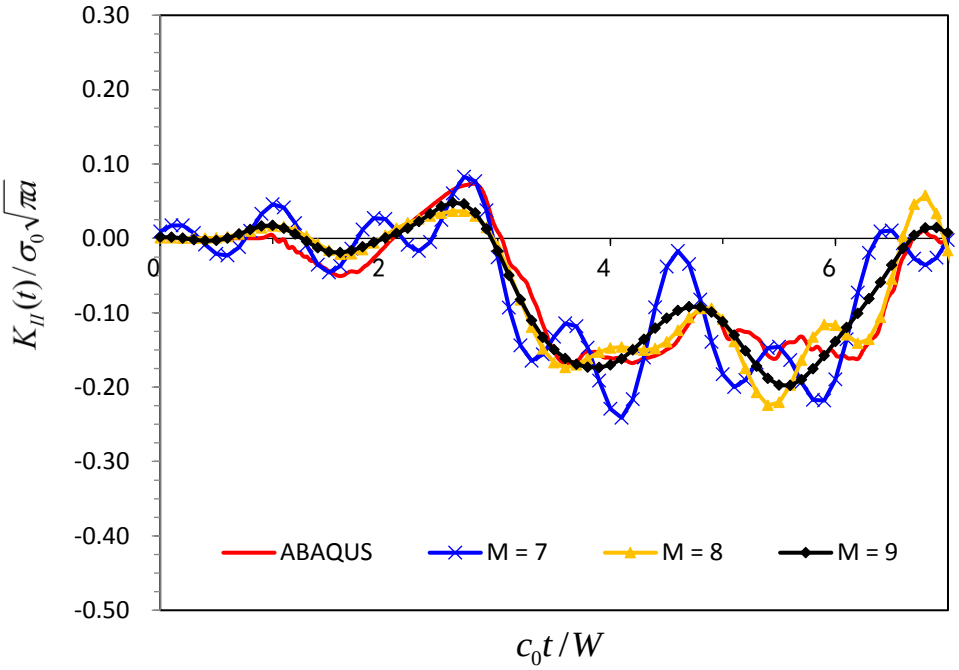

Figure 6.10 Normalised stress intensity factor $K_{II}(t)/\sigma_0\sqrt{\pi a}$ for the different collocation point densities versus the normalised time $c_0 t/W$.

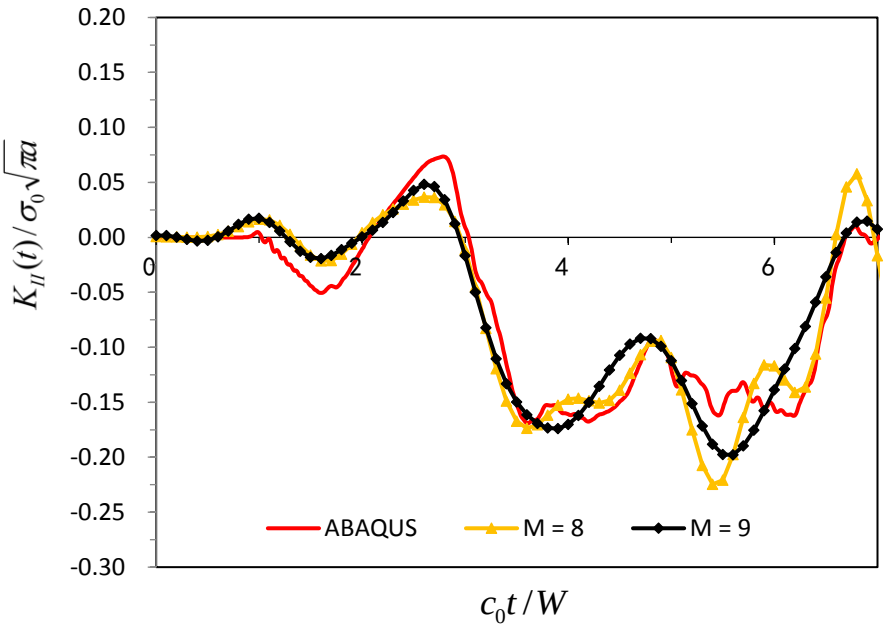

Figure 6.11 Normalised stress intensity factor $K_{II}(t)/\sigma_0\sqrt{\pi a}$ for the different collocation point densities versus the normalised time $c_0 t/W$. $M=7$ omitted from the graph.

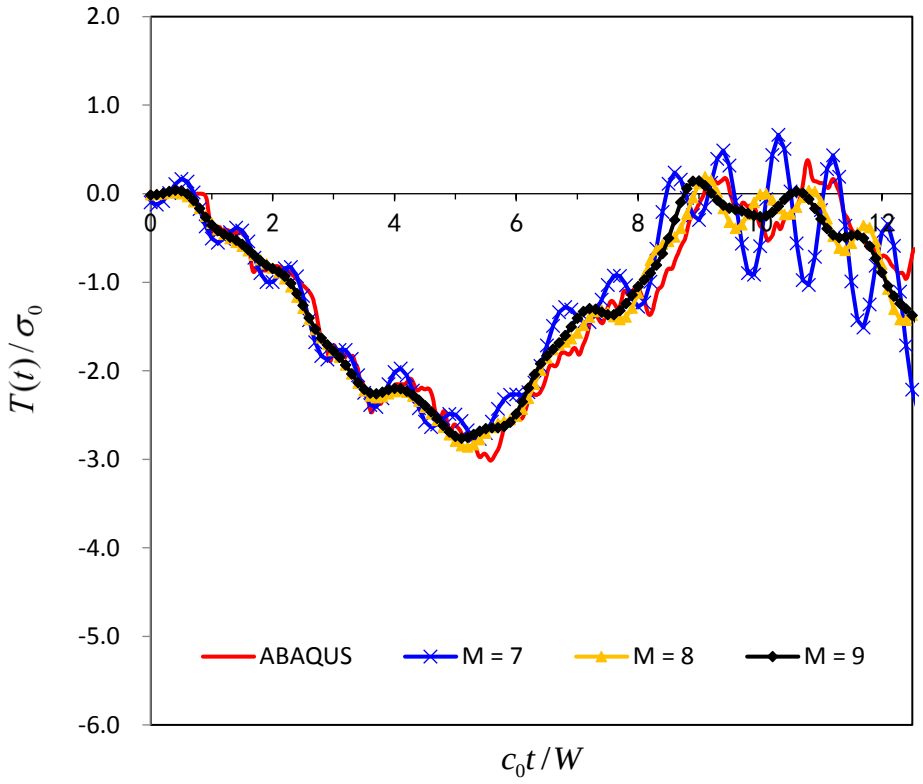

Figure 6.12 Normalised T-stress $T(t)/\sigma_0$ for the different collocation point densities versus the normalised time $c_0 t/W$.

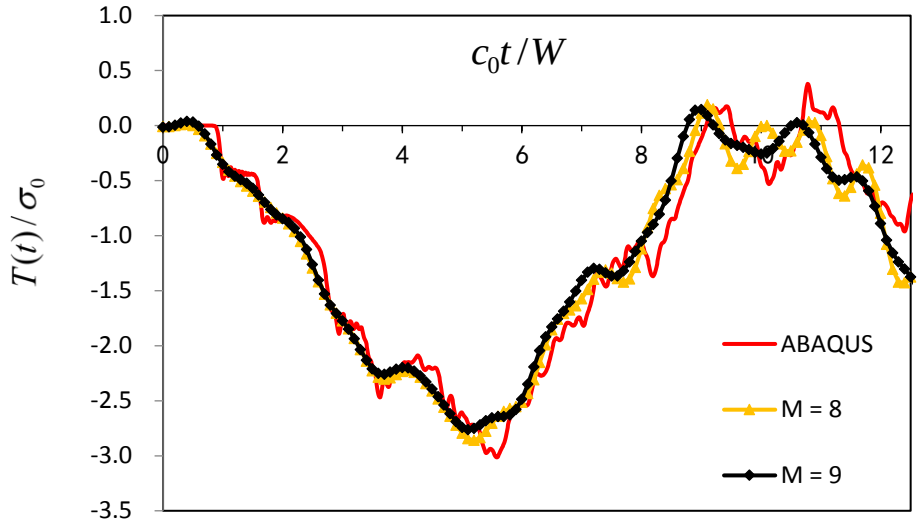

Figure 6.13 Normalised T-stress $T(t)/\sigma_0$ for the different collocation point densities versus the normalised time $c_0 t/W$. $M = 7$ omitted from the graph.

From Fig. 6.9, the normalised dynamic stress intensity factor for mode I in a homogeneous plate gives very good result when compared with the FEM (ABAQUS) analysis. This is true for all collocation point densities M = 7, 8 and 9. However, the same cannot be said for the mode II dynamic stress intensity factor. Due to the small magnitude of the $K_{II}(t)$ value at the crack tip, it is observed that an increase in the number of collocation points at the crack tip is necessary.

As can be seen from Fig. 6.10 the dynamic stress intensity factor is directly influenced by the number of nodes used in the analysis. From Fig. 6.10 we can see that when M = 7, there is a high level of resonance or fluctuations of the dynamic stress intensity factor for $K_{II}(t)$. By omitting M = 7 from the plotted result, Fig. 6.11 shows a much stable result for collocation point densities M = 8 and M = 9.

In Fig. 6.10, the instability of the $K_{II}(t)$ value is noted to be along all-time variables for M = 7. The same cannot be said for the dynamic T-stress values shown in Fig. 6.12. The dynamic T-stress values shows high resonance regions where the calculated magnitude of the T-stress is very small or close to zero. By increasing the collocation point densities to M = 8 and M = 9, a stable result is produced by the finite block method. Fig. 6.13 shows that the dynamic T-stress as calculated by the finite

block method is in good agreement with FEM (ABAQUS) results when using collocation point densities M = 8 and M = 9.

6.6. Numerical Assessment 3

6.6.1 Convergence Study: singular core

The convergence study continues from Numerical Assessment 2. In the finite block method dynamic analysis, the effect of the singular core size is observed for the different ratios of r_0/W. In this assessment, r_0/W is observed at $r_0/W = 0.2, 0.25$ and 0.3. For simplicity, the homogeneous plate from Fig. 6.2 and a collocation point density $M = 8$ is considered.

The dynamic stress intensity factor and the T-stress are shown in Fig. 6.14 to 6.16 for different sizes of the singular core centred at the crack tip.

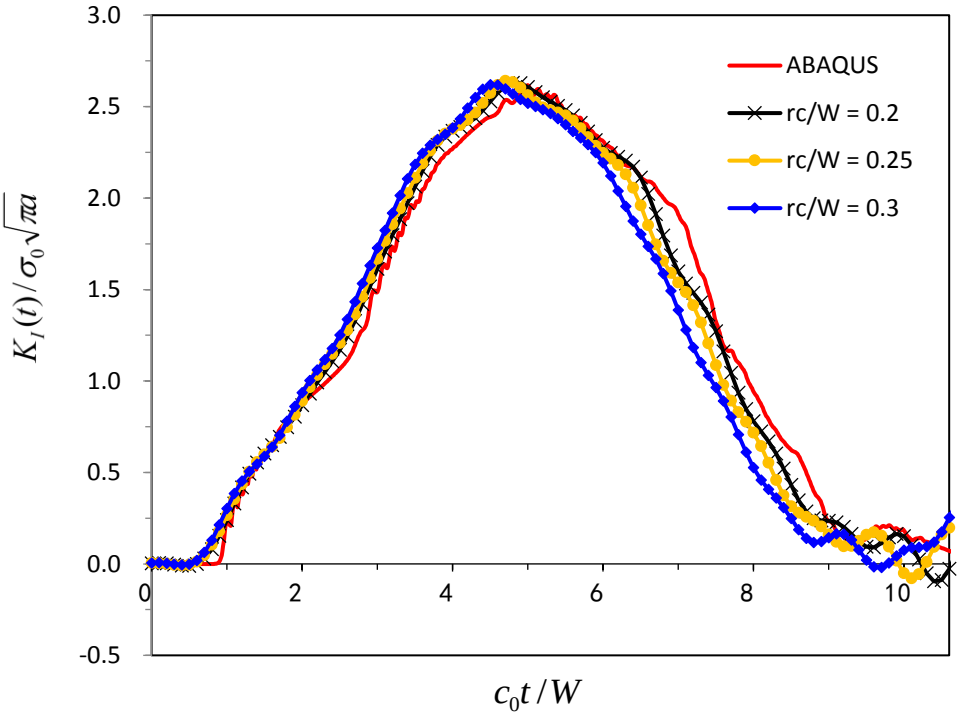

Figure 6.14 Normalised stress intensity factor $K_I(t)/\sigma_0\sqrt{\pi a}$ for the different singular core size versus the normalised time $c_0 t/W$.

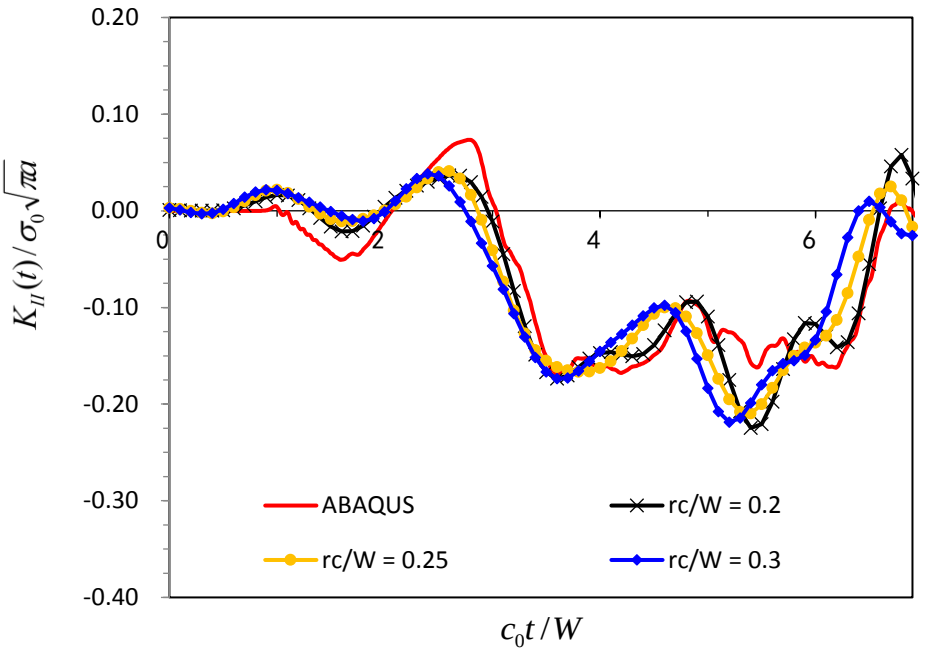

Figure 6.15 Normalised stress intensity factor $K_{II}(t)/\sigma_0\sqrt{\pi a}$ for the different singular core size versus the normalised time $c_0 t/W$.

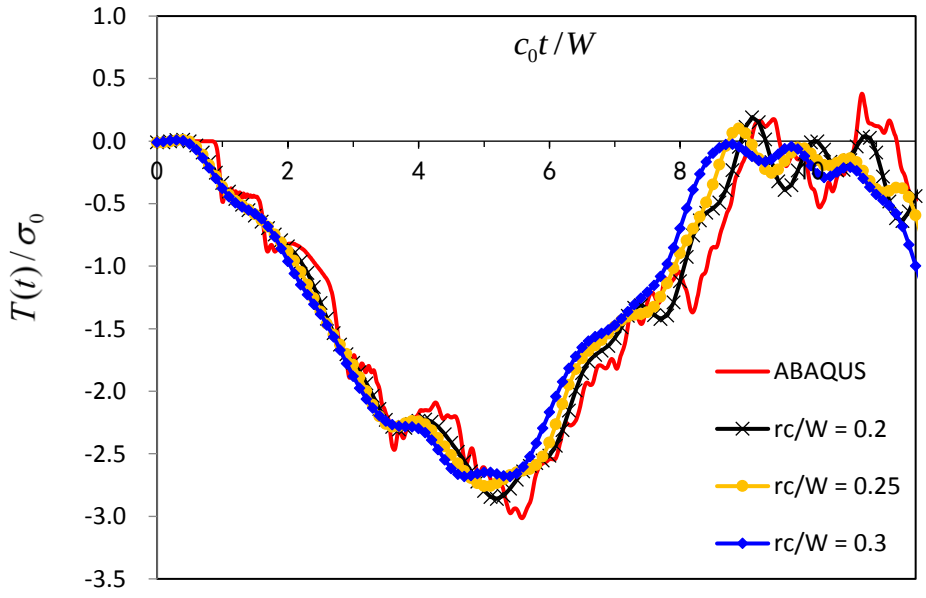

Figure 6.16 Normalised T-stress $T(t)/\sigma_0$ for the different singular core size versus the normalised time $c_0 t/W$.

Based on the observations from Numerical Assessment 1 and 2, it was reasonable to evaluate the influence of the singular core on the dynamic stress intensity factor values and the dynamic T-stress values. Using a collocation point density M = 8, Fig. 6.14 shows that the core size has little influence on the calculated $K_I(t)$ values by the finite block method. However, in Fig. 6.15 the calculated $K_{II}(t)$ values by the finite block method shows that by reducing the core size from $r_0/W = 0.3$ to $r_0/W = 0.2$, the relative error between the FEM (ABAQUS) results and the finite block results is significantly reduced and the $K_{II}(t)$ values were brought closer together.

Hence, using a smaller core size will produce accurate results by the finite block method even at a moderate level collocation point density of M = 8. A similar pattern is seen from Fig. 6.16 where the dynamic T-stress value $T(t)$ shows no substantial changes from the normalised time $c_0 t/W = 0$ to $c_0 t/W = 9$. Beyond normalised time $c_0 t/W = 9$, the $T(t)$ values as calculated by the finite block method are still closer to the FEM (ABAQUS) results.

6.7. Numerical Assessment 4

6.7.1 Interface Crack

In this assessment of the finite block method, a centre interface crack between a bi-material plate and under the same loading condition as in Numerical Assessment 1 is considered. All parameters are the same except the Young's modulus $E^{(1)} = E$, $E^{(2)} = 2E$ for the first bi-material combination and $E^{(1)} = E$ and $E^{(2)} = 3E$ for the second bi-material combination. The ratio for the singular core size $r_0/W = 0.2$ is maintained for the different bi-material combinations and the number of nodes $M = 8$. The time dependent normalised stress intensity factors $K_I(t)/\sigma_0\sqrt{\pi a}$, $K_{II}(t)/\sigma_0\sqrt{\pi a}$ and the T-stress $T(t)/\sigma_0$ are shown in Fig. 6.17 to 6.22 respectively.

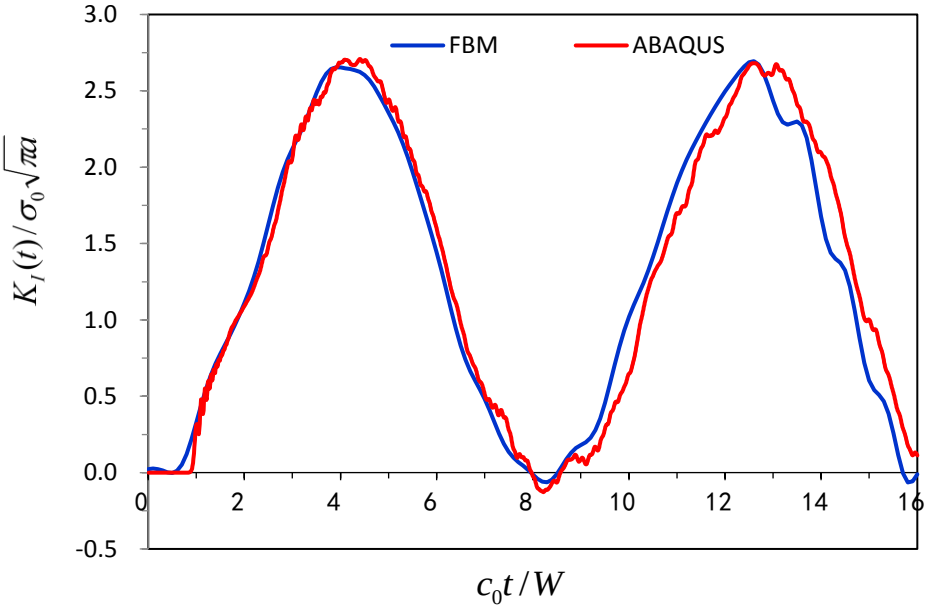

Figure 6.17 Normalised stress intensity factor $K_I(t)/\sigma_0\sqrt{\pi a}$ versus the normalised time $c_0 t/W$. Young's modulus $E^{(1)} = E$, $E^{(2)} = 2E$.

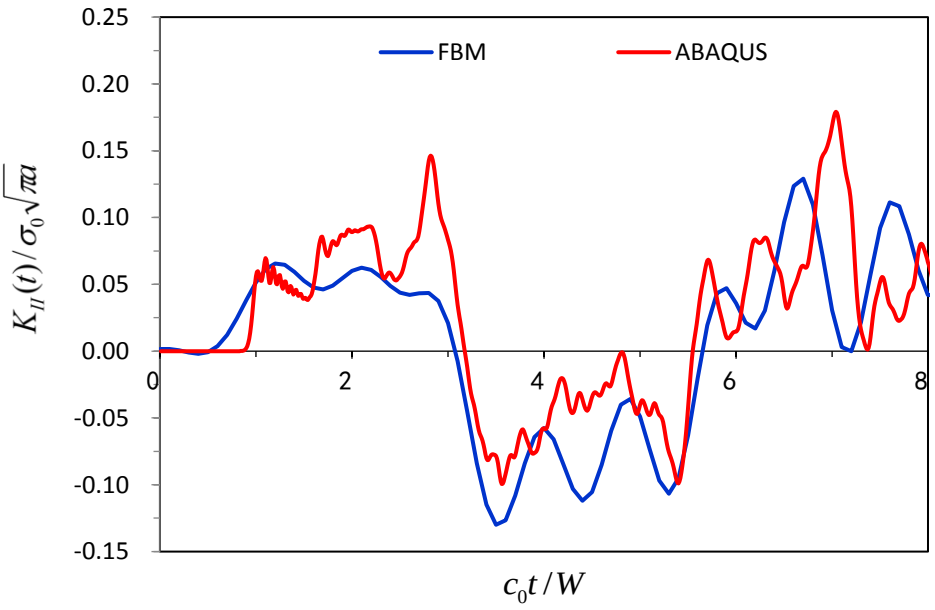

Figure 6.18 Normalised stress intensity factor $K_{II}(t)/\sigma_0\sqrt{\pi a}$ versus the normalised time $c_0 t/W$. Young's modulus $E^{(1)} = E$, $E^{(2)} = 2E$.

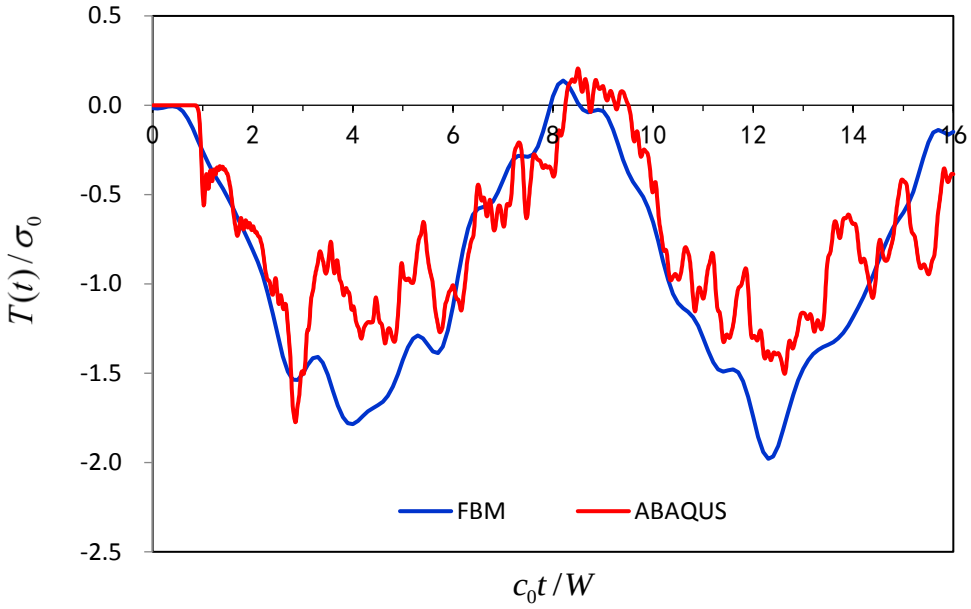

Figure 6.19 Normalised T-stress $T(t)/\sigma_0$ versus the normalised time $c_0 t/W$. Young's modulus $E^{(1)} = E$, $E^{(2)} = 2E$.

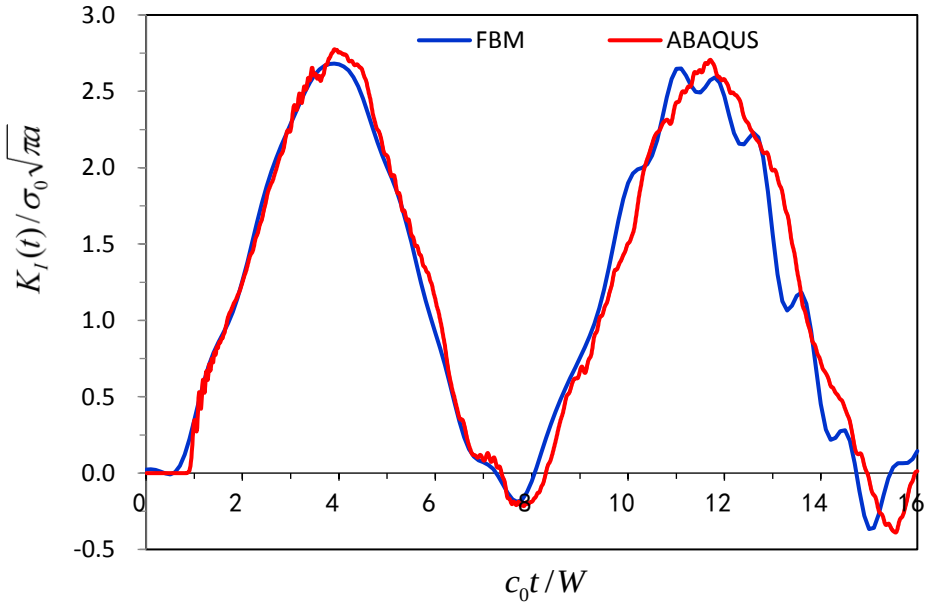

Figure 6.20 Normalised stress intensity factor $K_I(t)/\sigma_0\sqrt{\pi a}$ versus the normalised time $c_0 t/W$. Young's modulus $E^{(1)} = E$, $E^{(2)} = 3E$.

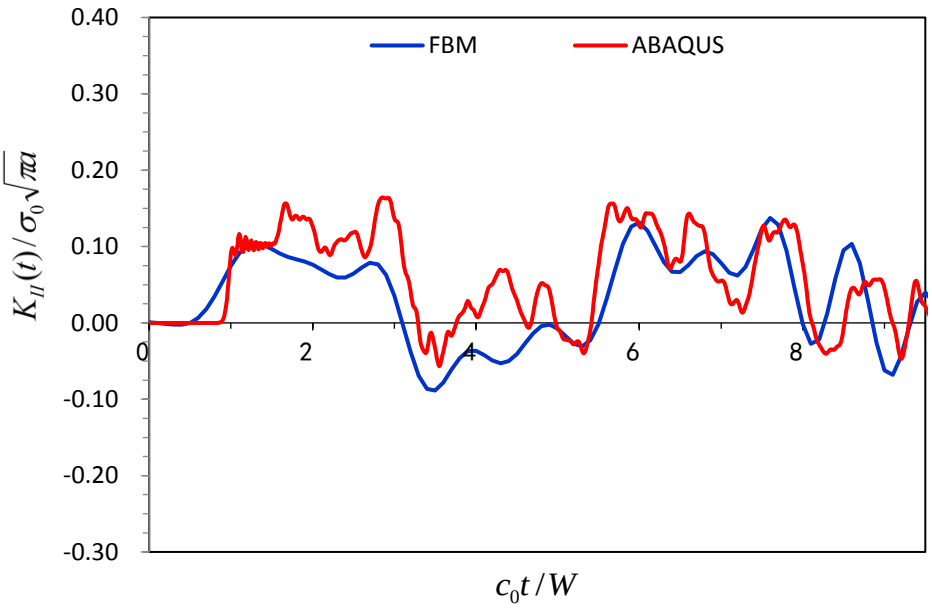

Figure 6.21 Normalised stress intensity factor $K_{II}(t)/\sigma_0\sqrt{\pi a}$ versus the normalised time $c_0 t/W$. Young's modulus $E^{(1)} = E$, $E^{(2)} = 3E$.

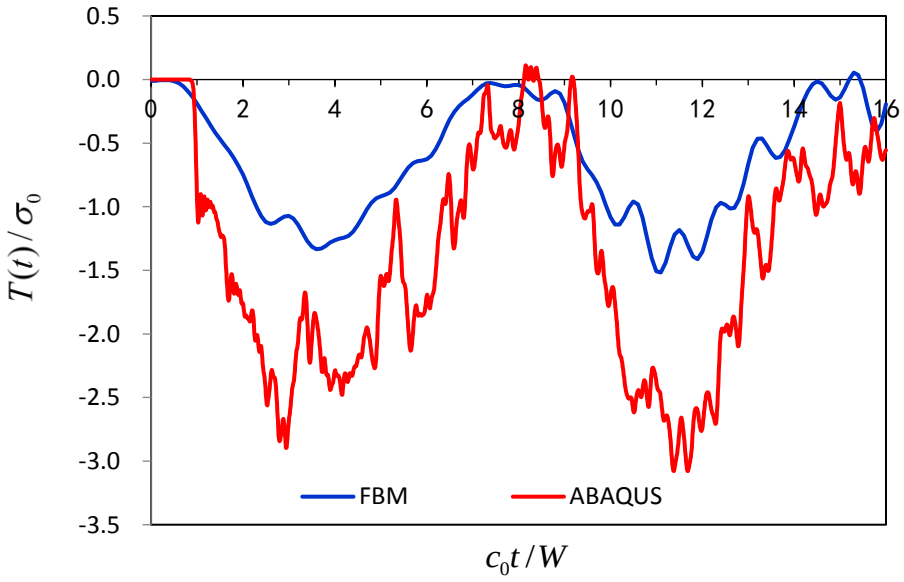

Figure 6.22 Normalised T-stress $T(t)/\sigma_0$ versus the normalised time $c_0 t/W$. Young's modulus $E^{(1)} = E$, $E^{(2)} = 3E$.

The previously acquired results from Numerical Assessments 1 through 3 has shown that in order to determine the dynamic stress intensity factors and the dynamic T-stress accurately for a bi-material, the optimum values of the following parameters were chosen; the collocation point density M = 8, the free parameter K = 25 and the core size $r_0/W = 0.2$.

In Fig. 6.17 and 6.20, the normalised dynamic stress intensity factor values for mode I is presented for $E^{(1)}/E^{(2)} = 2$ and $E^{(1)}/E^{(2)} = 3$. The normalised $K_I(t)$ values as calculated by the finite block method shows good agreement when compared with the FEM (ABAQUS) results after observing a complete wave cycle.

As noted in the previous numerical assessment, the normalised dynamic stress intensity factor values of $K_{II}(t)$ can become unstable. According to the results presented in Fig. 6.18 and Fig. 6.21, the $K_{II}(t)$ values for an interface crack as determined by the finite block method gives good result when compared against the FEM (ABAQUS) result.

6.8. Summary

In this chapter, the elastodynamic formulation for assessing interface cracks by the finite block method is developed. The Williams series interpolation for a static case was employed in constructing the finite block method. The developed elastodynamic problem as expressed in the Laplace transform domain is approximated by the Durbin's inversion method. Also, the singular core as explained in Chapter 4 was utilised to improve the calculation of the dynamic stress intensity factor and the dynamic T-stress.

In this study, several numerical assessments were carried out for a 2D plate with a centre crack. A homogeneous plate with a centre crack and subjected to dynamic loads was used in the convergence study. This was followed by the dynamic assessment of interface crack for several bi-material combinations. In all cases, the achieved dynamic stress intensity factor and the T-stress were directly compared against FEM (ABAQUS) analysis.

CHAPTER 7

The Assessment of FBM Method Against Other Numerical Techniques

7.1. Introduction

Extensive reviews of interface crack by the finite element method has revealed several techniques for determining the complex stress intensity factor between bi-materials. The complex stress intensity factor of an interface crack can be extracted by the displacement approach or the interaction integral approach [86, 106, 107]. Another common technique includes using the finite element method to obtain the displacement field around the crack tip. Using the displacement along with formulations in linear elastic fracture mechanics, the SIF of the crack can be extrapolated after discarding estimates within the vicinity of the crack tip [37]. In most cases this technique is applied to a cracked homogeneous material. However, applying this technique to an interface crack between bi-material in order to ascertain the complex SIF can be challenging.

Also, the study of bi-materials which is an important part of this research is not limited to the combination of two plates with different material properties, it can also be extended to composite materials. Thus, the study of debonding between a fibre and a

matrix is warranted. Using the FEM method, Aslantas [80] analysed the interface crack of a matrix with a single fibre. The cracked interface is assumed to take the shape of a ring. The complex stress intensity factors are then determined using the displacement correlation technique. In this particular piece of work, the near crack tip nodal displacement, used in the displacement correlation technique was determined by the FEM method.

On the other hand, there are fracture analysis methods and formulations that struggles to calculate accurately the SIF of an interface crack by utilizing just the crack tip nodal displacements and stresses produced by an FEM analysis. For example, the fracture analysis results produced by the near crack tip nodal stress is shown to be unstable for an interface crack [137]. This is due to the oscillatory effect of the stresses near the crack tip.

Additionally, a strong deformation of the elements along the crack face can be observed from an FEM interface crack analysis. Hence, the nodes along the crack face will also see a strong deformation near the crack tip. This means, a fine mesh would be required around the crack tip in order to reduce the effects of the deformation. Therefore, using the Displacement Correlation Technique for an interface crack assessment can be difficult and computationally costly.

For a bi-material made of two isotropic media, the interaction integral method in conjunction with the finite element method is a common approach in determining the complex SIF. The interaction integral method is based on the *J*-Integral which is widely accepted as a fracture mechanic parameter. The *J*-Integral can be directly related to the stress intensity factor and the energy release rate. Some of the main advantages of the interaction integral method include the provision of numerical efficiency and the high level of accuracy in determining the complex stress intensity factor. The interaction integral method as explained in [107] can also be used for evaluating the T-stress of an interface crack. The interaction integral is based on a conservative integral for two admissible state of an elastic solid, where the two states are defined by an actual and auxiliary state [77, 109, 110].

The success of the interaction integral method has led to an extensive commercial usage in evaluating the stress intensity factor of a cracked elastic media. The commercial FEM software ABAQUS is a good advocate of the interaction integral method. ABAQUS analyses interface cracks using this technique in order to determine the complex stress intensity factor and the T-stress. In addition to the study of bi-materials using the FEM method, Amit and Kim [111] evaluated the stress intensity factor and the T-stress in a functionally graded material using the interaction integral method and the FEM method.

As reported previously in Chapter 4, the finite block method has demonstrated a strong capability in determining the complex stress intensity factor of an interface crack. The FBM method starts the interface crack analysis by approximating the nodal displacements around the crack tip using a singular core. This is then followed by approximating the complex stress intensity factor using the Williams series. Indeed, it can be said that the strength of the FBM is in its ability to approximate the nodal displacement around the crack tip region and then eventually the constants of the Williams series.

This section of the thesis compares the FBM method against other numerical techniques in order to assess the sheer capability for accurately calculating the complex SIF. Previously, the calculated FBM results for the complex SIF was compared against the *J*-Integral technique, which is the fracture formulation used by ABAQUS. This section allows the FBM crack analysis technique, mainly the Williams eigenfunction series to be compared against the stress proportionality method and the displacement correlation technique.

In the interest of balance and credibility of the comparison, enhancements have been made to the DCT method and the proportionality method in order to improve the accuracy of the stress intensity factor. The remainder of this chapter is therefore dedicated to the explanation of the detailed improvements to the DCT method and the proportionality method. The improved results are then compared against the FBM results for a cracked plate.

The chapter is organised in the following manner. The stress intensity factor is approximated using the finite element method and the proportional method. This will lead to the proposed technique called the stress proportionality method and allows for reasonable approximation of the stress intensity factors for various interface cracks and material combinations. This is followed-up by the determination of the complex stress intensity factor for interface crack by making some modifications to the displacement correlation technique.

7.2. Evaluation of Interface Crack by the Finite Element Method

Several techniques for evaluating the interface crack of bi-materials using the FEM method has been reviewed for this chapter. As a result of this review, the need for further FEM techniques to efficiently determine the stress intensity factor for interface crack is always desirable. Hence, the work on the proportionality method in conjunction with the FEM method as reported below.

7.2.1 The Proportionality Method for Interface Crack

Nisitani has been credited with some of the early works on FEM study of cracks of a homogeneous plate [135]. Teranishi [139] and Nisitani [140] determined the stress intensity factor for a mode I crack based on the effectiveness of the crack tip stresses determined by the finite element method. Since the proposed stress method for evaluating a homogeneous crack by Nisitani, the proportionality method has been extended to the study of interface crack. Although the proportionality method is deemed to be simple it is also regarded as a very effective technique in evaluating interface crack by the finite element method.

The use of FEM nodal stresses ahead of the crack tip to determine the stress intensity factor of an interface crack has proven to be unstable [137]. This is due to the oscillatory effect of the interface crack and this can lead to higher error margins. By contrast, the FEM nodal displacement of the crack opening can produce a far better result when utilised in a COD method to determine the SIF. The COD method can produce a much better result when compared with the stress approach.

Another limiting factor of the proportionality method is the use of the same FEM mesh in the reference problem as well as the given unknown problem. This is quite difficult to achieve unless the same crack tip mesh is carved out from one model and used in another.

The next section describes the principles of the proportionality method. Using the finite element analysis in conjunction with a reference model, the stress intensity factor of a given problem is determined using the proportionality method.

7.2.2 Principles of the Proportionality Method in Homogeneous Materials

The proportionality method is explained by considering a crack in a homogeneous plate. Under normal mode I loading of a homogeneous plate with a crack plane at $\theta = 0$, the stress distribution ahead of the crack tip is given by

$$\sigma_y = \frac{K_I}{\sqrt{2\pi r}} \ , \tag{7.1}$$

where σ_y is the crack tip stress acting in the *y*-direction. For a given radius from the crack tip the function in Eq. (7.1) is said to be constant, therefore, given the expression

$$\frac{\sigma_y}{K_I} = constant \ . \tag{7.2}$$

Based on the fact established in Eq. (7.2), a stress intensity factor expression can be made between two different crack problems. If the stress intensity factor for a reference problem *A* is known then by equating Eq. (7.2) for a given unknown problem *B* at the same radius from the crack tip gives

$$\frac{K_I^*}{\sigma_y^*} = \frac{K_I}{\sigma_y} \ . \tag{7.3}$$

In Eq. (7.3), K_I^* is termed the stress intensity factor for the reference problem which is known. The stress intensity factor for the given unknown problem K_I is easily

determined using Eq. (7.3). The reference stress and the stress from the given unknown problem can be deduced from a finite element analysis.

7.2.3 Principles of the Proportionality Method for Interface Crack

The proportionality method cannot be used for evaluating interface crack without some level modification. This is due to the oscillatory effect of the stress component at the crack tip. In general terms, the stress at the crack tip is related to the complex stress intensity factors according to

$$\sigma_y + i\tau_{xy} = \frac{K_I + iK_{II}}{\sqrt{2\pi r}}\left(\frac{r}{2a}\right)^{i\varepsilon}, \tag{7.4}$$

and expressed in terms of K_I and K_{II} gives [136], [137]

$$K_I = \lim_{r\to 0}\sqrt{2\pi r}\sigma_y\left(\cos Q + \frac{\tau_{xy}}{\sigma_y}\sin Q\right), \tag{7.5}$$

$$K_{II} = \lim_{r\to 0}\sqrt{2\pi r}\tau_{xy}\left(\cos Q + \frac{\sigma_y}{\tau_{xy}}\sin Q\right), \tag{7.6}$$

where $Q = \varepsilon \ln\left(\frac{r}{2a}\right)$.

For a constant radius emanating from the crack tip the oscillatory terms are said to be the same for two different crack problems, therefore,

$$\varepsilon = \varepsilon^*, \quad \frac{\tau_{xy}}{\sigma_y} = \frac{\tau_{xy}^*}{\sigma_y^*}. \tag{7.7}$$

In the same way as a homogeneous crack problem, a similar proportionality expression is developed for an interface crack, given as

$$\frac{K_I^*}{\sigma_y^*} = \frac{K_I}{\sigma_y}, \quad \frac{K_{II}^*}{\tau_{xy}^*} = \frac{K_{II}}{\tau_{xy}}. \tag{7.8}$$

As noted, the stress intensity factors with the asterisk superscript represent the reference problem determine by the finite element method.

For an interface crack, a similar stress distribution around the crack tip can be obtained by the finite element method according to the following condition

$$\frac{\tau_{xy,FEM}^{*}}{\sigma_{y,FEM}^{*}} = \frac{\tau_{xy,FEM}}{\sigma_{y,FEM}} \ . \tag{7.9}$$

In this case the stress values $\tau_{xy,FEM}^{*}$, $\sigma_{y,FEM}^{*}$, $\tau_{xy,FEM}$ and $\sigma_{y,FEM}$ are calculated by FEM.

Therefore, the stress intensity factors of a given interface crack problem based on the known stress values is given by

$$K_I = \frac{\sigma_{y,FEM}}{\sigma_{y,FEM}^{*}} K_I^{*} \quad , \tag{7.10}$$

$$K_{II} = \frac{\tau_{xy,FEM}}{\tau_{xy,FEM}^{*}} K_{II}^{*} \ . \tag{7.11}$$

7.2.4 Loading Stress for the Reference Problem

The stress intensity factor for the reference problem based on the model and loading shown in Fig. 7.1 is defined as

$$K_I^{*} + iK_{II}^{*} = (T + iS)\sqrt{\pi a}(1 + 2i\varepsilon) \ . \tag{7.12}$$

In order to determine the values of *T* and *S*, a tensile and shear stress are superimposed on the reference problem. Additionally, the stresses near the interface crack subjected to the loads *T* and *S* are given by

$$\sigma_{y,FEM}^{*} = \sigma_{y,FEM}^{T=1,S=0} * T + \sigma_{y,FEM}^{T=0,S=1} * S \ , \tag{7.13a}$$

$$\tau_{xy,FEM}^{*} = \tau_{xy,FEM}^{T=1,S=0} * T + \tau_{xy,FEM}^{T=0,S=1} * S \ , \tag{7.13b}$$

where $\sigma_{y,FEM}^{T=1,S=0} *$ and $\tau_{y,FEM}^{T=1,S=0} *$ are the stresses for $T = 1$, $S = 0$, $\sigma_{y,FEM}^{T=0,S=1} *$ and $\tau_{y,FEM}^{T=0,S=1} *$ are the stresses for $T = 0$, $S = 1$ respectively.

By setting $T = 1$ and substituting Eq. (7.13) into (7.9) yields

$$S = \frac{\sigma_{y,FEM} \cdot \tau_{xy,FEM}^{T=1,S=0} * - \tau_{xy,FEM}^{T=0,S=1} * \cdot \sigma_{y,FEM}^{T=1,S=0} *}{\tau_{xy,FEM} \cdot \sigma_{y,FEM}^{T=1,S=0} * - \sigma_{y,FEM} \cdot \tau_{xy,FEM}^{T=0,S=1} *} . \tag{7.14}$$

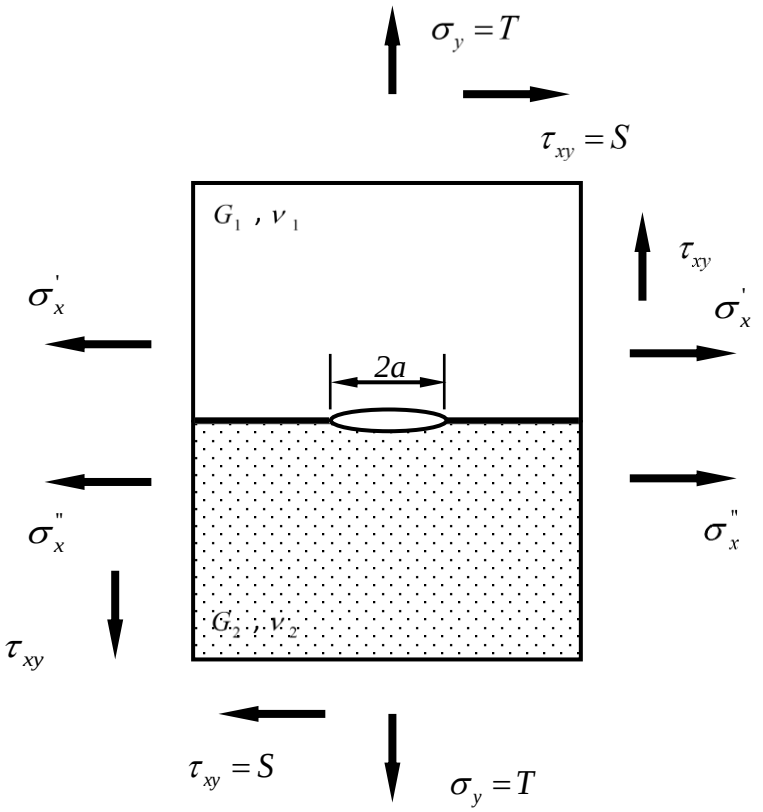

Figure 7.1 The reference problem.

7.2.5 Conditions of the Proportionality Method

The use of the proportionality method requires certain conditions in order to achieve good results. These conditions include;

- The same crack length for both the reference problem and the given unknown problem.
- The oscillatory term of the reference problem and the given unknown problem must be changed to be the same. This is achieved by selecting a nodal stress at the same radius from the crack tip, only then is this condition satisfied.

- The same Finite Element mesh has to be used around the crack tip. The main error in using the proportionality method is said to stem from the differences in crack tip mesh in terms of mesh size and pattern.

7.2.6 Conditions for the Newly Proposed Stress Proportionality Method

The stress proportionality method as presented here utilises the basic principles as explained in the preceding sections. In addition to that, the stress proportionality method is an improvement to some of the challenges outlined in section 7.2.5. This includes the ability to determine the stress intensity factor of a two-dimensional plate without the need to equate the near crack tip mesh. The reference problem of any crack plate can be used to determine the stress intensity factor of an unknown given problem without necessarily having the same crack length.

One of the main challenges in using the proportionality method is down to the issue of reducing the FEM approximation error. Some of the solutions presented include the use of the same mesh for both the reference problem and the given unknown problem. However, this limits the number of problems that can be tackled without encountering some FEM modelling challenges. The stress proportionality method resolves this in the following order;

- For both the reference problem and the unknown given problem a fine mesh is applied near the crack tip region. This way the FEM error is reduced when it comes to the analysis of the stress intensity factor. The use of fine mesh also increases the chance of finding a node with marginally the same radius in both the reference problem and the given unknown problem. As will be shown in the numerical assessments, this method does not require the radius to be equal but requires the crack tip radius differences for both the reference problem and the given unknown problem nodes used in the estimation to be reasonably small in order not to distort the result.
- The determined stress intensity factor values for the given unknown problem is then plotted on a scattered graph against the radius. A correlation line is used to

optimise the results further to give the final stress intensity factor as determined by the equation of a straight line.

The stress proportionality method has only been applied to the investigation of stress intensity factor for a two-dimensional plate without the need to equalise the FEM mesh. In the first instance, a two-dimensional homogeneous plate with a centre crack is examined for different crack lengths. This technique is extended to the study of interface cracks. All achieved results are compared with published results in order to determine the accuracy of this technique.

7.3. Numerical Assessment 1

In the assessment of the proposed method (Stress Proportionality Method), a homogeneous plate with a centre crack is analysed for both the given unknown problem and the reference problem. The SIF is determined for several plate dimensions and crack lengths. In all cases, the appropriate reference problem is stated for clarity of the analysis. Fig. 7.2 shows a typical 2D plate for the given unknown problem and the given reference problem including the dimensions.

Using an FEM program (ABAQUS), the nodal stress ahead of the crack tip is determined. For simplicity, the SIF for the given reference problems are also determined using ABAQUS. Now, the stress proportionality method is applied to determine the SIF. As part of the stress proportionality method, an optimization process is achieved by a scatter plot of the SIF versus the radius, and this is shown in Fig. 7.3 to 7.8.

For the homogeneous plate assessment, several plate geometries are considered. In most cases, the crack length for the given unknown problem is the same as the given reference problem. For cases where the crack length differs significantly (longer or shorter than each other) we only use the equivalent radius from the crack tip for the given problem.

In this assessment, the SIF for all given unknown problems are also determined using the COD method. The achieved results using the stress proportionality method will be compared to the equivalent COD results and reference [161].

The achieved SIF and reported errors for the stress proportionality method, COD method and the reference [161] is outlined in Table 7.1, where K_I is normalised by $K_0 = \sigma_0 \sqrt{\pi a}$.

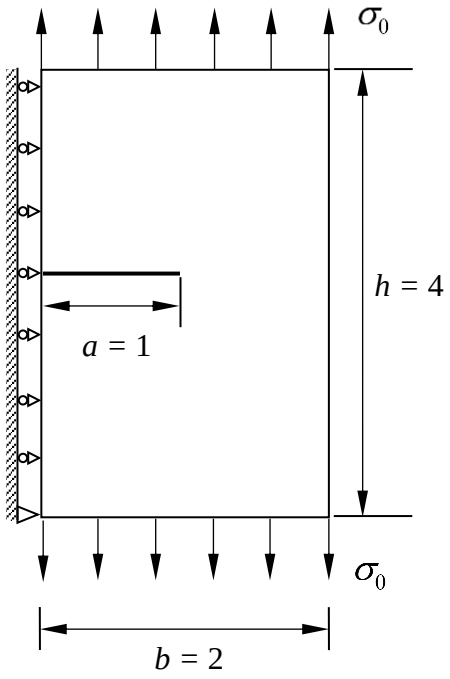

Figure 7.2 2D plate of the given unknown problem with dimensions 4 x 4 and crack length *a*/b = 0.5. Only half of the plate is analysed due to symmetry along the *y* axis.

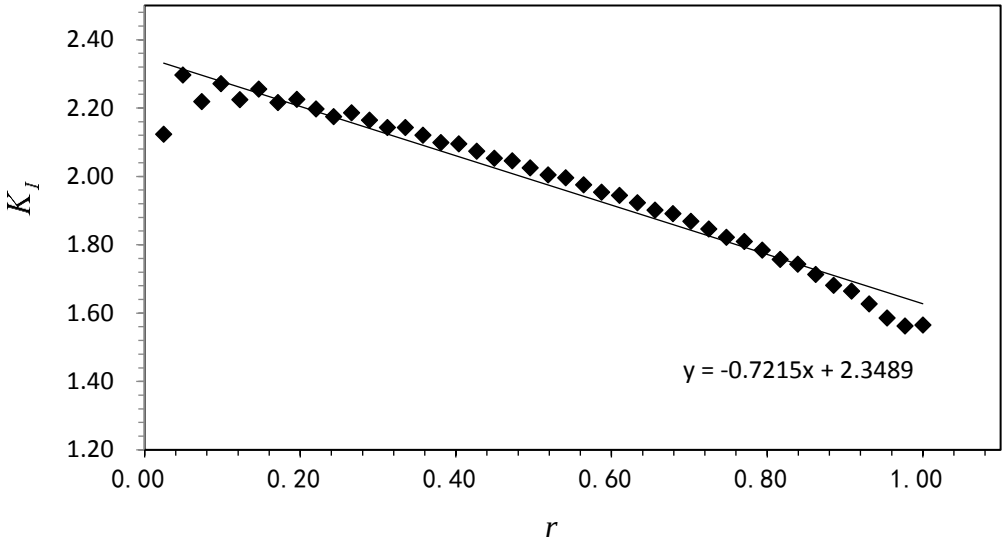

Figure 7.3 The SIFs of the given unknown problem is plotted against the nodal radius ahead of the crack tip. This is for a homogeneous plate of dimension 4 x 4 with a centre crack, a/b = 0.5. Stress Proportionality Method uses a reference problem of plate dimension 4 x 8 and a/b = 0.5.

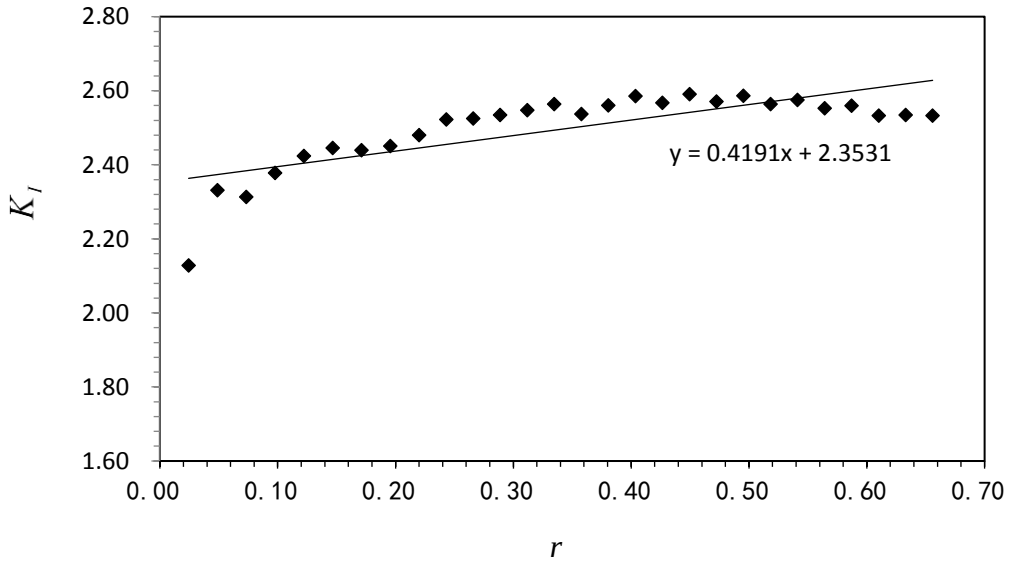

Figure 7.4 The SIFs of the given unknown problem is plotted against the nodal radius ahead of the crack tip. This is for a homogeneous plate of dimension 4 x 4 with a centre crack, a/b = 0.5. Stress Proportionality Method uses a reference problem of plate dimension 20 x 12 and a/b = 0.4.

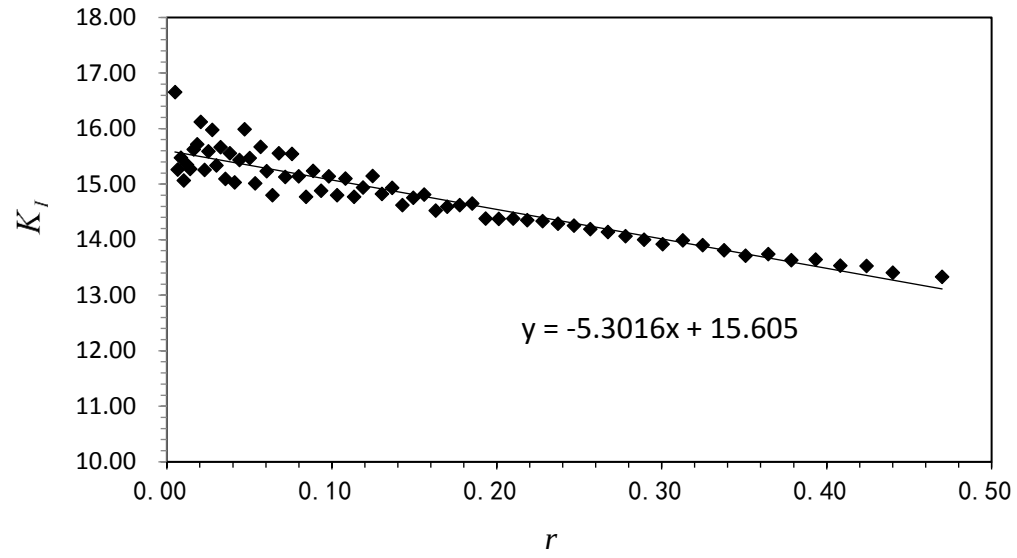

Figure 7.5 The SIF of the given unknown problem is plotted against the nodal radius ahead of the crack tip. This is for a homogeneous plate of dimension 20 x 8 with a centre crack, *a/b* = 0.2. Stress Proportionality Method uses a reference problem of plate dimension 4 x 8 and *a/b* = 0.5.

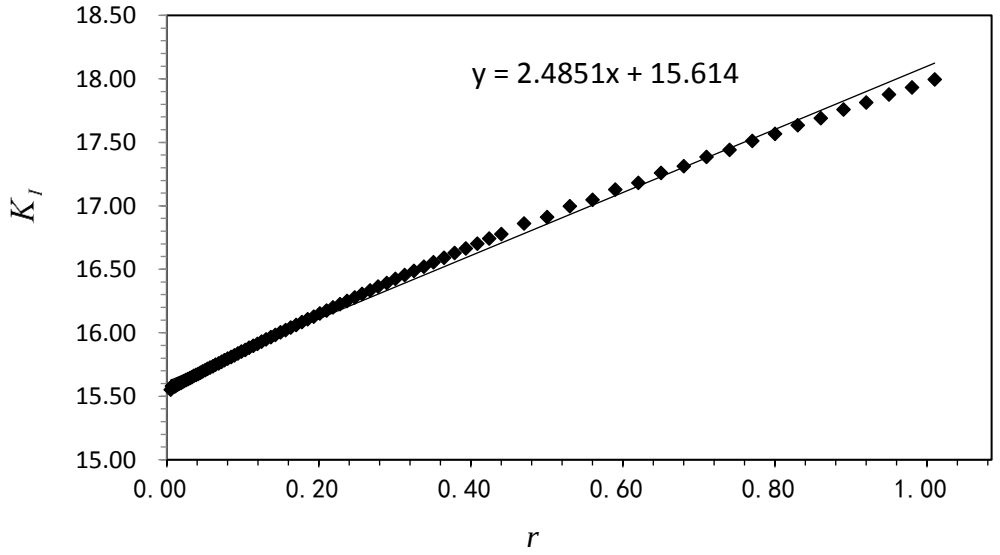

Figure 7.6 The SIFs of the given unknown problem is plotted against the nodal radius ahead of the crack tip. This is for a homogeneous plate of dimension 20 x 8 with a centre crack, *a/b* = 0.2. Stress Proportionality Method uses reference problem of plate dimension 20 x 12 and *a/b* = 0.4.

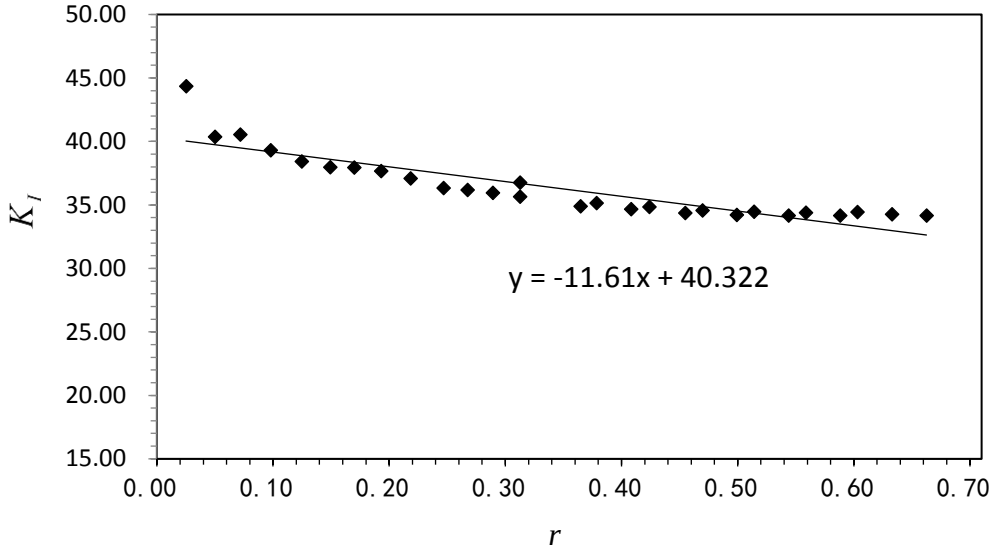

Figure 7.7 The SIFs of the given unknown problem is plotted against the nodal radius ahead of the crack tip. This is for a homogeneous plate of dimension 20 x 14 with a centre crack, a/b = 0.6. Stress Proportionality Method uses a reference problem of plate dimension 4 x 4 and a/b = 0.5.

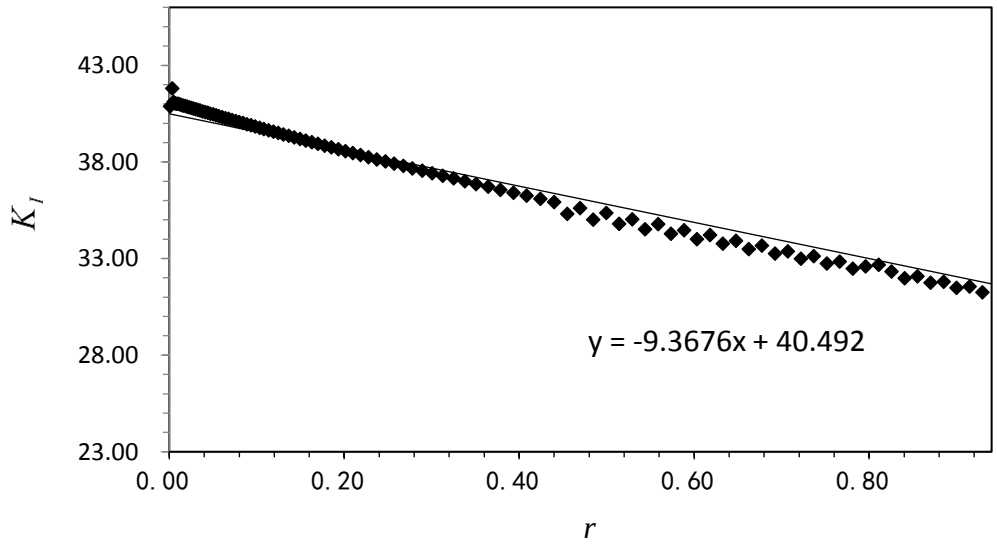

Figure 7.8 The SIFs of the given unknown problem is plotted against the nodal radius ahead of the crack tip. This is for a homogeneous plate of dimension 14 x 20 with a centre crack, a/b = 0.6. Stress Proportionality Method uses a reference problem of plate dimension 20 x 8 and a/b = 0.2.

2D Plate Dimensions of Unknown Problem	Given Problem *a/b*	Ref. Problem Dimensions	*Ref. Problem a/b*	*h/b*	Rooke [161]	COD Method		Stress Prop. Method	
					K_I / K_0	K_I / K_0	Error (%)	K_I / K_0	Error (%)
4 x 4	0.5	4 x 8	0.5	1	1.33	1.322	0.60	1.325	0.36
4 x 4	0.5	20 x 12	0.4	1				1.328	0.18
20 x 8	0.2	4 x 8	0.5	0.4	1.25	1.263	1.05	1.245	0.39
20 x 8	0.2	20 x 12	0.4	0.4				1.246	0.34
20 x 12	0.4	4 x 8	0.5	0.6	1.48	1.520	2.65	1.479	0.05
20 x 12	0.4	20 x 12	0.4	0.6				1.484	0.29
20 x 14	0.6	4 x 4	0.5	0.7	1.865	1.946	4.17	1.857	0.41
20 x 14	0.6	4 x 8	0.5	0.7				1.861	0.23
20 x 14	0.6	20 x 8	0.2	0.7				1.865	0.02

Table 7.1 Comparing the normalised SIF values for a homogeneous centre crack plate with reference and COD method. The errors as calculated in the table is with respect to Rooke [161].

The Stress Proportionality Method is first tested on a 2D homogeneous plate with a centre crack. The calculated stress intensity factor for several 2D plate dimensions were assessed and the results were compared with the COD method and reference result [161]. In this study, it was shown that the stress intensity factor error of less than 0.5% was achieved by the Stress Proportionality Method when compared against the reference [161] result. The COD method achieved a maximum error of 4.17% and this is for all the different 2D plates and crack sizes.

7.4. Numerical Assessment 2

In this assessment, the SIF is determined for interface crack using the stress proportionality method. A bi-material plate of dimension 10 x 20 is considered for the given unknown problem and this is shown in Fig. 7.9. The elastic modulus combinations for the given unknown problem is chosen to be $E^{(1)}/E^{(2)} = 1,\ 2,\ 5$ and 10 respectively. For the given reference problem, a plate of dimension 4 x 8 is chosen and the elastic modulus combinations $E^{(1)}/E^{(2)} = 1$ and 2. In all cases only half of the plate is analysed by ABAQUS due to symmetry along the *y* axis.

As in Numerical Assessment 1, the nodal stresses ahead of the crack tip is determined for the homogeneous case using ABAQUS. The SIF K_I for the given unknown problem is then determined using the equivalent $E^{(1)}/E^{(2)} = 1$ for the given reference problem. The graph used in approximating the K_I value is shown in Fig. 7.10 and 7.11. For the remaining elastic modulus combination ($E^{(1)}/E^{(2)} = 2,\ 5$ and 10) for the given unknown problem, the SIF values for K_I and K_{II} are determined using $E^{(1)}/E^{(2)} = 2$ for the given reference problem. The achieved K_I and K_{II} values are plotted in Fig. 7.12 to 7.17. Table 7.2 also shows the error margins for the stress proportionality method when compared against FEM (ABAQUS) calculated K_I and K_{II} values.

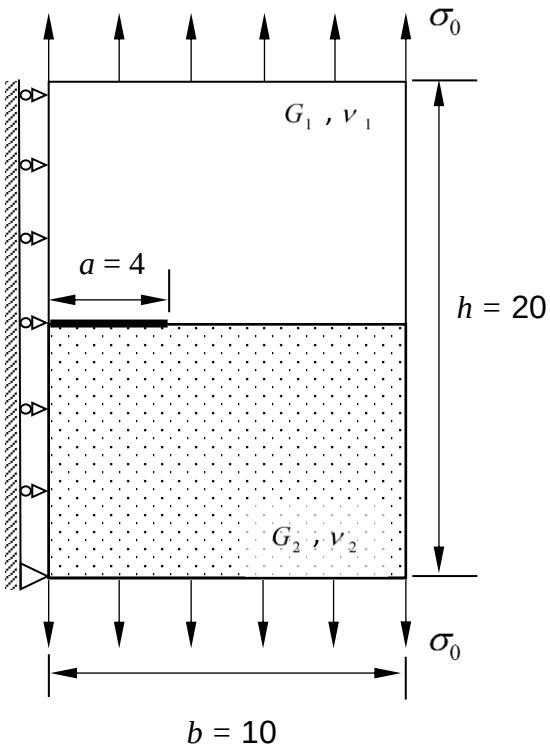

Figure 7.9 Bi-material plate of the given unknown problem with dimensions 10 x 20 and crack length a/b = 0.4. Only half of the plate is analysed due to symmetry along the y axis.

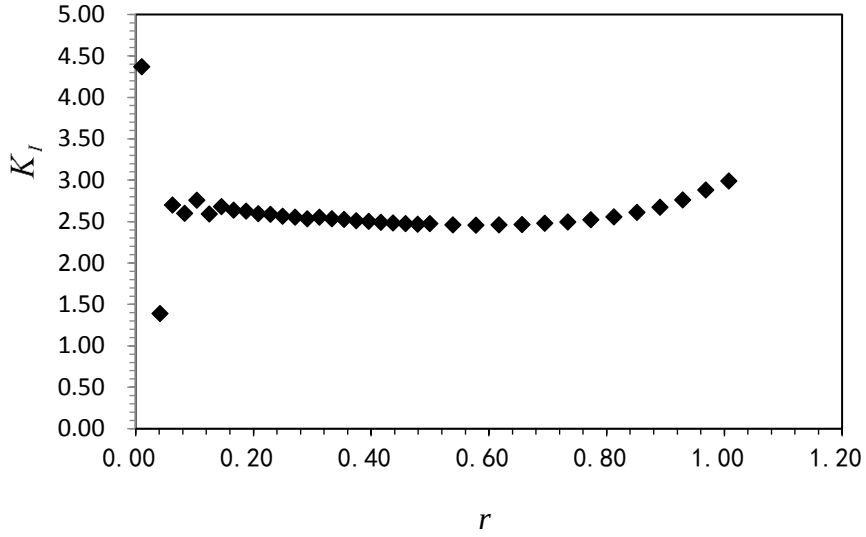

Figure 7.10 A plot of the stress intensity factor K_I for plate with dimension 10 x 20 with a centre crack, *a/b* = 0.4. Stress Proportionality Method using reference problem with plate dimension 4 x 8 and *a/b* = 0.5. Material elastic constant used for the reference and given unknown problem $E^{(1)}/E^{(2)}=1$. The reported analysis shows the K_I values as estimated along the entire interface bond. The K_I values diverge at the trailing end of the graph.

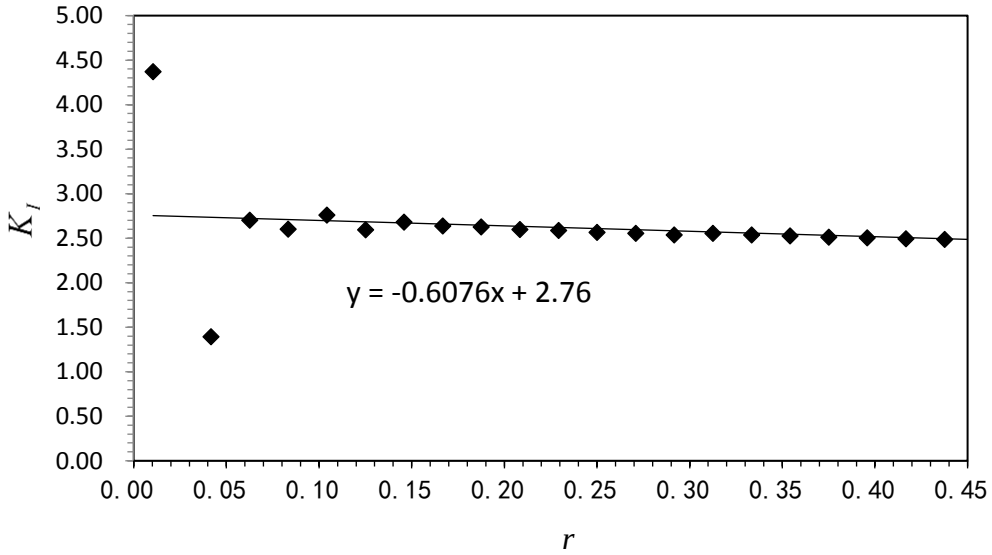

Figure 7.11 A plot of the stress intensity factor K_I for plate with dimension 10 x 20 with a centre crack, *a/b* = 0.4. Stress Proportionality Method using reference problem of plate dimension 4 x 8 and *a/b* = 0.5. Material elastic constant used for the reference and given unknown problem $E^{(1)}/E^{(2)}=1$. K_I values considered is truncated at radius *r* = 0.45.

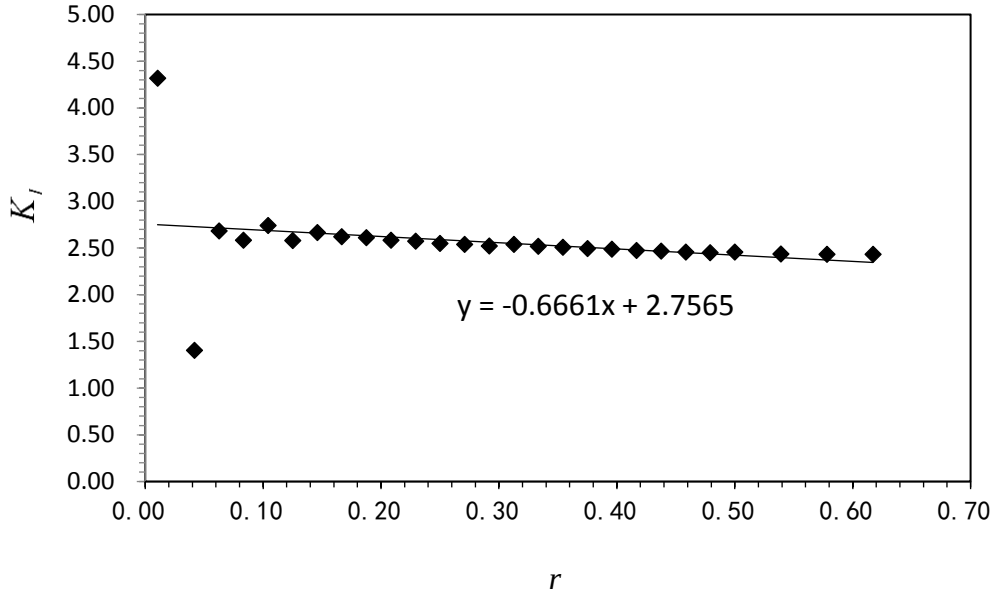

Figure 7.12 A plot of the stress intensity factor K_I for plate with dimension 10 x 20 with a centre crack, *a/b* = 0.4. Stress Proportionality Method using reference problem with plate dimension 4 x 8 and *a/b* = 0.5. Material elastic constant used for the reference and given unknown problem $E^{(1)}/E^{(2)} = 2$.

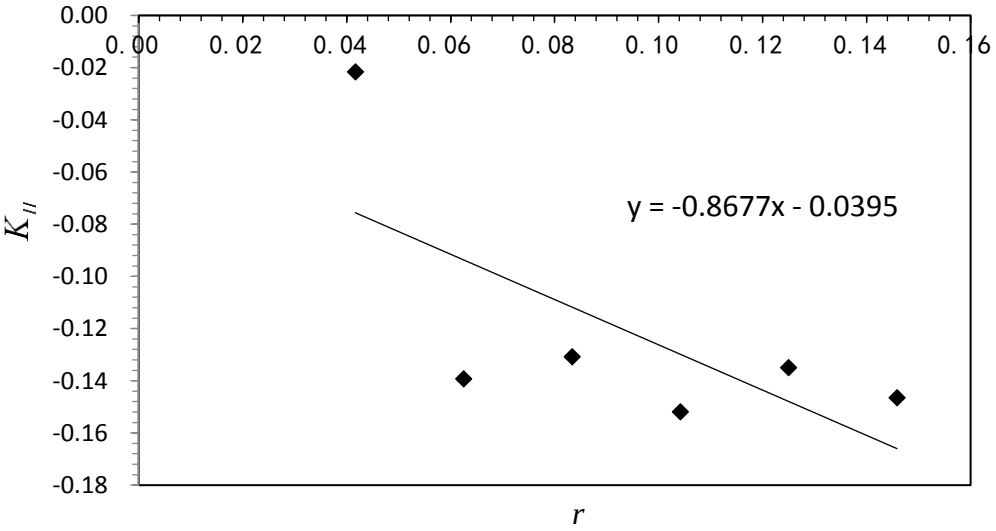

Figure 7.13 A plot of the stress intensity factor K_{II} for plate with dimension 10 x 20 with a centre crack, *a/b* = 0.4. Stress Proportionality Method using reference problem with plate dimension 4 x 8 and *a/b* = 0.5. Material elastic constant used for the reference and given unknown problem $E^{(1)}/E^{(2)} = 2$.

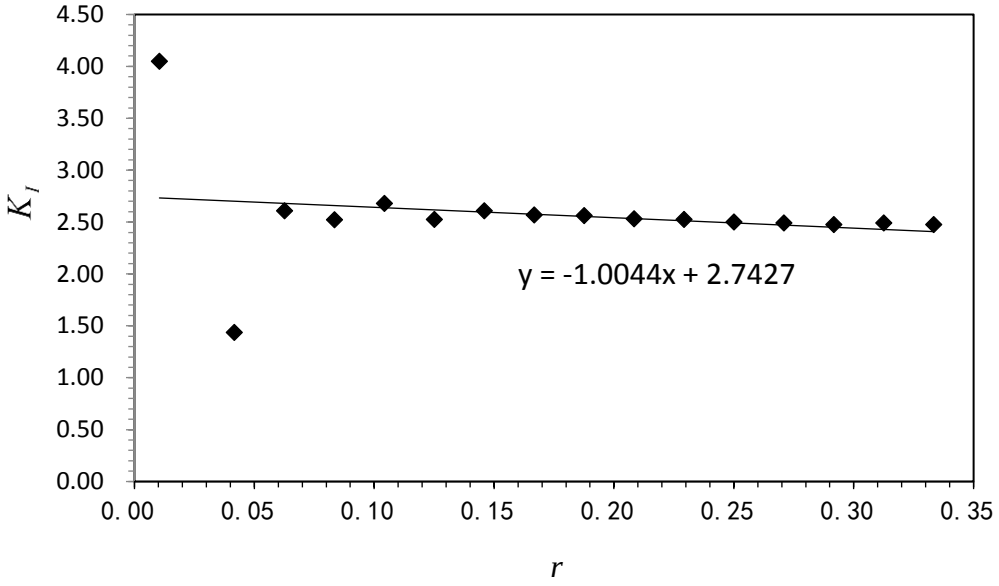

Figure 7.14 A plot of the stress intensity factor K_I for plate with dimension 10 x 20 with a centre crack, *a/b* = 0.4. Stress Proportionality Method using reference problem with plate dimension 4 x 8 and *a/b* = 0.5. Material elastic constant used for the reference $E^{(1)}/E^{(2)} = 2$ and given unknown problem $E^{(1)}/E^{(2)} = 5$.

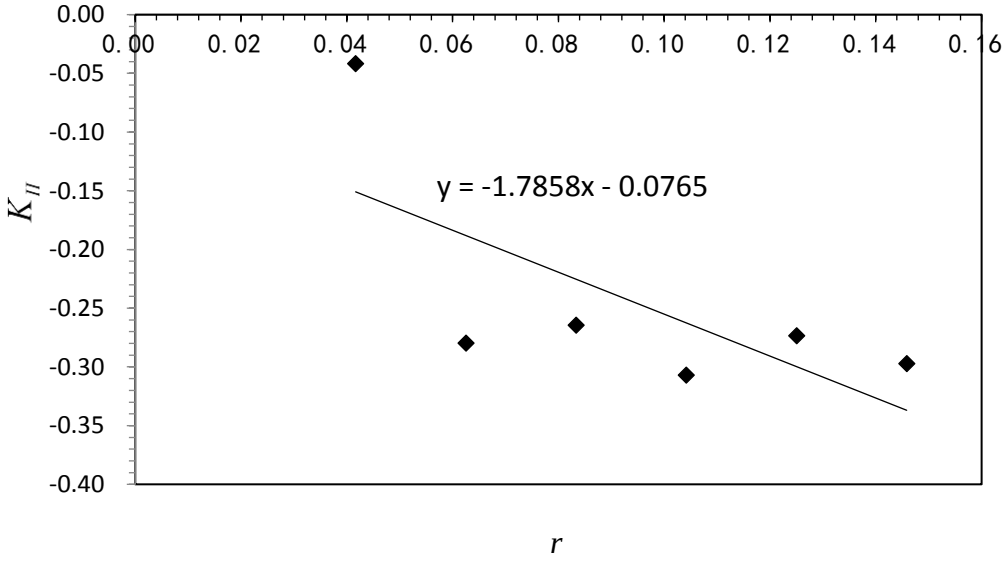

Figure 7.15 A plot of the stress intensity factor K_{II} for plate with dimension 10 x 20 with a centre crack, *a/b* = 0.4. Stress Proportionality Method using reference problem with plate dimension 4 x 8 and *a/b* = 0.5. Material elastic constant used for the reference $E^{(1)}/E^{(2)} = 2$ and given unknown problem $E^{(1)}/E^{(2)} = 5$.

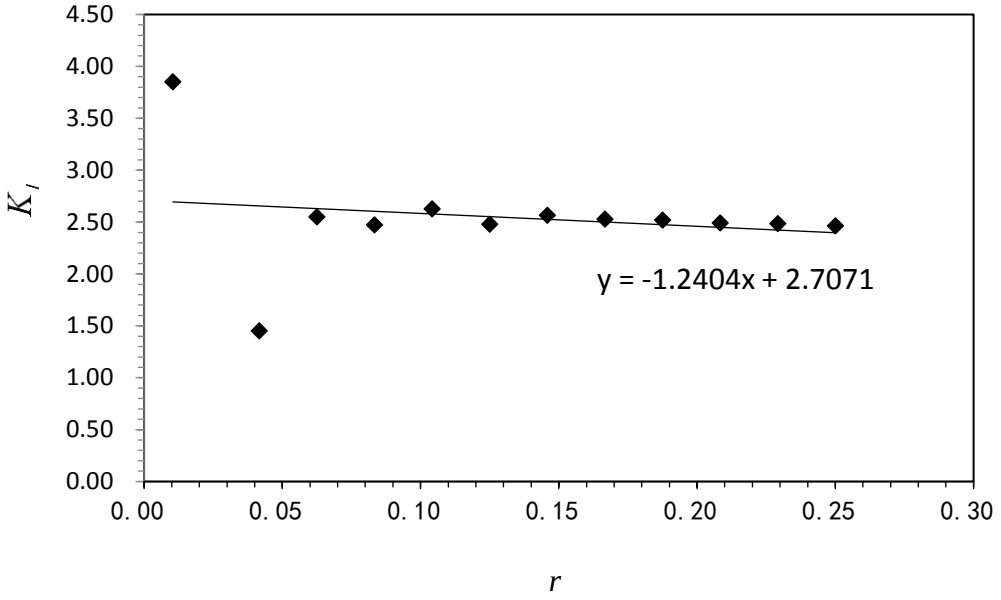

Figure 7.16 A plot of the stress intensity factor K_I for plate with dimension 10 x 20 with a centre crack, *a/b* = 0.4. Stress Proportionality Method using reference problem with plate dimension 4 x 8 and *a/b* = 0.5. Material elastic constant used for the reference $E^{(1)}/E^{(2)} = 5$ and given unknown problem $E^{(1)}/E^{(2)} = 10$.

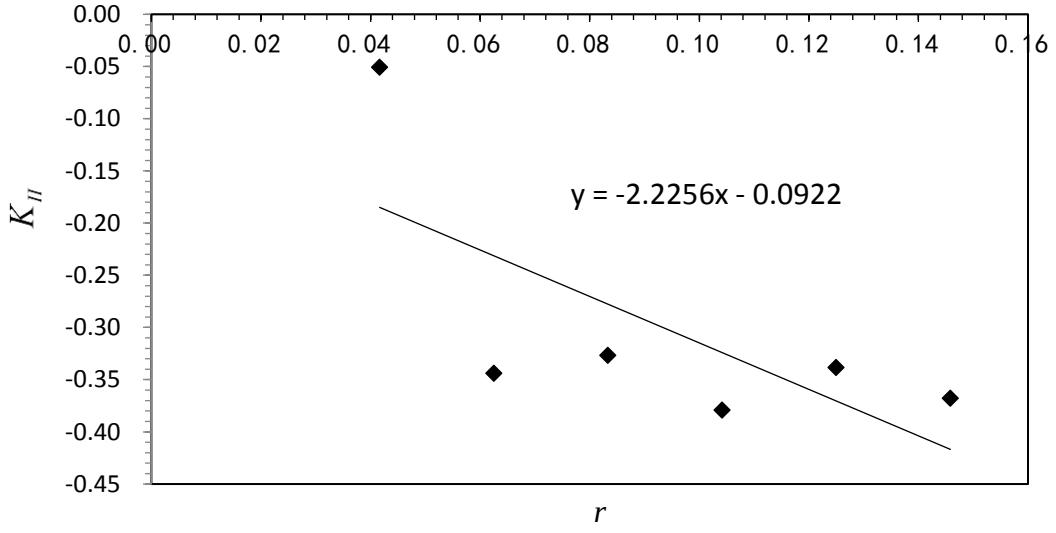

Figure 7.17 A plot of the stress intensity factor K_{II} for plate with dimension 10 x 20 with a centre crack, *a/b* = 0.4. Stress Proportionality Method using reference problem with plate dimension 4 x 8 and *a/b* = 0.5. Material elastic constant used for the reference and given unknown problem $E^{(1)}/E^{(2)} = 10$.

The Stress Proportionality Method, as reported, was also applied to a cracked 2D bi-material plate and several material combinations were considered. Using the Stress Proportionality Method in assessing the interface crack, it was observed that the plotted result will begin to diverge at the trailing end of the plotted data points (Fig 7.10). In order to achieve good and accurate result, it is important to identify the point at which the data point begins to diverge and then truncate the data at this point (Fig 7.11). This way, the stress intensity factor results as given by the correlation line (line of fit) are not greatly affected. This statement is true for determining the K_I and K_{II} values. The K_I and K_{II} values as determined by the Stress Proportionality Method is compared against an equivalent ABAQUS result. For the K_I value, the error is less than 1% when compared with ABAQUS.

In this study, it can be observed that any plate of arbitrary crack length can be used to determine the SIF of a given problem. In cases where the crack length in the reference problem is shorter, the scatter graph shows a strong negative correlation. The reverse is observed for a reference problem where the crack length is longer than the given problem crack length. The plotted data of SIF versus the nodal radius from the crack tip shows a strong positive correlation. Consequently, the use of a longer crack length for the reference problem against a shorter crack length in a given problem has been proven to be irrelevant when using the Stress Proportionality Method.

The Stress Proportionality Method has some limitations when trying to determine the SIF of a given problem. The difference between the nodal radius from the crack tip of the given problem and the reference problem must be obtained first and the error margin between the two radii must be determined. The smaller this error margin the higher the accuracy of the result. This study has shown that an error margin of 6% does not have a significant effect on the overall result.

Given Problem			**Reference Problem**			K_I			K_{II}		
2D Plate	***a/b***	$E^{(1)}/E^{(2)}$	**2D Plate**	***a/b***	$E^{(1)}/E^{(2)}$	**Stress Prop. Method**	**ABAQUS**	**Error** (%)	**Stress Prop. Method**	**ABAQUS**	**Error** (%)
10 x 20	0.4	1	4 x 8	0.5	1	2.76	2.78	0.72	0	0.000	0.00
10 x 20	0.4	2	4 x 8	0.5	2	2.76	2.77	0.36	-0.04	-0.040	0.00
10 x 20	0.4	5	4 x 8	0.5	2	2.74	2.74	0.00	-0.08	-0.075	6.67
10 x 20	0.4	10	4 x 8	0.5	2	2.71	2.70	0.37	-0.09	-0.090	0.00

Table 7.2 The SIF values as determined by the stress proportionality method is compared to SIF values calculated by ABAQUS. The errors between the K_I and the K_{II} values are shown to be marginal.

7.5. Numerical Assessment 3

In this assessment, the SIF is determined for interface crack using the stress proportionality method. A bi-material plate of dimension 4 x 8 with a centre crack length a/b = 0.5 is considered for the given unknown problem and the model set-up is similar to that shown in Fig. 7.9. The elastic modulus combinations for the given unknown problem is chosen to be $E^{(1)}/E^{(2)} = 1,\ 2,\ 5$ and 10 respectively. For the given reference problem, a plate of dimension 10 x 20 with a centre crack length a/b = 0.4 is chosen and the elastic modulus combinations $E^{(1)}/E^{(2)} = 1$ and 2. In all cases only half of the plate is analysed by ABAQUS due to symmetry along the y axis.

The aim of this analysis is to compare the stress proportionality technique against ABAQUS (J-Integral method), FBM (Williams series) and the xSBFEM method [78]. The results are presented in Table 7.3 and 7.4, and a graphical representation of the results are shown in Fig 7.18 and 7.19.

$E^{(1)}/E^{(2)}$	$K_I / \sigma_0 \sqrt{\pi a}$			
	SPM Method	FBM (Williams Series)	ABAQUS (J-Integral)	xSBFEM Method [78]
1	1.188	1.182	1.179	1.180
2	1.189	1.154	1.148	1.148
5	1.160	1.131	1.123	1.124
10	1.136	1.190	1.188	1.189

Table 7.3 The normalised K_I values as calculated by the stress proportionality method (SPM) is compared against different numerical techniques. The numerical techniques considered are ABAQUS (J-Integral method), FBM (Williams series) and the xSBFEM Method [78]. The reference problem considered is a 2D plate with dimension 4 x 8 and crack length a/b = 0.5.

$E^{(1)}/E^{(2)}$	$K_{II}/\sigma_0\sqrt{\pi a}$			
	SPM Method	FBM (Williams Series)	ABAQUS (J-integral)	xSBFEM Method [78]
1.00	0.000	0.000	0.000	0.000
2.00	-0.044	-0.056	-0.051	-0.057
5.00	-0.089	-0.110	-0.098	-0.105
10.00	-0.109	-0.132	-0.116	-0.124

Table 7.4 The normalised K_{II} values as calculated by the stress proportionality method (SPM) is compared against different numerical techniques. The numerical techniques considered are ABAQUS (J-integral method), FBM (Williams series) and the xSBFEM Method [78]. The reference problem considered is a 2D plate with dimension 4 x 8 and crack length *a/b* = 0.5.

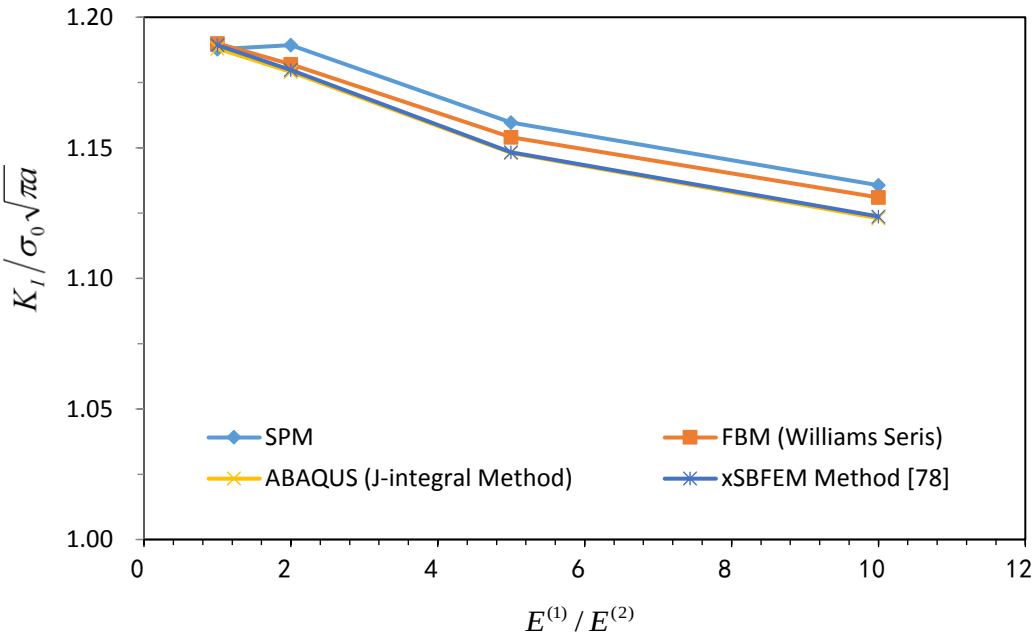

Figure 7.18 Normalised K_I for various elastic modulus combinations, $E^{(1)}/E^{(2)}$. Centre crack with length *a/W* = 0.5.

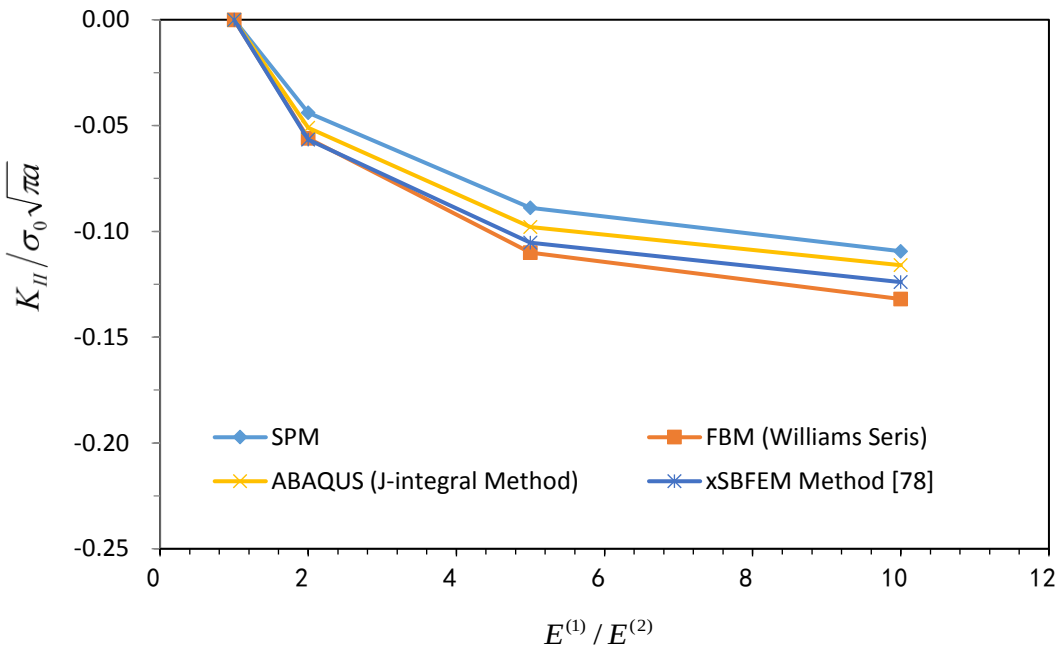

Figure 7.19 Normalised K_{II} for various elastic modulus combinations, $E^{(1)}/E^{(2)}$. Centre crack with length $a/W = 0.5$.

In this section of the thesis, the newly proposed semi-analytical technique called the stress proportionality method (SPM) is compared against several numerical techniques used in calculating the stress intensity factors for interface cracks between bi-materials. Clearly, from Fig. 7.18 and 7.19 it is shown that the SPM can produce accurate results. Also, since the SPM employs the nodal stresses at the crack tip in calculating the stress intensity factor, it can be implemented in different numerical methods including the FBM method. However, since this technique depends on the reference values of a predetermined SIF value and nodal stresses, it should be noted that the process to obtain these reference values is performed one-time and can be used in repeated analysis to determine the SIF of an unknown problem.

7.6. The Displacement Correlation Technique

In the previous section, the stress ahead of the crack tip was used in calculating the stress intensity factor. In this section, the near-tip nodal displacement as extracted from a finite element analysis is utilized in determining the stress intensity factor. The displacement approach to investigating the stress intensity factor is often seen to be less accurate when compared with other numerical methods. Nonetheless, the results obtained by the displacement method is within an acceptable level of accuracy for various engineering applications. In addition, the displacement method is very easy to implement without a significant amount of distortion of the estimated result.

In terms of stress intensity factor investigations, the displacement approach can be categorized as follows; the displacement extrapolation method, the quarter point displacement method and the displacement correlation technique. An extensive review of the various displacement methods can be found in several papers [1, 37, 158, 159, 160].

The accurate use of any displacement method requires a good interpretation of the displacement field around the crack tip. This can be achieved by the use of special near-tip elements or simply by increasing the element refinement at the crack tip.

The singular finite element as developed by Barsoum [38] is a step forward to improve the numerical analysis near the crack tip. In his development, the mid-side nodes near the crack tip are moved to a quarter position from the crack tip. As a result of the quarter point, the critical square root singularity as postulated in fracture mechanics is replicated. Furthermore, the Williams series stipulate that the crack open displacement around a crack tip irrespective of the problem geometry and boundary conditions can be express as follows [132];

$$\Delta u_k(r,\theta) = b_k(\theta) r^{1/2} + c_k(\theta) r + d_k(\theta) r^{3/2} + \dots \ , \tag{7.15}$$

where r is the distance originating from the crack tip, θ is the direction and $k = 1,\ 2$ (x and y axis). From Eq. (7.15) the $\sqrt{r}$ expression is incorporated into the quarter-point method [38].

In a recent work by Gray [132] it is emphasised that the C_k value for Δu along the crack surface should equate to zero. However, this is not the case and as a result the quarter point element fails to satisfy this condition. To achieve an accurate result in the vicinity of the crack tip, the linear term is forced to be zero. Using the quarter point elements around the crack tip, the stress intensity factor is determined using the displacement correlation technique.

In the remainder of this chapter, the stress intensity factor components K_I and K_{II} for interface crack is evaluated by making enhancements to the various displacement correlation techniques. The quarter point element which is a standard for crack analysis in the finite element program ABAQUS is employed in the FEA analysis. The accuracy of the proposed technique is confirmed by performing some numerical examples of interface crack for several material combinations $\left(E^{(1)}/E^{(2)}\right)$. Comparisons of K_I and K_{II} are made with ABAQUS estimates using the *J*-Integral approach.

7.5.1 Enhanced Element Shape Function for Crack Opening Displacement (COD)

The crack surface is purposely assigned to lie on the same plane as the quarter point element as shown in Fig. 7.20. The same emphasis can be made for a 1D element with three grid points lying along the plane of the crack face, and this is illustrated in Fig. 7.21. For a 1D element with three grid points, a quadratic shape function can be easily determined [132]. The shape function is given by the following expression;

$$\psi_1(t) = (1-t)(1-2t) \text{ ,}$$

$$\psi_2(t) = 4t(1-t) \text{ ,} \tag{7.16}$$

$$\psi_3(t) = t(2t-1) \text{ .}$$

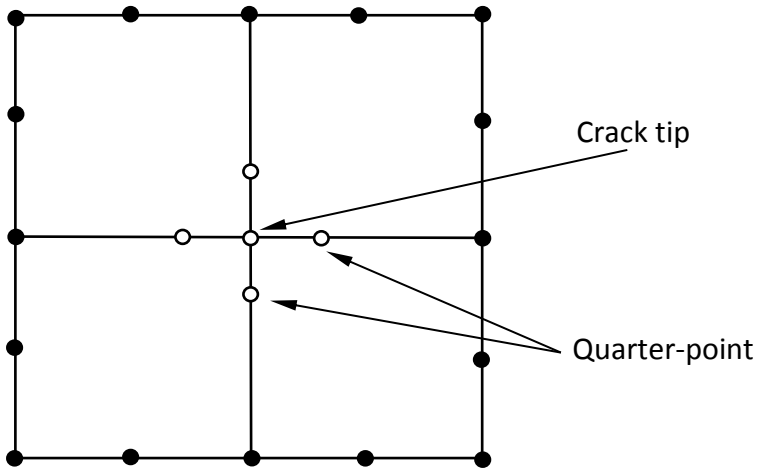

(a)

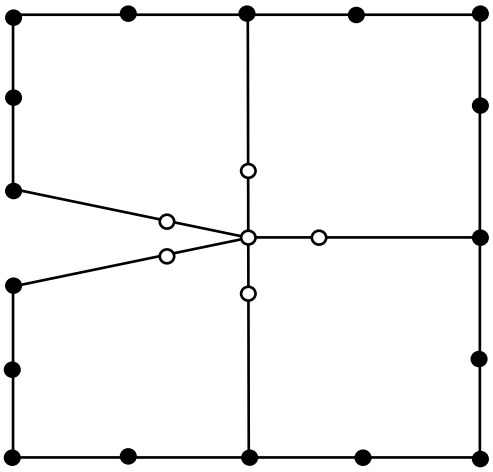

(b)

Figure 7.20 a) Quarter point element around crack tip. b) A quarter point element showing the crack surface opening.

According to Fig. 7.21 the Δu is zero at the crack tip, hence $t = 0$ reducing the displacement equation for the one-dimension quadratic element to

$$\Delta u_k(t) = \sum_{j=2}^{3} (\Delta u_1^j \psi_j(t), \Delta u_2^j \psi_j(t)) \quad . \tag{7.17}$$

According to work by Barsoum [38] moving the mid-side grid point to a quarter of the element length leads to $\sqrt{r/L}$. Where L is the length of the element. According

to Gray [132] the result of moving the mid-side node to the quarter position will result in the leading order term for Δu at the crack tip which is t to be the square root of the distance. Further work by Gray and Paulino have also shown that the next term in the order of Δu which is $t^2 = r/L$ should vanish.

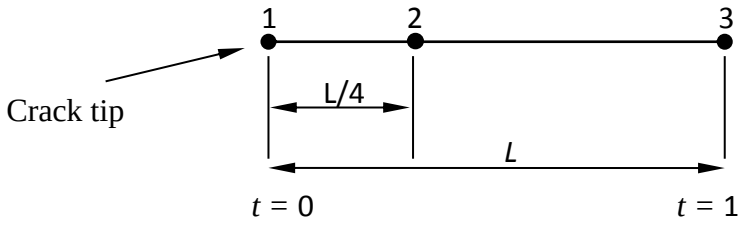

Figure 7.21 One-dimensional crack surface element

The general form of the combined standard quadratic shape function and the modified quarter point shape function [132] is given by;

$$\hat{\psi}_j = \psi_j(t) + \alpha\beta_j t(1-t)(1-2t), \tag{7.18}$$

where $\alpha = 0$ is for crack tip element and $\alpha = 1$ is for all other regular elements. β is a constant assigned with the following values, $\beta_1 = \beta_3 = \pm 2/3$ and $\beta_2 = \mp 4/3$. The top sign is used when the crack tip is located at $t = 0$ and the lower sign is used when the crack tip is located at $t = 1$. Since the displacement produced by the standard quarter point elements in ABAQUS [133] embody the standard shape function, there is no need to directly adjust the element code and shape function. However, any enhancement to the shape function can be applied directly to the displacement as determined by the quarter point element.

From Eq. (7.18) a cubic term is defined for the shape function to be applied to the COD as determined by the standard quarter point element. For a 1D element with three grid points (Fig. 7.21), the cubic shape function at point 2 and 3 is given by

$$\hat{\psi}_2(t) = -\frac{8}{3}(t^3 - t) \ ,$$
$$\hat{\psi}_3(t) = \frac{1}{3}(4t^3 - t) \ . \tag{7.19}$$

The general expression for the displacement correlation technique [33, 37, 95, 132, 134] in terms of mode I and mode II stress intensity factor (homogeneous case) is given by;

$$K_I = \frac{G}{\kappa + 1}\sqrt{\frac{2\pi}{L}}\left[4\left(\Delta v_{i=2}\right) - \left(\Delta v_{i=3}\right)\right] , \tag{7.20}$$

$$K_{II} = \frac{G}{\kappa + 1}\sqrt{\frac{2\pi}{L}}\left[4\left(\Delta u_{i=2}\right) - \left(\Delta u_{i=3}\right)\right] . \tag{7.21}$$

Applying the modified quarter point shape function in Eq. (7.19) to the near crack tip COD gives

$$\Delta u_k = \Delta u_k^{node2}\hat{\psi}_2(t) + \Delta u_k^{node3}\hat{\psi}_3(t) \ . \tag{7.22}$$

For the displacement correlation technique, the above expression reduces to

$$\Delta u_k = \frac{1}{3}\left(8\Delta u_k^{\text{node2}} - \Delta u_k^{\text{node3}}\right)t + \frac{4}{3}\left(\Delta u_k^{\text{node3}} - \Delta u_k^{\text{node2}}\right)t^3 , \tag{7.23}$$

where $t = \sqrt{r/L}$.

7.5.2 Displacement Correlation Technique Using the General Interface Crack Formulation

In a provisional assessment of interface crack by the displacement correlation technique, a Quarter-Point Element (QPE) was used to determine the near-tip displacements. The enhanced quarter point element shape function technique was then implemented on the generalised formulation for an interface crack. Thus, the generalised interface crack formulation for computing the complex stress intensity

factor components K_I and K_{II} are related to the near crack tip displacement [123] by the following expression

$$K = \frac{2(1+2i\varepsilon)\cosh(\pi\varepsilon)}{\beta^{[1]}+\beta^{[2]}}\exp(-i\varepsilon\ln(r))\sqrt{\frac{2\pi}{r}}\left[\Delta u_2 - i\Delta u_1\right] \ , \tag{7.24a}$$

where K is the complex stress intensity factor and the constants of bi-material are given as

$$\alpha = 1,2 \ , \ \beta^{[\alpha]} = \frac{1+\kappa^{\alpha}}{\mu^{\alpha}} \ , \ \varepsilon = \frac{1}{2\pi}\ln(\hat{\kappa}) \ , \ \hat{\kappa} = \frac{\kappa^{[1]}\mu^{[2]}+\mu^{[1]}}{\kappa^{[2]}\mu^{[1]}+\mu^{[2]}}$$

and $\kappa^{[\alpha]} = 3-4\nu^{[\alpha]}$ for plane strain and $\kappa^{[\alpha]} = \frac{3-4\nu^{[\alpha]}}{1-\nu^{[\alpha]}}$ for plane stress.

By employing the modified displacement correlation technique of Eq. (7.23), the SIF for an interface crack is expressed in terms of the near crack tip displacement where $\bar{r} = r/L$ is given by

$$K = \frac{2(1+2i\varepsilon)\cosh(\pi\varepsilon)}{\beta^{[1]}+\beta^{[2]}}\exp(-i\varepsilon\ln(\bar{r}))\sqrt{\frac{2\pi}{L}}\cdot\frac{1}{3}\left[\left(8\Delta u_2^{\text{node2}} - \Delta u_2^{\text{node3}}\right)\right. \\ \left. - i\left(8\Delta u_1^{\text{node2}} - \Delta u_1^{\text{node3}}\right)\right] . \tag{7.24b}$$

By virtue of Eq. (7.24a), it is quite clear the displacement correlation technique cannot be fully implemented as the general interface crack Eq. (7.24a) is formulated for a single grid point along the crack surface. Extending this to include the displacement from two grid points can produce reasonable results. This will be shown by the interface crack analysis presented in section 7.5.4, Numerical Assessment 4. Also, a comparison of the results obtained for a homogeneous plate using Eq. (7.24b) and the standard DCT Eq. (7.25a) is reported in Table 7.4.

7.5.3 Enhanced Displacement Correlation Technique for Interface Crack Using the Enhanced Element Shape Function

Here, the standard displacement correlation technique seemingly developed for the evaluation of interface crack is discussed. Aslantas [80] used the DCT to investigate the interface crack of a composite material (matrix with a single fibre). The mode I and

II interface SIFs K_I and K_{II} are given in terms of the displacement correlation technique as

$$K_I = \sqrt{\frac{2\pi}{L}}\left(D_1\left[-v_3^{lower}+4v_2^{lower}-3v_1^{crack-tip}\right]-D_2\left[-v_3^{upper}+4v_2^{upper}-3v_1^{crack-tip}\right]\right), \qquad (7.25a)$$

$$K_{II} = \sqrt{\frac{2\pi}{L}}\left(D_1\left[-u_3^{lower}+4u_2^{lower}-3v_1^{crack-tip}\right]-D_2\left[-u_3^{upper}+4u_2^{upper}-3u_1^{crack-tip}\right]\right). \qquad (7.25b)$$

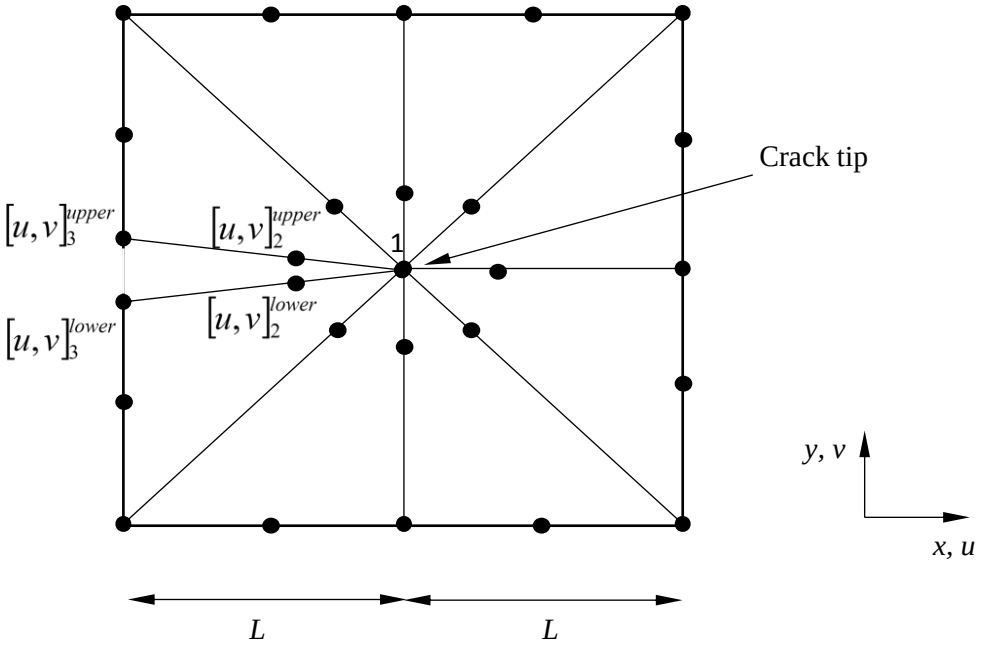

Figure 7.22 The definition of the interface crack displacement correlation technique

where L retains its meaning as the length of the near-tip element between node 1 and 3. D_1 and D_2 can be expressed as follow

$$D_1 = \frac{(1+\gamma)\lambda_0}{\cosh(\pi\varepsilon)}\cdot\frac{G_1}{\kappa_1 e^{\pi\varepsilon}+\gamma e^{-\pi\varepsilon}},$$

$$D_2 = \frac{(1+\gamma)\lambda_0}{\cosh(\pi\varepsilon)}\cdot\frac{G_2}{\kappa_2\gamma e^{-\pi\varepsilon}+e^{\pi\varepsilon}},$$

where $\varepsilon = \frac{1}{2\pi}\ln\gamma$, $\gamma = \frac{G_1 + \kappa_1 G_2}{G_2 + \kappa_2 G_1}$, $\lambda_0 = \left(\frac{1}{4} + \varepsilon^2\right)^{1/2}$, G_i and ν_i are the shear modulus and the Poisson's ratio for the respective materials, $i = 1,\ 2$. Eq. (7.25a) and (7.25b) can be re-organised to give

$$K_I = \sqrt{\frac{2\pi}{L}}\left[\left(D_2 v_3^{upper} - D_1 v_3^{lower}\right) + \left(D_1 4v_2^{lower} - D_2 4v_2^{upper}\right) + \left(D_2 3v_1^{crack-tip} - D_1 3v_1^{crack-tip}\right)\right], \tag{7.26a}$$

$$K_{II} = \sqrt{\frac{2\pi}{L}}\left[\left(D_2 u_3^{upper} - D_1 u_3^{lower}\right) + \left(D_1 4u_2^{lower} - D_2 4u_2^{upper}\right) + \left(D_2 3u_1^{crack-tip} - D_1 3u_1^{crack-tip}\right)\right]. \tag{7.26b}$$

Using a Quarter-Point Element (QPE) where only node 2 is considered, Eq. (7.26a) and (7.26b) can be reduced to

$$K_I = \sqrt{\frac{2\pi}{L}}\left[D_1 v_2^{lower} - D_2 v_2^{upper}\right], \tag{7.27a}$$

$$K_{II} = \sqrt{\frac{2\pi}{L}}\left[D_1 u_2^{lower} - D_2 u_2^{upper}\right]. \tag{7.27b}$$

By applying the enhanced quarter point shape function of Eq. (7.19) to the above Eq. (7.26a) and (7.26b), this will result in an expression of the Displacement Correlation Technique (DCT) for mode I and mode II SIF given as

$$K_I = \frac{1}{3}\sqrt{\frac{2\pi}{L}}\left[8\left(D_1 v_2^{lower} - D_2 v_2^{upper}\right) + \left(D_2 v_3^{upper} - D_1 v_3^{lower}\right)\right], \tag{7.28a}$$

$$K_{II} = \frac{1}{3}\sqrt{\frac{2\pi}{L}}\left[8\left(D_2 u_2^{upper} - D_1 u_2^{lower}\right) + \left(D_2 u_3^{upper} - D_2 u_3^{lower}\right)\right]. \tag{7.28b}$$

7.5.4 Numerical Assessment 4

7.5.4.1 Evaluating the Use of DCT in the General Interface Crack Formulation

In this assessment, the SIF is determined by the DCT method using the general interface crack formulation and the enhanced quarter point shape function. A center crack of length *2a* in a bi-material plate is studied in this example. The plate has width *b* = 2 and height *h* = 4. A uniform distributed load σ_0 is applied on the top and bottom. Owing to the symmetry with respect to the *y* axis, it is equivalent to solve the boundary value problem for a half plate with a reasonable mesh. The FEM (ABAQUS) analysis was conducted under plane stress condition with Poisson's ratios $\nu_1 = \nu_2 = 0.3$ and the crack length $a = 0.4$ and $a = 0.5$. The results of SIFs versus the ratio of Young's modulus $E^{(1)}/E^{(2)}$ are shown in Table 7.5 for different cases. The solutions given by ABAQUS are provided in the table for comparison.

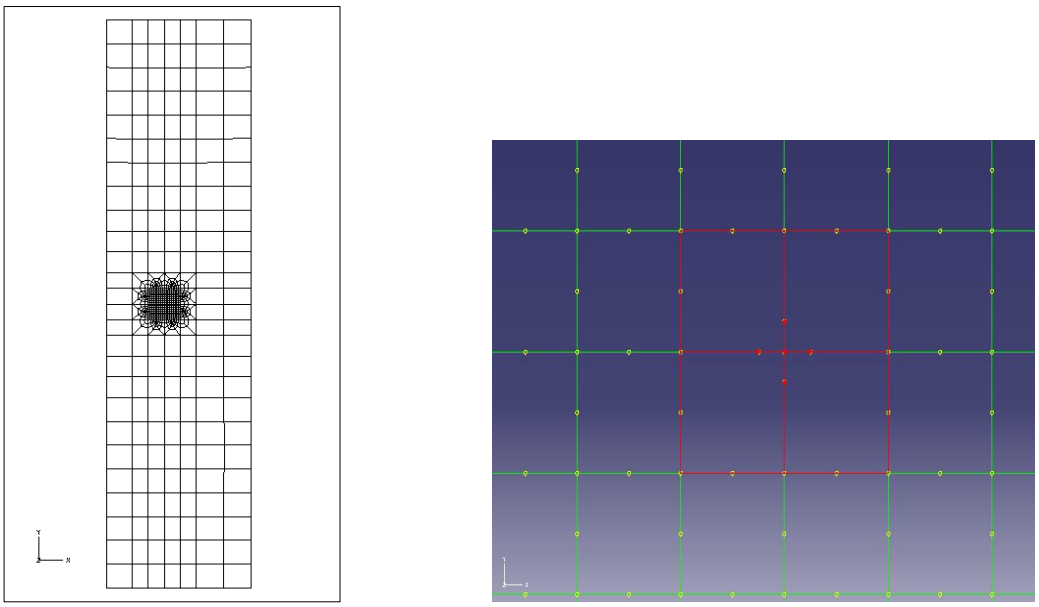

(a) (b)

Figure 7.23 a) FEM (ABAQUS) model of a 2 x 4 plate with a centre crack and a mesh around the crack tip region. b) The quarter point elements around the crack tip, as seen in ABAQUS.

a/b	$E^{(1)}/E^{(2)}$	$K_I/\sigma_0\sqrt{\pi a}$		$K_{II}/\sigma_0\sqrt{\pi a}$	
		Present	ABAQUS	Present	ABAQUS
0.4	1.00	1.14	1.11	0.00	0.00
	2.00	1.10	1.11	-0.07	-0.08
	5.00	0.97	1.07	-0.16	-0.19
	10.00	0.88	1.09	-0.22	-0.15
0.5	1.00	1.22	1.19	0.00	0.00
	2.00	1.17	1.18	-0.08	-0.07
	5.00	1.03	1.16	-0.17	-0.15
	10.00	0.94	1.14	-0.23	-0.18

Table 7.5 The normalised stress intensity factors of a centre crack bi-material plate. The table shows a comparison of ABAQUS results and the results achieved by the general interface crack formulation with the enhanced quarter point shape function, Eq. (7.24b).

E	$K_I/\sigma_0\sqrt{\pi a}$				
	Present	ABAQUS	Error with ABAQUS	Fehl [95]	Error with ABAQUS
1.00	1.14	1.11	2.80	1.17	5.18

Table 7.6 The stress intensity factors for a homogeneous centre crack plate. The SIF determined by the enhanced general interface crack Eq. (7.24b) is compared with the standard DCT in Eq. (7.25a). a/b = 0.4

As part of a review on the use of displacement techniques to determine the stress intensity factor, the Displacement Correlation Technique was modified using a 1D

element along the crack surface. Comparing the K_I values for a homogeneous crack shows that the modified displacement correlation technique using the general interface crack Eq. (7.24b) gives an error of 2.89% and the conventional displacement correlation technique Eq. (7.25a) gives an error of 5.18%. For centre crack where $E^{(1)}/E^{(2)} < 5$ in Table 7.5, it is easily observed that the relative errors of the stress intensity factors against ABAQUS are within 3%. A further improvement of the grid point displacement and the shape function is required for higher $E^{(1)}/E^{(2)}$, and this can be developed as part of a future study to obtain a more stable solution.

7.7. Summary

In this chapter, various nodal displacement and stress methods used in evaluating interface cracks of bi-materials is discussed with much focus on the proportionality method and the displacement correlation technique. An improvement to the proportionality method termed the stress proportionality method is presented. This improved technique was used in estimating the stress intensity factor for a bi-material plate. The validity of the stress proportionality method was confirmed by performing several numerical tests. Results obtained by the stress proportionality method were checked against COD and FEM (ABAQUS) results.

The displacement correlation technique was investigated to improve the accuracy of the stress intensity factor by the FEM method. The general equation for determining the stress intensity factor using the quarter point node was modified to include the remaining nodes along the crack surface. The new equation was applied to the study of interface cracks. A significant improvement can be seen for the K_I value of a homogeneous plate.

CHAPTER 8

Conclusion and Perspective

8.1. Thesis Concluding Remarks

The finite block method has been developed in this research for two-dimensional elastostatic and elastodynamic fracture mechanics with dissimilar bi-materials interface cracks. In this research, the Lagrange series interpolation which forms the basis for the finite block method was successfully implemented and validated by several numerical examples.

In applying the finite block method to the study of elasticity, the physical domain is divided into sub-regions, named blocks and each block is mapped using a predefined sets of collocation points distributed in a square normalised domain. The first order partial differential matrices can be constructed straight-away by using the Lagrange series interpolation and the collocation points. The nodal values of displacement can be obtained from a set of linear algebraic equations in a strong form from both the governing equation and the boundary conditions.

In Chapter 3, the Lagrange series interpolation is developed for the finite block method. Using a uniform or regular nodal arrangement, the first order derivative of a given function is presented for a one-dimensional case. As a result, the first order differential matrix is determined for both a regular and irregular nodal distribution. For

a two-dimensional case, a square domain in a normalised coordinate system was defined. In the 2D case the partial derivatives of a function across the domain is determined. The differential matrix construction is made easy by using the 1D differential matrix to form the 2D matrix. Hence, for a 2D case, the storage for the system matrix is largely reduced.

In order to demonstrate the accuracy of the finite block method and the use of the Lagrange series interpolation, a simple 1D problem is assessed for a regular and irregular nodal arrangement. Analytical solutions were presented alongside the numerical results by the FBM method for comparison. From the 1D assessment, the following can be deduced from the study;

- The average error decreases with an increase in the number of nodes for the interpolation. This is true for both regular and irregular nodal distribution.

The mapping technique is developed for a 2D case using one block. This allows a real or a physical domain to be mapped using a square normalised domain and then eventually the real or a physical domain is transformed to a 2D mapping domain. Also, since the 1D partial differential is determined initially during the construction of the square normalised domain, the computational effort is reduced remarkably. The Lagrange series interpolation and the mapping technique for a 2D case are assessed for several nodal distributions. The result obtained by the 2D FBM analysis shows a significant improvement in the average error when compared with an analytical solution.

In Chapter 4, the FBM was developed for an interface crack using the Williams asymptotic expansion series. Furthermore, the Williams series was expressed in both the Cartesian coordinate system and the polar coordinate system. This would allow the FBM to be tested under different scenarios. In order to calculate the stress intensity factor at the crack tip accurately, a singular core was used in all the numerical assessments in this chapter.

Firstly, a numerical study of FBM parameters for an interface crack was conducted using a circular disk with an edge crack and a singular core. In the study, the number of collocation points and the impact on the accuracy of the K_I and K_{II} values were prioritised. The following conclusion can be drawn from the study;

- The K_I and K_{II} value for several bi-material combinations obtained by the FBM is compared against the BCM. The result shows good agreement.
- The Poisson's ratio was varied to obtain the K_I and K_{II} values. This result was compared with the BCM and good agreement was observed.
- The K_I and K_{II} values are obtained for several singular core sizes. At small core sizes, good results can be achieved. The result also shows good agreement with the BCM.

This was followed by further numerical assessment of the FBM in the Cartesian coordinate system and the polar coordinate system for an interface crack. In the Cartesian coordinate system, a 2D plate with eight blocks was used for a centre crack and an edge crack analysis. The K_I and K_{II} values were determined for several elastic moduli ratios. The results were compared with reference papers and ABAQUS, and the FBM method is said to give very good results.

Using the polar coordinate system, a circular disk with an edge crack is assessed for the FBM. In this study, the effects of the number of collocation points on the K_I and K_{II} values were examined. The results were compared with ABAQUS and BCM. For the number of different collocation points, the K_I and K_{II} values for the various bi-material combinations were stable.

In Chapter 5, the finite block method was used to evaluate the T-stress of an interface crack. Using the William's series interpolation and the eigenfunction approach, the T-stress formulation is developed for the FBM. The crack tip singular core, introduced in Chapter 4 was also employed in the T-stress numerical calculation.

Initially, parameters influencing the FBM and the T-stress results were examined. This include the number of collocation points and the core size. In all cases, the normalised T-stress is compared against the BCM. The result shows good convergence as the number of collocation points increased. Also, a smaller core size will give good result.

In the various numerical assessments in this chapter, the FBM was used to calculate the T-stress for an interface crack in a 2D plate. Three different crack cases

were considered, a centre crack (CCP), a single edge notched (SEN) and a double edge notched (DEN). The calculated T-stress values were compared to reference paper to ascertain the accuracy of the FBM. The plotted FBM results alongside the BEM method [34] results shows an excellent agreement.

In Chapter 6, the elastodynamic study of interface crack was performed. The dynamic stress intensity factors and the dynamic T-stress of interface crack was calculated using the finite block method. By substituting the FBM expression for stress and strain into the equilibrium equation, a finite block dynamic formulation for an elastic medium was established. The Laplace transform technique was applied to the finite block equilibrium equation. In solving the Laplace Transform, Durbin's inversion method was adopted.

In this study, a 2D plate with a centre crack is dynamically loaded. Due to symmetry, only half of the plate was considered and the FBM setup for this assessment had only 6 blocks.

An elastodynamic analysis of a homogeneous plate was first assessed using the finite block method and this is covered by Numerical Assessment 1, section 6.4. It is apparent, before the arrival time of the dilatation wave travelling from the top of the plate to the crack tip, the SIF and the T-stress remain zero approximately. By observing the results produced by the FBM method when plotted directly alongside the FEM solution, we may conclude that the two numerical methods are in good agreement.

In Numerical Assessment 2, section 6.5, it was shown that by varying the number of collocation points, the K_{II} values obtained by the finite block method are stable for $M \geq 8$. However, when the number of nodes M is larger than 12, the divergence of numerical solution occurs.

The computational times (PC with Intel CoreTM i5-3470) for these three densities of node (M = 7, 8 and 9) are 218(s), 437(s) and 795(s) respectively. In the finite element analysis, 8850 quadratic elements are used and computational cost is 246(s) on the computer Brokers Trader Workstation. It is evident that the degree of accuracy is not affected significantly by the change of node density.

In Numerical Assessment 3, section 6.6, as expected, for a smaller ratio of r_0/W, the results are closer to that provided by the FEM method (ABAQUS). The maximum values of SIF obtained by FBM and FEM are close to each other for mode I SIF. Therefore, it also indicates that the Williams series for a static interfacial crack can be used directly in the transformed domain analysis with a reasonable level of accuracy. As the absolute values of mode II SIF is much smaller than mode I, the effect of the approximation using Williams series in the singular core is significant.

In Numerical Assessment 4, section 6.7, additional analyses consider a bi-material plate with a centre crack. The dynamic stress intensity factors and the dynamic T-stress plotted alongside an FEM (ABAQUS) result shows good agreement.

In Chapter 7, a new technique called the Stress Proportionality Method based on the proportionality method is proposed. By using the stress intensity factor and the nodal stress ahead of the crack tip for a known problem, the stress intensity factor of an unknown given problem can be determined easily. This method shows that the stress intensity factor can be determined via nodal stress. The stress approach in this chapter tries to diffuse the notion by which the use of nodal stress gives unstable results for the stress intensity factor. For convenience, ABAQUS was used for calculating the nodal stress ahead of the crack tip for both the given known problem and the given unknown problem. The extracted stress intensity factor for the given known problem is utilised in calculating the stress intensity factor for the given unknown problem.

8.2. General Observation

Seeing from the numerical assessments, it is clear that the finite block method for a static load problem is very efficient, stable and accurate. In addition, due to the difficulty in resolving the Williams series solution in the transformed domain, the approximation by using static Williams series is shown to have been successfully applied to a cracked plate under dynamic loading. The Williams series for a static case can capture the dynamic stress intensity factor and the T-stress for an interface crack between bi-materials. The finite block method is of the following characteristics when compared with other numerical schemes:

1) A physical problem with a complex geometry can be easily represented by very few blocks (similar to an element).
2) Collocation points for each block are determined using the mapping technique.
3) Using the Lagrange series interpolation, one-dimensional differential matrix $\mathbf{D}_0$ is easily obtained.
4) Higher order partial differential matrices can be determined straight-away from $\mathbf{D}_0$.
5) The governing equations are in a strong form which means it can be extended to any type of partial differential equation including elasticity problems.
6) In the applications of fracture mechanics, a high degree of accuracy is obtained for static cases as the singular core is introduced centred at the crack tip.
7) The FBM method is sensitive for a large number of nodes due to high order Lagrange expansion.

8.3. Technical Contributions to Knowledge

The technical findings and original contributions to knowledge that has resulted from this research can be summarised as follows:

- In this research, a meshless method called the finite block method is proposed for the first time to evaluate interface crack between bi-materials. The advantages of the finite block method over other meshless methods will become prevalent with further studies and evaluation of different types of cracks.
- Using a defined set of collocation points, the first order one-dimensional differential matrix is developed in terms of the nodal values. The Lagrange interpolation series was adopted for the construction of the first order differential matrix.
- For a two-dimensional domain, the transformation matrix is applied to the derivative on the primary axis in order to determine the unknown derivative along a secondary axis.
- For a two-dimensional problem, the mapping technique is also implemented using a quadratic block or element with 8 nodes. This means the first order differential

matrix is calculated once and can be mapped onto all the blocks in a physical domain. Unlike the FBM, the Meshless Local Petrov-Galerkin Method, the Meshless Collocation Method and the Point Interpolation Method employ a support domain in their numerical analysis.

- The finite block method incorporates all the major advantages of meshless method. When compared against other meshless methods, parameters such as the size or number of nodes in a local support domain is not required in the finite block method. The use of the local support domain is a prominent technique used by the MLPG method [52, 62]. In the finite block method, a block called the normalised square domain is proposed instead. By using a single block with prescribed nodes at the beginning of the analysis the first order one-dimensional differential matrix is determined.
- As presented in this research, a single normalised square domain is defined at the beginning of each analysis and the first order one-dimensional differential matrix is determined using the Lagrange interpolation series. Thus, the FBM interpolations of differential equations are in the strong form. There is no need for background mesh or cells prior to the numerical interpolation which is the standard approach used by the Element Free Galerkin method.
- The Lagrange series is proposed for evaluating the governing equations for the two-dimensional bi-material plate.
- The polar form of the equilibrium equation for plane elasticity is developed for the first time using the first order one-dimensional differential matrix. The formulations for the finite block method in the polar form is systematically presented.
- The stresses and displacements in the Williams series is developed using the complex potential method proposed by Kolosov and Muskhelishvili. The constant values A_{In} and A_{Cn} resulting from this version of the Williams series are determined by the finite block method using the singular core centred at the crack tip. Subsequently, the stress intensity factors and the T-stresses are calculated for interface cracks between bi-materials.
- A relationship between the singular core centred at the crack tip and the Williams series is presented for both the Cartesian coordinate system and the polar

coordinate system. For the Cartesian coordinate system, a polygonal core is implemented and for the polar coordinate system, it was practical to apply a circular core.

- In this research, the Williams expansion series for an interface crack and a singular core is proposed for the first time. To accurately calculate the stress intensity factor and the T-stress, a technique which combines the Williams expansion series and a singular core centred at the crack tip is proposed for interface crack between bi-materials. By using the singular core, the finite block will approximate the constants from the Williams expansion series and in turn calculate the SIF and the T-stress. The FBM uses the singular core for the approximation of the near crack tip displacements and stresses for the interface crack between bi-materials. Meanwhile, other numerical methods like the FEM (ABAQUS) method and BEM method [34] incorporates techniques like the interactive integral method for crack analysis.
- In most FEM programs, the quarter-point element is utilised for crack analysis. However, this technique requires a high mesh density in order to get accurate results. This can be avoided by applying a high mesh density localised at the crack tip. The introduction of localised meshes will also require transitional meshes as we move further away from the crack tip region. It is very difficult to achieve a smooth transitional mesh between the fine mesh region and the course mesh. By contrast, transitional blocks or meshes are not required in the FBM method. Hence, the use of a singular core around the crack tip by the FBM method is a significant advantage over the equivalent FEM model. In the FBM program, the implementation of a singular core has shown to be robust in calculating the stress intensity. The number of blocks required in forming the singular core is only a fraction of the elements applied in an equivalent FEM analysis.
- After an extensive investigation into elastodynamics of interface cracks, it was concluded that there are no analytical solutions for interface crack between bi-materials. Therefore, an elastodynamic solution proposed for the FBM is presented. The dynamic SIF and the dynamic T-stress are calculated by adopting the Durbin [115] strategy for dynamic analysis and replacing the transformed solution with the Williams series for a static state. The accurate calculation of the

dynamic SIF and the dynamic T-stress is credited to the control of the singular core at the crack tip.

- The FBM program for dynamic analysis needs some form of verification. However, due to the unavailability of dynamic numerical solutions for interface crack between bi-materials, the only alternative is to perform a numerical analysis using an existing numerical program. At the time of this research, the ABAQUS commercial software was deemed credible for the verification of the FBM program. Work done in this research has shown that the FBM can produce results which can match the credibility and accuracy of ABAQUS but using minimum resources and computational effort. With further development and verification, the FBM method can serve as a benchmark and a verification tool for other numerical methods in the future.
- The FBM method has an alternative approach to analysing interface cracks when compared to the FEM method. The difference between the two numerical methods is the use of elements or blocks. The framework and mathematical concepts of the FBM method developed for static and elastodynamic analyses of interface cracks will definitely add to the existing knowledge on fracture dynamics.
- As a result of comparing the FBM to other numerical techniques, improvements to the proportionality method is proposed. The improved technique based on the proportionality method called the Stress Proportionality Method is presented. The development of this technique is presented in Chapter 7 of this thesis and some of the major disadvantages of the original proportionality method were addressed. The accuracy of this new technique is demonstrated by comparing the SIF results against ABAQUS (*J*-Integral technique) and the FBM method (Williams series). The success of this technique means, the nodal values of displacement and stress from the FBM can be utilised in the future to determine the SIF for an interface crack between bi-materials.

8.4. Future Work

Some features and capabilities of the finite block method as presented in this thesis remain open for further study. Thus, future studies can focus on the following aspects;

- In this thesis, the finite block method is developed in the strong form. A future study can focus on developing a weak form of the FBM method. This can lead to a more stable and convergence solution.
- The crack length use in the finite block model were chosen without increasing the number of blocks. This can lead to a suppression of the blocks ahead the crack tip. Future work should consider using blocks with equal length on each side of the crack tip. Priority should be given to the shape and dimensions of the singular core. This can reduce or eliminate the nodal density distortions around the crack tip.
- This research mainly focused on simple geometry and straight-line cracks. However, the finite block method can be extended to study complex geometries with cracks. By introducing a slant crack in to the geometry, a mixed mode fracture effect is created. For mixed mode crack, it means a derivation of the William's series expansion will be required to cover the different crack modes and then combining their results.
- Dynamic study of stationary cracks is presented in this thesis. Therefore, further work on the Finite Block Method can be extended to the prediction of crack extension since the meshless nature of this method requires no remeshing. However, some special treatment of the blocks arrangement and the singular core at the crack tip may require some rework.

8.5. List of Publication

Aspects of the work presented in this thesis have been published or presented in the following journal papers and conferences:

Hinneh, P., and P. H. Wen. "Evaluation of Bi-material crack using the finite block method." Journal of Physics: Conference Series. Vol. 734. No. 3. IOP Publishing, 2016.

Li, M., Meng, L. X., Hinneh, P., & Wen, P. H. "Finite block method for interface cracks." Engineering Fracture Mechanics 156 (2016): 25-40.

Hinneh, P., & Wen, P. H. "Displacement Correlation Technique for Interface Crack by FEM." Key Engineering Materials. Vol. 713. Trans Tech Publications, 2016.

Bibliography

[1] Li, Fang Zhong, C. Fong Shih, and A. Needleman. "A comparison of methods for calculating energy release rates." Engineering Fracture Mechanics 21, no. 2 (1985): 405-421.

[2] Irwin, George R. "Analysis of stresses and strains near the end of a crack traversing a plate." J. appl. Mech. (1957).

[3] Westergaard, Harold M. "Bearing pressures and cracks." Journal of applied mechanics 6, no. 2 (1939): A49-A53.

[4] Griffith, Alan A., and M. Eng. "VI. The phenomena of rupture and flow in solids." Phil. Trans. R. Soc. Lond. A 221, no. 582-593 (1921): 163-198.

[5] Fett T and Munz D: 'Stress intensity factors and weight functions', Computational Mechanics Publications, Southampton, 1997.

[6] Mandell, John F., Douglas S. Cairns, Daniel D. Samborsky, Robert B. Morehead, and Darrin H. Haugen. "Prediction of delamination in wind turbine blade structural details." In ASME 2003 Wind Energy Symposium, pp. 202-213. American Society of Mechanical Engineers, 2003.

[7] Broek, D., "Elementary Engineering Fracture Mechanics," 4th Edition, Kluwer Academic Publishers, 1986.

[8] Hadj-Ahmed, Réda, Gilles Foret, and Alain Ehrlacher. "Probabilistic analysis of failure in adhesive bonded joints." Mechanics of materials 33.2 (2001): 77-84.

[9] Freund LB. Dynamic fracture mechanics. Cambridge: Cambridge University Press; 1990.

[10] Sladek, J., V. Sladek, and P. Fedelinski. "Computation of the second fracture parameter in elastodynamics by the boundary element method." Advances in Engineering Software 30.9 (1999): 725-734.

[11] Sladek, J., V. Sladek, and P. Fedelinski. "Contour integrals for mixed-mode crack analysis: effect of nonsingular terms." Theoretical and applied fracture mechanics 27.2 (1997): 115-127.

[12] Sladek, J., V. Sladek, M. Repka, and C. L. Tan. "Evaluation of the T-stress for cracks in functionally graded materials by the FEM." Theoretical and Applied Fracture Mechanics 86 (2016): 332-341.

[13] Mataga, P. A., L. B. Freund, and J. W. Hutchinson. "Crack tip plasticity in dynamic fracture." Journal of Physics and Chemistry of Solids 48.11 (1987): 985-1005.

[14] Anderson, Ted L., and T. L. Anderson. Fracture mechanics: fundamentals and applications. CRC press, 2005.

[15] Kundu, Tribikram. Fundamentals of fracture mechanics. CRC press, 2008.

[16] Banerjee, Sourav, and Tribikram Kundu. "Elastic wave propagation in sinusoidally corrugated waveguides." The Journal of the Acoustical Society of America 119.4 (2006).

[17] Comninou, Maria. "An overview of interface cracks." Engineering Fracture Mechanics 37.1 (1990): 197-208.

[18] Williams, M. L. "The stresses around a fault or crack in dissimilar media." Bulletin of the seismological society of America 49.2 (1959): 199-204.

[19] Rice, J. R., and George C. Sih. "Plane problems of cracks in dissimilar media." Journal of Applied Mechanics 32.2 (1965): 418-423.

[20] Hutchinson, John W. "Mixed mode fracture mechanics of interfaces." Metal-ceramic interfaces (1990): 295-306.

[21] Hutchinson, John W., M. E. Mear, and James R. Rice. "Crack paralleling an interface between dissimilar materials." Journal of Applied Mechanics 54.4 (1987): 828-832.

[22] Atkinson, C. "On stress singularities and interfaces in linear elastic fracture mechanics." International Journal of Fracture 13.6 (1977): 807-820.

[23] Zak, A. R., and M. L. Williams. "Crack point stress singularities at a bi-material interface." (1962).

[24] Savage, W. F., E. F. Nippes, and E. S. Szekeres. "Study of weld interface phenomena in a low alloy steel." Welding Journal 55.9 (1976): 260.

[25] Godiganur, Vishwanath S., and Shivakumar Biradar. "Comparison of friction stirs welding technique with conventional welding methods." International Journal of Research in Engineering and Technology 3 (2014): 572-6.

[26] Kim, Y. G., H. Fujii, T. Tsumura, T. Komazaki, and K. Nakata. "Three defect types in friction stir welding of aluminum die casting alloy." Materials Science and Engineering: A 415, no. 1-2 (2006): 250-254.

[27] Li, Ying, L. E. Murr, and J. C. McClure. "Flow visualization and residual microstructures associated with the friction-stir welding of 2024 aluminum to 6061 aluminum." Materials Science and Engineering: A 271.1 (1999): 213-223.

[28] Ilangovan, M., S. Rajendra Boopathy, and V. Balasubramanian. "Effect of tool pin profile on microstructure and tensile properties of friction stir welded dissimilar AA 6061–AA 5086 aluminium alloy joints." Defence Technology11.2 (2015): 174-184.

[29] FRANC, Aleš. "heterogeneous joints between steel and aluminium made by modified MIG process." (Metal 2010).

[30] Yılmaz, M., M. Çöl, and M. Acet. "Interface properties of aluminum/steel friction-welded components." Materials Characterization 49.5 (2002): 421-429.

[31] Rice, James R. "A path independent integral and the approximate analysis of strain concentration by notches and cracks." Journal of applied mechanics35.2 (1968): 379-386.

[32] Zhu, W. X., and D. J. Smith. "On the use of displacement extrapolation to obtain crack tip singular stresses and stress intensity factors." Engineering Fracture Mechanics 51.3 (1995): 391-400.

[33] Fu, Pengcheng, Scott M. Johnson, Randolph R. Settgast, and Charles R. Carrigan. "Generalized displacement correlation method for estimating stress intensity factors." Engineering Fracture Mechanics 88 (2012): 90-107.

[34] Sladek, J., and V. Sladek. "Evaluations of the T-stress for interface cracks by the boundary element method." Engineering fracture mechanics 56.6 (1997): 813-825.

[35] Miyazaki, N., T. Ikeda, T. Soda, and T. Munakata. "Stress intensity factor analysis of interface crack using boundary element method—application of contour-integral method." Engineering Fracture Mechanics 45, no. 5 (1993): 599-610.

[36] Lee, S. S., J. G. Kim, and J. K. Hwang. "Boundary element analysis of stress intensity factor for interface crack in elastic and viscoelastic bimaterials." WIT Transactions on Modelling and Simulation 15 (1970).

[37] Courtin, S., C. Gardin, G. Bezine, and H. Ben Hadj Hamouda. "Advantages of the J-integral approach for calculating stress intensity factors when using the commercial finite element software ABAQUS." Engineering Fracture Mechanics 72, no. 14 (2005): 2174-2185.

[38] Barsoum, Roshdy S. "On the use of isoparametric finite elements in linear fracture mechanics." International journal for numerical methods in engineering 10.1 (1976): 25-37.

[39] Tan, C. L., and X. Wang. "The use of quarter-point crack-tip elements for T-stress determination in boundary element method analysis." Engineering fracture mechanics 70.15 (2003): 2247-2252.

[40] Dolbow, J. O. H. N., and Ted Belytschko. "A finite element method for crack growth without remeshing." International journal for numerical methods in engineering 46.1 (1999): 131-150.

[41] Belytschko, Ted, and Tom Black. "Elastic crack growth in finite elements with minimal remeshing." International journal for numerical methods in engineering 45.5 (1999): 601-620.

[42] Belytschko, Ted, Nicolas Moës, Shuji Usui, and Chandu Parimi. "Arbitrary discontinuities in finite elements." International Journal for Numerical Methods in Engineering 50, no. 4 (2001): 993-1013.

[43] Belytschko, Ted, et al. "Dynamic crack propagation based on loss of hyperbolicity and a new discontinuous enrichment." International journal for numerical methods in engineering 58.12 (2003): 1873-1905.

[44] Song, Jeong-Hoon, Pedro Areias, and Ted Belytschko. "A method for dynamic crack and shear band propagation with phantom nodes." International Journal for Numerical Methods in Engineering 67.6 (2006): 868-893.

[45] Tan, C. L., and Y. L. Gao. "Treatment of bimaterial interface crack problems using the boundary element method." Engineering Fracture Mechanics 36.6 (1990): 919-932.

[46] Kalthoff, J. F. "Fracture behavior under high rates of loading." Engineering fracture mechanics 23.1 (1986): 289-298.

[47] Huang, Z., P. Kumar, I. Dutta, J. H. L. Pang, and R. Sidhu. "A general methodology for calculating mixed mode stress intensity factors and fracture toughness of solder joints with interfacial cracks." Engineering Fracture Mechanics 131 (2014): 9-25.

[48] Owen, David Roger Jones, and A. J. Fawkes. "Engineering fracture mechanics: numerical methods and applications." Pineridge Press Ltd, 91 West Cross Lane, West Cross, Swansea, UK, 1983. 305 (1983).

[49] Sladek, J., V. Sladek, and P. Fedelinski. "Integral formulation for elastodynamic T-stresses." International journal of fracture 84.2 (1997): 103-116.

[50] Monaghan, Joe J. "Smoothed particle hydrodynamics." Annual review of astronomy and astrophysics 30 (1992): 543-574.

[51] Liu, M. B., and G. R. Liu. "Smoothed particle hydrodynamics (SPH): an overview and recent developments." Archives of computational methods in engineering 17.1 (2010): 25-76.

[52] Atluri, Satya N., and Tulong Zhu. "A new meshless local Petrov-Galerkin (MLPG) approach in computational mechanics." Computational mechanics 22.2 (1998): 117-127.

[53] Belytschko, Ted, Yun Yun Lu, and Lei Gu. "Element-free Galerkin methods." International journal for numerical methods in engineering 37.2 (1994): 229-256.

[54] Lucy, Leon B. "A numerical approach to the testing of the fission hypothesis." The astronomical journal 82 (1977): 1013-1024.

[55] Gingold, Robert A., and Joseph J. Monaghan. "Smoothed particle hydrodynamics: theory and application to non-spherical stars." Monthly notices of the royal astronomical society 181.3 (1977): 375-389.

[56] Morris, Joseph Peter. Analysis of smoothed particle hydrodynamics with applications. Australia: Monash University, 1996.

[57] Monaghan, Joe J. "Why particle methods work." SIAM Journal on Scientific and Statistical Computing 3.4 (1982): 422-433.

[58] Monaghan, Joe J. "Smoothed particle hydrodynamics." Reports on progress in physics 68.8 (2005): 1703.

[59] Nayroles, B., G. Touzot, and P. Villon. "Generalizing the finite element method: diffuse approximation and diffuse elements." Computational mechanics 10.5 (1992): 307-318.

[60] Krysl, Petr, and Ted Belytschko. "Analysis of thin shells by the element-free Galerkin method." International Journal of Solids and Structures 33.20 (1996): 3057-3080.

[61] Hegen, D. "Element-free Galerkin methods in combination with finite element approaches." Computer Methods in Applied Mechanics and Engineering 135.1 (1996): 143-166.

[62] Atluri, Satya N., H-G. Kim, and J. Ya Cho. "A critical assessment of the truly meshless local Petrov-Galerkin (MLPG), and local boundary integral equation (LBIE) methods." Computational mechanics 24.5 (1999): 348-372.

[63] Gu, YuanTong, and Gui-Rong Liu. "A meshless local Petrov-Galerkin (MLPG) method for free and forced vibration analyses for solids." Computational Mechanics 27.3 (2001): 188-198.

[64] Atluri, S. N., and T-L. Zhu. "The meshless local Petrov-Galerkin (MLPG) approach for solving problems in elasto-statics." Computational Mechanics 25.2-3 (2000): 169-179.

[65] Gu, YuanTong, and Gui-Rong Liu. "A local point interpolation method for static and dynamic analysis of thin beams." Computer Methods in Applied Mechanics and Engineering 190.42 (2001): 5515-5528.

[66] Liu, Gui-Rong, and YuanTong Gu. "Meshless local Petrov–Galerkin (MLPG) method in combination with finite element and boundary element approaches." Computational Mechanics 26.6 (2000): 536-546.

[67] Wen, P. H., and M. H. Aliabadi. "An improved meshless collocation method for elastostatic and elastodynamic problems." Communications in Numerical Methods in Engineering 24.8 (2008): 635-651.

[68] Zhang, Xiong, Xiao-Hu Liu, Kang-Zu Song, and Ming-Wan Lu. "Least-squares collocation meshless method." International Journal for Numerical Methods in Engineering 51, no. 9 (2001): 1089-1100.

[69] Oñate, Eugenio, F. Perazzo, and J. Miquel. "A finite point method for elasticity problems." Computers & Structures 79.22 (2001): 2151-2163.

[70] Onate, E., S. Idelsohn, O. C. Zienkiewicz, R. L. Taylor, and C. Sacco. "A stabilized finite point method for analysis of fluid mechanics problems." Computer Methods in Applied Mechanics and Engineering 139, no. 1-4 (1996): 315-346.

[71] Li, M., and P. H. Wen. "Finite block method for transient heat conduction analysis in functionally graded media." International Journal for Numerical Methods in Engineering 99.5 (2014): 372-390.

[72] Wen, P. H., P. Cao, and T. Korakianitis. "Finite block method in elasticity." Engineering Analysis with Boundary Elements 46 (2014): 116-125.

[73] Liu, Gui-Rong, and YuanTong Gu. "A point interpolation method for two-dimensional solids." International Journal for Numerical Methods in Engineering 50.4 (2001): 937-951.

[74] Liu, G. R., and Y. T. Gu. "A local radial point interpolation method (LRPIM) for free vibration analyses of 2-D solids." Journal of Sound and vibration 246.1 (2001): 29-46.

[75] Wang, J. G., and G. R. Liu. "A point interpolation meshless method based on radial basis functions." International Journal for Numerical Methods in Engineering 54.11 (2002): 1623-1648.

[76] Song, Chongmin. "Evaluation of power-logarithmic singularities, T-stresses and higher order terms of in-plane singular stress fields at cracks and multi-material corners." Engineering Fracture Mechanics 72.10 (2005): 1498-1530.

[77] Shih, C. F., and R. J. Asaro. "Elastic-plastic analysis of cracks on bimaterial interfaces: part I—small scale yielding." Journal of Applied Mechanics 55.2 (1988): 299-316.

[78] Natarajan, Sundararajan, Chongmin Song, and Salim Belouettar. "Numerical evaluation of stress intensity factors and T-stress for interfacial cracks and cracks terminating at the interface without asymptotic enrichment." Computer methods in applied mechanics and engineering 279 (2014): 86-112.

[79] An, X. M., Z. Y. Zhao, H. H. Zhang, and L. He. "Modeling bimaterial interface cracks using the numerical manifold method." Engineering Analysis with Boundary Elements 37, no. 2 (2013): 464-474.

[80] Aslantaş, K., and S. Taşgetiren. "Finite element analysis of longitudinal debonding between fibre and matrix interface." (2004).

[81] Fett, Theo. "Stress intensity factors and T-stress for internally cracked circular disks under various boundary conditions." Engineering Fracture Mechanics 68.9 (2001): 1119-1136.

[82] Zanganeh, M., R. A. Tomlinson, and J. R. Yates. "T-stress determination using thermoelastic stress analysis." The Journal of Strain Analysis for Engineering Design 43.6 (2008): 529-537.

[83] Bouchard, P-O., Marc Bernacki, and David M. Parks. "Analysis of stress intensity factors and T-stress to control crack propagation for kerf-less spalling of single crystal silicon foils." Computational Materials Science 69 (2013): 243-250.

[84] Ayatollahi, M. R., M. J. Pavier, and D. J. Smith. "Determination of T-stress from finite element analysis for mode I and mixed mode I/II loading." International journal of fracture 91.3 (1998): 283-298.

[85] Chen, Buo, and David A. Dillard. "The effect of the T-stress on crack path selection in adhesively bonded joints." International journal of adhesion and adhesives 21.5 (2001): 357-368.

[86] Kim, Jeong-Ho, and Glaucio H. Paulino. "T-stress, mixed-mode stress intensity factors, and crack initiation angles in functionally graded materials: a unified approach using the interaction integral method." Computer Methods in Applied Mechanics and Engineering 192.11 (2003): 1463-1494.

[87] Toshio, Nakamura, and David M. Parks. "Determination of elastic T-stress along three-dimensional crack fronts using an interaction integral." International Journal of Solids and Structures 29.13 (1992): 1597-1611.

[88] Kodancha, K. G., and S. K. Kudari. "Variation of stress intensity factor and elastic T-stress along the crack-front in finite thickness plates." Frattura ed Integrità Strutturale 8 (2009): 45.

[89] Thompson, Joe F., Zahir UA Warsi, and C. Wayne Mastin. Numerical grid generation: foundations and applications. Vol. 45. Amsterdam: North-holland, 1985.

[90] Khursheed, Anjam. The finite element method in charged particle optics. Vol. 519. Springer Science & Business Media, 2012.

[91] Gupta, M., R. C. Alderliesten, and R. Benedictus. "A review of T-stress and its effects in fracture mechanics." Engineering Fracture Mechanics 134 (2015): 218-241.

[92] Fett, T. "A Green's function for T-stresses in an edge-cracked rectangular plate." Engineering Fracture Mechanics 57.4 (1997): 365-373.

[93] Fett, T. "T-stresses in rectangular plates and circular disks." Engineering Fracture Mechanics 60.5 (1998): 631-652.

[94] Li, J., X. Wang, and C. L. Tan. "Weight functions for the determination of stress intensity factor and T-stress for edge-cracked plates with built-in ends." International journal of pressure vessels and piping 81.3 (2004): 285-296.

[95] Fehl, Barry D., and Kevin Z. Truman. "An evaluation of fracture mechanics quarter-point displacement techniques used for computing stress intensity factors." Engineering Structures 21.5 (1999): 406-415.

[96] Fett, Theo. "Stress intensity factors and T-stress for single and double-edge-cracked circular disks under mixed boundary conditions." Engineering Fracture Mechanics 69.1 (2002): 69-83.

[97] Kfouri, A P. "Some evaluations of the elastic T-term using Eshelby's method." International Journal of Fracture 30, no. 4 (1986): 301-315.

[98] Du, Z. Z., and J. W. Hancock. "The effect of non-singular stresses on crack-tip constraint." Journal of the Mechanics and Physics of Solids 39, no. 4 (1991): 555-567.

[99] Larsson, Stig-Göran, and A_J Carlsson. "Influence of non-singular stress terms and specimen geometry on small-scale yielding at crack tips in elastic-plastic materials." Journal of the Mechanics and Physics of Solids 21, no. 4 (1973): 263-277.

[100] Novotný, Ladislav. "Calculation of T–stress on 3D specimens with crack." Procedia Engineering 48 (2012): 489-494.

[101] O'Dowd, Noel P., C. F. Shih, and Robert H. Dodds. "The role of geometry and crack growth on constraint and implications for ductile/brittle fracture." Constraint Effects in Fracture Theory and Applicatons: Second Volume. ASTM International, 1995.

[102] Cotterell, B. "Notes on the paths and stability of cracks." International Journal of Fracture Mechanics 2.3 (1966): 526-533.

[103] Chen, Chuin-Shan, Paul A. Wawrzynek, and Anthony R. Ingraffea. "Prediction of residual strength and curvilinear crack growth in aircraft fuselages." Aiaa Journal 40.8 (2002): 1644-1652.

[104] Williams, M. L. On the stress distribution at the base of a stationary crack. J. Appl. Mech., 1957, 24, 109–114.

[105] Shah, P. D., C. L. Tan, and X. Wang. "Evaluation of T-Stress for an Interface Crack Lying Between Dissimilar Anisotropic Solids Using BEM." ICCES: International Conference on Computational & Experimental Engineering and Sciences. Vol. 1. No. 2. 2007.

[106] Kim, Jeong-Ho, and Glaucio H. Paulino. "The interaction integral for fracture of orthotropic functionally graded materials: evaluation of stress intensity factors." International Journal of Solids and Structures 40.15 (2003): 3967-4001.

[107] Sutradhar, Alok, and Glaucio H. Paulino. "Symmetric Galerkin boundary element computation of T-stress and stress intensity factors for mixed-mode cracks by the interaction integral method." Engineering Analysis with Boundary Elements 28.11 (2004): 1335-1350.

[108] Shivakumar, K. N., and I. S. Raju. "An equivalent domain integral method for three-dimensional mixed-mode fracture problems." Engineering fracture mechanics 42.6 (1992): 935-959.

[109] Yu, Hongjun, Linzhi Wu, and Hui Li. "T-stress evaluations of an interface crack in the materials with complex interfaces." International journal of fracture (2012): 1-13.

[110] Walters, Matthew C., Glaucio H. Paulino, and Robert H. Dodds. "Interaction integral procedures for 3-D curved cracks including surface tractions." Engineering Fracture Mechanics 72.11 (2005): 1635-1663.

[111] Amit, K. C., and Jeong-Ho Kim. "Interaction integrals for thermal fracture of functionally graded materials." Engineering Fracture Mechanics 75.8 (2008): 2542-2565.

[112] Koppenhoefer, Kyle C., and Robert H. Dodds. "Constraint effects on fracture toughness of impact-loaded, precracked Charpy specimens." Nuclear engineering and design 162.2-3 (1996): 145-158.

[113] Rice, James R. "Conserved integrals and energetic forces." Fundamentals of Deformation and Fracture. Cambridge University Press, Cambridge (1985): 33-56.

[114] Sladek J, Sladek V. Evaluation of T-stresses and stress intensity factors in stationary thermoelasticity by the conservation integral method. Int J Fract 1997;86(3):199–219.

[115] Durbin, F. "Numerical inversion of Laplace transforms: an efficient improvement to Dubner and Abate's method." The Computer Journal 17.4 (1974): 371-376.

[116] Liu, P., T. Q. Bui, Ch Zhang, T. T. Yu, G. R. Liu, and M. V. Golub. "The singular edge-based smoothed finite element method for stationary dynamic crack problems in 2D elastic solids." Computer Methods in Applied Mechanics and Engineering 233 (2012): 68-80.

[117] Deng, Xiaomin. "The asymptotic structure of transient elastodynamic fields at the tip of a stationary crack." Proceedings of the Royal Society of London A: Mathematical, Physical and Engineering Sciences. Vol. 446. No. 1926. The Royal Society, 1994.

[118] Fett, T. Stress Intensity Factors, T-Stresses, Weight Functions. Universitätsverlag Karlsruhe, 2008. ISBN 978-3-86644-235-1.

[119] Yu, Tiantang, Tinh Quoc Bui, Peng Liu, Chuanzeng Zhang, and Sohichi Hirose. "Interfacial dynamic impermeable cracks analysis in dissimilar piezoelectric materials under coupled electromechanical loading with the extended finite element method." International Journal of Solids and Structures 67 (2015): 205-218.

[120] Bui, Tinh Quoc, and Chuanzeng Zhang. "Extended finite element simulation of stationary dynamic cracks in piezoelectric solids under impact loading." Computational Materials Science 62 (2012): 243-257.

[121] Liu, Peng, Tiantang Yu, Tinh Quoc Bui, and Chuanzeng Zhang. "Transient dynamic crack analysis in non-homogeneous functionally graded piezoelectric materials by the X-FEM." Computational Materials Science 69 (2013): 542-558.

[122] Bui, Tinh Quoc. "Extended isogeometric dynamic and static fracture analysis for cracks in piezoelectric materials using NURBS." Computer Methods in Applied Mechanics and Engineering 295 (2015): 470-509.

[123] Hadjesfandiari, Ali R., and Gary F. Dargush. "Analysis of bi-material interface cracks with complex weighting functions and non-standard quadrature." International Journal of Solids and Structures 48.10 (2011): 1499-1512.

[124] Nagashima, Toshio, Youhei Omoto, and Shuichi Tani. "Stress intensity factor analysis of interface cracks using X-FEM." International Journal for Numerical Methods in Engineering 56.8 (2003): 1151-1173.

[125] Rice, JRf. "Elastic fracture mechanics concepts for interfacial cracks." J. Appl. Mech.(Trans. ASME) 55.1 (1988): 98-103.

[126] Dally, J. W., and D. B. Barker. "Dynamic measurements of initiation toughness at high loading rates." Experimental Mechanics 28.3 (1988): 298-303.

[127] Owen, D. M., S. Zhuang, A. J. Rosakis, and G. Ravichandran. "Experimental determination of dynamic crack initiation and propagation fracture toughness in thin aluminum sheets." International Journal of Fracture 90, no. 1-2 (1998): 153-174.

[128] Owen, David M., Ares J. Rosakis, and William L. Johnson. "Dynamic failure mechanisms in beryllium-bearing bulk metallic glasses." MRS Proceedings. Vol. 554. Cambridge University Press, 1998.

[129] Basu, Sumit, and R. Narasimhan. "Finite element simulation of mode I dynamic, ductile fracture initiation." International journal of solids and structures 33.8 (1996): 1191-1207.

[130] Basu, Sumit, and R. Narasimhan. "A numerical investigation of loss of crack tip constraint in a dynamically loaded ductile specimen." Journal of the Mechanics and Physics of Solids 48.9 (2000): 1967-1985.

[131] Houbolt, J. C. "A recurrence matrix solution for the dynamic response of elastic aircraft." Journal of the Aeronautical Sciences 17, no. 9 (1950): 540-550.

[132] Gray, L. J., A-V. Phan, Glaucio H. Paulino, and T. Kaplan. "Improved quarter-point crack tip element." Engineering Fracture Mechanics 70, no. 2 (2003): 269-283.

[133] Abaqus/Standard user manual, version 6.9-2. Dassault Systemes Simulia Corp, USA

[134] Paulino, Glaucio H., and Leonard J. Gray. "Crack tip interpolation, revisited." SIAM Journal on Applied Mathematics 58.2 (1998): 428-455.

[135] Noda, Nao-Aki, and Xin Lan. "Stress intensity factors for an edge interface crack in a bonded semi-infinite plate for arbitrary material combination." International Journal of Solids and Structures 49.10 (2012): 1241-1251.

[136] Zhang, Yu, Nao-Aki Noda, Ken-Taro Takaishi, and Xin Lan. "Stress intensity factors of a central interface crack in a bonded finite plate and periodic interface cracks under arbitrary material combinations." Engineering Fracture Mechanics 78, no. 6 (2011): 1218-1232.

[137] Oda, Kazuhiro, Naoaki Noda, and Satya N. Atluri. "Accurate determination of stress intensity factor for interface crack by finite element method." Key Engineering Materials. Vol. 353. Trans Tech Publications, 2007.

[138] Lan, Xin, Nao-Aki Noda, Kengo Mithinaka, and Yu Zhang. "The effect of material combinations and relative crack size to the stress intensity factors at the crack tip of a bi-material bonded strip." Engineering Fracture Mechanics 78, no. 14 (2011): 2572-2584.

[139] Teranishi, Takahiro, and Hironobu Nisitani. "Determination of highly accurate values of stress intensity factor in a plate of arbitrary form by FEM." Transactions of the Japan Society of Mechanical Engineers, Series A 65.638 (1999): 2032-2037.

[140] Nisitani, H., and T. Teranishi. "Highly accurate values of K_I and K_{II} of axially symmetrical cracked body subjected to tension obtained by FEM." WIT Transactions on Engineering Sciences 26 (2000).

[141] Newmark, Nathan M. "A method of computation for structural dynamics." Journal of the engineering mechanics division 85.3 (1959): 67-94.

[142] Nistor, Ionel, Olivier Pantalé, and Serge Caperaa. "Numerical implementation of the extended finite element method for dynamic crack analysis." Advances in Engineering Software 39.7 (2008): 573-587.

[143] Wen, P. H., and M. H. Aliabadi. "Elastodynamic problems by meshless local integral method: Analytical formulation." Engineering Analysis with Boundary Elements 37.5 (2013): 805-811.

[144] Nishioka, Toshihisa. "The state of the art in computational dynamic fracture mechanics." JSME international journal. Ser. A, Mechanics and material engineering 37.4 (1994): 313-333.

[145] Geubelle, Philippe H., and James R. Rice. "A spectral method for three-dimensional elastodynamic fracture problems." Journal of the Mechanics and Physics of Solids 43.11 (1995): 1791-1824.

[146] Achenbach, J. D. "Elastodynamic Fracture Mechanics." In SIAM AMS Proc, vol. 12, pp. 3-20. 1979.

[147] Sladek, J., and V. Sladek. "Computation of thermoelastoplastic stresses in crack problems by the BEM." International journal of Fracture 83.4 (1997): 359-378.

[148] Smith, D. J., M. R. Ayatollahi, and M. J. Pavier. "On the consequences of T-stress in elastic brittle fracture." In Proceedings of the Royal Society of London A: Mathematical, Physical and Engineering Sciences, vol. 462, no. 2072, pp. 2415-2437. The Royal Society, 2006.

[149] Finnie, I., and A. Saith. "A note on the angled crack problem and the directional stability of cracks." International Journal of Fracture 9.4 (1973): 484-486.

[150] Williams, J. G., and P. D. Ewing. "Fracture under complex stress—the angled crack problem." International Journal of Fracture 8.4 (1972): 441-446.

[151] Smith, D. J., M. R. Ayatollahi, and M. J. Pavier. "The role of T-stress in brittle fracture for linear elastic materials under mixed-mode loading." Fatigue & Fracture of Engineering Materials & Structures 24.2 (2001): 137-150.

[152] Matvienko, Yu G. "Maximum average tangential stress criterion for prediction of the crack path." International Journal of Fracture (2012): 1-6.

[153] Wang, X. "Elastic T-stress for cracks in test specimens subjected to non-uniform stress distributions." Engineering Fracture Mechanics 69.12 (2002): 1339-1352.

[154] Su, R. K. L., and H. Y. Sun. "A brief note on elastic T-stress for centred crack in anisotropic plate." International journal of fracture 131.1 (2005): 53-58.

[155] Shim, Do-Jun, Glaucio H. Paulino, and Robert H. Dodds. "A boundary layer framework considering material gradation effects." Engineering fracture mechanics 73.5 (2006): 593-615.

[156] Shim, Do-Jun, Glaucio H. Paulino, and Robert H. Dodds. "J resistance behavior in functionally graded materials using cohesive zone and modified boundary layer models." International Journal of Fracture 139.1 (2006): 91-117.

[157] Kim, Jeong-Ho, and K. C. Amit. "A generalized interaction integral method for the evaluation of the T-stress in orthotropic functionally graded materials under thermal loading." Journal of Applied Mechanics 75.5 (2008): 051112.

[158] Banks-Sills, Leslie, and Dov Sherman. "Comparison of methods for calculating stress intensity factors with quarter-point elements." International Journal of Fracture 32.2 (1986): 127-140.

[159] Lim, I. L., I. W. Johnston, and S. K. Choi. "On stress intensity factor computation from the quarter-point element displacements." International Journal for Numerical Methods in Biomedical Engineering 8.5 (1992): 291-300.

[160] Lim, I. L., I. W. Johnston, and S. K. Choi. "Comparison between various displacement-based stress intensity factor computation techniques." International Journal of Fracture 58.3 (1992): 193-210.

[161] Rooke, David Percy, and David John Cartwright. "Compendium of stress intensity factors." Procurement Executive, Ministry of Defence. H. M. S. O. 1976, 330 p(Book). (1976).

[162] Nishioka, T., and S. N. Atluri. "Path-independent integrals, energy release rates, and general solutions of near-tip fields in mixed-mode dynamic fracture mechanics." Engineering Fracture Mechanics 18.1 (1983): 1-22.

[163] Nishioka, T., and S. N. Atluri. "On the computation of mixed-mode K-factors for a dynamically propagating crack, using path-independent integrals J'k." Engineering Fracture Mechanics 20.2 (1984): 193-208.

[164] Irwin, George Rankin. Onset of fast crack propagation in high strength steel and aluminum alloys. No. NRL-4763. Naval Research Lab Washington DC, 1956.

[165] Inglis, Charles Edward. "Stresses in a plate due to the presence of cracks and sharp corners." Transactions of the institute of naval architects 55, no. 219-241 (1913): 193-198.

[166] Zhu, Xian-Kui, and James A. Joyce. "Review of fracture toughness (G, K, J, CTOD, CTOA) testing and standardization." Engineering Fracture Mechanics 85 (2012): 1-46.

[167] Li, M., M. Lei, C. Shi, P. H. Wen, and M. H. Aliabadi. "On the validation of Williams' stress function for dynamic fracture mechanics." Key Engineering Materials 665 (2015): 257.

[168] Hilber, Hans M., Thomas JR Hughes, and Robert L. Taylor. "Improved numerical dissipation for time integration algorithms in structural dynamics." Earthquake Engineering & Structural Dynamics 5, no. 3 (1977): 283-292.

[169] Williams, M. L. "Stress singularities resulting from various boundary conditions in angular corners of plates in extension." Journal of applied mechanics 19, no. 4 (1952): 526-528.

[170] Muskhelishvili, N.I., “Some Basic Problems of the Mathematical Theory of Elasticity”, P. Noordhoff Ltd., Groningen, Holland, 1953.

[171] Timoshenko, S. P., and J. N. Goodier. "Theory of Elasticity”, McGraw-Hill, New York, 1970.

Appendix A

A.1 Algorithms for Constructing the Differential Matrix D_0

In Chapter 3 of this thesis, the Lagrange series interpolation is employed for the numerical interpolation of the finite block method. The following algorithm computes the first order differential matrix $\mathbf{D_0}$ which is the coefficient term from the Lagrange series interpolation.

The code below is for MATLAB:

```
clear all
% Number of points for Lagrange interpolation
nx=11;
ny=11;
x=linspace(-1,1,nx);
y=linspace(-1,1,ny);
% Points in global numbering system
[xm,ym]=meshgrid(x,y);
%Total number of nodes
M=nx*ny;
X=reshape(xm',M,1);
Y=reshape(ym',M,1);
% Construct first order differential matrix D0
for i=1:nx
   xi=x(i);
   U=routine_lag_D0(nx,x,xi);
   for j=1:ny
```

```
        D0(i,j)=U(j);
    end
end
%Function for construct first order differential matrix D0
function [U]=routine_lag_D0(n,x,xi)
for k=1:n
    DC=1;
    for i=1:n
        if k~=i
            DC=DC*(x(k)-x(i));
        end
    end
    D1=0;
    for i=1:n
        if i~=k
        D2=1;
            for j=1:n
                if j~=k && j~=i
                    D2=D2*(xi-x(j));
                end
            end
            D1=D1+D2;
        end
```

```
    end
    U(k)=D1/DC;
end
```

Appendix B1

B1.1 Standard Elasticity Equations

In the absence of body forces, the equilibrium equation for a plane elasticity (plane strain and plane stress) problem is given as

$$\frac{\partial \sigma_{xx}}{\partial \sigma_x} + \frac{\partial \sigma_{xy}}{\partial \sigma_y} = 0 \quad ,$$

$$\frac{\partial \sigma_{xy}}{\partial \sigma_x} + \frac{\partial \sigma_{yy}}{\partial \sigma_y} = 0 \quad , \tag{B1.1}$$

where σ_{xx}, σ_{yy} and σ_{xy} are the stress components in the Cartesian coordinate system.

Relationship between the strain-displacement is given by

$$\varepsilon_{xx} = \frac{\partial u_x}{\partial x} \quad , \tag{B1.2a}$$

$$\varepsilon_{yy} = \frac{\partial u_y}{\partial y} \quad , \tag{B1.2b}$$

$$\varepsilon_{xy} = \frac{1}{2}\left(\frac{\partial u_x}{\partial y} + \frac{\partial u_y}{\partial x} \right) \quad , \tag{B1.2c}$$

where ε_{xx}, ε_{yy} and ε_{xy} are the strain components, u_x and u_y are the displacement components in Cartesian coordinate system (x,y).

The stress-strain relationship

$$\sigma_{xx} = \lambda^* \left(\varepsilon_{xx} + \varepsilon_{yy} \right) + 2\mu\varepsilon_{xx} \quad ,$$

$$\sigma_{yy} = \lambda^* \left(\varepsilon_{xx} + \varepsilon_{yy} \right) + 2\mu\varepsilon_{yy} \quad ,$$

$$\sigma_{xy} = 2\mu\varepsilon_{xy} \quad . \tag{B1.3}$$

Eq. (B1.3) can be written as such

$$\varepsilon_{xx} = \frac{1}{2\mu}\left[\sigma_{xx} - \frac{\lambda^*}{2\left(\lambda^* + \mu\right)}\left(\sigma_{xx} + \sigma_{yy}\right)\right],$$

$$\varepsilon_{yy} = \frac{1}{2\mu}\left[\sigma_{yy} - \frac{\lambda^*}{2\left(\lambda^* + \mu\right)}\left(\sigma_{xx} + \sigma_{yy}\right)\right],$$

$$\varepsilon_{xy} = \frac{1}{2\mu}\sigma_{xy}\ , \tag{B1.4}$$

where μ is the shear modulus and λ^* is given by

$\lambda^* = \frac{3-\kappa}{\kappa-1}\mu$. For Plane stress $\kappa = 3-\nu/1+\nu$ and for plane strain $\kappa = 3-4\nu$. ν is the Poisson's ratio.

B1.2 The Compatibility Equation

By differentiating Eq. (B1.2a) twice with respect to *y*, differentiating Eq. (B1.2b) twice with respect to *x* and differentiating Eq. (B1.2c) once with respect to *x* and *y*, we can eliminate the displacement from the equations. The final expression after the differentiation;

$$\frac{\partial^2 \varepsilon_{xx}}{\partial y^2} = \frac{\partial^3 u_x}{\partial x \partial y^2}\ , \tag{B1.5a}$$

$$\frac{\partial^2 \varepsilon_{yy}}{\partial x^2} = \frac{\partial^3 u_y}{\partial x^2 \partial y}\ , \tag{B1.5b}$$

$$\frac{\partial^2 \varepsilon_{xy}}{\partial x \partial y} = \frac{1}{2}\left(\frac{\partial^3 u_x}{\partial x \partial y^2} + \frac{\partial^3 u_y}{\partial x^2 \partial y}\right). \tag{B1.5c}$$

Substituting Eq. (B1.5a) and Eq. (B1.5b) into Eq. (B1.5c) give the compatibility equation as follows

$$\frac{\partial^2 \varepsilon_{xx}}{\partial y^2} + \frac{\partial^2 \varepsilon_{yy}}{\partial x^2} = 2\frac{\partial^2 \varepsilon_{xy}}{\partial x \partial y}\ . \tag{B1.6a}$$

Pulling together Eq. (B1.1) and Eq. (B1.4), Eq. (B1.6a) can be written as

$$\nabla^2\left(\sigma_{xx}+\sigma_{yy}\right)=0\ , \tag{B1.6b}$$

where the Laplace operator ∇^2 is given by

$\nabla^2=\dfrac{\partial^2}{\partial x^2}+\dfrac{\partial^2}{\partial y^2}$ in the Cartesian coordinate system and in the polar coordinate system (r,θ), $\nabla^2=\dfrac{\partial^2}{\partial r^2}+\dfrac{1}{r}\dfrac{\partial}{\partial r}+\dfrac{1}{r^2}\dfrac{\partial^2}{\partial \theta^2}$.

B1.3 The Airy Stress Function

The Airy stress function is an effective technique used for solving two-dimensional equilibrium problems. For a two-dimensional elasticity problem, the stresses are expressed in terms of the Airy stress function ϕ as

$$\sigma_{xx}=\frac{\partial^2\phi}{\partial y^2}\ ,\ \sigma_{yy}=\frac{\partial^2\phi}{\partial x^2}\ ,\ \sigma_{xy}=-\frac{\partial^2\phi}{\partial x\partial y}\ . \tag{B1.7}$$

B1.4 The Biharmonic Equation

For an elasticity problem, it is normal to solve for the displacement, the strain and the stress in the order as it is stated. However, by expressing the stress in terms of the Airy stress function we can bypass the displacement approach completely. Therefore, the displacement can be ignored and we can solve for only the stress and the strain. However, there is a caveat. When solving for the strain without the displacement, it is expected that the compatibility equation is satisfied.

Since the equilibrium equation Eq. (B1.1) is satisfied by the conditions of the compatibility equation according to the definitions in Eq. (B1.7). Thus, the compatibility equation Eq. (B1.6b) can be expressed as

$$\nabla^4\phi=\nabla^2\nabla^2\phi=0\ , \tag{B1.8}$$

where

$$\nabla^4=\nabla^2\nabla^2=\frac{\partial^4}{\partial x^4}+\frac{\partial^4}{\partial y^4}+2\frac{\partial^4}{\partial x^2\partial y^2} \tag{B1.9}$$

is the biharmonic operator. Leading to

$$\frac{\partial^4\phi}{\partial x^4}+\frac{\partial^4\phi}{\partial y^4}+2\frac{\partial^4\phi}{\partial x^2\partial y^2}=0 \text{ for plane stress and} \tag{B1.10}$$

$$\left(\frac{\partial^4\phi}{\partial x^4}+\frac{\partial^4\phi}{\partial y^4}+2\frac{\partial^4\phi}{\partial x^2\partial y^2}\right)(1-\nu)=0 \text{ for plane strain.} \tag{B1.11}$$

Eq. (B1.10) and Eq. (B1.11) are termed the biharmonic equations.

B1.5 The Williams Eigenfunction Expansion Series

The Williams [18,104] eigenfunction expansion method is fundamental to the study of the stress and displacement fields near the crack tip. As it was explained in Chapter 4, the stress and displacement can be expressed in terms of the Airy stress function ϕ which satisfies the biharmonic equation, Eq. (B1.8).

It has been shown that an expansion of the Airy stress function around the crack tip as shown in Fig. B1.1 can be written in a series form [104] as follows

$$\phi=\sum_{n=0}^{\infty} r^{\lambda_{n+1}}F_n(\theta)\ , \tag{B1.12}$$

where λ_n as expressed in the series are the eigenvalues which is yet to be determine. $F_n(\theta)$ are the corresponding eigenfunctions.

Substituting Eq. (B1.12) into the biharmonic equation Eq. (B1.11) where the Laplace operator is in the polar form (r,θ) as defined in Fig. B1.1, gives

$$\frac{d^4F_n(\theta)}{d\theta^4}+2\left(\lambda_n^2+1\right)\frac{d^2F_n(\theta)}{d\theta^2}+\left(\lambda_n^2-1\right)^2F_n(\theta)=0\ . \tag{B1.13}$$

By integrating Eq.(B1.13) leads to the following solution

$$\begin{aligned}F_n(\theta)=&A_n\sin(\lambda_n+1)\theta+B_n\cos(\lambda_n+1)\theta\\&+C_n\sin(\lambda_n-1)\theta+D_n\cos(\lambda_n-1)\theta\quad ,\end{aligned} \tag{B1.14}$$

where A_n, B_n, C_n and D_n are unknown constants which are yet to be determined using the stress boundary conditions

$\sigma_{\theta\theta} = \sigma_{r\theta} = 0$, at $\theta = \pm\pi$ along the crack surface. (B1.15)

B1.5.1 Mode I Crack for a Homogeneous Plate

For a mode I crack, the Airy stress function is described as an even function of θ. Therefore, the constants A_n and C_n in Eq. (B1.14) becomes zero. Therefore, Eq. (B1.12) is updated to give

$$\phi = \sum_{n=0}^{\infty} r^{\lambda_n+1}\left[B_n \cos(\lambda_n+1)\theta + D_n \cos(\lambda_n-1)\theta\right]. \quad \text{(B1.16)}$$

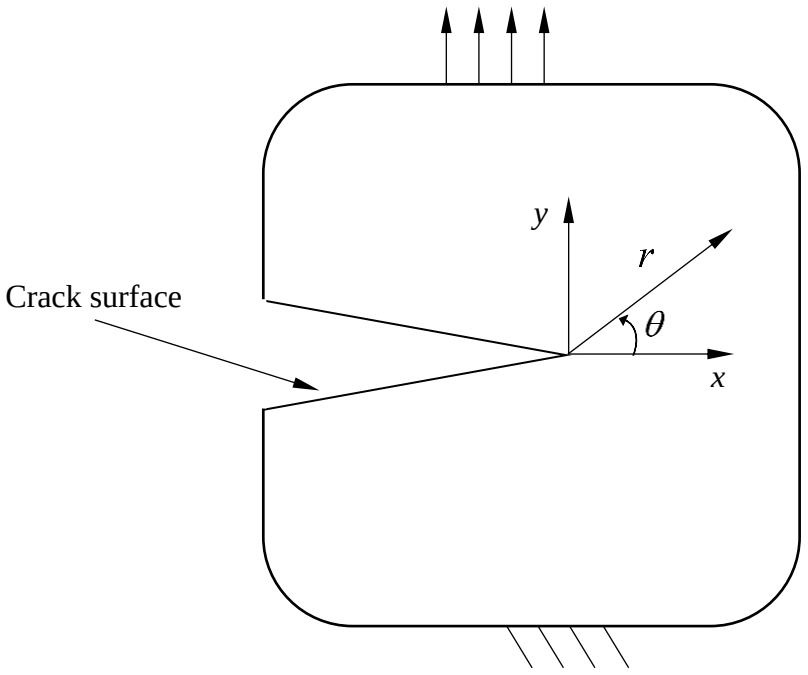

Figure B1.1 The 2D cracked plate showing the coordinate system.

Using the Airy stress function in the polar form, the stresses around the crack tip is approximated as follows

$$\sigma_{rr} = \frac{1}{r}\frac{\partial\phi}{\partial r} + \frac{1}{r^2}\frac{\partial^2\phi}{\partial\theta^2}$$

$$= \sum_{n=0}^{\infty} r^{\lambda_n - 1}\left[F_n^{''}(\theta) + (\lambda_n + 1)F_n(\theta)\right]$$

$$= -\sum_{n=0}^{\infty} \lambda_n r^{\lambda_n - 1}\left[B_n(\lambda_n + 1)\cos(\lambda_n + 1)\theta + D_n(\lambda_n - 3)\cos(\lambda_n - 1)\theta\right] \quad , \tag{B1.17a}$$

$$\sigma_{\theta\theta} = \frac{\partial^2 \phi}{\partial r^2} = \sum_{n=0}^{\infty} \lambda_n r^{\lambda_n - 1}(\lambda_n + 1)F_n(\theta)$$

$$= \sum_{n=0}^{\infty} \lambda_n r^{\lambda_n - 1}(\lambda_n + 1)\left[B_n \cos(\lambda_n + 1)\theta + D_n(\lambda_n - 1)\cos(\lambda_n - 1)\theta\right] , \tag{B1.17b}$$

$$\sigma_{r\theta} = -\frac{\partial}{\partial r}\left(\frac{1}{r}\frac{\partial \phi}{\partial \theta}\right) = -\sum_{n=0}^{\infty} \lambda_n r^{\lambda_n - 1}F_n^{'}(\theta)$$

$$= \sum_{n=0}^{\infty} \lambda_n r^{\lambda_n - 1}\left[B_n(\lambda_n + 1)\sin(\lambda_n + 1)\theta + D_n \sin(\lambda_n - 1)\theta\right] . \tag{B1.17c}$$

An expression for the displacement in the polar form is achieved using Hooke's law and strain-displacement relationship stated as follows:

$$\frac{\partial u_r}{\partial r} = \varepsilon_{rr} = \frac{1}{2\mu}\left[\sigma_{rr} - \frac{3-\kappa}{4}(\sigma_{rr} + \sigma_{\theta\theta})\right] \quad , \tag{B1.18a}$$

$$\frac{u_r}{r} + \frac{1}{r}\frac{\partial u_\theta}{\partial \theta} = \varepsilon_{\theta\theta} = \frac{1}{2\mu}\left[\sigma_{\theta\theta} - \frac{3-\kappa}{4}(\sigma_{rr} + \sigma_{\theta\theta})\right] \quad , \tag{B1.18b}$$

$$\frac{1}{r}\frac{\partial u_r}{\partial \theta} + r\frac{\partial}{\partial r}\left(\frac{u_\theta}{r}\right) = \varepsilon_{r\theta} = \frac{1}{2\mu}\sigma_{r\theta} , \tag{B1.18c}$$

where κ and μ retain the same definitions as stated in Eq. (B1.4).

Replace the stresses in Eq. (B1.18) with the definitions from Eq.(B1.17) to get

$$u_r = \frac{1}{2\mu}\sum_{n=0}^{\infty} r^{\lambda_n}\left\{-(\lambda_n + 1)F_n(\theta) + (1+\kappa)D_n \cos(\lambda_n - 1)\theta\right\} , \tag{B1.19a}$$

$$u_\theta = \frac{1}{2\mu}\sum_{n=0}^{\infty} r^{\lambda_n}\left\{-F_n^{'}(\theta) + (1+\kappa)D_n \sin(\lambda_n - 1)\theta\right\} . \tag{B1.19b}$$

Now, apply the boundary conditions from Eq. (B1.15) to the stress equations, Eq. (B1.17) and this will result in the following simultaneous equation in terms of B_n and D_n .

$$B_n \cos(\lambda_n + 1)\pi + D_n \cos(\lambda_n - 1)\pi = 0 \ , \tag{B1.20a}$$

$$B_n(\lambda_n + 1)\sin(\lambda_n + 1)\pi + D_n(\lambda_n - 1)\sin(\lambda_n - 1)\pi = 0 \ . \tag{B1.20b}$$

For non-trivial solution of B_n and D_n , the following characteristic equation of the eigenvalue λ_n is valid;

$$\sin(2\lambda_n \pi) = 0 \tag{B1.21}$$

and the corresponding eigenvalues are

$$\lambda_n = \frac{n}{2}, \quad n = 0, \ \pm 1, \ \pm 2, \ \ldots . \tag{B1.22}$$

Ignore all negative values since it has no physical meaning. Also, for $n = 0$ will lead to infinite displacement. Thus, Eq. (B1.22) reduces to

$$\lambda_n = \frac{n}{2}, \quad n = 1, \ 2, \ \ldots \tag{B1.23}$$

Applying the eigenvalues from Eq. (B1.23) to Eq. (B1.20) leads to

$$B_n = -\frac{\left(\frac{n}{2} - 1\right)\sin\left(\frac{n}{2} - 1\right)\pi}{\left(\frac{n}{2} + 1\right)\sin\left(\frac{n}{2} + 1\right)\pi} D_n = -\left(\frac{n-2}{n+2}\right) D_n \ , \text{ valid for } n = 1, 3, 5, ... \tag{B1.24a}$$

$$B_n = -\frac{\cos\left(\frac{n}{2} - 1\right)\pi}{\cos\left(\frac{n}{2} + 1\right)\pi} D_n = -D_n \ , \text{ valid for } n = 2, \ 4, 6, ... \tag{B1.24b}$$

By substituting the eigenvalues from Eq. (B1.23) into the stress equations, Eq. (B1.17) gives

$$\sigma_{rr} = -\sum_{n=0}^{\infty} \frac{n}{2} r^{\frac{n}{2}-1} \left[B_n \left(\frac{n}{2}+1 \right) \cos\left(\frac{n}{2}+1 \right)\theta + D_n \left(\frac{n}{2}-3 \right) \cos\left(\frac{n}{2}-1 \right)\theta \right] \quad , \tag{B1.25a}$$

$$\sigma_{\theta\theta} = \sum_{n=0}^{\infty} \frac{n}{2} r^{\frac{n}{2}-1} \left(\frac{n}{2}+1 \right) \left[B_n \cos\left(\frac{n}{2}+1 \right)\theta + D_n \cos\left(\frac{n}{2}-1 \right)\theta \right] , \tag{B1.25b}$$

$$\sigma_{r\theta} = \sum_{n=0}^{\infty} \frac{n}{2} r^{\frac{n}{2}-1} \left[B_n \left(\frac{n}{2}+1 \right) \sin\left(\frac{n}{2}+1 \right)\theta + D_n \left(\frac{n}{2}-1 \right) \sin\left(\frac{n}{2}-1 \right)\theta \right] . \tag{B1.25c}$$

Note that the above equation is satisfied by the relationship between B_n and D_n as expressed in Eq. (B1.24).

Eq. (B1.25) is rearranged as follows, using the first two terms $n = 1,\ 2$ from Eq. (B1.24) and expressed in terms of D_n :

$$\sigma_{rr} = D_1 r^{-\frac{1}{2}} \left[-\frac{1}{4} \cos\left(\frac{3\theta}{2} \right) + \frac{5}{4} \cos\left(\frac{\theta}{2} \right) \right] + 2D_2 \cos(2\theta) + 2D_2 + O\left(r^{\frac{1}{2}} \right) , \tag{B1.26a}$$

$$\sigma_{\theta\theta} = D_1 r^{-\frac{1}{2}} \left[\frac{1}{4} \cos\left(\frac{3\theta}{2} \right) + \frac{3}{4} \cos\left(\frac{\theta}{2} \right) \right] - 2D_2 \cos(2\theta) + 2D_2 + O\left(r^{\frac{1}{2}} \right) , \tag{B1.26b}$$

$$\sigma_{r\theta} = D_1 r^{-\frac{1}{2}} \left[\frac{1}{4} \sin\left(\frac{3\theta}{2} \right) + \frac{1}{4} \sin\left(\frac{\theta}{2} \right) \right] - 2D_2 \sin(2\theta) + O\left(r^{\frac{1}{2}} \right) \quad . \tag{B1.26c}$$

By setting $n = 1$ in Eq. (B1.26a), the first term results in a singularity at the crack tip. Therefore, D_1 in the first term relates to the stress intensity factor and D_2 in the second term relates to the T-stress at the crack tip.

The Cartesian form of the above stress expressions for the series is given below:

$$\sigma_{xx} = D_1 r^{-\frac{1}{2}} \cos\frac{1}{2}\theta \left(1 - \sin\frac{1}{2}\theta \sin\frac{3}{2}\theta \right) + T + O\left(r^{\frac{1}{2}} \right) \quad , \tag{B1.27a}$$

$$\sigma_{yy} = D_1 r^{-\frac{1}{2}} \cos\frac{1}{2}\theta \left(1 + \sin\frac{1}{2}\theta \sin\frac{3}{2}\theta \right) + O\left(r^{\frac{1}{2}} \right) , \tag{B1.27b}$$

$$\sigma_{xy} = D_1 r^{-\frac{1}{2}} \sin\frac{1}{2}\theta \cos\frac{1}{2}\theta \cos\frac{3}{2}\theta + O\left(r^{\frac{1}{2}} \right) \quad . \tag{B1.27c}$$

where $T = 4D_2$ is the T-stress.

A similar process exists for deriving the mode II and mode III expressions for the Williams expansion series. Further information is covered by the following references [15, 104].

Appendix B2

B2.1 The Method of Complex Potentials

The displacement and stress field for a two-dimensional plane elasticity problem are easily evaluated using the complex potential method proposed by Muskhelishvili [170]. The viability of this method is based on the Airy stress functions ϕ.

B2.1.1 Airy Stress Function Expressed in Terms of Complex Potential

The complex variable *z* in the Cartesian coordinate system is defined as

$$z = x + iy \tag{B2.1}$$

and the complex conjugate

$$\bar{z} = x - iy \tag{B2.2}$$

where $i = \sqrt{-1}$.

The polar form of the complex variable is expressed as

$$z = r(\cos\theta + i\sin\theta) = re^{i\theta} \tag{B2.3}$$

and the complex conjugate

$$\bar{z} = r(\cos\theta - i\sin\theta) = re^{-i\theta}. \tag{B2.4}$$

Using the complex variable *z*, a complex function $f(z)$ can exist. Therefore, the derivative of the function $f(z)$ is easily determined with respect to *z*.

According to the Cauchy-Riemann equation, the function $f(z)$ can be shown to be analytical when the real and imaginary parts are harmonic.

Also, stated in Eq. (B1.7) the Airy stress function is a biharmonic function, therefore we can introduce a new function $P(x, y)$ as such

$$\nabla^2\phi = P \tag{B2.5}$$

From Eq. (B2.5), it can be said that the function $P(x,y)$ is harmonic when expressed as

$$\nabla^2 P = \nabla^2\nabla^2\phi = 0 \tag{B2.6}$$

Now let $Q(x,y)$ be the harmonic conjugate of $P(x,y)$. Therefore, the analytical function $f(z)$ can be expressed as

$$f(z) = P + iQ = 0 \ . \tag{B2.7}$$

Likewise, let

$$\psi(z) = \frac{1}{4}\int f(z)dz = p + iq \ . \tag{B2.8}$$

Then the derivative of ψ

$$\psi'(z) = \frac{1}{4} f(z) \tag{B2.9a}$$

and according to the Cauchy-Riemann equations gives

$$\psi'(z) = \frac{\partial p}{\partial x} + i\frac{\partial q}{\partial x} = \frac{\partial p}{\partial y} - i\frac{\partial q}{\partial y} \ . \tag{B2.9b}$$

Thus

$$\frac{\partial p}{\partial x} = \frac{\partial q}{\partial y} = \frac{1}{4}P \ , \ \frac{\partial p}{\partial y} = -\frac{\partial q}{\partial x} = -\frac{1}{4}Q \ . \tag{B2.10}$$

Making *P* and *Q* the subject of the equation gives

$$P = 4\frac{\partial p}{\partial x} = 4\frac{\partial q}{\partial y} \ , \ Q = -4\frac{\partial p}{\partial y} = 4\frac{\partial q}{\partial x} \ . \tag{B2.11}$$

Now consider the function $\phi - (xp + yq)$ which can be shown to be harmonic is defined as

$$\nabla^2\left[\phi - (xp + yq)\right] = 0 \tag{B2.12}$$

and forms a real or imaginary part of another function $\chi(z)$.

Now consider the real part of the function $\chi(z)$

$$\phi-(xp+yq)=\mathrm{Re}[\chi(z)]\ . \tag{B2.13}$$

Using the relationship where $\bar{z}=x-iy$ gives

$$(xp+yq)=\mathrm{Re}[\bar{z}\,\psi(z)]. \tag{B2.14}$$

Substituting Eq. (B2.14) into Eq. (B2.13) gives the Airy stress function expressed in terms of the complex potential method as

$\phi(x,y)=\mathrm{Re}\{\bar{z}\,\psi(z)+\chi(z)\}$ or

$$2\phi(x,y)=\bar{z}\,\psi(z)+z\overline{\psi(z)}+\chi(z)+\overline{\chi(z)}\ . \tag{B2.15}$$

Using the definitions for the Airy stress function in Eq. (B1.7) and Eq. (B2.15), we obtained

$$\frac{\partial\phi}{\partial x}+i\frac{\partial\phi}{\partial y}=\psi(z)+z\overline{\psi'(z)}+\overline{\chi'(z)}\ . \tag{B2.16}$$

Noting the following definitions

$$\frac{\partial}{\partial x}=\frac{\partial}{\partial z}+i\frac{\partial}{\partial\bar{z}} \text{ and } \frac{\partial}{\partial y}=i\left(\frac{\partial}{\partial z}-\frac{\partial}{\partial\bar{z}}\right) \text{ gives} \tag{B2.17}$$

$$2\frac{\partial\phi}{\partial x}=\psi(z)+\bar{z}\,\psi'(z)+\overline{\psi(z)}+z\overline{\psi'(z)}+\chi'(z)+\overline{\chi'(z)}\ ,$$

$$2\frac{\partial\phi}{\partial y}=i\left\{-\psi(z)+\bar{z}\,\psi'(z)+\overline{\psi(z)}-z\overline{\psi'(z)}+\chi'(z)-\overline{\chi'(z)}\right\}. \tag{B2.18}$$

A simple way to express the stress and displacement in the complex potential is by using the above relationships and Eq. (B2.15) to obtain

$$\frac{\partial\phi}{\partial x}+i\frac{\partial\phi}{\partial y}=\psi(z)+z\overline{\psi'(z)}+\overline{\chi'(z)}\ . \tag{B2.19}$$

By substituting Eq. (B2.19) into a definition of stress using the Airy stress function, Eq. (B1.7) gives

$$\sigma_{xx}+i\sigma_{yy}=\psi'(z)+\overline{\psi'(z)}-z\overline{\psi''(z)}-\overline{\chi''(z)}\ , \tag{B2.20}$$

$$\sigma_{yy} - i\sigma_{xy} = \psi'(z) + \overline{\psi'(z)} + z\overline{\psi''(z)} + \overline{\chi''(z)} \ . \tag{B2.21}$$

Adding Eq. (B2.20) and (B2.21) will lead to

$$\sigma_{xx} + \sigma_{yy} = 2\left[\psi'(z) + \overline{\psi'(z)}\right] = 4\,\mathrm{Re}\left[\psi'(z)\right] . \tag{B2.22}$$

Subtracting Eq. (B2.20) from (B2.21) will lead to

$$\sigma_{yy} - \sigma_{xx} - 2i\sigma_{xy} = 2\left[z\overline{\psi''(z)} + \overline{\chi''(z)}\right] . \tag{B2.23}$$

Applying the conjugate on both sides of Eq. (B2.23) gives

$$\sigma_{yy} - \sigma_{xx} + 2i\sigma_{xy} = 2\left[\bar{z}\psi''(z) + \chi''(z)\right] . \tag{B2.24}$$

B2.1.2 Complex Potential Representation of Displacement

Using the strain-displacement relationship from Eq. (B1.18) and the stress expression in terms of the Airy stress function, Eq. (B1.7), we can substitute into Eq. (B1.3) which is the stress-strain relationship to get

$$2\mu\frac{\partial u_x}{\partial x} = \frac{\partial^2\phi}{\partial y^2} - \frac{\lambda^*}{2\left(\lambda^* + \mu\right)}\nabla^2\phi \ , \tag{B2.25}$$

$$2\mu\frac{\partial u_y}{\partial y} = \frac{\partial^2\phi}{\partial x^2} - \frac{\lambda^*}{2\left(\lambda^* + \mu\right)}\nabla^2\phi \quad , \tag{B2.26}$$

$$\mu\frac{\partial u_x}{\partial y} + \frac{\partial u_y}{\partial x} = -\frac{\partial^2\phi}{\partial x\partial y} . \tag{B2.27}$$

Substituting Eq.(B2.11) into Eq. (B2.25) and Eq. (B2.26) leads to

$$2\mu\frac{\partial u_x}{\partial x} = -\frac{\partial^2\phi}{\partial x^2} + \frac{2\left(\lambda^* + 2\mu\right)}{\left(\lambda^* + \mu\right)}\frac{\partial p}{\partial x} \ , \tag{B2.28}$$

$$2\mu\frac{\partial u_y}{\partial y} = -\frac{\partial^2\phi}{\partial y^2} + \frac{2\left(\lambda^* + 2\mu\right)}{\left(\lambda^* + \mu\right)}\frac{\partial q}{\partial y} \ . \tag{B2.29}$$

Integrate Eq. (B2.28) and (B2.29) to get the following expressions

$$2\mu u_x = -\frac{\partial \phi}{\partial x} + \frac{2\left(\lambda^* + 2\mu\right)}{\left(\lambda^* + \mu\right)} p + f_1(y) \quad \text{and} \tag{B2.30}$$

$$2\mu u_y = -\frac{\partial \phi}{\partial y} + \frac{2\left(\lambda^* + 2\mu\right)}{\left(\lambda^* + \mu\right)} q + f_2(x)\,, \tag{B2.31}$$

where $f_1(y)$ and $f_2(x)$ are the rigid body displacements which can be ignored.

Using the definition, $\psi(z) = p + iq$ from Eq. (B2.8), and the expressions from Eq. (B2.30) and Eq. (B2.31), we can substitute into the complex potential equation Eq. (B2.16) to get the following complex expression

$$2\mu\left(u_x + iu_y\right) = \kappa\psi(z) - z\overline{\psi'(z)} - \overline{\chi'(z)}\,, \tag{B2.32}$$

where $\kappa = \dfrac{\left(\lambda^* + 3\mu\right)}{\left(\lambda^* + \mu\right)}$

Altogether, the Kolosov-Muskhelishvili formulas from Eq. (B2.22), (B2.24) and (B2.32) are written below for convenience;

$$\sigma_{xx} + \sigma_{yy} = 2\left[\psi'(z) + \overline{\psi'(z)}\right] = 4\,\mathrm{Re}\left[\psi'(z)\right]\,,$$

$$\sigma_{yy} - \sigma_{xx} + 2i\sigma_{xy} = 2\left[\bar{z}\psi''(z) + \chi''(z)\right]\,,$$

$$2\mu\left(u_x + iu_y\right) = \kappa\psi(z) - z\overline{\psi'(z)} - \overline{\chi'(z)}\,. \tag{B2.33}$$

Appendix C

C.1 Introduction

In Chapter 6 of this thesis, a two-dimensional bi-material plate with a centre crack was examined under dynamic conditions using the newly developed finite block method. Due to the unavailability of an analytical solution for the two-dimensional interface cracked plate, FEM (ABAQUS) was used for the verification of the FBM method analysis.

Since FEM (ABAQUS) analysis will serve as the benchmark for the verification of the FBM solution, the accuracy of the FEM (ABAQUS) analysis is highly significant. Therefore, a mesh convergence study is required to ensure the result of the FEM (ABAQUS) dynamics analysis is not affected by a changing element size. Furthermore, the mesh convergence study must be performed under static conditions. Details of the FEM analysis is outlined below.

C.1.1 Details of FEM (ABAQUS) Model

A two-dimensional plate with a centre crack is considered for the mesh convergence study. The two-dimensional plate has the same dimensions as used in the finite block dynamic analysis. Due to symmetry with respect to the *y* axis, it is equivalent to solve the boundary value problem for a half plate. The ABAQUS model of the plate and the various boundary conditions is shown in Fig. C.1. The static analysis is performed for a plane stress state. The stress intensity factor has been deemed to be the critical parameter for the mesh convergence study. Therefore, an output request for the SIF was chosen in ABAQUS. Since ABAQUS uses the contour integral to determine the stress intensity factor, the total number of contours for this analysis is chosen to be 5. The elastic modulus $E=1$ and Poisson's ratio $\nu=0.3$. These values of the material property are maintained for the different convergence trial study. A uniform tensile stress $\sigma=1$ is applied at the top and bottom of the plate.

Since the stress at the crack tip will lead to large deformations, the standard quadratic elements provided by ABAQUS is deemed adequate for the mesh convergence study.

The version of ABAQUS used for this study: ABAQUS/CAE 6.9-2

ABAQUS quadratic element type: CPS8R

Quarter point elements with ABAQUS singularity control was employed in this analysis.

The FEM model showing the different number of elements is presented in Fig. C.2 through C.4.

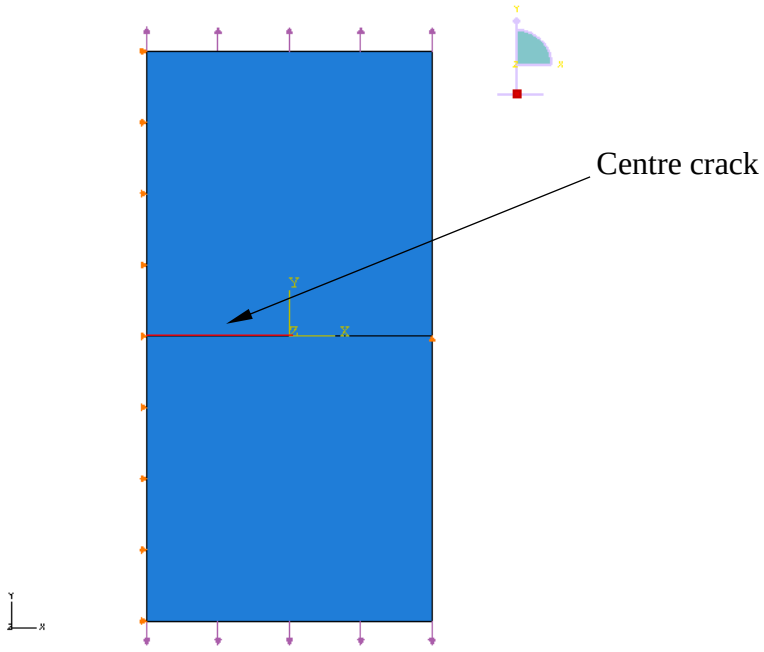

Figure C.1 An FEM model of the cracked plate subjected to a uniform uniaxial stress at the top and bottom.

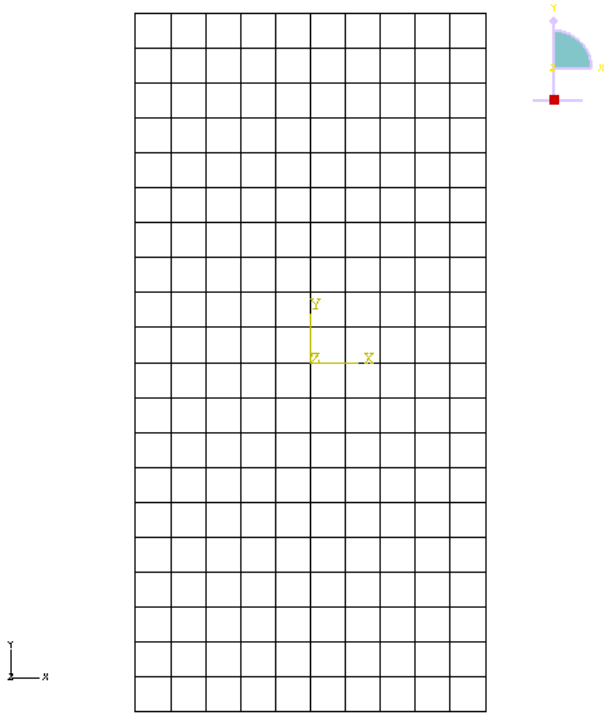

Figure C.2 FEM model with 10 x 20 elements

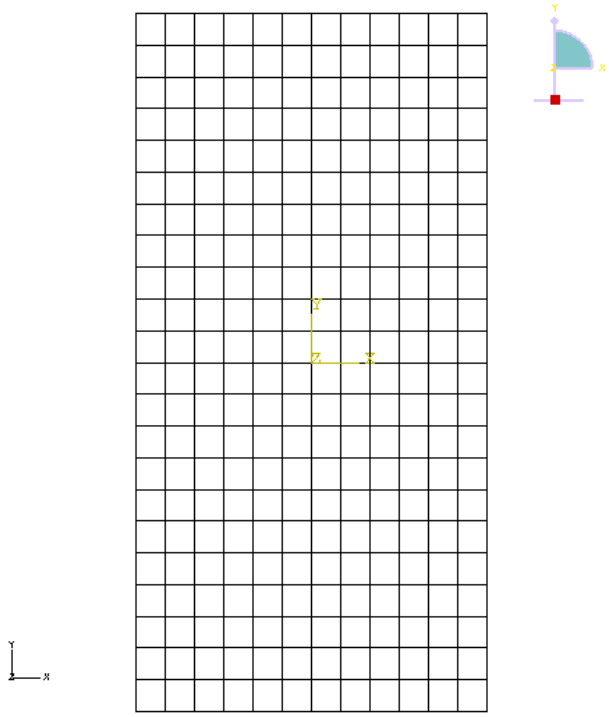

Figure C.3 FEM model with 12 x 22 elements

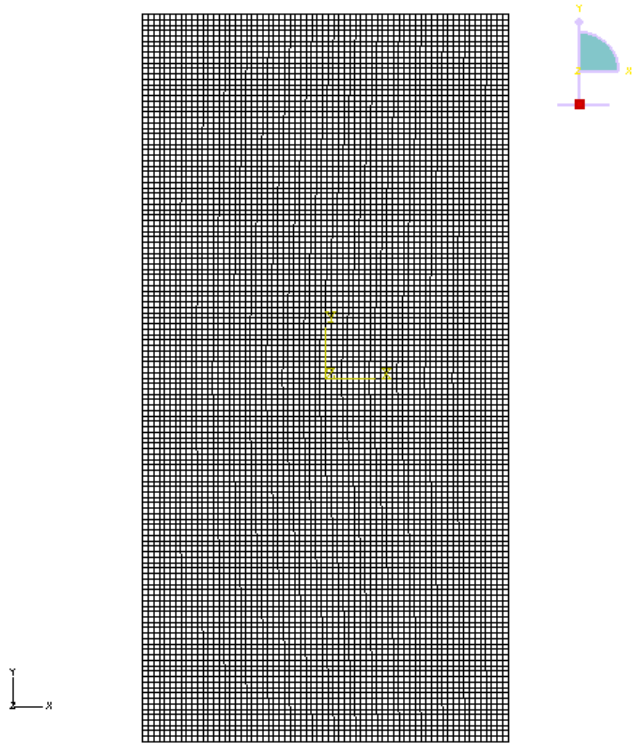

Figure C.4 FEM model with a total number of elements = 8978

C.1.2 Mesh Convergence Analysis and Results

In performing the convergence study, 8 successive runs of the FEM analysis were carried out and each time the number of elements was increased. The number of elements used in this study ranges from 200 to 8978. For every run of the FEM analysis the average stress intensity factor is recorded as shown in Table C.1.

The stress intensity factors are plotted against the number of elements as shown in Fig C.5. For verification purposes, the analytical solution for the stress intensity factor as provided by Rooke [161] is also plotted on the same graph.

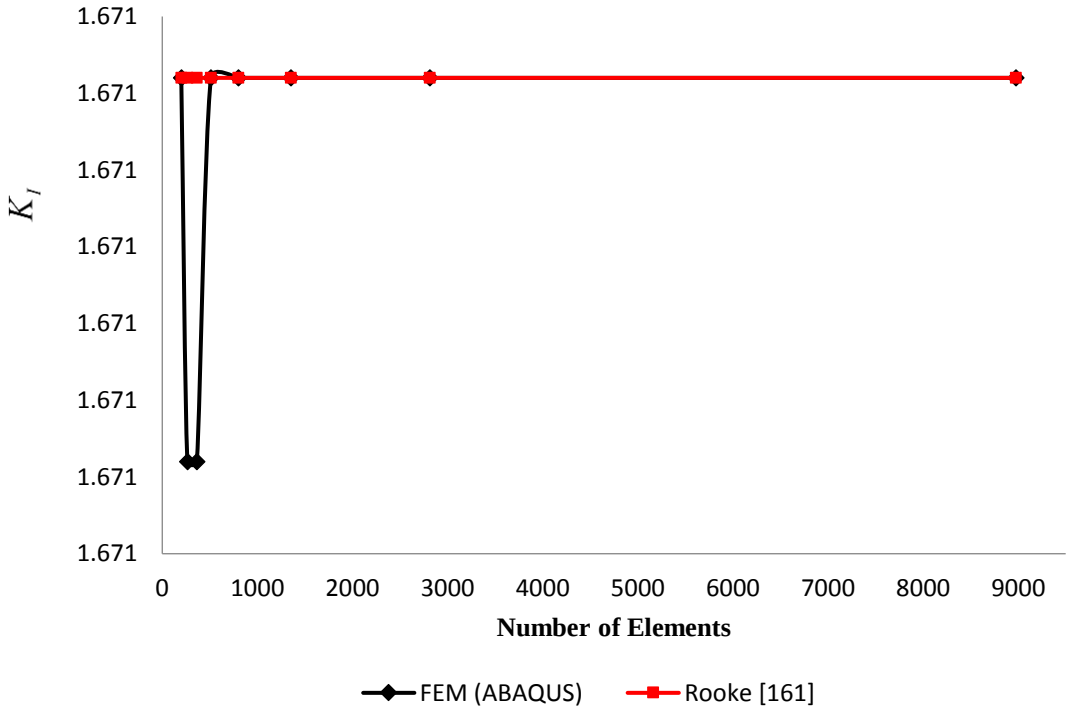

Figure C.5 An 8-point convergence graph. By using the stress intensity factor as the critical parameter which is determined by ABAQUS for every variation in the number of elements.

Analysis No.	Number of Nodes	Number of Elements	Average K_I
1	671	200	1.6713
2	873	264	1.6710
3	1187	364	1.6710
4	1649	512	1.6713
5	2541	800	1.6713
6	4239	1352	1.6713
7	8699	2812	1.6713
8	27405	8978	1.6713

Table C.1 The average stress intensity factor values as determined by ABAQUS using 5 contours for the *J*-Integral method.

The last 5 points shows that the stress intensity factor has converged. Therefore, the ABAQUS dynamic analysis as reported in this thesis utilised the final mesh with a total of 8978 elements.